University of Bath

PHD

Development, evaluation and applications of the Cyclops-DP Weather Radar Processing system

Darlington, Timothy

Award date:
2015

Awarding institution:
University of Bath

Link to publication

Alternative formats
If you require this document in an alternative format, please contact:
openaccess@bath.ac.uk

Copyright of this thesis rests with the author. Access is subject to the above licence, if given. If no licence is specified above, original content in this thesis is licensed under the terms of the Creative Commons Attribution-NonCommercial 4.0 International (CC BY-NC-ND 4.0) Licence (https://creativecommons.org/licenses/by-nc-nd/4.0/). Any third-party copyright material present remains the property of its respective owner(s) and is licensed under its existing terms.

Take down policy
If you consider content within Bath's Research Portal to be in breach of UK law, please contact: openaccess@bath.ac.uk with the details. Your claim will be investigated and, where appropriate, the item will be removed from public view as soon as possible.

Download date: 05. May. 2023

THE UNIVERSITY OF BATH

Development, evaluation and applications of the Cyclops-DP Weather Radar Processing system

by

Timothy Darlington

A thesis submitted for the degree of Doctor of Philosophy

University of Bath
Faculty of Engineering and Design
Department of Electronic and Electrical Engineering

September 2013

Copyright

Attention is drawn to the fact that copyright of this thesis rests with the author. A copy of this thesis has been supplied on condition that anyone who consults it is understood to recognise that its copyright rests with the author and that they must not copy it or use material from it except as permitted by law or with the consent of the author. This thesis may not be consulted, photocopied or lent to other libraries without the permission of the author for 3 years from the date of acceptance of the thesis.

_____

Timothy Darlington

Abstract

The move to increasingly high resolution numerical weather prediction models has created a demand for high resolution observations over wide areas, for model initialisation. The weather radar network is a valuable source of such observations. To address this requirement and increasing concerns of obsolescence in the UK Weather Radar network a program of renewal was undertaken. This resulted in the creation of the Cyclops-DP, dual polarisation weather radar processing and control system, which was used as a platform from which investigation of novel radar observables could be undertaken.

The retrieval of near-surface refractivity changes, using fixed clutter targets is investigated. It is shown that by combining dual polarisation measurements, an improvement in the correlation with surface observations is obtained. A novel method of determining the target location within the range gate, with the aim of reducing the bias and error in the refractivity retrievals, is tested but not shown to give benefit.

The development of, what is thought to be, the first combined dual polarization weather radar and radiometer is described. It is shown that useful radiometric measurements can be made using conventional radar hardware and with relatively minor changes, the radar radiometric sensitivity is improved by a factor of 3.5. The sensitivity of the atmospheric background noise temperature to changes in temperature and pressure, as a function of elevation, at C band is investigated for the purposes of radiometric calibration. It is shown that a climatological profile can be used in calibrations with certain caveats. A comparison of different methods of estimating the path integrated attenuation is presented and demonstrates that the radiometry-based estimates have skill and benefits compared to other techniques. The potential for using radiometric measurements to estimate partial beam blocking is demonstrated.

Acknowledgements

I would like to thank my supervisor, Robert Watson for his support and encouragement. The members of the Met Office radar development team, for making this work possible. In particular I would like to thank Malcolm Kitchen, and Jacqueline Sugier, Mike Edwards, Vic Lissaman, and Richard Riley. My family for all their love and support through the years. And Katie Norman for all her love and encouragement.

Dedication

To the memory of Linda Darlington.

Contents

List of Figures

List of Tables

Abbreviations

ADC	Analogue to Digital Converter
ADER	Additional Data from Existing Radars
AFC	Automatic Frequency Control
CAN	Controller Area Network
CFIR	Compensating FIR
CI	Clutter Indicator
CIC	Cascaded Integrator-Comb
ρ_{hv}	Co-polar correlation coefficient
CPA	Clutter Phase Alignment
ϕ_{dp}	Differential phase
DAC	Digital to Analogue Converter
DDC	Digital Down Conversion
DDS	Direct Digital Synthesizer
DMA	Direct Memory Access
DSP	Digital Signal Processor
EEC	Enterprise Electronics Corporation
ENOB	Equivalent number of bits.
ENR	Excess Noise Ratio
FIFO	First in first out
FIR	Finite Impulse Response filter
FPGA	Field Programmable Gate Array

HDL	Hardware Design Language
HIL	Hardware interface layer
I and Q	In-phase and Quadrature baseband complex signals
IF	Intermediate Frequency
IGBT	Insulated Gate Bipolar Transistor
IO	Input/Output
IP	Internet Protocol
II	Innovative Integration
LDR	Linear Depolarisation Ratio
LP	Long Pulse
LUT	Look-Up Table
LVCMOS	Low Voltage Complementary Metal Oxide Semiconductor
LVTTL	Low Voltage Transistor-Transistor Logic
MSPS	Mega Samples per Second
NCO	Numerically Controlled Oscillator
NWP	Numerical Weather Prediction
OSA	Open System Architecture
PCI/PCIe	Peripheral Component Interconnect/Express
PFIR	Programmable FIR
PLL	Phase Locked Loop
PMC	PCI Mezzanine Card
PPI	Plan Position Indicator

PPP	Pulse Pair Processing
PRF	Pulse Repetition Frequency
PRT	Pulse Repetition Time
QPE	Quantitative precipitation estimation
RHI	Range Height Indicator
RMS	Root Mean Square
Rx	Receiver
SDRAM	Synchronous Dynamic Random Access Memory
SHV	Simultaneous Horizontal and Vertical
SSI	Synchronous Serial Interface
SQI	Signal Quality Indicator
SP	Short Pulse
STaR	Simultaneous Transmit and Receive
STALO	STable Local Oscillator
TCP	Transmission Control Protocol
TTL	Transistor to Transistor Logic
Tx	Transmitter
UKMO	United Kingdom Met Office
USB	Universal Serial Bus
VCO	Voltage Controlled Oscillator
VHDL	Very High Speed Integrated Circuit HDL
WRNR	Weather Radar Network Renewal
Z_{DR}	Differential Reflectivity

Chapter 1

Introduction

An introduction to the historical background of this project, the relevance of the work to be carried out to the project sponsor, the Met Office, and wider community, progress of the work to date, its scientific output and future plans are discussed.

1.1 Motivation

Advances in electrical hardware, over the years, have allowed more and more information to be extracted from weather radars. The first weather radars simply measured the returned power (reflectivity) of targets to be displayed on long-persistence cathode-ray tubes. With the advent of digital data acquisition it became possible to digitally process the received signal to remove unwanted artefacts and produce wide area composites of data from several neighbouring radars.

Developments in hardware, in particular more stable frequency and power sources, have made it possible to make measurements of the phase of the received signals. This leads to the possibility of measuring pulse to pulse auto-correlations, or indeed full spectra of the received signal. These, in turn, can be used to estimate both the radial component of the velocity

of the target, via the Doppler effect, and also the spectral width of the received signal. The spectral width of precipitation targets is related to the turbulence of the atmosphere, or additional scattering, indicative of hail in the sample volume [1].

The operational introduction of Dual Polarisation weather radars means that the number of parameters being produced by weather radars will increase. In addition to Dual Polarisation, it is also possible to make more novel measurements such as Refractivity and Emissions. By using the phase of returns from stable clutter targets, the near-surface refractivity of the air could be operationally measured using magnetron-based radars, as has already been demonstrated in klystron-based radars [2, 3, 4].

The advances in radar hardware have been mirrored by advances in computing hardware, which has led to increasingly high resolution numerical weather prediction (NWP) models, both spatially and temporally. This has created demand for sources of higher resolution observations over wide areas to initialise these models. The weather radar network is a valuable source of such observations as it is capable of supplying observations over the whole of the UK, typically at 2km resolution (figure 1-1).

1.1.1 Current Radar data assimilation in the Met Office

Observations assimilation is a process which adjusts the NWP model's previous estimate of the state of the atmosphere to account for the newly available observation information and its associated errors. If an observation corresponds directly to a parameter used within the model, for example temperature and pressure, that observation can be directly assimilated, however if the observation does not, as is the case for reflectivity, an observation operator must be used to derive the model's estimate of that observation which can then be used in the minimization. A wide range of literature is available which discusses the assimilation process in detail [5][6][7][8][9].

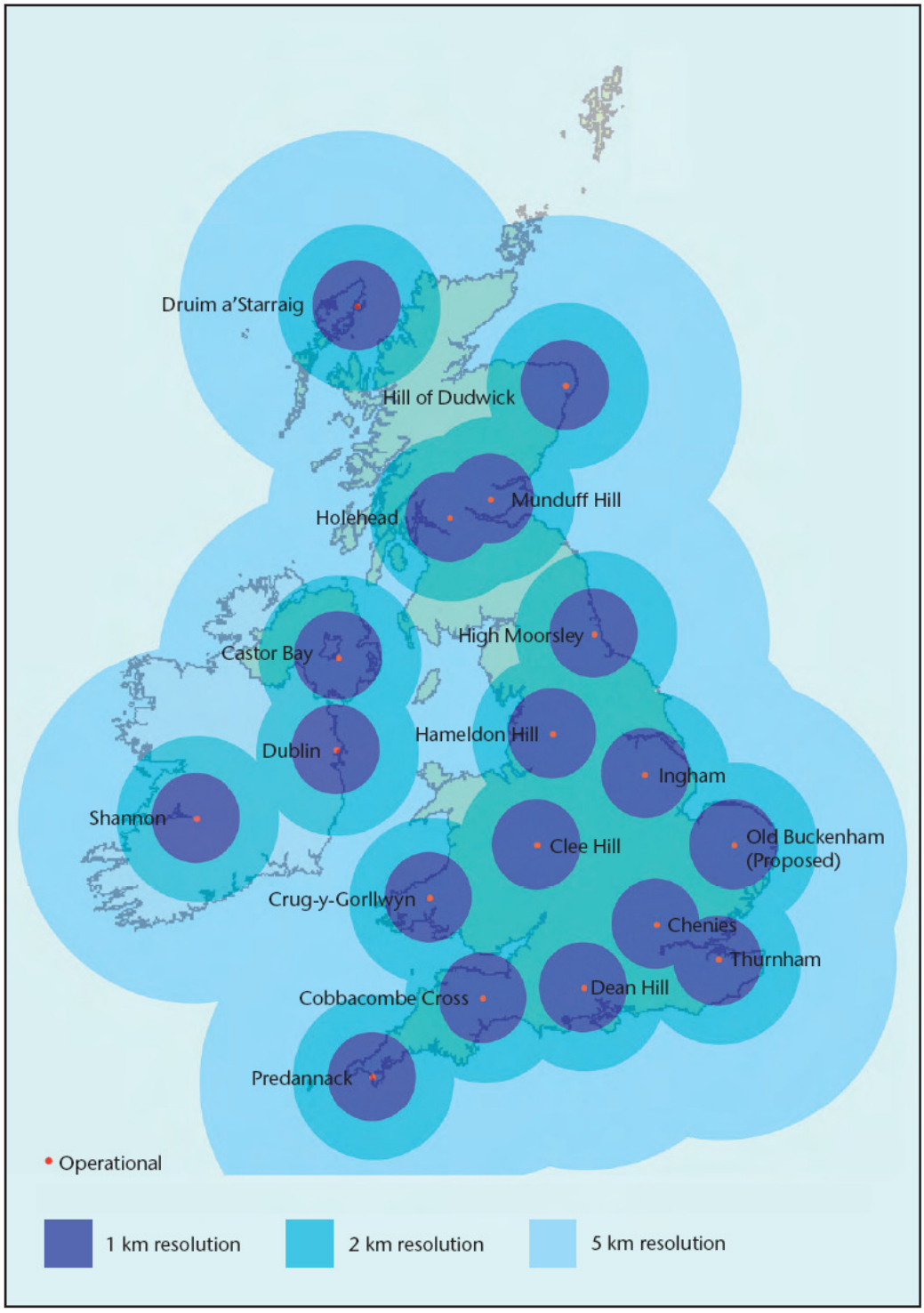

Figure 1-1: The UK and Irish Weather Network showing coverage area at resolutions of 1, 2 and 5 km

The data produced by the weather radar network is currently not fully exploited by NWP data assimilation systems. While some assimilation of radar data into numerical models is carried out, it is in the form of 2-D information on the surface rain rates from the UK weather radar composite image, an example of which can be seen in figure 1-2.

The UK surface precipitation rate composite is assimilated into the UK Met Office unified model in order to adjust model profiles of latent heating [10]. This process does not take full advantage of the 4 dimensional information available in the raw polar reflectivity data due to the difficulty in assimilating reflectivity, it not being an direct prognostic variable within the model. The radar polar data is more useful to the model than the currently assimilated Cartesian surface rain rates as the multiple scan elevations contain information about the vertical structure of the atmosphere, rather than just the surface conditions.

More recently it has become possible to achieve the indirect 4 dimensional variational assimilation of Doppler radial wind data [11, 12] and so while there is some benefit to weather forecasts from the assimilation of the polar format radar reflectivity information produced by the weather radar network; for maximum benefit, Doppler radial wind data would also need to be produced by the network and assimilated [13]. It was this requirement that the Additional Data from Existing Radars (ADER) project was initiated to address. The aim of the ADER project was to produce an in-house Doppler Weather radar processing and control system.

1.1.2 History of In-house development of Radar processing systems in the Met Office

Some of the newer Radars in the UK network have the capability to carry out Doppler processing via the manufacturer-supplied processing system, but this capability was abandoned in late 90s and early 2000s due to lack of a clear requirement from end users at that time. Other issues included on-going software/hardware issues with the original processing system and

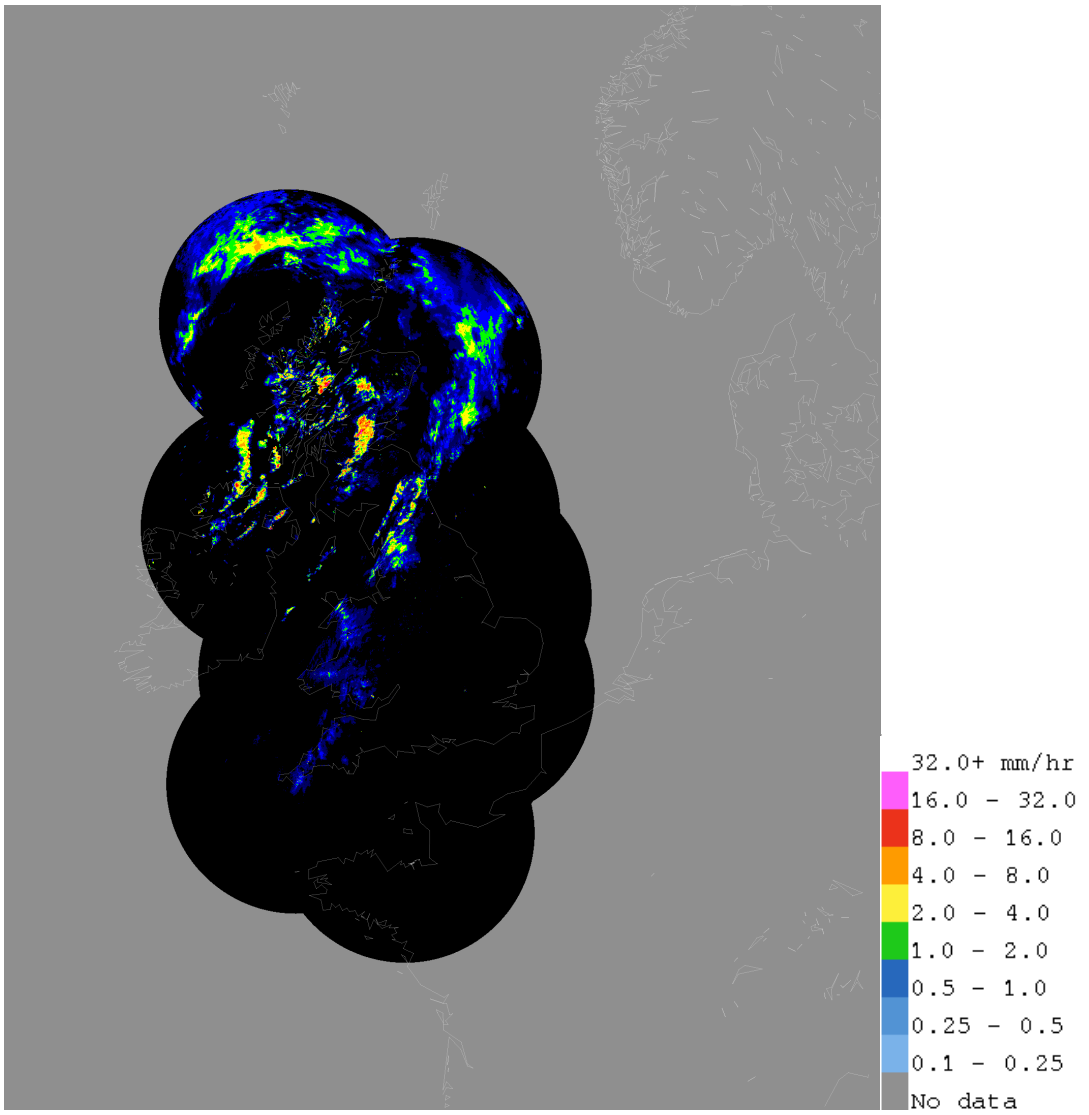

Figure 1-2: UK Weather radar precipitation rate composite (1km resolution)

increasing costs of support contracts. For these reasons, the Met Office decided to develop an in-house weather radar control and processing system for reflectivity only (at this time there was no customer for the Doppler radial wind data).

This line of processing and control systems was named “Cyclops”, which was a mixture of custom, in-house designed, interface hardware, and Commercial Off The Shelf (COTS) data acquisition and processing hardware, running on a standard Windows NT4 PC. The software was developed in-house and was responsible for the routine running of the radar, data collection and product generation. The project was broadly considered a success leading to the possibility of further in-house development.

Following the original Cyclops project, and once the value of Doppler radial wind data to NWP was recognised by the Met Office and its customers, the “Additional Data from Existing Radars” (ADER) project developed Cyclops-D, D standing for Doppler and investigated the feasibility of novel new sources of observations from weather radars in the future. The aim of the Cyclops-D part of the project was to produce a low-cost operational Doppler wind processing system for the Met Office Siemens Plessey 45C “Doppler capable” radars, at the same time as maintaining all the functionality developed in the original Cyclops, where possible using commercial off the shelf (COTS) hardware. The project also served to combat obsolescence issues arising from the increasingly outdated technology used in the original Cyclops system and provides a platform from which future research and development can be undertaken. It was expected that with modern technology the radar interface can be simplified and a number of obsolete and redundant systems be removed.

The ADER project proved to be successful in delivering a Doppler capable radar processing platform from which further development could be undertaken.

1.1.3 The Weather Radar Network Renewal project

In 2005 the Met Office purchased a COTS dual polarisation radar, for installation at the Thurnham site (fig. 1-1), in order to evaluate the possible benefits of dual polarisation technology for improved precipitation rate estimation. The data produced by the system was of insufficient quality, in terms of its dual polarisation moments, to be truly useful for dual polarisation radar hydrology/meteorology but did serve as a valuable learning experience in terms of the parameters that should be optimized in order to build a successful dual polarisation weather radar. Specifically, the poor cross-polar isolation between the horizontally and vertically polarised channels resulted in inter-channel interference reducing the peak co-polar correlation coefficient value. This lack of correlation in the two channels leads to noise on the differential reflectivity(Z_{dr}) measurement; raising its standard deviation above 0.2 dB (the limit above which Z_{dr} ceases to be useful [14] in improving rain rate estimation.)

As one of the first radars of its type to be produced by the manufacturer, a number of reliability and maintenance issues were identified, leading to unsustainable support costs and, ultimately, its retirement from the Met Office network.

At the time of starting this work it was hoped but not confirmed that permission would be granted by the Met Office board to proceed with a project to renew the entire UK weather radar network and upgrade the systems to dual polarisation capability: The aim of the Weather Radar Network Renewal (WRNR) project is twofold: the first and foremost being to address hardware obsolescence and the associated operational cost of maintaining the Siemens Plessey 45C system, and secondly, to exploit the benefits of dual polarisation technology for quantitative precipitation estimation (QPE), which is increasingly moving out of the research area, and in to operational networks [15, 16]. The success of the Doppler processing system and demonstration of the associated in-house development skills provided a strong case for continued in-house development. However, a business case had to be put forward to consider all available options for

renewing the network. The options put to the Met Office board were:

1. Do nothing.
2. Develop an in-house upgrade solution, comprising new drive system, receiver, and transmitter; refurbishment of the existing pedestal; and either dual polarisation antennas or upgrades to the current ones.
3. Buy in new dual polarisation radars from commercial manufacturers .
4. Outsource the running of the network to an external company, with appropriate dual polarisation data requirements stipulated in the contract.

A cost/benefit analysis was produced for each option, with appropriate costs, strengths, weaknesses, opportunities and threats. Option 2 was selected on this basis, being chosen on grounds of cost, opportunity to develop new radar observables, desire to maintain in-house expertise and control the quality of the final product. As such, the WRNR project continues the in-house radar signal processing and hardware development begun by the ADER project.

Given that the processing system developed for the WRNR project, know as Cyclops-DP, can be considered to be a superset of that developed for the ADER project (Cyclops-D), the Cyclops-D configuration will only be described in limited fashion. The Cyclops-D system is simply a single channel version of the Cyclops-DP system with the software able to sense the appropriate hardware configuration, set up the present hardware and carry out the processing appropriate to the number of channels present. Likewise, the software is capable of detecting the installed drive interface hardware, enabling control of either the renewed or original servo system.

1.1.4 Refractivity measurements

One aspect of the project of particular interest to the Met Office is the use of the radar network as a source of information on the near-surface refractivity

of the atmosphere. This information can be used to estimate near-surface humidity changes over time, which give greater insight to forecasters and NWP, on areas of convective initiation which can lead to severe weather which is difficult to forecast. No other observing system is able to provide areal estimates of humidity in the boundary layer of the atmosphere, where convection is initiated (Table 1.1).

Table 1.1: Summary of observing area covered by different observing systems used to measure humidity

Observing System	Measurement area	Measured Variable
Radiosonde	Vertical profile, as carried by wind	Humidity
Automated Weather Station	Point measurement at 1.25m above ground	Humidity
GPS	Integrated column above receiver	Propagation Delay
Weather Radar	Near surface radials where clutter is present	Propagation Delay

This technique is a relatively new one to the field of weather radar observables, and was first demonstrated by Fabry et al. in 1997 [2] using an S-band klystron based radar. It exploits the properties of the propagation of EM waves through a given medium, specifically the relationship between the speed of propagation and the refractive index of the medium. Any variation in the perceived distance from the radar to a stationary clutter target can be attributed to changes in the refractive index of the atmosphere between the radar and the target. A detailed description of this technique is given in chapter 4. If sufficient numbers of these targets are present, a map of the changes in the refractive index of the atmosphere can be calculated. In this respect it is similar to the technique used to derive integrated column water vapour measurements from GPS systems which, after accounting for other sources of path delay in the GPS signal; and knowing the receiver and satellite positions, is able to infer the contribution to the delay from the water vapour content of the atmosphere[17].

The refractivity technique was demonstrated by Fabry et al. (1997) [2, 18] using klystron-based transmitters at S-band. These have the advantage of being very stable in their frequency of transmission. The transmitters used in the Met Office weather radar network, and commonly within Europe, are magnetron-based, which have the disadvantage of drifting in frequency; even on relatively short time-scales. This is problematic for the measurement of the phases of targets on time scales of hours or even days. At the time of writing, no commercial radar processing system manufacturer offers the facility to make the required phase measurements using magnetron transmitters.

1.1.5 Emissions Measurement

C-band frequencies suffer from attenuation in heavy rain, unlike lower frequencies such as S band and below. Clearly this is undesirable and can lead to significant underestimation of the precipitation rate in very heavy storms. This is particularly troublesome as it is in situations with heavy rain that radar QPEs are most needed. The Met Office use an attenuation correction scheme developed by Hitschfield and Bordan [19], where-in a gate by gate running attenuation estimate is calculated and added to subsequent gates. This integration-based approach is clearly unstable and sensitive to calibration errors [20]. The instability is dealt with by capping the maximum attenuation correction to a factor of 3 on the reflectivity measurement [21].

An alternative to this unstable correction could make use of radiometric measurements of emissions from storms: It was noted, again by Fabry [22] in 2001, that there is a good deal of hardware in common between radars and radiometers. Using the radar receiver in a radiometric fashion, could provide additional useful information about the atmosphere. In 1964, Dicke et al stated that “in order to be a good emitter of microwaves, a body must be a good absorber” [23]

Using the radar hardware to radiometrically measure the amount of absorption present along a given path, the Path Integrated Attenuation (PIA)

[24], means this can be used as a constraint on the attenuation correction, improving QPEs in strongly attenuating cases.

With the majority of European national weather services introducing dual polarisation technology in the near future, it is expected that the differential phase parameter (ϕ_{dp}) will be used to provide a direct measure of the attenuation from a given range gate [25],[26] and so reduce the need for the PIA. However this does not account for attenuation due to radome wetting; which for some types of radome, at C band, can amount to as much as 5dB at rain rates of 50 mm/hr [27]. Therefore it is expected that even with dual polarisation technology there would still be benefit from the radiometric technique [28].

Unfortunately, emissions from the atmosphere and liquid water at C-band are small. Even compared to weak signals returned from precipitation. This is why C-band is a relatively good frequency for making radar measurements of precipitation; if emissions were greater, then attenuation would also. The difficulty in making such measurements accurately is likely to have prevented the technique from being adopted by the wider weather radar community. Furthermore, the promise of dual polarisation based correction [29] may have lead to the conclusion that the issue of attenuation had been addressed, however it is still the subject of ongoing study with a number of unresolved issues [30].

By using a calibrated noise source, to measure the receiver noise factor, and the tipping curve technique, [31] used to calibrate ground based radiometers, it is possible to separate the effects of receiver noise and gain variation. From this it is possible to accurately measure the changes in brightness temperature associated with storm emissions and relate them to the PIA.

1.2 Scope of this study

Chapter 1 briefly introduced the motivation behind this work - the Met Offices desire to remove obsolescence from its radar network and access new

and improved sources of observations for NWP, leading to the opportunity to investigate novel radar measurements which, it is hoped, are able to address known weaknesses in the observing capabilities of weather radars.

In chapter 2 the theory required to build a dual polarisation radar processing system is reviewed. Chapter 3 describes the design of the WRNR radar, including a review of the key parameters required to build a high quality dual polarisation radar, and an assessment of the quality of the resulting radar. Chapter 4 describes the application of radar to make near surface refractivity measurements, including evaluation of a method to improve correlation with surface observations using dual polarisation measurements. A novel use of magnetron characteristics to try to reduce bias and noise on refractivity measurements is described. Chapter 5 details the use of the WRNR radar to make radiometric measurements to measure PIA, including methods of improving the sensitivity of the WRNR receiver.

While some of the hardware described is specific to the Met Office radars, which reflects the status of the Met Office as project sponsor, the techniques developed and general principles described herein in order to build a high quality dual polarisation radar, make refractivity measurements and measure storm emission, are generally applicable to other radar systems.

Chapter 2

Theory

In this chapter a review of the theory applicable to the design of a dual polarisation Doppler weather radar processing system is presented.

2.1 Introduction

A wide range of literature is available which discusses the concepts in detail e.g. [11], [32], [33], [34] and it is from these works that the information in this section is based.

Precipitation forms a medium which can be considered to be a set of randomly distributed targets. As such, the precipitation signal is complex zero-mean Gaussian random process [35] This medium is capable of back-scattering an electromagnetic pulse of carefully chosen wavelength. From the known transmitted power, measured back-scattered power and the time to receive the back-scattered pulse compared to the time of transmission, the distance and radar cross-section of the target can be measured. Using information from the phase of the returns, the radial velocity and spectral width of the targets can be estimated.

By transmitting signals with controlled, known polarisation characteristics, the polarisation characteristics of the target can be measured with a suitable

receiver. This provides additional information about the type of target present in the sample volume which can be the used to make a more accurate conversion from the received power to precipitation rate [14].

2.1.1 Range Measurement

The distance to an illuminated target r, can be determined from the speed of the propagation of the electromagnetic wave, c, and the time, t, elapsed between transmission and reception of the backscattered signal [34]:

$$r = \frac{c \times t}{2} \tag{2.1}$$

In the case of pulsed radar systems, such as the Met Office radars, the maximum range that can be usefully measured is governed by the pulse repetition time (PRT), also given as the pulse repetition frequency (PRF = 1/PRT) of the radar. Unless pulses are coded somehow, to make them distinguishable from each other, there is an ambiguity as to which pulse any received signal is coming from. This is called range aliasing and may lead to so-called "second trip echoes" appearing in the data, which are actually from targets beyond the maximum unambiguous range. The maximum range beyond which this effect occurs is given by :

$$r_{max} = \frac{c \times PRT}{2} \tag{2.2}$$

or more usually in terms of the PRF:

$$r_{max} = \frac{c}{2PRF} \tag{2.3}$$

2.1.2 Reflectivity Measurement

For any given radar, the transmission and reception characteristics, such as the transmitted pulse power, system gain, antenna characteristics etc.,

should be well known. The received power from a target can be found using the radar equation for a volume filled with distributed scatterers as given in [34]:

The usual form of the Radar Equation for a single target is given as [34]:

$$P_r = P_t \frac{G^2 \lambda^2 \sigma_T}{(4\pi)^3 r^4} \tag{2.4}$$

Where P_r is the received power, P_t is the transmitted power, G is the gain of the antenna, λ is the transmitted wavelength, σ_T is the radar cross section of the target and r is the distance to the target from the radar.

In the case of weather radar, a large number of distributed targets fill the observation volume [33]. The radar cross section must be summed over all these targets [34] .

$$\sigma_T = V \sum_{i=1}^{N} \sigma_i \tag{2.5}$$

Where σ_T represents the total radar cross section, $\Sigma\sigma_i$ the average total backscatter cross section of the particles per unit volume, and V is the volume sampled. Here we assume that the sample volume is filled by identical targets.

The sampled volume is the range sample resolution multiplied by an integral over the beam shape giving the azimuthal and elevational sample resolution. The range sample resolution is given by the volume over which it would not be possible to distinguish one target from another, i.e. the entire volume is contributing to the returned power. This is governed by the transmitted pulse duration τ and is given by:

$$r_{min} = \frac{c\tau}{2} \tag{2.6}$$

For a circular, parabolic antenna of diameter d with Gaussian illumination, as is used in the Met Office network, the 3 dB beam width, from [36], is given by:

$$\Theta_{3dB} \cong \frac{70\lambda}{d} \tag{2.7}$$

where, Θ_{3dB} is the 3 dB beam width in both the elevation and azimuthal planes due to the circular symmetry of the dish and illumination. However in the more general case, given in [34], the horizontal beamwidth is given by θ_b and the vertical beamwidth by ϕ_b.

The pulse length and beam profile allow the sample volume to be calculated:

$$V \approx \frac{4}{\pi}(R\theta_b)(R\phi_b)\frac{c\tau}{2} \tag{2.8}$$

However, it was noted by Probert-Jones [37] that due to non-uniform illumination of the volume by the beam, which can be approximated to a 2 dimensional Gaussian, an additional factor of $2ln(2)$ must be included.

And so the radar equation becomes:

$$P_r = \frac{P_t G^2 \lambda^2 \theta_b \phi_b c\tau}{1024(ln2)\pi^2 R^2} \sum_i \sigma_i = \frac{P_t G \lambda^2 c\tau}{1024(ln2)R^2} \sum_i \sigma_i \tag{2.9}$$

by substituting $G = \pi^2/(\theta_b\phi_b)$ for a Gaussian beam shape [37].

In the case of Rayleigh scattering, where the targets (rain droplets) are small relative to the wavelength being used (5 cm) the radar cross section of a target is given by [38]:

$$\sigma_i = \frac{\pi^5 D^6}{\lambda^4} |K|^2 \tag{2.10}$$

where D is the diameter of a given drop and $|K|^2 = (\epsilon - 1/(\epsilon + 2)$, and ϵ is the dielectric constant of scattering particles [34]. The radar equation then becomes:

$$P_r = \frac{\pi^5 P_t G c \tau}{1024(ln2)R^2\lambda^2}|K|^2 Z \tag{2.11}$$

where Z, the radar reflectivity factor, is defined as:

$$Z = \int_0^\infty D^6 N_V(D) dD \tag{2.12}$$

where $N_v(D)dD$ represents the mean number (N) of raindrops with equivalent spherical diameters between D and $D + dD$ present per unit volume (V) sampled: This accounts for the probability distribution of droplet diameters in the sample volume.As the typical units used to measure rain droplet sizes are mm and volumes; m^3, the units of the radar reflectivity factor are conventionally given as $mm^6 m^{-3}$.

It is interesting to note that the received power from a given range is inversely proportional to square of the distance, rather than the fourth power as is the case for a point target. This is due to the broadening of the beam with range, which illuminates a larger sample volume; effectively increasing the radar cross-section by a factor that cancels out the broadening.

From the point of view of weather radar signal processing it is perhaps more useful to write 2.11 in the form:

$$Z = \frac{1024(ln2)R^2\lambda^2 P_r}{\pi^5 P_t G c \tau}|K|^2 \tag{2.13}$$

The probability distribution of droplet size is commonly modelled by normalized gamma functions [39]. In the UK an empirically derived, Marshall-Palmer relation [40] is used to convert from Z to instantaneous rain rate R (mm/h):

$$Z = aR^b \tag{2.14}$$

Where the a and b coefficients are 200 and 1.6, respectively [41].

While it is known that the drop size distribution does vary, at the moment this is not accounted for when estimating R operationally at the Met Office. With the introduction of dual polarisation radars, additional information is available which makes it possible to alter the coefficients to better estimate the true rain rate [14].

2.1.3 Radial Velocity Estimation

The term "Doppler" processing implies that a frequency shift, due to the radial component of a target's motion relative to the observer, is measured. The frequency shift due to the Doppler effect, assuming a stationary observer, is given by:

$$\delta f = \frac{2v_r f_{tx}}{c} \tag{2.15}$$

Where δf is the shift in frequency due to the target's motion, v_r is the component of the target's velocity along the line of sight between the transmitter/receiver and f_{tx} is the transmission frequency. For a C-band system (~5.625 GHz) a target moving at 10 m/s gives a frequency shift of 375 Hz. This is many orders of magnitude smaller than the transmission frequency, and such a shift on top of the already very high transmission frequency is difficult to detect. However, a change in the phase of these returns from one pulse to the next, relative to a local known stable reference source, is measureable.

2.1.4 Phase measurements for radial velocity estimation

Following the analysis in [33] 3.4.3, consider the complex form of the electric field of the transmitted pulse:

$$E(t,r) = A_t e^{j2\pi f_t(t-\frac{r}{c})+j\phi_t} \sqcap (t - \frac{2r}{c}) \tag{2.16}$$

Where A is the field amplitude, f_t is the transmitter frequency, ϕ_t is the phase of transmission and $\sqcap(t - \frac{2r}{c})$ approximates the transmitted pulse shape as a top hat function, equal to 1 when its argument is between 0 and τ, where τ is the transmitted pulse length and zero everywhere else.

The signal returned to the receiver after interaction with a single moving target is then given by :

$$E(t,r) = A_r e^{j2\pi f_t(t-\frac{2r}{c})+j\phi_r} \sqcap (t - \frac{2r}{c}) \tag{2.17}$$

Where ϕ_r is the reflected phase. ϕ_r is the sum of ϕ_t, ϕ_s a phase shift due to the properties of the scatterer, and the phase offset due to the position of the target given by :

$$\phi_p = 2\pi\frac{2r}{\lambda} = \frac{4\pi r}{\lambda} \tag{2.18}$$

i.e. the number of fractional wavelengths to the target in radians.

Considering the phase of the received signal from the subsequent pulse (after τ_2) and assuming that the transmitter frequency does not vary on the inter-pulse time scale, it would be expected that ϕ_s would not have changed either and so:

$$\phi_{r1} - \phi_{r2} = \frac{4\pi(r_1 - r_2)}{\lambda} + \phi_{t1} - \phi_{t2} \tag{2.19}$$

The transmitted phase can be measured for each pulse and subtracted from the subsequent phase measurements giving:

$$\frac{\nabla\phi_r}{\nabla t} = \frac{-4\pi}{\lambda}\frac{\nabla r}{\nabla t} = -\frac{4\pi v_r}{\lambda} \tag{2.20}$$

This relationship determines the unambiguous velocity v_{max}, limited by the ability to distinguish the amount of phase shift between the two pulses. v_{max} is related to the wavelength transmitted and the time between observations of the phase i.e. the PRT. Specifically, v_{max} is measured when the phase shift equals π radians, i.e.:

$$v_{max} = \frac{\pm PRF\lambda}{4} \tag{2.21}$$

The measurement of the phase itself is done in a mixing process. The transmitted and received signals are initially mixed with a signal that, in the Met Office case, has a frequency 30 MHz below the transmitted frequency in the analogue domain, to generate a signal with an intermediate frequency (IF). A similar process then happens in the digital domain, however here it is done numerically (see section 3.5.2). The IF is then digitised and a multiplication in the time domain occurs, with discrete numerical values of sine and cosine corresponding to 30 MHz.

2.1.5 Doppler Dilemma

The fact that the maximum unambiguous velocity is proportional to the PRF, while the maximum unambiguous range is inversely proportional to the PRF leads to the so called Doppler Dilemma [33]. Substituting 2.3 into 2.21 gives:

$$v_{max}r_{max} = \frac{\pm c\lambda}{8} \tag{2.22}$$

therefore the product of $v_{max}$and $r_{max}$is a constant.

For example, typical transmitted pulse characteristics of the UK weather radar are a 2μs pulse width with a maximum PRF of 300 Hz when performing a scan for QPE and a 0.5 μs pulse width with a maximum PRF of 1200 Hz when carrying out a Doppler scan. This leads to a maximum unambiguous velocity and range of 4 m/s and 500 km respectively in 2μs - “long pulse”

mode and 12 m/s unambiguous velocity and 125 km unambiguous range in 0.5 μs - “short pulse” mode. In practice the short 1200 Hz PRF is alternated with a 900 Hz PRF allowing further unfolding of v_r to $\pm$48 m/s [42] (See section 2.2.2 for details).

2.2 Single polarisation baseband processing algorithms

Phase correction

Magnetron based radars have a random start-up phase every pulse, due to the fact a magnetron is a power oscillator rather than a power amplifier. Ideally a coherent source would be used to make Doppler measurements, such as a power amplifier based transmitter; for example a Klystron or Travelling Wave Tube (TWT) which can be locked in phase and frequency to suitable reference sources. To make Doppler measurements using magnetron based radars, the initial random pulse phase must be measured and corrected for in a process known as “coherent on receive” [43].

The in-phase and quadrature (I and Q) samples of a transmitted pulse give the phase of that pulse, with a constant offset between it and the subsequently received signal. This allows the received signal for that pulse to be phase corrected. This takes the form of a vector rotation of the data. Here it is advantageous to view the I and Q as a real and complex value. The complex transmitted sample pair is r_0 and the received data complex sample values are r_n , where the n denotes the range sample bin number. The phase correction of the received data sample is given by s_n:

$$s_n = r_0^* r_n \tag{2.23}$$

at each range gate, where r_0^* is the complex conjugate of r_0.

This is equivalent to a negative vector rotation of all values by the phase of the transmitted pulse; the rotation of the pulse by itself leads to a sample with all I and no Q.

The modulus of each sample pair is proportional to the received power, but because of the nature of this phase rotation, the modulus of the received sample pair is multiplied by that of the transmitted sample pair. This is best illustrated by considering the I & Q pair as complex numbers and rewriting in the phasor representation:

$$r_n = I_n + jQ_n = |z_n| \, e^{-j\phi} \tag{2.24}$$

When multiplying the samples, the z terms multiply and the ϕ terms add, or, in the case of the complex conjugate, subtract. The lengthening of the vector by a factor z_n must be corrected for by normalizing the values after the rotation by dividing them by z_0, or by normalizing r_0 before the rotation.

2.2.1 Pulse Pair Processing

Pulse Pair Processing (PPP) is a time domain method of calculating the average power, Doppler shift, and Signal Quality Indicator (SQI) parameters. It is possible to carry out frequency domain processing of the data following a FFT/DFT however it has been shown that PPP shows better results where there is a low signal to noise ratio [44] and is much more straightforward to implement.

The PPP technique is based on the calculation of different lag auto-correlations of the phase corrected data [45]. The auto-correlations are defined follows:

$$\begin{aligned} R_0 &= \tfrac{1}{n} \textstyle\sum_{n=1}^{n} s_n^* s_n \\ R_1 &= \tfrac{1}{n-1} \textstyle\sum_{n=2}^{n} s_{n-1}^* s_n \\ R_2 &= \tfrac{1}{n-2} \textstyle\sum_{n=3}^{n} s_{n-2}^* s_n \end{aligned} \tag{2.25}$$

Where R_0 is the zeroth lag auto-correlation, R_1 is the complex first lag auto-correlation and R_2 is the complex second lag auto-correlation, s_n is the complex phase corrected sample at a given range gate for the latest pulse and s^*_{n-1} is the complex phase corrected sample at the range gate for the previous pulse, etc.

It should be noted that the formulae for the calculation of the lag 1 and lag 2 complex auto-correlations are very similar to those used to carry out the vector rotation in the phase correction (equation 2.23). This is not surprising as the auto-correlation is calculating the power weighted average phase difference between two pulses. One way of viewing this is as subtracting the phase of one sample from that of the next and integrating the resultant vector difference. The lag 0 auto-correlation is simply calculating the average vector magnitude and so is wholly real. Once the auto-correlations have been calculated is it straightforward to calculate the desired signal parameters.

2.2.2 Moment calculation

Reflectivity Calculations

The reflectivity is a range normalized, calibrated form of received power and is typically given in its logarithmic form as $Z = 10\log_{10}(z/z_r)$ where by convention the reference level z_r is 1 mm^6m^{-3}. From eq. 2.13 in logarithmic form this can be calculated as:

$$Z = 10\log_{10}(R_0) + 20\log_{10}(r) + Z_0 \tag{2.26}$$

Where $20\log_{10}(r)$ is the range squared correction, and $10\log_{10}(R_0)$ is 10 times the log of the lag zero auto-correlation. By injection of known signals, the factor required for conversion from $10\log_{10}(R_0)$ to a dBm power can be determined and included in Z_0. The Z_0 value also contains those terms from eq. 2.13 which are held constant for a given radar sampling sequence. The

terms in Z_0 from eq. 2.13 are independent of the receiver and are generally known as the "Radar constant", despite varying between short and long pulse scans.

In practice the R_0 values are composed of the signal returned from precipitation, and atmospheric and system noise. It is usual to subtract the value of the atmospheric and system noise from the R_0 values before they are used to calculate the reflectivity value in dBZ. By subtracting out this system noise the signals at the bottom end of the calibration curve are re-linearised to some extent. The value for the system noise is measured either when the transmitter is off or when the transmitted pulse is at very long range, where no atmospheric returns would be expected.

Velocity calculations

The mean radial velocity is calculated from the first lag auto-correlation. The average phase shift at each range gate is given by:

$$\bar{\phi_r} = arg(R_{T_s}) \tag{2.27}$$

and the velocity is given by:

$$v_r = -\left(\frac{\lambda}{4\pi T_s}\right) arg(R_{T_s}) \tag{2.28}$$

Where v_r is the velocity, λ is the wavelength, $R_{T_s}$is the auto-correlation at a given time where, T_s is the the PRT, and $\bar{\phi_r}$ is the average phase shift.

Dual PRF Unfolding

"The Doppler dilemma" at C band with a PRF of 1200 Hz gives maximum unambiguous velocity of ~16 m/s and a maximum unambiguous range of ~

125 km. 16 m/s is not really enough to be useful for meteorological observations, but there are techniques that can be used to increase the maximum unambiguous velocity without reducing the maximum unambiguous range. One of these techniques is the Dual PRF technique [42]. It is this method that has been used in Cyclops-D.

The basis of the technique is to sample with two different PRFs in the same sample volume. The two PRFs should have a known ratio between them, giving known, but different, unambiguous velocities. If a target's radial velocity, measured using both PRFs, is the same, the target's velocity does not exceed the maximum unambiguous velocity of either PRF. However if the two velocity measurements do not agree, the velocity of the target must have exceeded the maximum unambiguous velocity. As the velocity at which the phase from each PRF aliases is known, it is possible to increase the effective unambiguous velocity by calculating the number of times that the velocity has folded. The effect of this on the measured pulse to pulse phase shifts for each PRF at a given target velocity is shown in figure 2-1.

It is desirable to have a ratio between the two PRFs which is close to one. This maximizes the number of times the velocity can fold without both PRFs producing the same velocity, however having a ratio close to one means that velocity difference picked up when they do wrap is small. This makes distinguishing the number of times the velocity has wrapped more difficult, i.e. there is a trade off between the number of times the data can be unfolded and how distinguishable each folding state is.

The dual PRF technique gives the final unfolded velocity as [33]:

$$\hat{v} = \frac{\lambda}{4\pi(T_{s2} - T_{s1})} arg\left(\frac{R_{1_{High}}}{R_{1_{Low}}}\right) \tag{2.29}$$

Where the $R_{1_{High/Low}}$ values are the lag 1 auto correlations at each PRF, the T_s values are the pulse repetition times used and λ is the transmission wavelength. As can be seen from equation 2.29 and figure 2-1, if one reaches the state where the argument is outside the range $-\pi, \pi$ then velocity is

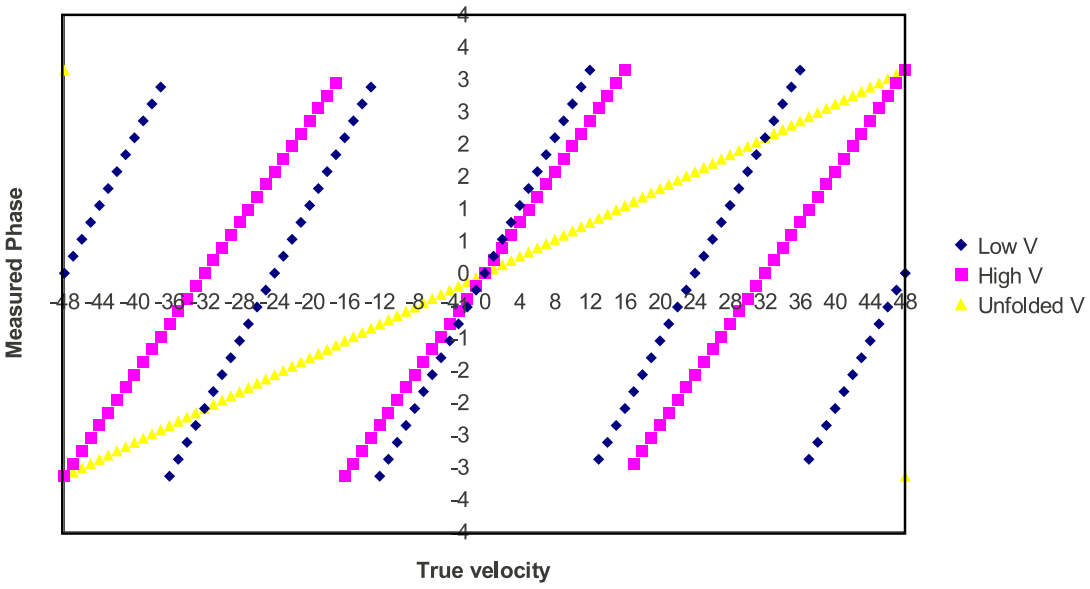

Figure 2-1: Effect on measured phase change (radians) at PRF's of 1200Hz (High) and 900 Hz (Low) for given target velocities (m/s)

once again ambiguous, and so the maximum unfolded unambiguous velocity is:

$$v_{max} = \pm \frac{\lambda}{4(T_{s2} - T_{s1})} \tag{2.30}$$

In Cyclops-D, PRFs of 1200 Hz and 900 Hz are used, with a ratio of 4:3. This gives unambiguous velocities of 16 m/s and 12 m/s, a maximum range of 120 km and 4 m/s between each different folded value and from equation 2.30 a maximum unfolded velocity of 48 m/s.

In practice, equation 2.29 is only used to estimate the degree of folding. It has been shown [46, 47] that an improved estimate of the velocity is obtained by using the degree of foding to calculate the unfolded velocities from values derived from each PRF.

Clutter Indicator

The clutter indicator (CI) is used to distinguish between clutter and precipitation [48]. It is a measure of the signal variability. This is useful because precipitation has high signal variability and clutter has a low signal variability. It was developed for the original Cyclops processors because no phase information, which would be used for clutter filtering in more modern Doppler processors, was available. In Cyclops the clutter indicator is defined as

$$\Delta_k = 10|\log_{10}(z_k - z_{k-\tau})| \tag{2.31}$$

$$CI = \frac{1}{M-1}\sum_{k}^{M}\Delta_k \tag{2.32}$$

Where CI is the average signal variability in dB, Δ_k represents a measure of signal variability in dB, z_k is the reflectivity signal at a particular range gate, $z_{k-\tau}$ is the reflectivity signal at a particular range gate for a transmitted pulse $k-\tau$, that precedes pulse k by a time delay and M is the number of samples used in the calculation.

In practice, a lag of 2 pulses is used in Cyclops but the optimum value to separate the two populations will vary with rotation rate and PRF.

It is not sensible, in terms of computational efficiency, to calculate the CI values in this way with Cyclops-D because at the processing stage the measured power values are still in linear form.

As a result in Cyclops-D the CI is calculated as:

$$\begin{aligned} If\ Z_k > Z_{k-\tau}: \quad 10^{\Delta_k} &= \prod_{k=0}^{M-1}\frac{Z_k}{Z_{k-\tau}} \\ Else: \quad 10^{\Delta_k} &= \prod_{k=0}^{M-1}\frac{Z_{k-\tau}}{Z_k} \end{aligned} \tag{2.33}$$

$10\log_{10}(\sigma)$ is then taken when all the pulses in the current ray have been processed and then the values are averaged.

It should be noted that the actual values in the calculation of the CI in the DSP are not true Z values. In practice they are only proportional to Z with the same factor of proportionality at each range gate. Because of this, and the fact that at the lower end of the calibration range noise contamination takes place, it is found that the nature of the CI values in noise will be different from the logarithmic CI calculation which sampled the logarithmic amplifier.

Clutter Phase Alignment

The availability of phase information allows improved clutter indicator - Clutter Phase Alignment (CPA) [49][50] to be calculated:

$$CPA = \frac{\left|\sum_{n=1}^{N} s_i\right|}{\sum_{ns=1}^{N} |s_i|} \tag{2.34}$$

CPA can be used in a similar manner to CI to filter ground clutter from the data.

2.2.3 Phase calculation for refractivity

The phase can be calculated as from the raw I and Q values:

$$\phi = arg\left(\sum_{n=1}^{N} real(s_n) + \sum_{n=1}^{N} imag(s_n)\right) \tag{2.35}$$

Whilst the voltages are contaminated by noise, the fact that the phase of signals returned from clutter are coherent, whereas noise is not, means that in the coherent integration process the noise signal tends to zero. Also, as

phase measurements from only high power signals i.e. from clutter targets, are used to calculate refractivity, any effects of noise on the measurement can be considered to be negligible.

A target quality indicator (QI) is calculated to aid quality control of the clutter targets. This calculated by adding in quadrature the standard deviation of I and Q(σ_i and σ_q) and then power normalizing the result 2.36.

$$QI = \frac{\sigma_i^2 + \sigma_q^2}{R_0} \tag{2.36}$$

2.3 Dual polarisation moment calculation

2.3.1 Differential reflectivity calculation

As droplets grow in size they become more oblate as they fall, as shown in figure 2-2 [51]. As the reflectivity factor is proportional to the sixth power of the drop-size, useful meteorological information can be measured using this characteristic. The differential reflectivity is the ratio of the horizontal to vertical reflectivity and therefore is sensitive to this property.

The Z_{dr} of a target is defined as:

$$Z_{dr} = 10 \log_{10} \left(\frac{z_h}{z_v} \right) \tag{2.37}$$

Where $z_{h/v}$ are the linear horizontally (h) and vertically (v) polarised reflectivity measurements at a given range gate. This represents an idealised version of the measurement. In reality the calculation of Z_{dr} has to be made on the basis of the measured voltages in each channel. These voltages include the noise power, which is likely to be different in each channel. If not correctly accounted for this can cause a bias in Z_{dr}, particularly at low signal to noise ratios. It is recommended that dynamic noise measurements

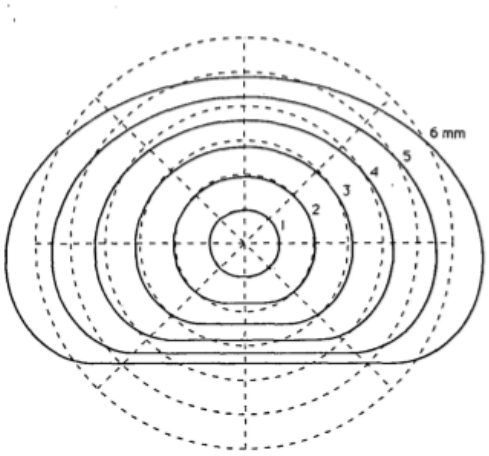

FIG. 2. Sessile drop profiles for d = 1, 2, 3, 4, 5 and 6 mm. Shown for comparison are dashed circles of diameter d divided into 45 degree sectors.

Figure 2-2: Modelled effect of drop size on axial ratio. Extract from Beard and Chaung, 1987 [51]

are made and subtracted from the estimated z_h, z_v before calculation of the Z_{dr}. If a dynamic noise measurement cannot be used the noise value to be used should be made at the elevation at which the data is collected as the noise power varies with elevation (See 5.2.2). The noise can also be affected by heavy precipitation as will be seen in chapter 5.

2.3.2 Cross polar parameters

The cross polar correlation is calculated as:

$$R_{hv} = \frac{1}{N}\sum_{N=1}^{N} s_{hn} s_{vn}^{*} \tag{2.38}$$

From this the differential phase shift (ϕ_{dp}) and co-polar correlation coefficient (ρ_{hv}) can be calculated:

$$\phi_{dp} = arg(R_{hv}) \tag{2.39}$$

A linearly polarised wave travelling through a medium containing liquid water will be retarded as a function of the amount of liquid water in the medium. Therefore if a given polarisation has to travel through more liquid water than the other, the difference in the retardation of each signal contains information about the difference in the media. In the case of rain drops the horizontally polarised signal will lag the vertical one (figure 2-2) in heavy rain, due to the oblate nature of large rain droplets. The measurement of this phase lag is ϕ_{dp}. ϕ_{dp} can be used to estimate the attenuation of the signal, which will be greater in the horizontal than the vertical plane in attenuating (heavy) precipitation, independent of the reflectivity.

The rate of change of ϕ_{dp} with distance is known as the "specific differential phase" and is typically denoted by K_{dp}, in units of $^{\circ}/km$. The use of K_{dp} has been proposed as an estimator of rain rate[52], particularly at higher rates where the phase shift becomes significant and well correlated with rain rate.

ρ_{hv} may also be calculated using the phase properties:

$$\rho_{hv} = \frac{|R_{hv}|}{\sqrt{R_h * R_v}} \tag{2.40}$$

where $R_{h/v}$ are the lag zero correlations in each polarisation state.

The correlation between the two channels (ρ_{hv}) is a useful indicator of droplet type or non-meteorological targets, as in these situations the two polarisation states are being affected differently by the targets in the sample volume.

2.3.3 Linear depolarisation calculation

If transmission occurs entirely in one linear polarisation state and reception in two, the depolarisation of the signal due to the targets can be measured.

With horizontal transmission, depolarisation is sensitive to particle orientation and canting, in addition to being useful for clutter and mixed phase precipitation identification [32]. This measurement is formulated as the Linear Depolarisation Ratio (Ldr).

The Ldr is calculated as:

$$Ldr = 10 \log_{10} \left(\frac{z_{cross}}{z_{co}} \right) \tag{2.41}$$

Where Z_{cross} is the cross-polar reflectivity and Z_{co} is the co-polar reflectivity, relative to the transmission polarisation plane.

The typical form of Ldr is given by:

$$Ldr_{vh} = 10 \log_{10} \left(\frac{z_{vh}}{z_{hh}} \right) \tag{2.42}$$

Where z_{vh} denotes the z value measured by transmission in the horizontal plane and reception in the vertical plane, and z_{hh} denotes the z value measured by transmission in the horizontal plane and reception in the horizontal plane [32].

Chapter 3

A renewed radar for the UK network

This chapter provides a review of the requirements to produce a high quality dual polarisation radar, details of the upgrade of the Siemens Plessey 45C to remove all obsolescence issues and upgrade the radars to full high quality dual polarisation capability and an evaluation of the dual polarisation quality of the WRNR radar.

3.1 The Weather Radar Network Renewal project

Background

Some radars in the UK weather radar network are now approximately 30 years old. Although they are robust and reliable from a mechanical point of view, it is becoming increasingly costly to support the associated electronic elements; particularly the drive system and transmitter. The increasing failure rate has lead to an increase in the number of occasions when a radar engineer has to visit a site, impacts to data availability and associated costs. Receiver obsolescence issues were addressed as part of the ADER project.

3.2 Quality requirements for a dual polarisation radar

As part of the upgrade process there is a requirement to add high quality dual polarisation measurement technology to the radars. This provides additional information about the drop size distribution and target type, which it is hoped will allow for improved QPE via a dynamic reflectivity to rain rate conversion [14], improved non-hydrometeor target rejection [53],[54], leading to improved QPE [55] and improved radar calibration, by using the self-consistency between dual polarisation parameters [56], in which those that are based on phase have the advantage of being power calibration independent.

As Z_{dr} is sensitive to the droplet shape, it can be used to make improved QPEs, however the use of inaccurate Z_{dr} values can lead to a degradation of the QPE [57]. In order to be of use, the standard deviation of the Z_{dr} measurement should be less than 0.2 dB [14].

In addition to rain-rate estimation improvement by use of differential reflectivity, the differential phase shift ϕ_{dp} can also be used to improve QPEs, particularly at high rain rates [58]. Useful ϕ_{dp} based QPEs require a standard deviation of less than 2° [59].These requirements were used to guide the design of the Met Office OSA radar system.

The system should be able to make measurements of Zdr and ϕ_{dp}, in addition to measurements of the depolarization of the transmission caused by targets from horizontal polarization to vertical polarization - the Ldr. As such a so called “Simultaneous Horizontal and Vertical” (SHV) design was chosen, in which transmission happens in both horizontal and vertical polarizations at the same time. In the so called SHV approach, the transmitter power is usually split equally and each part sent to the horizontal and vertical inputs of an ortho-mode transducer (OMT) and suitable scalar feed horn. This then transmits the power to air in a polarisation state which is determined by the magnitude and phase of the inputs. With identical power into the H and V ports of the OMT the output polarisation is linear 45° if the two input

are in phase, circular if they are 90/270° out of phase, and varying degrees of elliptical for other values. In general the system should be described as resulting in slant elliptical transmission.

A waveguide switch is used to allow transmission entirely in the horizontal polarization in-order to make Ldr measurements (See sec. 3.3 and sec. 3.4.9 for details).

An alternate slant elliptical transmission design makes use of 2 transmitters [60]. Whilst this removes the need to split the power, which maintains the sensitivity of the single polarisation system, it adds complexity and cost to the design and so was not considered for this project.

It has been shown that for slant elliptical transmission radars [59], the standard deviations are affected by the number of independent samples, atmospheric turbulence, the signal to noise ratio (SNR), and ρ_{hv}:

$$\sigma_{Z_{dr}} = \frac{10}{M^{1/2} ln(10)} \left[\frac{1 + 2SNR_h}{SNR_h^2} + \frac{1 + 2SNR_v}{SNR_v^2} + \frac{1.13(1 - \rho_{hv}^2)}{\sigma_{vn}} \right]^{1/2} (dB) \quad (3.1)$$

and

$$\sigma_{\phi_{dp}} = \frac{1}{(2M)^{1/2} \rho_{hv}} \left[\frac{SNR_h + SNR_v + 1}{SNR_v SNR_H} + \frac{0.56(1 - \rho_{hv}^2)}{\sigma^2} \right]^{1/2} (rad.) \quad (3.2)$$

Where σ_{vn} is normalised spectral width and M is the number of samples. This result is somewhat surprising in that it might be expected that an increased spectral width would lead to more noise on a measurement, whereas in fact it results in an increase in the number of independent samples and therefore reduces the measurement error.

While it has also been shown that in a slant elliptical transmission dual polarisation radar, the component of the standard deviation of Z_{dr} due

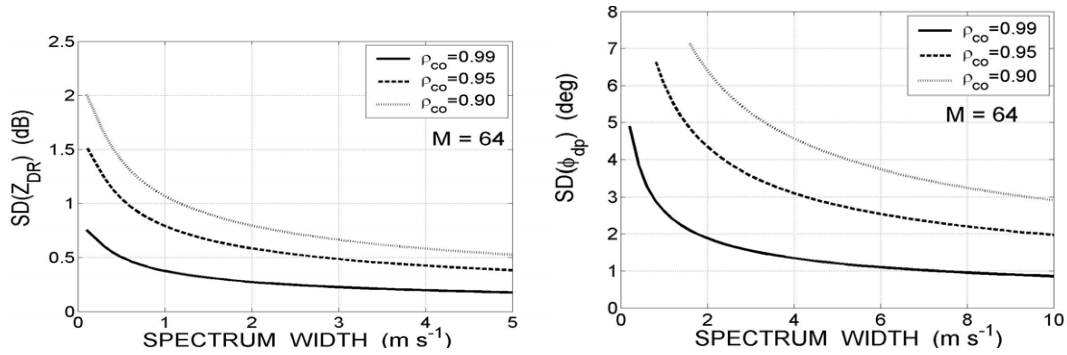

Figure 3-1: Extract from Melnikov and Zrnic, 2004: "Statistical biases and standard deviations of polarimetric variables" showing the effect of spectral width on the standard deviation of Z_{dr} and ϕ_{dp} for varying ρ_{hv} values

to the antenna is primarily governed by the maximum ρ_{hv} measurable by that antenna [59], which in turn is limited by the system cross-polar isolation (Ldr limit), the bias is also a function of the polarisation state on transmission [61] as shown in figure 3-2.

The minimum observed Ldr can be used as a measure of the isolation between the two channels, if a suitable target is chosen, ideally small droplets which will be spherical. As not all dual polarization radars are equipped with a switch to enable measurements of Ldr, the peak value of ρ_{hv} measured from circular droplets is sometimes used as a proxy for the minimum Ldr, as the system Ldr sets a limit on the maximum observable correlation between the two channels.

It has been shown that for "well-designed radars with parabolic, center-fed antennas, the dominant cross-coupling factor is the antenna" [32]. While it is relatively straightforward to achieve good cross-polar isolation in the receiver, a great deal of care must therefore be taken to ensure the reflector, OMT and feed horn are of good quality and so do not degrade the measurement.

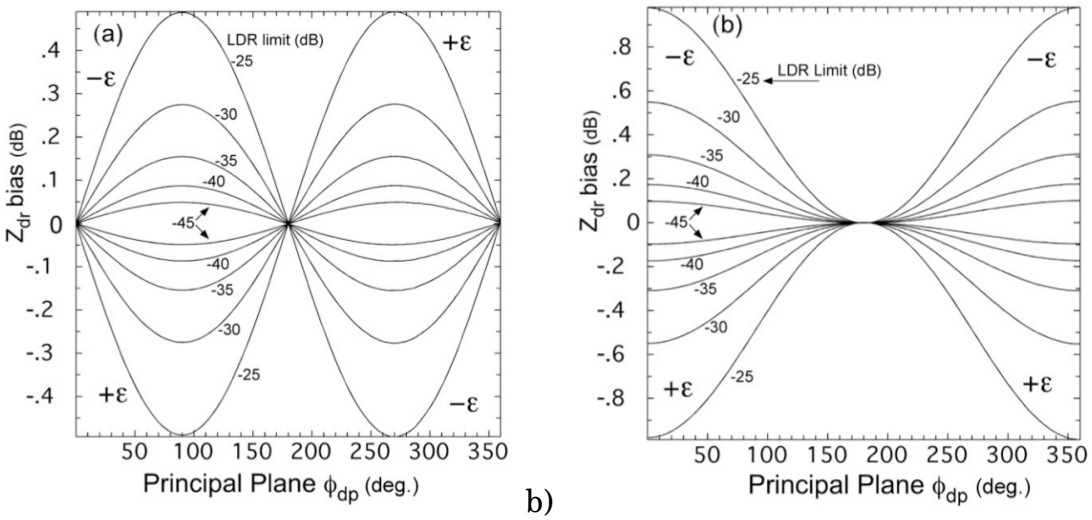

a) b)

Figure 3-2: "SHV mode Z_{dr} bias as a function of principal plane ϕ_{dp} with LDR system limit as a parameter. The antenna polarisation errors are assumed to be orthogonal ellipticity angles. The sign of the H ellipticity angle is given in each quadrant. (a) The transmitting polarisation is 45° linear, that is E_h= E_y . The curves all mimic a sine wave shape. (b) The transmitting polarisation is circular. The curves are symmetric about the vertical line through 180°" Extract from Hubbert et al. 2012 [61].

3.3 Design overview of the Weather Radar Network Renewal radar

While the overall design of the Met Office's Weather Radar Network Renewal project (WRNR) radar was a group effort by the radar hardware team, the author was responsible for the design, selection, and integration of all the digital processing and control aspects of the project and all software development.

It was decided that the system should be switchable between making measurements of Z_{dr} and Ldr. The Z_{dr} measurements are made using a Simultaneous Horizontal and Vertical architecture; as this is in many ways a simpler design, when compared to designs which alternate polarisation with each pulse, and has the advantage of measuring to higher correlations between channels in rain [32]. Selection between the two modes is via a high power waveguide switch (See 3.4.9 for details).

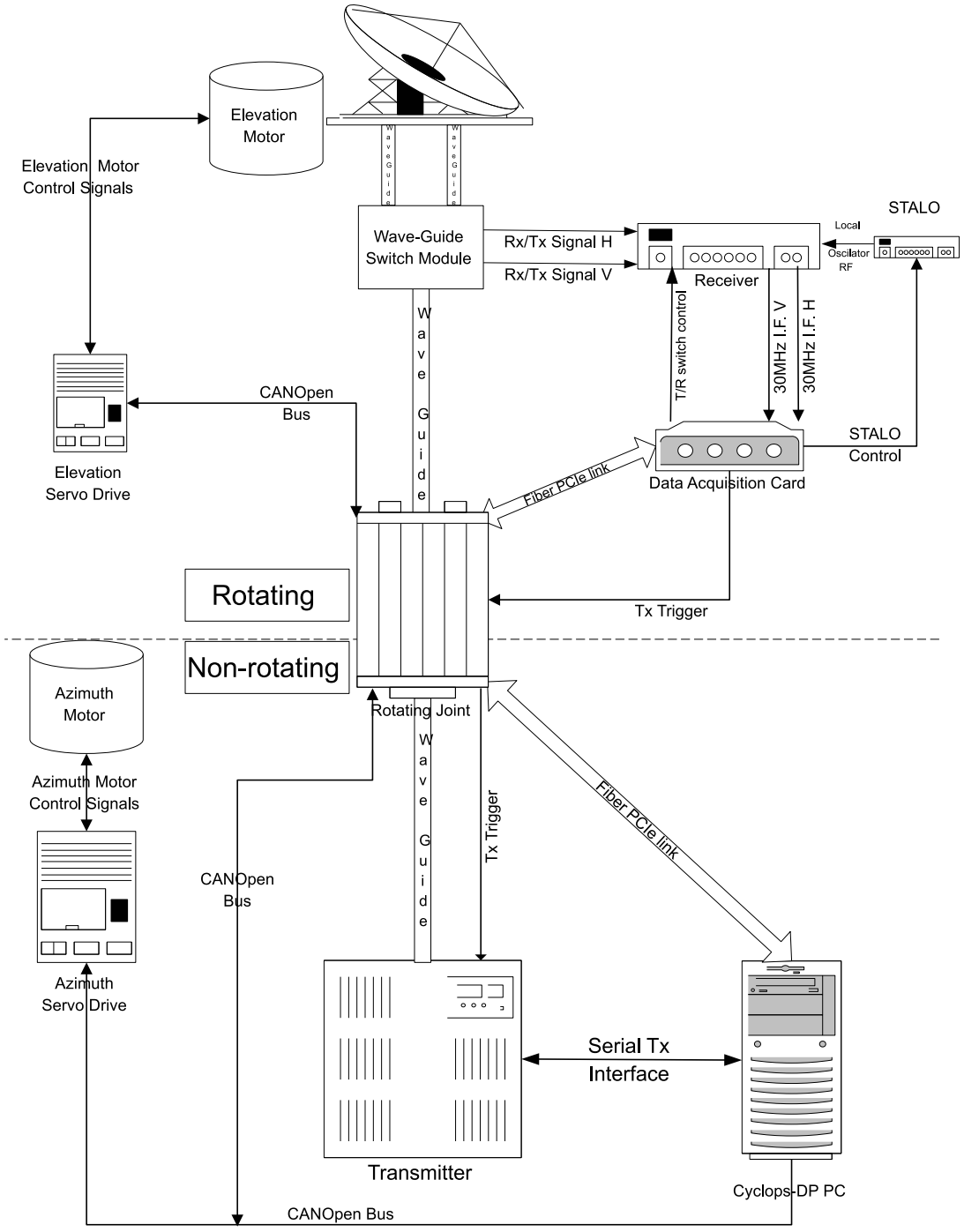

Figure 3-3: Dual polarisation weather radar renewal design overview

The design has an antenna mounted receiver; while this adds some complexity to the receiver design, it achieves better stability in $z_{dr}$and ϕ_{dp} than dual-waveguide rotating joints [16]. A single waveguide rotating joint is used to transfer the transmit pulse from the transmitter to above the axis of rotation, where depending on the type of data to be collected, it can be split to enable simultaneous horizontal and vertical transmission or routed entirely into one polarisation state (figure 3-9).

Some hardware components from the Siemens Plessey 45C system are being reused; this is beneficial as it makes the design very cost effective and sustainable, as a significant quantity of metal which makes up the pedestal, is reused rather than replaced, leading to a significant saving in CO_2 emissions.

3.4 Radar Hardware

3.4.1 Siemens Plessey 45C Radar Hardware

The weather radars in the Met Office network are Siemens Plessey 45C designs (hence SP45C). While all are of the same type, they were purchased over a considerable period of time (approximately 15 years) and so there are some minor variations in the system hardware. The radars in the UK network are old by radar standards (15 to 30 years), however tests show that they are still mechanically fit for purpose. It is hoped to increase their active lifespan by updating components as and when suitable technology becomes available.

3.4.2 Siemens Plessey Transmitter

The Met Office radars all use magnetron based transmitters in the C band (5.625 GHz $\pm$ 0.025 GHz allocated bandwidth/ ~5.3 cm). These are cross-field devices able to produce high power pulses of microwave energy. While

magnetrons are reliable and relatively inexpensive, high power devices, they do have a number of drawbacks. Specifically, in the case of the development of a Doppler system, that it is not possible to easily control the start-up phase of the device and so the phase of the transmitted pulse will be randomly different from one pulse to the next. The other disadvantage of using a magnetron stems from the fact that they depend on a resonant cavity to determine the transmitted frequency: This frequency then drifts as the size of the cavity changes due to thermal expansion and contraction of the metal. This is shown in 4-1. The receiver monitors and tracks the transmitter frequency in a process known as Automatic Frequency Control (AFC) in order to mitigate these variations.

The SP45C transmitters can be equipped with ether one or two pulse forming networks (PFNs) which are capable of producing a "Long Pulse" of 2μs, giving a range resolution of 300m, or additionally a "Short Pulse" of 0.5μs, giving a range resolution of 75 m, used to reduce the duty cycle for Doppler PRFs. Selection between the two modes is achieved by changing the state of a high voltage, high current electro-mechanical relay. Interlocks prevent the transmitter from discharging the PFNs when switching of this relay is taking place. The interface to the PFN relay is a Transistor to Transistor Logic (TTL) voltage level [62]. While the magnetron has proved to be reliable, the associated drive electronics have limitations: Specifically, with regards to reliability, the use of a high current gas valve - a thyratron, and the electro-mechanical pulse switching relays.

The peak power of the magnetron transmitter used in the UK radar network is 250 kW, however the maximum average transmitted power of the system is only 150 W. This is due to physical restrictions on the duty cycle of the magnetron, which means a maximum PRF of 300 Hz is possible when in long pulse mode and 1200 Hz when in short pulse mode.

3.4.3 WRNR Transmitter

As part of the WRNR project consideration was given to the type of transmitter to be purchased. An alternative to the current magnetron based trans-

mitters is a klystron based system. Klystrons have similar power output characteristics to magnetrons, with the advantage of being power amplifiers and so the characteristics of the transmitted pulse such as start-up phase and pulse modulation can be controlled. This leads to the possibility of pulse coding for identification and recovery of second trip echoes and improved spectral characteristics in terms of spurious emissions. A klystron transmitter has drawbacks associated with it, in that it is larger and heavier than an equivalent output power magnetron system, requires higher operating voltages, has lower efficiency and so higher power consumption and cooling requirements, and in general higher purchase costs.

The lower initial costs and operating cost - in terms of power consumption, associated cooling requirements and ease of servicing due to the reduced size, weight and technician familiarity, lead to the decision being made to continue using magnetron based transmitters.

The transmitter chosen for the WRNR radar is a Communications and Power Industries (CPI) system with very similar specifications to the SP45C transmitter described previously, primarily due to restrictions imposed by the physics of air cooled magnetron systems. An photograph of the new transmitter can be seen in figure 3-4.

The transmitter has a 250 kW peak power output with a maximum average power of 150 W. As such the limitations on the pulse width and PRFs are the same as before - a 2 μS pulse at 300 Hz or a 0.5 μS pulse at 1200 Hz. The transmitter uses a CPI VMC1891A magnetron to produce the RF power, which is capable of producing a nominal 270 kW peak output power (84 dBm peak) and is tunable in the range 5.210GHz to 5.700 GHz. An RF isolator is fitted to the output of the magnetron to provide protection against high reflected power in the event of an impedance mismatch in the waveguide. The addition of an isolator also reduces any pulling effects - in addition to heating based frequency changes, the magnetron frequency is affected by changes in the peak cathode current, an effect known as pushing (see figure 3-5 for typical response), and also by any changes in the level of matching into waveguide, known as pulling.

Figure 3-4: CPI WRNR C-band magnetron transmitter

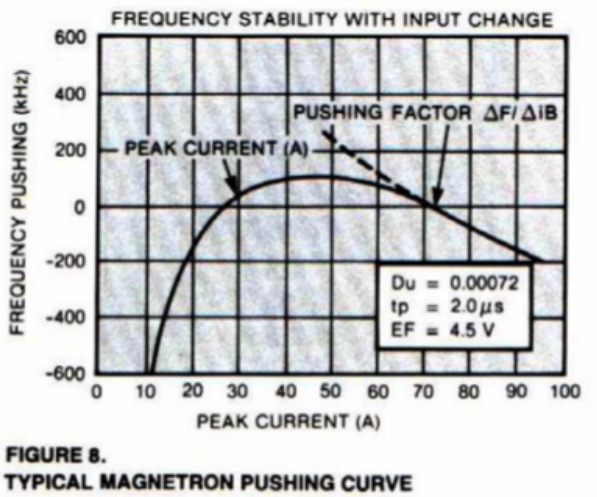

Figure 3-5: Typical pushing response of a magnetron (Extract from CPI technical report [63])

The main advantage of the CPI (WRNR) transmitter over the previous one is the solid state modulator. This controls the high voltage/current pulse to the magnetron using Insulated Gate Bipolar Transistors (IGBTs) [64]. These control the flow of current to the magnetron via a 1:30 ratio pulse transformer to give 25 kV, 40 A output from a 1 kV, 1200 A input from the IGBT array. It is expected that the solid state modulator will be much more reliable than the relays and gas valves previously used.

Transmitter control

In order to request the transmitter to fire, differential triggers are provided by the signal processing card (Hunt IO4 module: see sec. 3.5.2). The CPI transmitter has a somewhat novel method for determining the transmitted signal characteristics, in that the trigger signal determines both the pulse width and the PRF. It should be noted that an additional $0.2\mu s$ should be added to the trigger to produce the desired pulse width, due to losses and delays in the transmitter. This so call “composite” trigger means that the pulse transmission scheme is very flexible with full control being provided

by the signal processing system without the additional control lines needed by other transmitters. It is hoped that this can lead to a new “interleaved” short/long pulse with the pulse length varying on a pulse to pulse time scale allowing collection of useful Doppler and reflectivity information simultaneously. Examples of the usual pulse widths (2μs and 0.5μs) can be seen in figure 3-6.

The transmitter has a EIA-422 serial interface which is used for control and diagnostics. A USB to EIA-422 interface is used to communicate with the Tx using a C.P.I. custom protocol. This interface is provided by a USB-COMi-SI-M from Easy Sync Ltd. as shown in figure 3-7. This is configurable as a USB to RS232 or EIA-422 or RS485 interface. The Cyclops-DP software expects the Tx interface EIA-422 interface to be accessible as COM3.

3.4.4 Original Antenna

The SP45C radars in the Met Office network have a 3.66 m diameter circular parabolic reflector with a front horn feed, giving a -3 dB beamwidth of approximately 1°, a typical gain of 43 dBi and sidelobe levels of not greater than -25 dB within $\pm 10^\circ$ and not greater than -30 dB outside $\pm 10^\circ$. In contrast to the majority of weather radars in Europe, the SP45C radars are vertically polarised on transmit and receive, rather than horizontal. The exact reasons for this are not known but it has been proposed, in conversation, that this could be due to reduced attenuation relative to horzontal polarization, due to high Zdr present in intense storms or reduced sensitivity to sea clutter in the vertical polarisation. The antenna is mounted on the pedestal in an elevation over azimuth configuration.

3.4.5 WRNR Antenna

A survey of the market was performed and a number of options for the upgrade to a dual polarisation antenna were identified. In-keeping with the philosophy of reuse where possible, and from the specification of the original

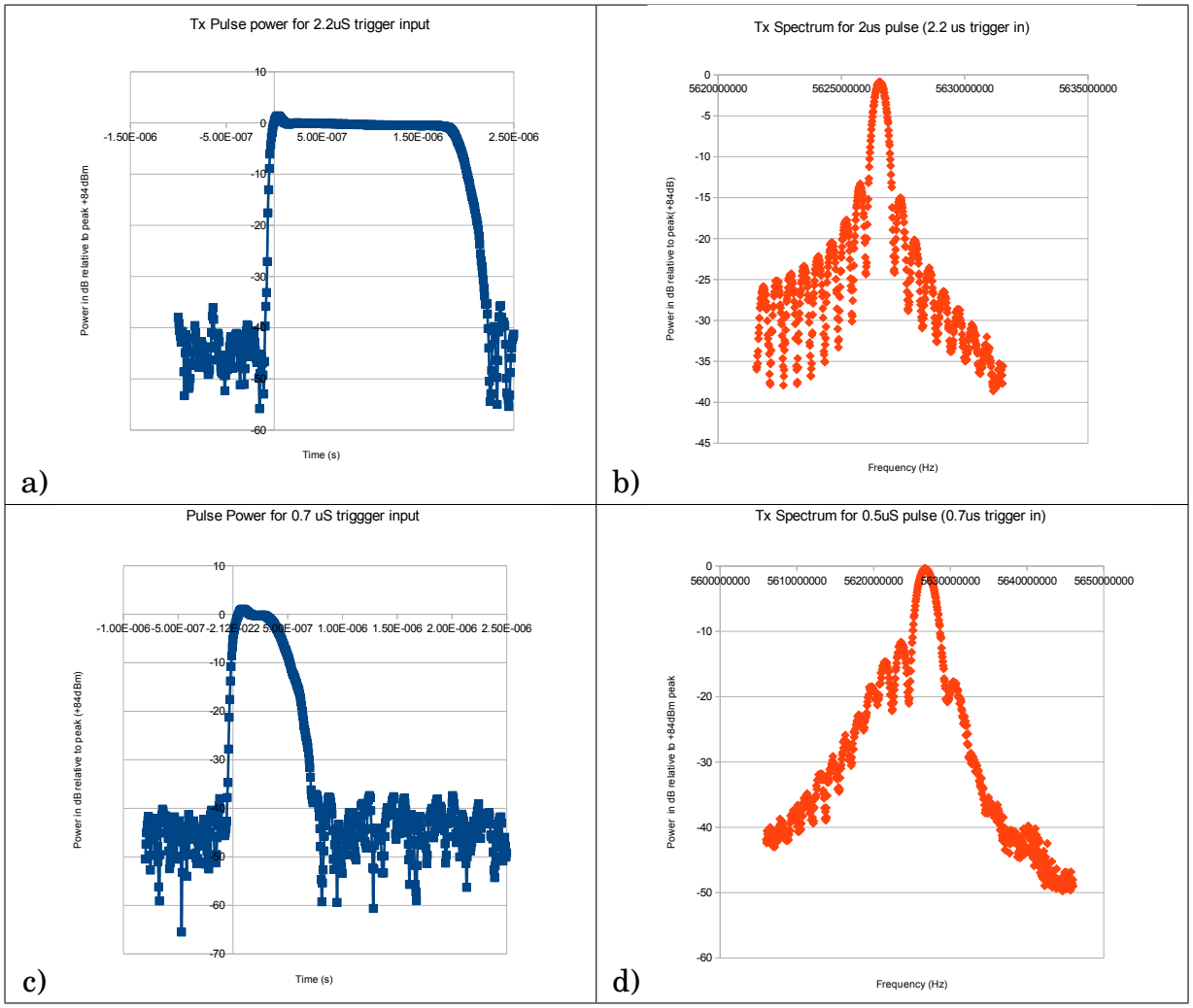

Figure 3-6: a) Transmitter pulse peak power for a 2.2 μs input trigger pulse
b) Spectrum resultant from a 2.2 μs input trigger pulse
c) Transmitter pulse peak power for a 0.7 μs input trigger pulse
d) Spectrum resultant from a 0.7 μs input trigger pulse

Figure 3-7: Easy Sync Ltd. USB-COMi-SI-M EIA-422 serial interface

parabola, it was decided that the original antenna should be upgraded with a dual polarisation feed horn, rather than purchasing a new parabola. The WRNR antenna therefore has the same beamwidth, diameter and gain as the SP45C. See Appendix A for post dual polarisation upgrade antenna beam patterns. The average cross-polar isolation for the upgraded antenna, from range testing was calculated to be -42.5dB.

3.4.6 WRNR Radome

When selecting a radome for a radar which is to make dual polarisation measurements, great care must be taken to minimise the impact of the radome on the sensitive dual polarisation measurements. It has been observed [65] that the radome can introduce artefacts into the Z_{dr} and ϕ_{dp} parameters, due to seams in the radome having differential transmission characteristics. As such, a radome with minimal differential transmission characteristics was selected for the WRNR project; Enterprise Electronics Corporation (EEC) “Stealth® Radome”.

3.4.7 SP45C Drive system

An analogue servo-drive system with a digital control interface, controls the motion of the antenna. This interface takes in TTL words from the control

system and drives the radar pointing as requested. There are control words to select the type of positioning to be carried out. These can be: pointing, rotating at a fixed elevation (known as Plan Position Indicator or PPI mode) or nodding in elevation at a fixed azimuth (known as Range Height Indicator or RHI mode). The type of scan requested determines the meaning of the rest of the inputs with regards to setting azimuth position or rotation rate and elevation position or rate.

The motor and associated gear box provide 136 Nm of torque at each axis. The gearboxes have an oil bath that requires changing every year.

The position of the radar is sensed using synchro-resolvers connected to anti-backlash gears on the elevation and azimuth gearing. Backlash is looseness that can sometimes be felt in geared systems when changing direction. The anti-backlash mechanism holds the resolver against the pinion gear preventing undesired movement. The synchro signal is passed down the tower and fed into synchro-to-digital converters housed within the radar drive interface racks. These give a 14 bit output word for each axis and provide a high resolution (0.02°) measure of the position of the antenna in a digitally readable form.

3.4.8 WRNR Drive System

A suitable replacement for the SP45C drive system was chosen by Richard Riley of the radar development team. This comprised a Danaher motion S300 Servo Drive, which is a digital servo amplifier, and has a CANOpen control and feedback interface.

The motor used is a AKM63 brush-less AC Motor. “Standstill torque 16.8Nm, Internal resolver for speed control, High output for frame size“. This is coupled to a sealed-for-life gearbox, which has a dual staged 30:1 ratio.

The positional information is fed from a data take-off gear attached to either the azimuth or elevation axis to a Hengstler 14 bit Synchronous Serial Interface (SSI) encoder to provide absolute position information. The SSI

signal is fed into the S300 drive and from there it is accessible via the CANOpen bus.

CAN/CANOpen Bus The servo systems use the CANOpen protocol to provide real-time control and feedback of the motors. The CANOpen protocol is a standard built on top of the CAN (Controller Area Network) standard. The protocol defines standard ways of communicating with a wide variety of industrial hardware. The CANOpen protocol defines standards for communicating with different types of device, such as motion control devices and IO/sensing devices.

The CAN bus on which the CANOpen protocol usually operates has its own communication protocol which is designed for real-time, fault sensitive applications.

A USB to CAN interface is required to communicate with the drive systems using the CANOpen protocol. A PEAK Systems USB to CAN interface is used to provide the physical CAN interface, the output of which is a standard 9 pin D sub connector (figure 3-8). The Cyclops software then uses the "CANOpen Magic Pro DLL" from Embedded Systems Academy to provide a CANOpen protocol stack on top of the CAN interface.

The CANOpen DLL provides the following features:

- "Send Network Management messages to all nodes or a single node
- Perform an SDO expedited or segmented download to a node
- Perform an SDO expedited or segmented upload from a node
- Progress callbacks during SDO transfers
- Operation result callback at the end of SDO transfers
- SDO transfers are non-blocking, allowing easier implementation of applications

Figure 3-8: PEAK Systems USB CAN interface

- Ability to cancel an SDO transfer currently in operation
- High speed network scan to determine nodes present.
- Typically completes in less than 0.5 seconds.
- All messages have typically 1us accuracy timestamps
- CAN 2.0A and CAN 2.0B messages supported
- Remote Transmission Request messages supported
- Transmit and receive plain CAN messages
- Callbacks for CAN messages sent and received
- Callback for events, such as bus off, timeout, hardware error and protocol error
- Ability to get a current timestamp for comparing with timestamps of messages received
- Switch networks and CAN interfaces on the fly
- High speed mass expedited write to all nodes

- Configurable timeouts and time delays
- Write Device Configuration Files to nodes
- Write Network Configuration Files to networks to configure all nodes at once
- Receives error frames
- Reset the CAN interface
- Can connect to internal networks with no CAN interface for CANOpen network simulation
- Able to find and interrogate LSS slaves on the network
- Able to configure the node IDs and bit timings of LSS slaves”

Upon start-up of Cyclops-DP, the library is used to scan for all available CANOpen nodes on CAN bus. Cyclops-DP expects that the lowest node ID and hence highest priority node will be the azimuth drive interface; the next lowest ID should then be the elevation drive and then the PEAK CANOpen micro-module, used to monitor the receiver voltages and temperatures. By default the azimuth motor should be set to Can Id. 5, the Elevation motor to Can Id. 10 and the MicroMod should be set to CAN Id. 40.

3.4.9 Waveguide

The waveguide run is designed to allow switching between SHV mode and transmitting solely in the horizontal polarisation in order to measure Ldr. As can be seen in figure 3-9 when the switch is configured for Ldr mode, all the transmitted power is routed directly to the H port of the OMT. When the switch is rotated the transmitter power is routed into a Magic-T which splits the power, with one output being routed back, via the 4 port switch, into the H port of the OMT, the other output being routed to the V port of the OMT.

On transmission the pulse is routed to the antenna using high power waveguide circulators, these then route the received signal to the receivers.

3.4.10 Slip-rings

As the receiver and digitiser were to be mounted above the azimuth plane of rotation, the digital data stream had to be transferred via slip-rings. It was an early design decision that the receiver should, be air-cooled only and therefore the amount of processing done in the receiver enclosure should be kept to a minimum by transferring the I&Q stream down the tower for processing. A conventional slip-ring would not be able to transfer the data rates that would be required and so an alternative solution was sought.

Typically this might be accomplished using a fiber optic connection and a fiber optic rotary joint. This would need to be placed at the axis of rotation, a position occupied by the waveguide in our case and so other options were sought. While a solution which uses a fiber optic coupler embedded within the waveguide rotary joint was considered, experience has shown that in the event of a loss of pressurisation of the waveguide with dry air, it is the the rotary joints that are most likely to undergo electrical breakdown, which in this case would be likely to damage the embedded optical components.

A wireless link was also considered, but there was concern that any RF interference would result in an interruption to the data stream which is unacceptable in an operational weather radar system. While no specific tests were carried out it was thought that due to the high powered microwave transmissions from the radar and potential for electrical noise to be generated by the drive equipment, the radome would not provide a benign environment for such a link.

The selected supplier was Schleifring who offered a conventional slip-ring assembly, for the transfer of power, drive control signals, transmitter triggers etc. with an additional high speed, non-contacting slip-ring assembly - their so-called GigaCap© system. This uses a pair of discs held a precise

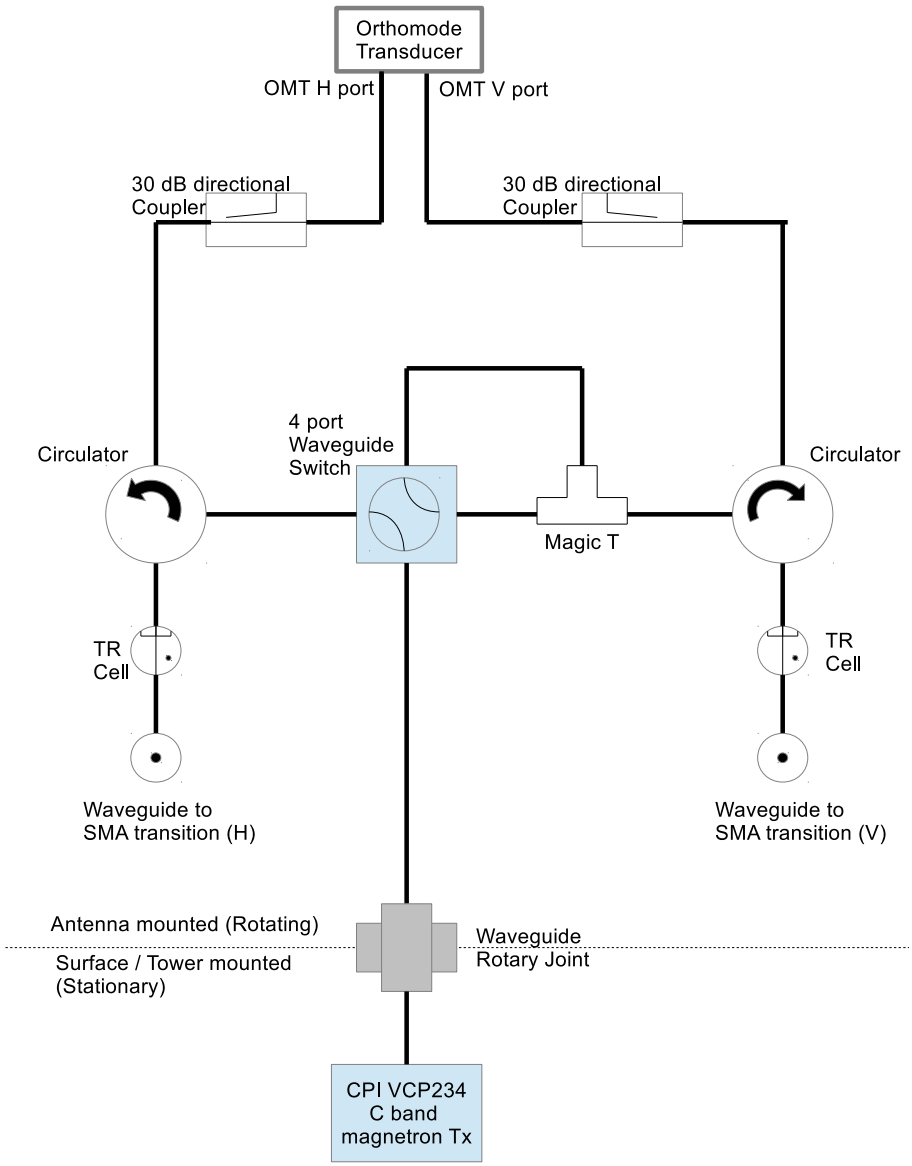

Figure 3-9: WRNR waveguide configuration with the 4 port waveguide switch set to select Ldr mode.

distance apart, which capacitively couple the signal from rotor to stator. This solution gives a maximum data rate of 10 GBit/s.

The Schleifring GigaCap© transmission system is a capacitive, non-contacting, signal transmission technique which by capacitively coupling data from the rotating part to the stationary part and vice-versa allows for very high data rates, while providing excellent wear resistance and low bit error rates. The GigaCap© system is supplied in the form of a ring which has two channels. Each ring is mono-directional and so two rings are required for full-duplex communication. As the CyclopsDP design only uses one channel this means that there is a spare channel in each ring which provides for future expansion capability and resilience.

Fiber Optic Converter boxes (FOC boxes) supplied by Schleifring translate optical signals to electrical signals for transmission over the GigaCap® high bit rate part of the slip ring. This solution is compatible with any balanced (e.g. 8b/10b encoded) high data rate signal such as Peripheral Component Interconnect Expresss (PCIe), Serial ATA (Advance Technology Attachment) (SATA), or Gigabit Ethernet.

3.5 The Cyclops-D/P receiver

3.5.1 Analogue

Single channel

The previous generation of Cyclops used a Hunt Engineering card to sample the Log Video output of the radar receiver. This is the output of a demodulating logarithmic amplifier connected to the IF signal. The use of a demodulating logarithmic amplifier means that a digitiser with a relatively low sample rate and low dynamic range can be used, as the log amplifier acts as an envelope detector giving an output voltage proportional to the

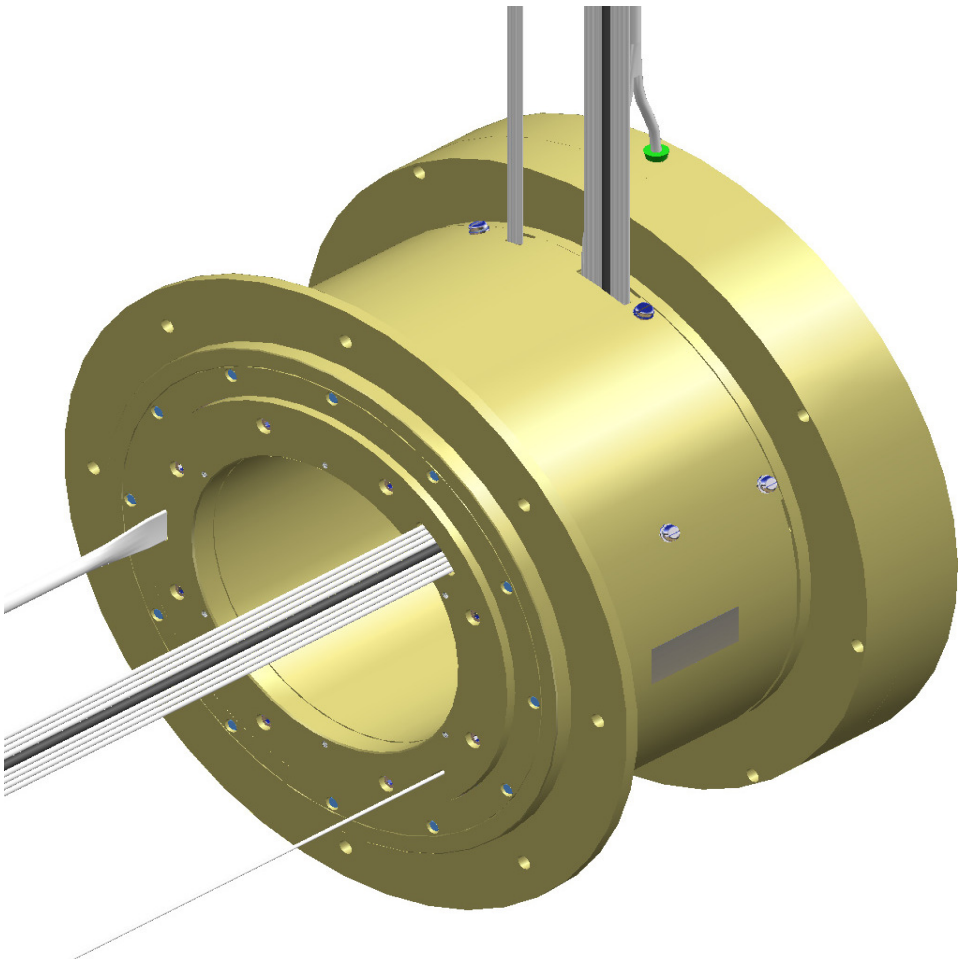

Figure 3-10: Rendered image of the Schleifring slipring, incorporating electrical and Gigacap rings

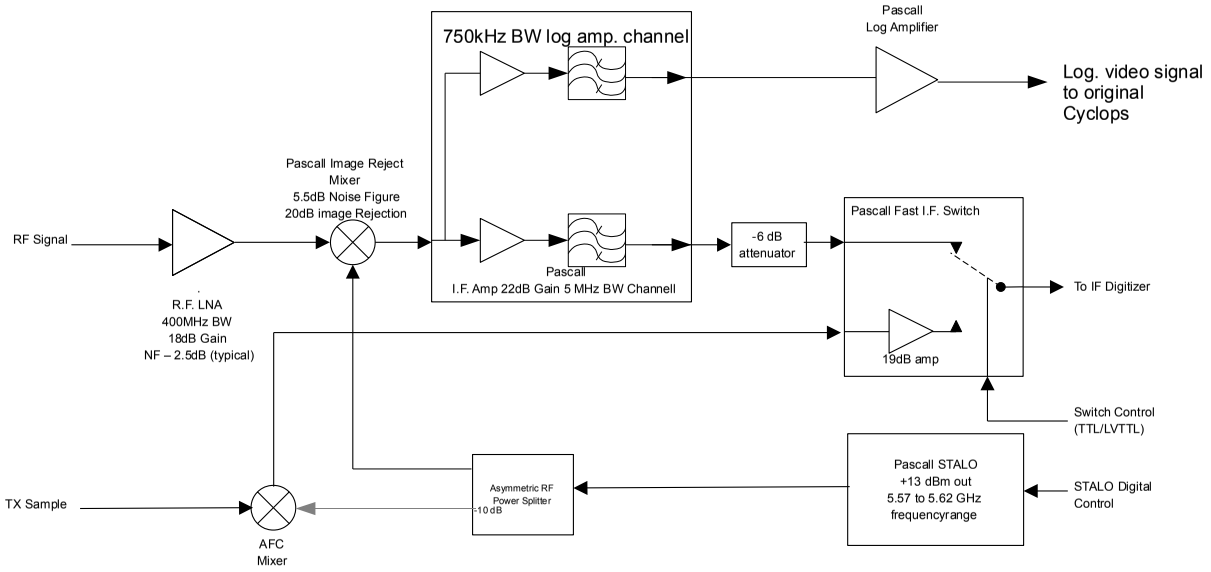

Figure 3-11: Schematic of the back/forward compatible signal channel Pascall receiver

logarithm of the input signal. This gives a very high dynamic range at the cost of the longer term stability of the system.

An earlier project to upgrade the analogue receiver resulted in an analogue receiver designed by the Met Office radar team in conjunction with engineers at Pascall Electronics (figure 3-11), with the ADER project in mind. The redesigned receiver maintained compatibility with the previous generation of Cyclops processors but allowed for easy access to the IF signal digitised by Cyclops-D.

The receiver low noise amplifier specification is as follows (from the Pascall specification document):

Frequency Range (GHz)	5.4 to 5.8
Gain	18-20dB
peak to peak flatness	1dB p-p max.
Output power @1dB GCP	10dBm min.
Noise Figure	3dB max. 2.5 dB typical

A Pascall STAble LOcal oscillator (STALO) is used to provide the frequency with which the LNA output signal is mixed to produce the IF signal. The STALO is of a digital phase locked (PLL) loop design, and has a digital interface allowing frequency control to a resolution of 100 kHz.

The IF amplifier used in the Met Office receiver is a Pascall Type 1-12310 Iss. 01, with a gain 22.8 dB and integrated filters giving a 3 dB bandwidth of 5 MHz on the IF channel to be used by Cyclops-D, and 750 kHz bandwidth on the channel used by the log amplifier. More detail on the receiver design and performance can be found in section 3.9 and chapter 5.

Dual Channel Receiver design

The dual channel WRNR receiver is based on the current operational network receiver with many of the components duplicated to allow for a second channel. Mr Mike Edwards was responsible for the analogue receiver design 3-12. More detail on the receiver design and performance can be found in section 3.9 and chapter 5.

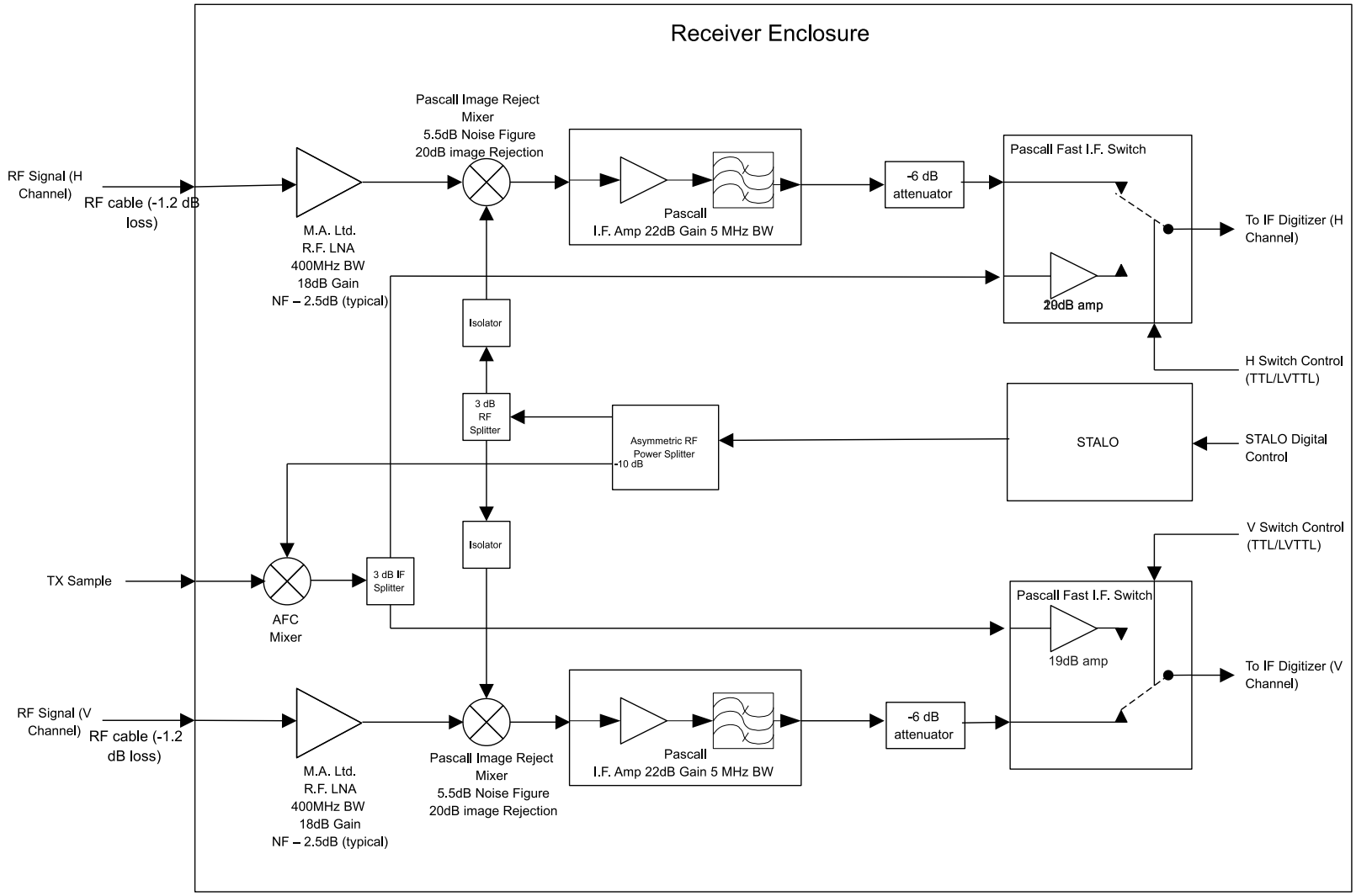

Figure 3-12: Dual Channel Cyclops-DP Receiver Schematic

3.5.2 Digital Receiver

Hunt Engineering Technology

The first stage of the development required a choice of a supplier for the data acquisition, radar interfacing and digital signal processing hardware for the ADER project. With the development of Cyclops-D it was decided to digitise the linear, IF signal and then convert to the lower rate base-band signal in the digital domain. This has a number of benefits including: reduced temperature sensitivity and no I and Q phase error, gain imbalance or offset (DC bias) errors – which manifest themselves as image spectra or clutter echoes in the Doppler spectra [66]. In addition to this it reduced the impact of the new processing system on hardware components of the radar as the current receiver design allows for easy access to the IF signal, making implementation of the new system within the Met Office radars more straightforward - this has a significant positive impact when the only radars available for testing are part of the Met Office operational weather radar network.

In order to carry out Nyquist sampling of a signal the sample rate must be at least twice the bandwidth of the signal. As the Met Office radars have an IF of 30 MHz this requires a sample rate of at least 60 MHz, however the bandwidth of interest, within the returned signal, is governed by the reciprocal of the radar pulse length. As such it is possible to sample the IF signal at rates below its Nyquist frequency and still retrieve all the information that would otherwise be available, provided care is taken to filter out all unwanted components. The downside to under-sampling the IF is that it would require the introduction of additional analogue filters to prevent unwanted signals being aliased into the pass-band where-as by Nyquist sampling the whole IF signal, relatively broadband filters (shown in figure 5-6) can be used, allowing the filtering to be carried out predominantly in the digital domain, where it is more straightforward to change the filters characteristics.

A survey of the market at the time of ADER project initiation showed that

Hunt Engineering had a very flexible, true real-time, expandable, system. This comprises a selection of PCI module-carrier boards, with a number of pluggable modules providing different capabilities. The module carrier provides true real-time links between modules on the carrier and, if required a PCI interface to the host PC, although the module carriers can be run in a stand-alone mode if power is supplied.

The Hunt Engineering modules for digitization and digital IO control all come with Field Programmable Gate Arrays or FPGAs. These are chips that have blocks of configurable logic, based on programmable Look Up Table (LUT) controlled input and output which can be used to create standard logical functions e.g. AND, NOT. In addition to this, some FPGAs come with dedicated embedded hardware functions for Digital Signal Processing (DSP) e.g. Multipliers or Accumulators and embedded memory. The logic blocks have interconnecting wires, the routing of which can be configured to allow the FPGA to effectively become a dedicated chip with the desired properties. A dedicated Hardware Design Language (HDL), such as VHDL (VHSIC hardware description language; VHSIC: very-high-speed integrated circuit) or Verilog is used to define the behaviour of the FPGA. In addition to the user being able to define the behaviour of the chip entirely, manufacturers of FPGAs supply libraries with commonly used DSP and interfacing "IP cores", included to simplify the task of designing a dedicated processing chip.

HE-IO4 The FPGA based modules include one with a 105 Mega Samples Per Second (MSPS) Analog Devices 6645-105 analogue to digital converter (ADC) and twin 125 MSPS digital to analogue converters (DACs) controlled by a Virtex-II 1M gate FPGA (XC2V1000), called the HE-IO4. The module also provides 8 bits of uncommitted digital I/O and a user configurable RS232/RS485/RS422 transceiver. The module comes fitted with a 100 MHz clock, which was upgraded to a higher precision part at the request of the Met Office.

FPGA3 A module with 90 pins of digital input or output, also controlled by a Virtex-II 1M gate FPGA, called the HE-FPGA3 was also chosen to

provide an interface to the digital position demand inputs of the radar and also to read the digital output word of the synchro-to-digital interfaces. This positional information can then be appended directly to the data stream in real time.

Hardware Interface Layer (HIL) Hunt Engineering provide a Hardware Interface Layer (HIL) to simplify programming the FPGA. This is VHDL code designed by Hunt to hide the implementation details of the modules' hardware interfaces, so that the user can simply clock data into and out of the components (e.g. ADC, First In First Out (FIFO) Interface) as required. It also configures any on module hardware.

HEPCI9 Module Carrier The modules were mounted in a HEPCI9 module carrier, providing a PCI interface and inter-module links - both data FIFOs and logic signals. The module carrier is mounted in a standard Dell PC running Windows XP. This operating system was chosen 1) for historical reasons: the previous versions of Cyclops were all Windows based. 2) For reasons of familiarity: the technicians who maintain the radars are more familiar with Windows than other operating systems such as Linux, VxWorks, QNX etc. 3) For reasons of convenience: some of the proprietary development tools required to program the FPGAs and the DSP were only available for Windows.

Realtime DSP The design of the Hunt engineering hardware and interface libraries is such that the movement of data from the card to the PC is co-ordinated by a bus-mastering PCI controller. As such, for large transfers of data no load is placed on the PC CPU and an interrupt is simply raised when a given transfer is complete. Provided the rate of interrupts is kept at a rate that the host operating system is able to deal with, no data will be lost and providing the host CPU is fast enough, all the required processing can be carried out in the intervening time. This means that careful buffering is required to prevent data being lost; this is achieved by using the embedded memory blocks in the Virtex-II FPGAs as FIFOs.

It proved to be possible to carry out the required processing on the PC provided all the embedded memory blocks in the FPGAs were used as FIFO buffers to prevent the loss of data, and provided the interrupt rate on the PC was kept below approximately 50Hz. This was accomplished by using reads of large Direct Memory Accessed (DMA)'d blocks of data in a dedicated thread which repeatedly checked whether or not the current transfer was complete, and restarted a read if it was.

Clocking of the ADC

One aspect critical to the performance of the sampling system is the jitter of the clock used to drive the ADC. The signal to noise ratio of an ADC can be severely degraded if a clock with poor jitter performance is used. The effect of this has been shown by [67]:

Consider sampling a sine wave,

$$V = Asin(2\pi ft) \tag{3.3}$$

where V is the measured voltage.

Jitter can be considered a small variation in t (δt) resulting in small error in the sampled voltage (δV). This is analogous to taking the derivative:

$$\frac{dV}{dt} = A2\pi fcos(2\pi ft) \tag{3.4}$$

The maximum error will occur when the rate of change is greatest (i.e. cos()= 1) which gives:

$$\frac{dV}{dt} = A2\pi f \tag{3.5}$$

It can be seen that the error increases linearly as a function of jitter and input frequency. Considering the resultant signal to noise ratio, the worst case effect on a sine wave is:

$$SNR = \frac{A}{(\delta V)} = \frac{1}{2\pi f(\delta t)} \tag{3.6}$$

Thus, the maximum possible signal to noise ratio is inversely proportionally affected by both the frequency that is to be measured and the clock jitter. The noise introduced by the clock jitter is multiplicative in nature rather than additive, i.e. it leads to a spreading of the input signal in the frequency domain, rather than intrinsically increasing the noise level of the system.

For weather radars, the signals of interest cover a range of not less than 90 dB. Given the radar's IF signal to be digitised is at 30 MHz, the clock jitter must be no greater than 0.16 ps. The clock that was originally fitted to the HE-IO4 had a jitter of 10ps which was clearly impacting the data. In practice the lowest jitter clock that could be found, which was compatible with the module, was specified as having 1 ps jitter. This implies a SNR of 72.4 dB. In practice, despite the fact that is is usual to assume 6 dB dynamic range for every bit of the ADC, the 14 bit AD6644-105 has a quoted signal to noise ratio of 72 dB. This is sometimes given as an Equivalent Number of Bits (ENOB) of 12.0.

Together, these facts would suggest that it is not possible to get the required performance from the system as specified, however this does not take into account that the actual bandwidth of interest is in fact much less than the bandwidth being sampled. If the noise is white and therefore distributed over the entire spectrum, over-sampling allows filtering to effectively gain SNR. The bandwidth of interest in the radar's long pulse mode is 0.5 MHz and so with a 100 MSPS ADC it is over-sampled by a factor of 200. The expected SNR from [68] is given as:

$$SNR = 6.02 * ENOB + 1.76 + +10\log_{10}(\frac{f_s}{2 * BW}) \tag{3.7}$$

where $f_s$is the sample frequency, BW is the bandwidth of the signal of interest and ENOB is the Equivalent Number of Bits of the converter. This should give 20 dB extra dynamic range, which is within the target dynamic range.

If the jitter performance of the on module default clock is found to be a problem, there are sites on the HE-IO4 module where alternate clocks can be fitted, if a suitable alternative can be found. If no surface mountable clock can be found, an external clock connected via a MMT connector can be used. It is this connector that allows for the synchronization of the sampling required to make dual polarization measurements. The spectrum of the external clock used in the dual polarization configuration is shown in figure 3-22.

HEART Technology

The Hunt Engineering HEPCI9 module carrier provides inter-module bandwidth of up to 3.2 Gbit/s. This is in the form of a 32 bit wide bus, clocked at 100 MHz. This real-time system is known as the Hunt Engineering Architecture using Ring Technology or HEART, with modules fitting this architecture known as Hunt Engineering REsource Nodes, or HERON modules. The HEART system has a number of desirable features. These are (from the Hunt Engineering documentation):

- "HEART uses Virtual FIFO connections – once connected they behave just like a hardware FIFO, providing data connections and the status flags etc. required by the HERON modules.
- The bandwidth of each Virtual FIFO is guaranteed in increments of 66 Mbytes/sec. If more than 66 Mbytes/sec are needed, then increments of 66 Mbytes/sec (timeslots) up to the full 400 Mbytes/sec can be added.
- Each node (including the Host Computer connection) has 6 independent input FIFOs and 6 independent output FIFOs.
- Multiple connections between the same nodes can be made, so that different streams of data can be separated.
- Multi-cast connections are supported, where the data sent by a node can be received by more than one node.

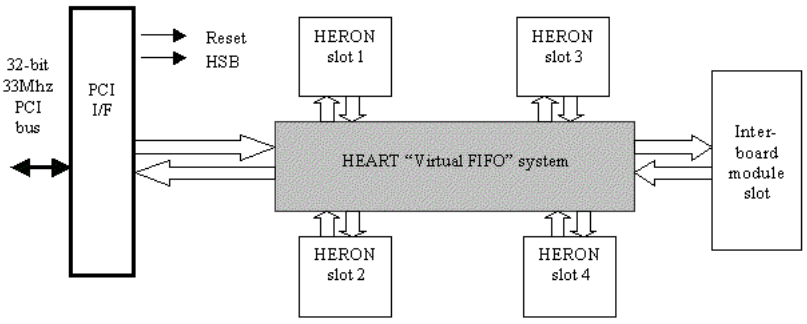

Figure 3-13: Hunt Engineering Architecture using Ring Technology or HEART (©Hunt Engineering Ltd.)

- Connections can be pre-allocated at boot time, and then re-assigned by the application as necessary.
- Connections between boards are identical to connections within a board (depending on an extra inter-board module)"

The HEART system uses user run-time configurable virtual FIFOs to transfer data between the different modules (figure 3-13). These FIFOs are of guaranteed bandwidth and latency. Each slot on the module carrier has a number which defines that module in the HEART configuration file. It is then possible to define which output FIFO number links from the module to another slots' input FIFO number. It is also possible to tie module carriers together via electrical or fibre optic links if it is necessary to use more than 4 modules. Again this works via the HEART and the additional module can be accessed just as any other FIFO once it has been configured.

Digital Down-Conversion

The information content of the radar pulse is governed by the bandwidth of the transmitted pulse. For a rectangular pulse with no intrinsic modulation it is generally quoted that the bandwidth of the pulse is approximately equal to the reciprocal of the pulse width [34]. For the $2\mu s$ pulse used in the Met Office radars this corresponds to a signal bandwidth of 0.5 MHz. It is

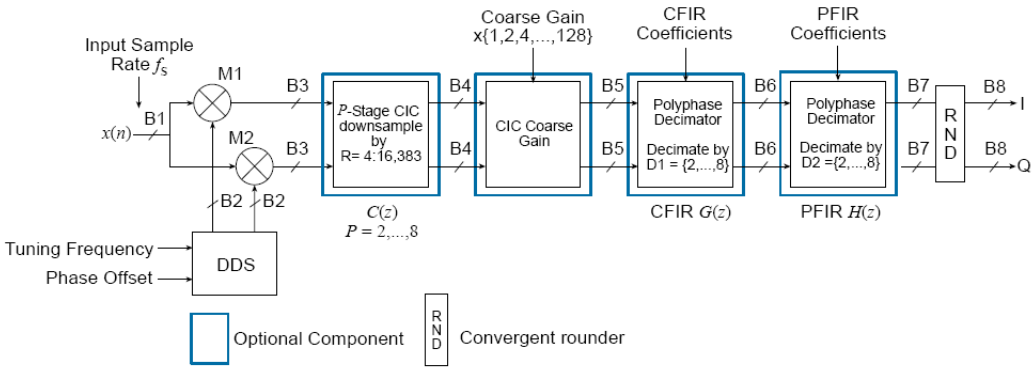

Figure 3-14: Xilinx DDC Core Generator Component

desirable to exclude any signal that is not related to that which has been transmitted; this is done by using analogue and digital filters to remove the excess, unused sampling bandwidth from the signal bandwidth. The analogue filters are defined by the analogue radar receiver hardware and allow a passband of ~5 MHz about the IF, further filtering is then carried out in the digital domain as part of the down-conversion to baseband. These filters are designed to match the bandwidth of the pulse and therefore change with pulse length.

The Core Generator tool provided by Xilinx as part of their ISE development environment includes a Digital Down Converter (DDC) IP Core. IP Cores are the FPGA equivalent of a library in traditional procedural programming, but are usually configured at the design stage and provide the specified functionality on synthesis of the FPGA layout. The DDC component uses a number of different blocks in its construction. These are the Direct Digital Synthesizer (DDS), a Cascaded Integrator-Comb (CIC) filter [69], and a number of Finite Impulse Response (FIR) filters. Convergent rounding is used at each stage in order to minimize the introduction of a DC bias offset.

Direct Digital Synthesizer

The direct digital synthesizer is used to generate numerical values of sine and cosine for mixing (multiplication) with the IF sample values from the

ADC. The frequency of the generated sine waves is digitally controlled and should be equal to the frequency of the IF.

As the frequency is generated numerically using a phase accumulator, it is possible to very accurately control the frequency of the output. It is possible to select frequency control down to 0.02333 Hz, but in practice for Cyclops-D an accuracy of 0.03 Hz is used. Of course this frequency control and accuracy assumes a perfectly accurate oscillator is used to clock the FPGA logic. In practice the same clock is used to drive the FPGA and to drive the sample clock.

The sine and cosine values from the DDS are mixed with the incoming samples of the IF generating I and Q data. (See figure 3-14)

Down-conversion Filtering

CIC filter The filtering which occurs in the FPGA is a multi-stage process. The first layer of filtering is a decimating CIC filter. The CIC filter has 7 stages, a differential delay of 1 and a decimation rate of 10, giving a frequency response as seen in figure 3-15.

Advantages of the CIC filter include good rejection, large decimation factors and that it is easily realisable in a relatively small amount of FPGA fabric. The main disadvantage is that it suffers from a large amount of droop in its pass band. As a consequence it is usually used in conjunction with a compensating finite impulse response (CFIR) filter.

The magnitude frequency response of a CIC filter $|H(f)|$ is given by:

$$|H(f)| = \left| \frac{sin(\pi M f)}{sin(\frac{\pi f}{R})} \right|^N \tag{3.8}$$

Where M is the differential delay, N is the order of the filter and R is the rate change.

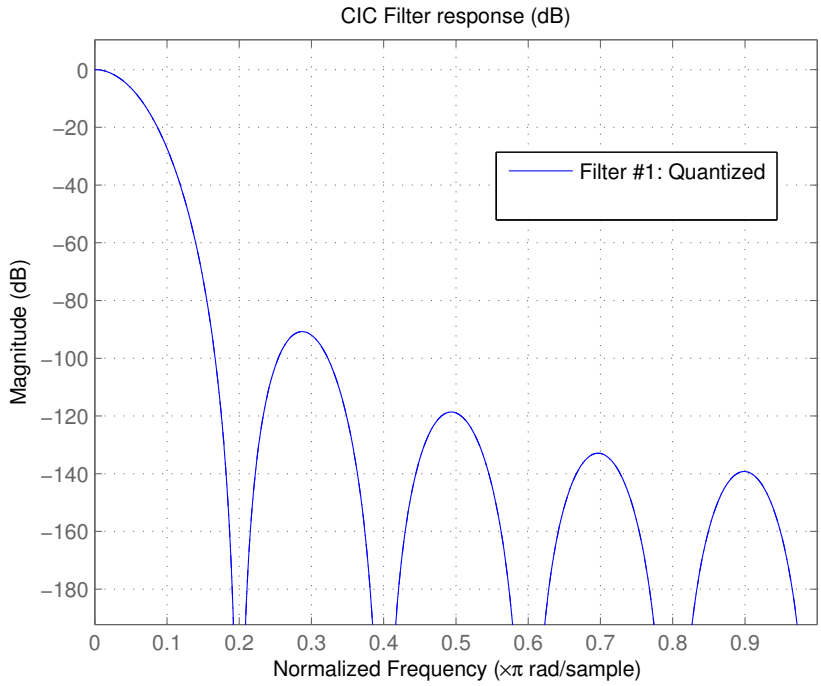

Figure 3-15: Cyclops CIC filter response

CFIR filter The compensating finite impulse response (CFIR) filter is used to correct for the droop introduced by the CIC in the pass-band. It can also carry out further decimation.

The FIR filter is one of the primary filter types used in digital signal processing, the other being the infinite impulse response filter. The impulse response is finite because there is no feedback in the filter. The advantages of a FIR filter are that it is easy to design to have linear phase (i.e. delay the input signal but do not distort its phase), they are easy to implement and are inherently numerically stable.

Once the droop in the pass-band is known (figure 3-15) it is relatively easy to design a FIR to compensate (figure 3-16). This is most easily done using a dedicated FIR filter design program or using Matlab's signal processing toolkit.

The resultant effect of a CIC with a CFIR is shown in figure 3-17.

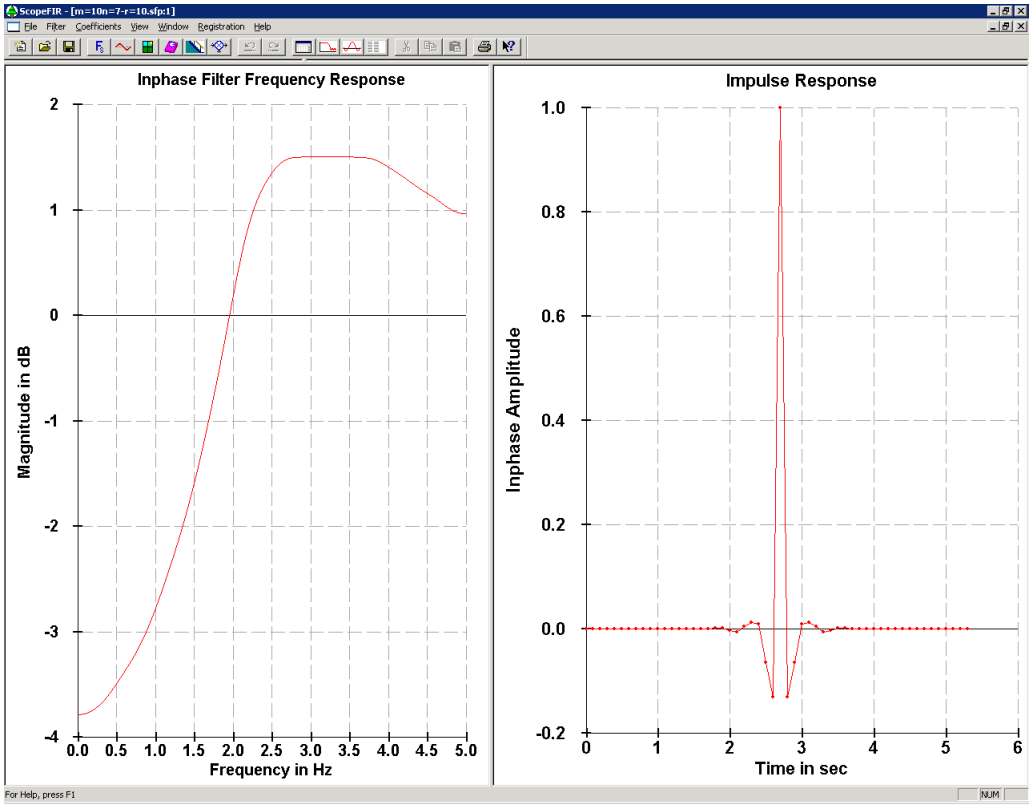

Figure 3-16: ScopeFIR plot showing CFIR frequency response designed to compensate for passband droop of CIC filter

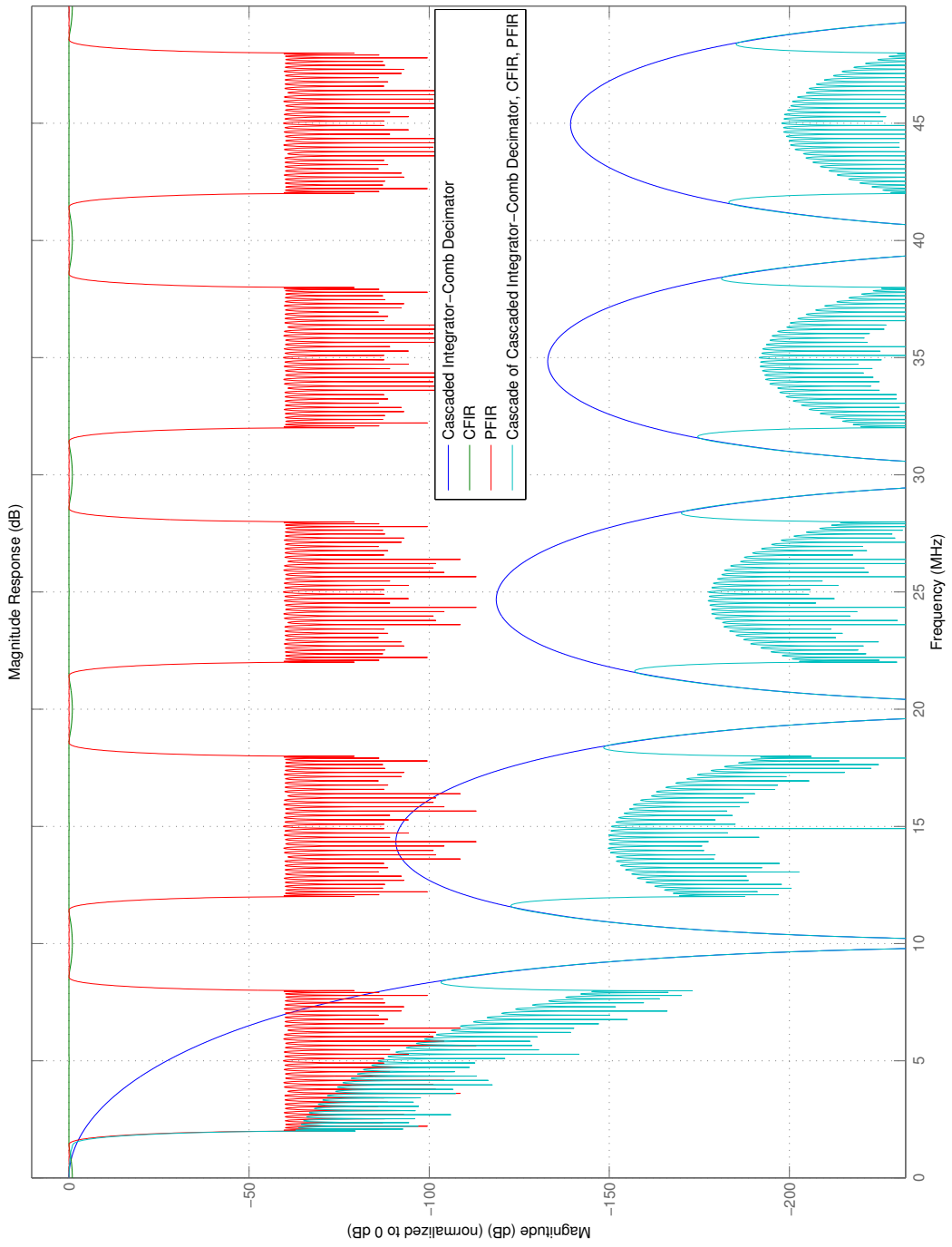

Figure 3-17: Composite Filter Response

PFIR filter Once the pass-band has been restored, an additional layer of filtering can be applied: a Programmable FIR (PFIR). This stage can also carry out further decimation, in the case of Cyclops-D by a factor of 5, reducing the data rate to the short pulse target rate of 2 MSPS. An additional stage of decimating FIR filtering is applied to the long pulse processing, further reducing the data rate and bandwidth, to 0.5 MSPS with a passband matched to that.

By using this array of cascaded filters the overall design provides good rejection and, in testing, gives noise rejection performance equivalent to that of the existing analogue filters (a requirement of the move to a digital IF based receiver).

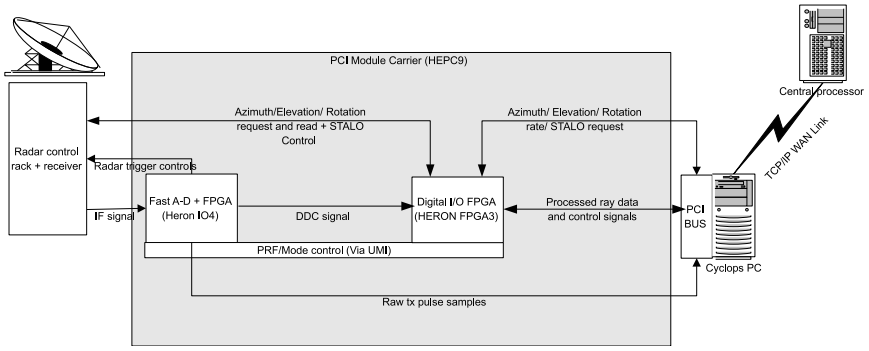

Figure 3-18: Architecture of Cyclops-D processor

Overview of the single polarisation Cyclops Doppler processing system

The overall architecture of the Cyclops-D system is shown in figure 3-18. In this design the IO4 module uses its digital outputs to request the firing of the transmitter at the required PRF, and switch the receiver to route the Tx burst to the input of the ADC. When the transmitted pulse is detected, raw samples of it are taken and routed to the PC for Automatic Frequency Control (AFC) purposes, as well as being routed into the DDC to create a baseband I and Q value of the transmitted burst for phase correction. The switch is then set to route the signal from the receiver into the ADC producing a received I and Q sample stream. This is then passed via the HEART FIFOs to the FPGA3 module.

The FPGA3 has control of the radar pointing, rotation rate, and STALO via some of its 90 digital IO pins. In addition, output from the synchro to digital converters are also routed to the digital IO pins: Upon detection of the firing of the transmitter, a sample of the current position value is clocked on to the FIFO to the PC, along with a start of ray tag and sequence number. The I and Q stream from the IO4 is then appended to this, having first been passed through the additional FIR filter, if long pulse mode is selected. The FPGA3 then sends completed I and Q streams to the PC.

The PC has FIFO links to the FPGAs in order to configure the type of processing to be done (LP/SP), to control the digital output, and so make

demands of the radar hardware. The PC carries out the required pulse pair processing and packages up the resultant data into polar data files in a Met Office internally specified format. The PC also takes the raw samples of the transmitter burst and uses them to estimate the current intermediate frequency. If required this is then used to send a message to either the IO4, to change the DDC NCO frequency or to the FPGA3 to change the STALO frequency.

3.6 ADNACO PCI/PCIe expansion system

Once a solution able deal with the required data transfer rates from the receiver, mounted on the rotating antenna was found (sec. 3.4.10), a protocol and hardware for transferring the data were needed. While it is possible to extend the HEART bus over multiple HEPC9 boards either electronically or optically, (one of which would be mounted in the receiver, the other in the PC); In order to provide future proofing and manufacturer independence an industry standard protocol was preferred.

A solution provided by Adnaco Technology was identified which transfers the PCIe protocol over a fibre-optic converter. The PCIe protocol is a self-clocking serial stream (8b10b encoded) with the PCIe 1.x standard being clocked at 2.5 GT/s and capable of data rates of 250 MB/s per lane. The Adnaco board provides a single PCIe 1.x lane link. This provides the required future proofing and manufacturer independence, as the PCIe standard is widely supported by multiple suppliers of suitable PCIe data acquisition cards.

A particularly desirable feature of this technology is that no additional development is required to deploy a PCI/PCIe card at the other end of the fibre. The Adnaco system comprises two boards, one of which plugs into any PCIe slot in the host PC and comprises a PCI bridge and electro-optical converter (in practice a Small Form Factor pluggable (SFP) transceiver [70]). The other board is at the other end of the fiber and again supplies an electro-optical converter (SFP) and another PCI bridge which is connected

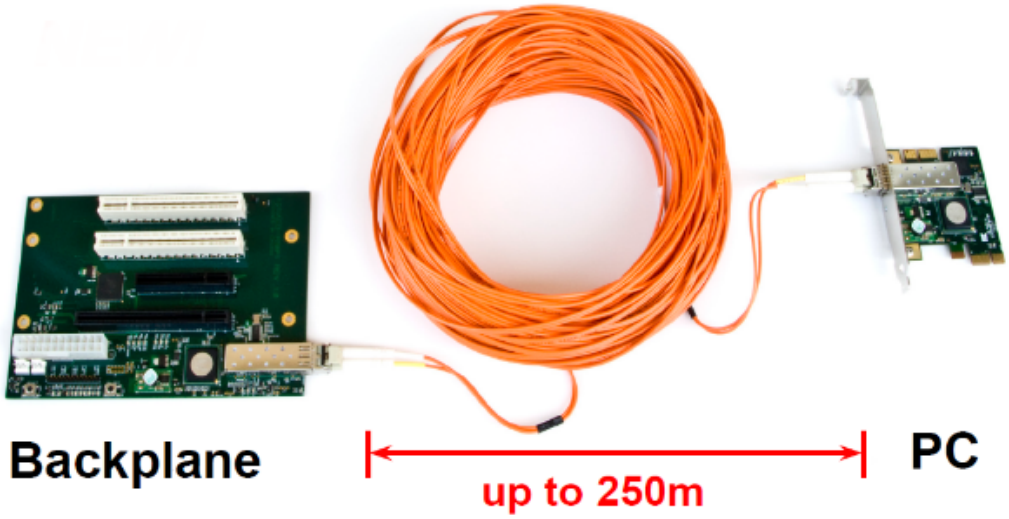

Figure 3-19: Adnaco PCIe over fiber interface

to 2 PCI slots, 1x4 PCIe slot and 1x8 PCIe slot, however both PCIe slots are wired as single lane slots. Due to the optical nature of the transfer and the electrical nature of the high speed slip-rings, a pair of electro-optical converters - Fibre Optic Converter (FOC) boxes - were mounted at either side of the slip rings.

The HEPC9 is mounted in a Adnaco-S1 PCI/PCIe expansion system, which can be seen in figure 3-19. This allows the digitiser to be installed up to 250 m away from the PC. The PCI/PCIe expansion module and digitiser are then mounted in the receiver on the back of the antenna.

3.7 Dual Channel Cyclops

The Cyclops-DP digital receiver is based on the previous network standard receiver but to enable the capture of dual polarisation data, an additional IO4 module is fitted. The new WRNR design receiver sees a major change in the architecture of the system: The receiver (analogue and digital) is now mounted on the back of the antenna and accessed via a fiber optic link. A

schematic of the signal paths within the WRNR radar can be seen in figure 3-20.

Several of the dual polarisation products are sensitive to the relative phases of the two signals. In-order to preserve this information it is necessary to synchronize the ADCs on each of the IO4 modules. Fortunately the modules come with the option of being driven by an external sample clock.

There is a “clocks” connector on each of the IO4 modules which allows for up to 4 external clock inputs, and a clock output. The A/C clock input can be used, either with a low level sinusoidal clock input or an LVTTL square wave input. When the correct jumpers are fitted, this clock drives the ADC directly with a 350 ps maximum delay, allowing a low phase error and no additional jitter. In this case, the ADC clock becomes an input to the FPGA for use in the associated logic design. In addition, the Uncommitted Module Interface (UMI) pins on the HEPC9 module connector can be used as a clock input, if another module in the system is programmed to drive that clock onto the UMI connection.

In practice the sample clock is provided by an Innovative Integration (II) ClockGen PCI Mezzanine Card (PMC) module (figure 3-21), mounted in an II PMC to PCI module carrier.

“The ClockGen is a precision clock generator on a PMC IO module for sample rate generation, system clock synchronization, and clock distribution. The four output clocks, external clock and reference clock inputs are front panel SMA connectors. Each output can drive a 50 ohm load. For sample rate generation, the ClockGen PMC generates four clock outputs over a frequency range of 100 kHz to 270 MHz. The clocks can be locked to a reference clock input or an optional Stratum III (200 ppb) stable reference. The clock outputs have a tuning resolution of < 0.1 Hz over the full output range.” [71].

- Four Programmable Clock Outputs
- 100 kHz to 270 MHz output range

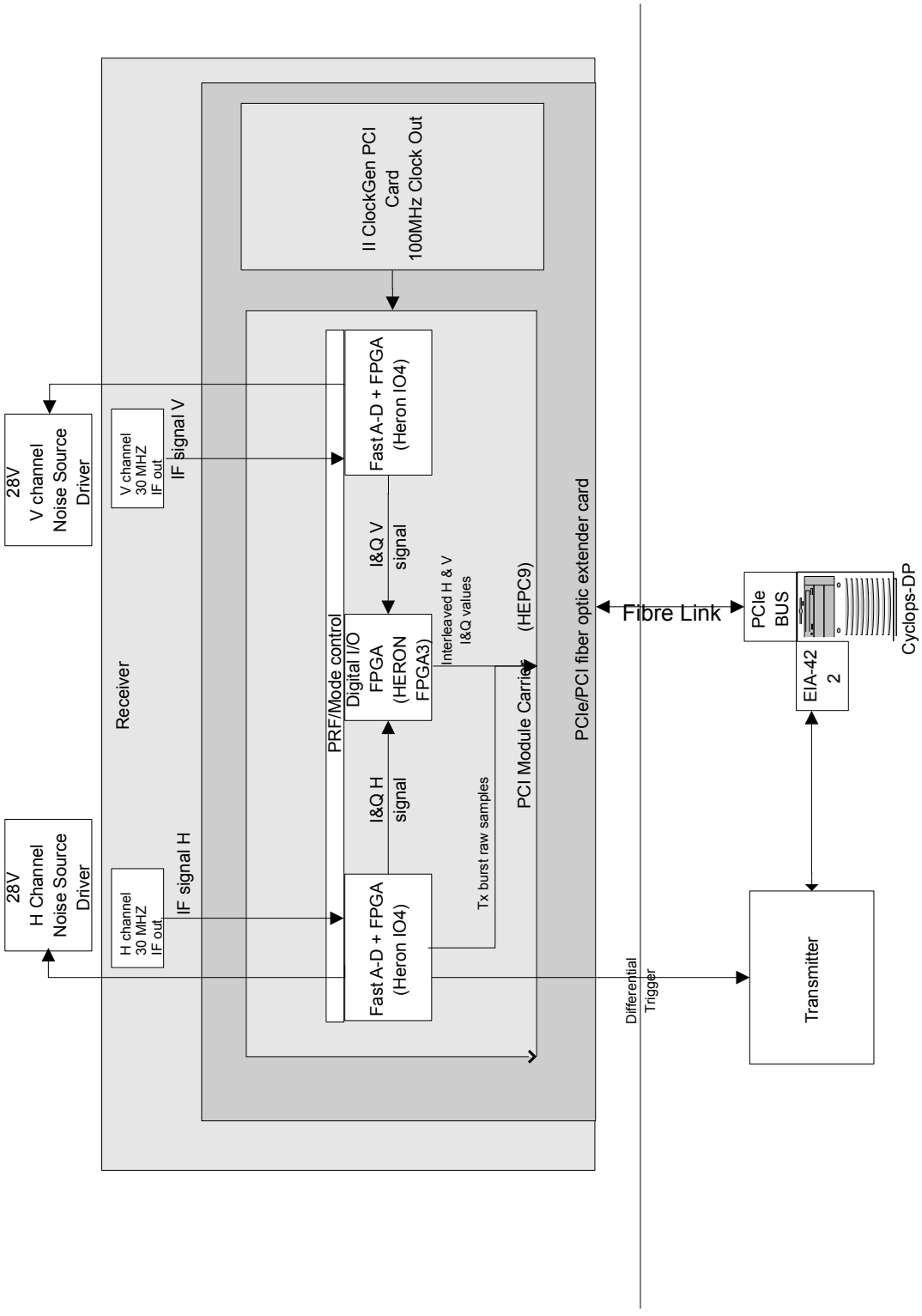

Figure 3-20: Schematic showing signal routing (analogue and digital) within the Cyclops-DP digital receiver

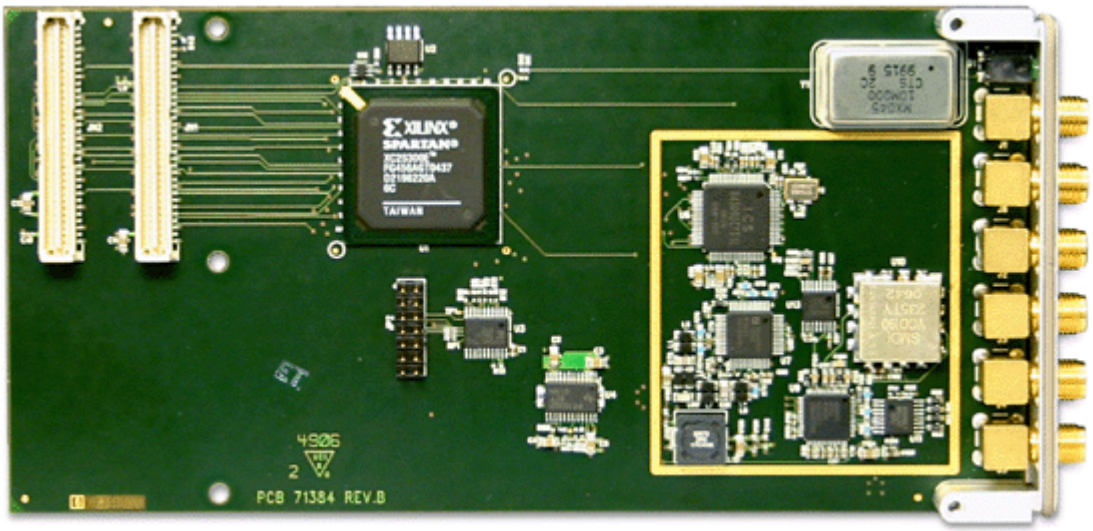

Figure 3-21: Innovative Integration ClockGen Module

- 0.01 Hz resolution
- < 1 ps rms jitter for 6.25 to 270 MHz clock range
- External Reference Clock Input
- Lock to reference clock input from 2.3 kHz to 100 MHz
- Buffer and redistribute 1:4 an external clock input
- Optional high stability, 0.5 ppb reference clock
- Drives 50 ohm loads
- SMA connectors
- PCI Interface

The output is Low Voltage Complementary Metal Oxide Semiconductor (LVCMOS) and is used to drive the LVTTL 50 ohm input to the sample clock of the IO4 module. For the HE IO4 module to use the correct clock, jumpers have to be fitted in the correct location to route the external clock input to the sample clock input of the ADC. The spectrum of the clock at the desired 100 MHz sample rate is shown in figure 3-22.

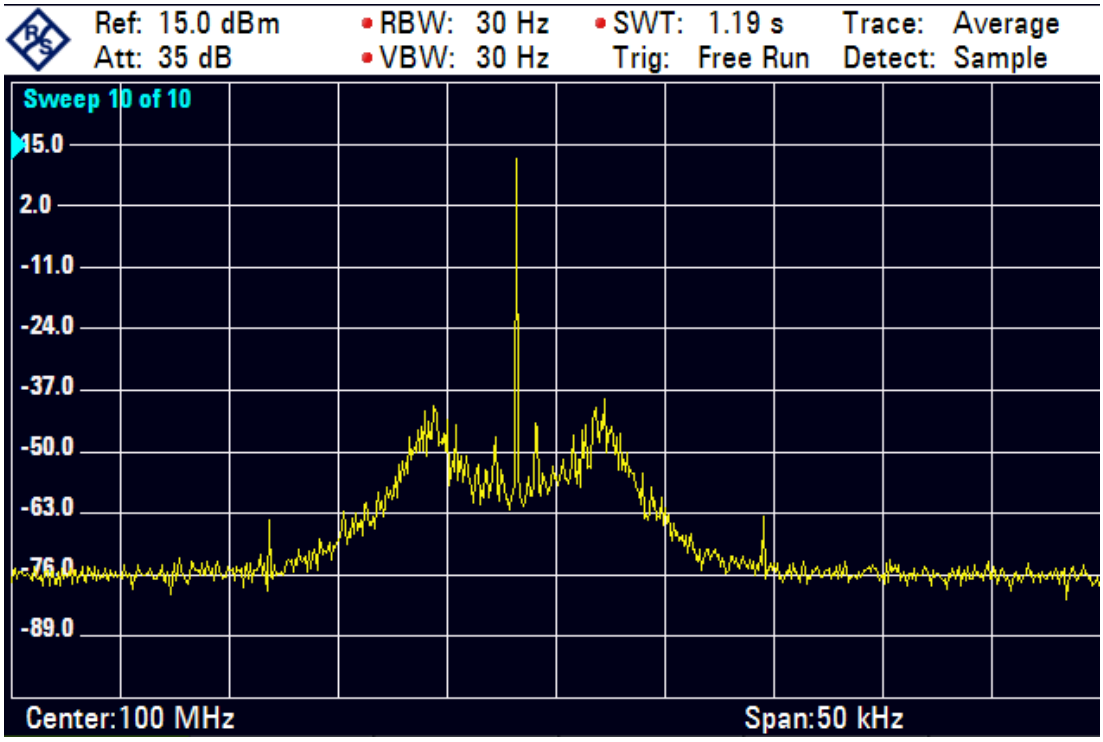

Figure 3-22: Spectrum of the clock produced by the Innovative Integration ClockGen module, as measured using a Rhode and Schwartz FSH8 spectrum analyser

The clock generated by the IICG module has less than 1 ps Root Mean Square (RMS) jitter. This is as low jitter a clock as is readily available at the time of this project. In the future this could perhaps be upgraded to a II X3-Timing module, which has a quoted jitter of a mere 0.2 ps RMS and has the added advantage of an on-board GPS receiver, to provide a known accurate reference.

3.8 Software Design

The Cyclops software primarily comprises a multi-threaded C++ program, responsible for scheduling scans, processing the resultant I and Q data, product generation, AFC and monitoring the status of the Radar and PC. Extensive use was made of the C++ Boost framework in order to make

the code as platform independent as possible. In addition any hardware interfaces were encapsulated so that any future hardware changes will not impact the routine radar processing aspects of Cyclops.

A number of utility programs have also been written to allow data visualisation at site, manual radar control and status monitoring.

The structure of the Cyclops software is shown in figure 3-23. Upon the Scheduler meeting the conditions for the start of a Volume scanning task, the Beam configuration of the radar for that scan is passed to the Radar object for it to configure the hardware appropriately. The Radar object sets the rotation rate, elevation, the sampling parameters of the data acquisition card and notifies the Scheduler that this has occurred. The specifications of the Product(s) to be generated from the resultant data for the scan are passed in to the Processing Thread. When this has occurred the Processing Thread reads the I and Q values for the pulse from the data acquisition card, phase corrects them, calculates the average Doppler and dual polarisation moments for 1 degree sectors (matched to the antenna beam width), and then passes the processed rays in to the Polar data products for population of their data stores and any additional averaging or processing that is required for that product. Upon completion of the Polar data file it will store itself to the disk for transfer to the central processing system and signal to the Scheduler that it is complete. If no more products exist in the processing thread then the scheduler will move to the next beam until the Volume is complete.

In a separate thread the AFC processor is responsible for reading raw samples of the transmit pulse at the intermediate frequency, estimating what the intermediate frequency is and requesting that the Radar update the STALO or NCO to match that transmit frequency, as required. As the STALO has a digital interface, which controls the multiplication or division factor in phase locked loops to generate the STALO output frequency, it is possible to measure the transmitter frequency with this system, it being the sum of the requested STALO frequency and the current IF estimate.

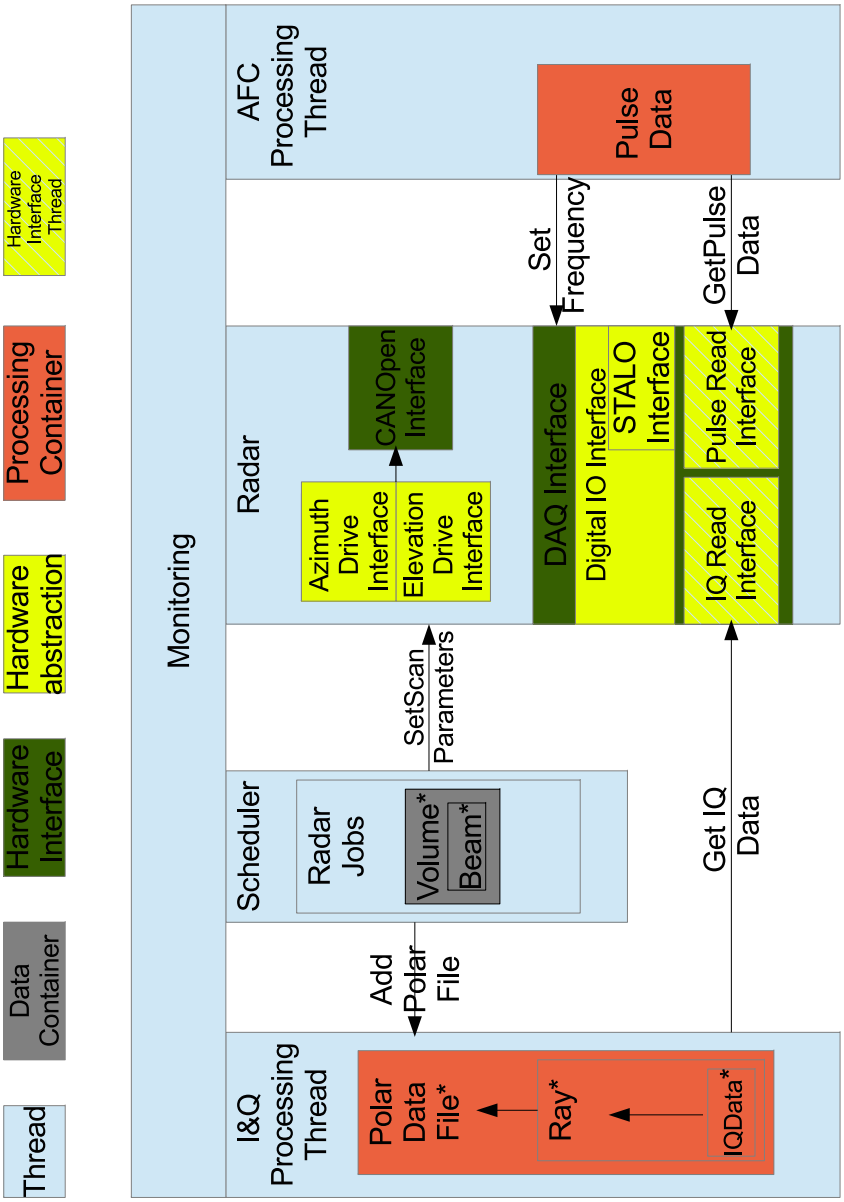

Figure 3-23: Processing software design overview (*denotes that multiple instances of the object can be instantiated at any time)

3.9 Quality Evaluation

Testing of the system(s) has taken place both in the lab, and using prototype systems built at the Met Office in Exeter and at Wardon Hill radar site in Dorset with positive results.

Dynamic Range Testing

In order to verify the power response of the system, signals are injected into each channel at varying power levels. This is to ensure that the power response of each channel is linear, has the required dynamic range (>80 dB [33]), and has sufficient cross channel isolation that the dual polarisation products will not be degraded.

The results of the power calibration for the H and V channels are shown in figures 3-24 a) and b) respectively. It can be seen that the system shows good linearity; meeting the required linear dynamic range specification needed to cover a reasonable breadth of rain rates at all measured ranges. The isolation between the two channels are 65 dB from V to H, and 70dB from H to V. As such, dual polarisation measurements will not be compromised by cross-channel interference in the receiver. The reason for this asymmetry is not well understood but could be related the different gains of the two channels and the manufacturing differences in the isolators used. As both channels exceed the required isolation it was not investigated further.

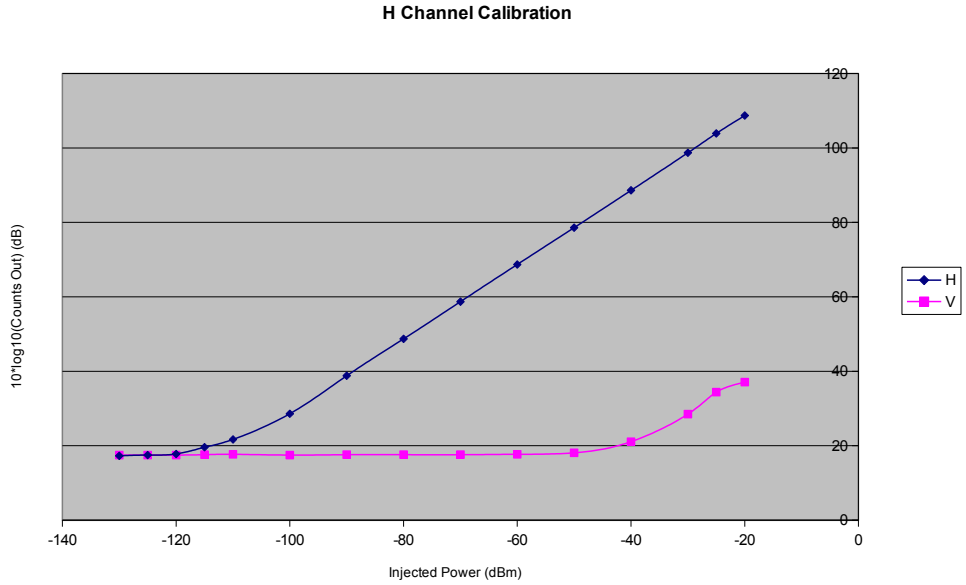

a) H channel calibration

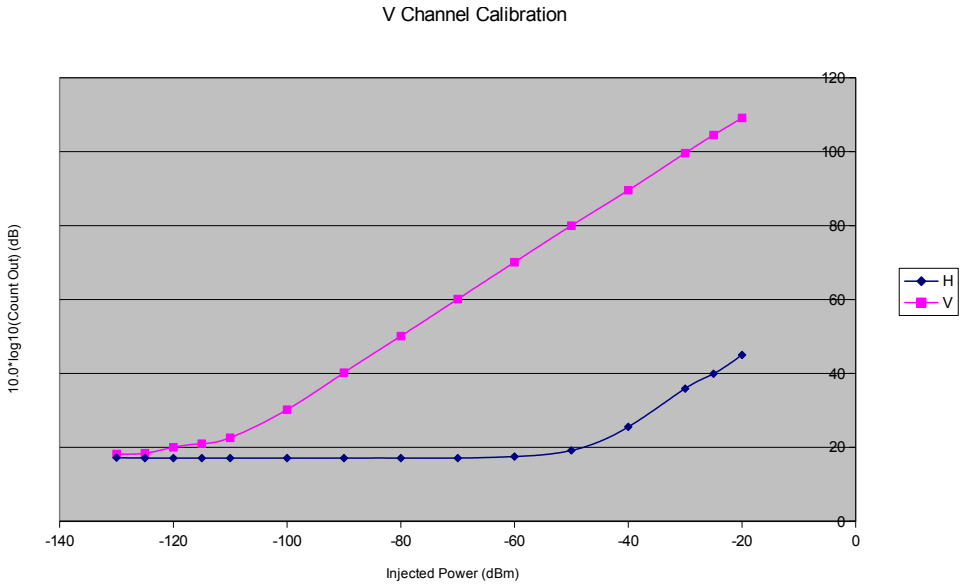

b) V channel calibration

Figure 3-24: Calibration of the Cyclops-DP receiver for a) the H channel and b) the V channel.

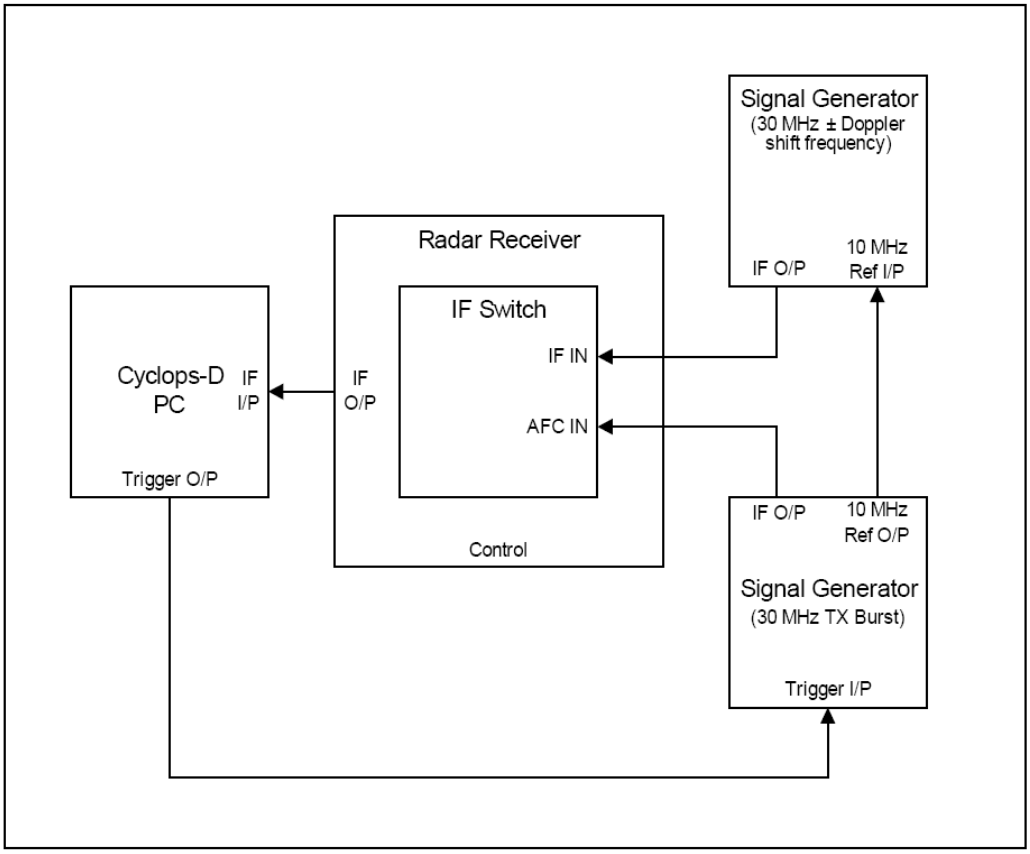

Figure 3-25: Velocity testing receiver configuration
(Figure taken from Met Office internal document authored by Mike Edwards)

Velocity testing

The verification of the velocity processing was carried out using two signal generators, by injecting signals at the IF into each channel. One acting as the transmitter and another acting as the received signal. If the two generators are phase locked together using the 10 MHz reference in/outputs on the signal generators, the frequencies can be tuned to simulate a Doppler velocity. The exact arrangement of test equipment can be seen in figure 3-25.

The results of the test can be seen in figure 3-26. As the agreement with the expected velocities is very good the figure shows the error in m/s from

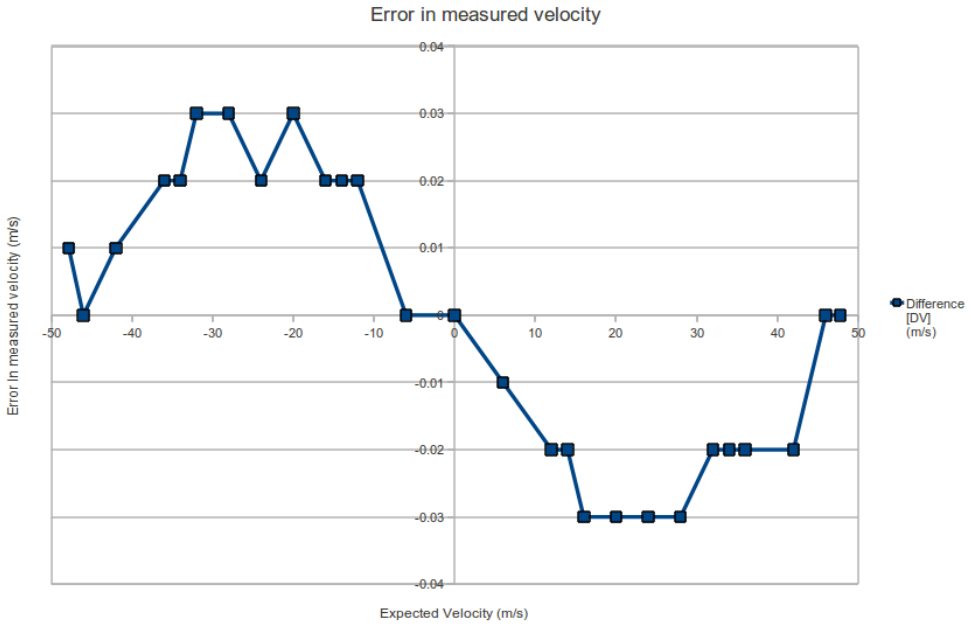

Figure 3-26: Error in measured velocity versus expected velocity from signal generator, injection based testing

the expected velocity. The sinusoidal nature of the error is unexplained but given that the maximum the error in velocity is 0.03 m/s, the error is negligible compared with the expected spectral widths of the meteorological echoes [72], so no further investigation was carried out.

Antenna range testing

The antenna for Wardon Hill radar was tested by Q-Par Angus Ltd at a far-field test range and the plots are included in Appendix A. The side lobes were, on average, at -30.2 dB and the average cross-polar isolation was -42 dB exceeding expectations.

While it would be desirable to carry out in-situ measurements of the antenna performance, no such facility was available at the Wardon Hill site. Such experiments have been carried out by DWD in order to evaluate the performance of the Stealth radome by making measurements of the an-

tenna pattern both with and without the radome installed [73]. They show that while the radome does have an negative effect on the beam patterns resulting in a 1.4 dB loss of sensitivity in the linear depolarization ratio, on average the resulting levels are still within specification.

3.9.1 Wardon Hill Site Testing

The Met Office research and development radar is located at Wardon Hill (50°49'9"N 2°33'23"W), a photograph of which can be seen in figure 3-27.

An example of Doppler data from Wardon Hill is shown in figure 3-28. The wind direction derived from the radial velocities matched the observed wind direction and the ground clutter has zero velocity. The fine structures in the precipitation field move with the direction of the wind when animated: This suggest these features are as a result of structures in the wind field being correctly observed, rather than noise in the system.

3.9.2 LDR quality

An example of Ldr data collected at Wardon Hill is shown in figure 3-29. In this image, the effect of decreasing SNR with range, on LDR can be seen.

In the case of light rain (20 dBZ $\lesssim$< Z $\lesssim$ 22 dBZ), it can be assumed that the droplets are spherical and therefore provide a target with as low an Ldr as is likely to be physically observed[32]. If this measurement is made with high SNR, i.e. close to the radar, it can be used to determine the cross-polar isolation performance of the radar. A histogram of this data from Wardon Hill is shown in figure 3-30 with a peak at -36.5 dB. Due to the random nature of the noise in the system it is possible to record spuriously low values of Ldr which are beyond the range of values that can be encoded in the Met Office Polar data format. This leads the anomalous peak seen in the data at -46 dB.

Figure 3-27: Wardon Hill Weather Radar

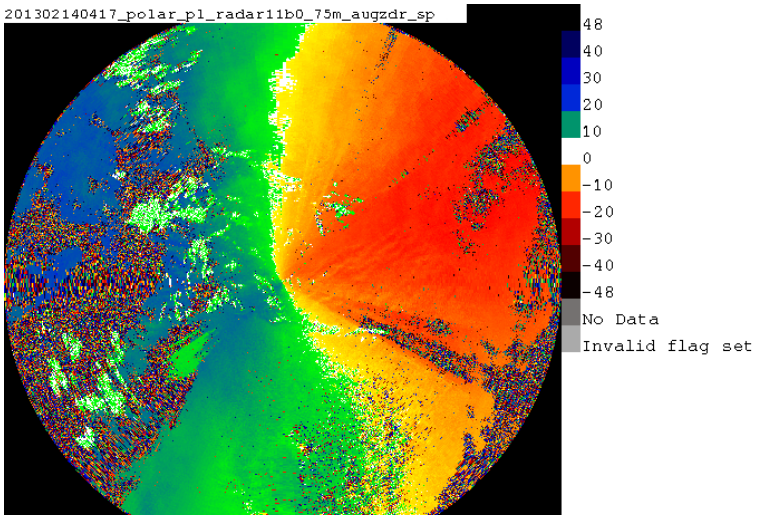

Figure 3-28: Example of Doppler radial wind data collected at Wardon Hill weather radar

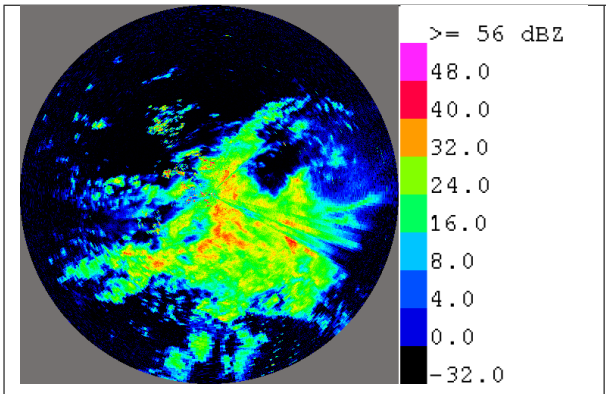

Reflectivity (dBZ)

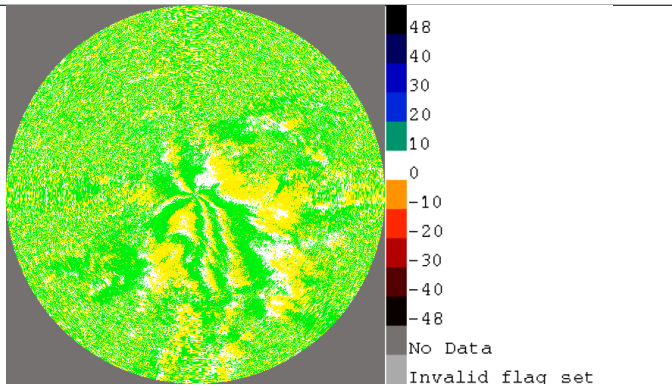

Radial Velocity ±4m/s unambiguous velocity

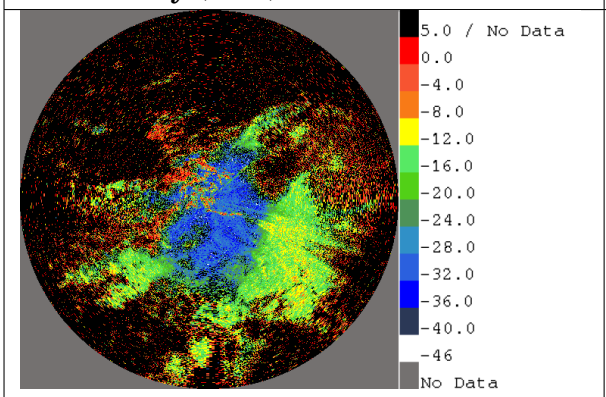

Linear depolarisation ratio (dB)

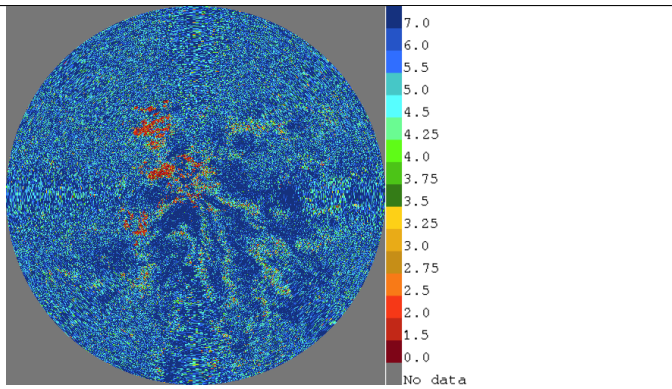

Clutter Indicator based on clutter phase alignment

Figure 3-29: Example of Ldr data from Wardon Hill on 2013/07/30 0709Z

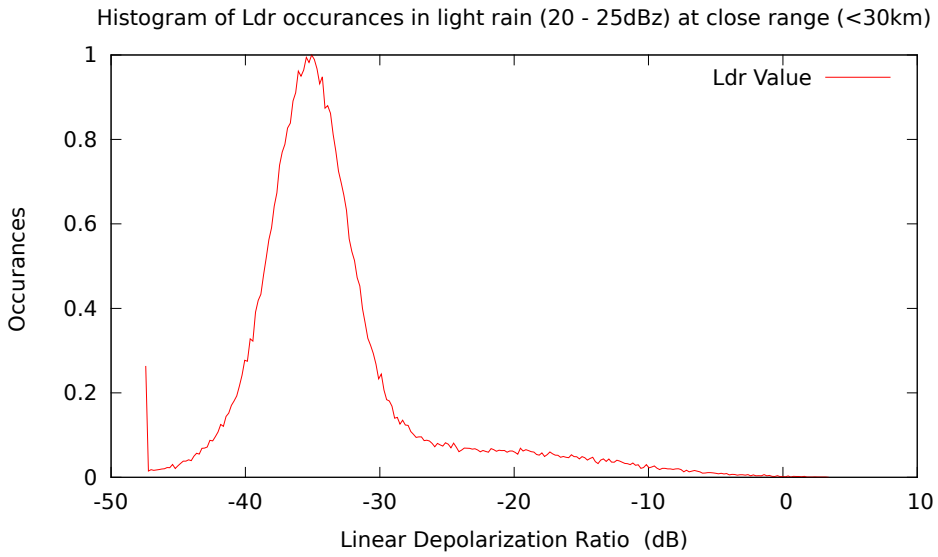

Figure 3-30: Histogram of Ldr values measured at high elevation in light rain

3.9.3 Z_{dr} Quality

An example of slant elliptical transmission data (Z_{dr},ρ_{hv},ϕ_{dp}) collected at Wardon Hill can be seen in figure 3-31, demonstrating high ρ_{hv} in areas with high SNR. ϕ_{dp} is showing increasing values with range, having passed through areas with high reflectivity, indicating that attenuation is occurring. Z_{dr} shows higher values co-located with higher reflectivity values, as would be expected due to larger droplets.

Peak ρ_{hv} measurements

The peak ρ_{hv} refers to the peak in a histogram of ρ_{hv} values when observing rain, from Wardon Hill Radar data shown in figure 3-32. The peak value of ρ_{hv} is significant as spherical rain droplets are expected to show a value of 1 and so any de-correlation can be attributed to the measurement system, specifically the antenna. As has been seen from the Ldr measurements it would be expected that the system would show very high correlation, meaning that limit on the quality of Zdr measurement would be qoverend

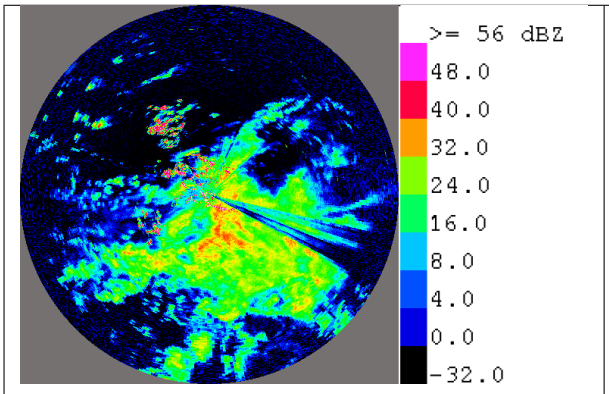

Reflectivity (dBZ)

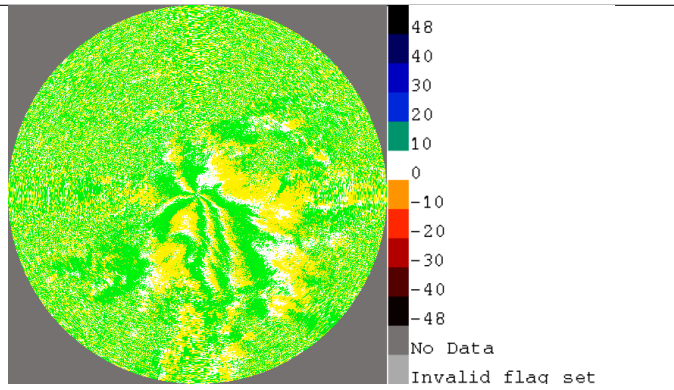

Radial Velocity ±4m/s unambiguous velocity

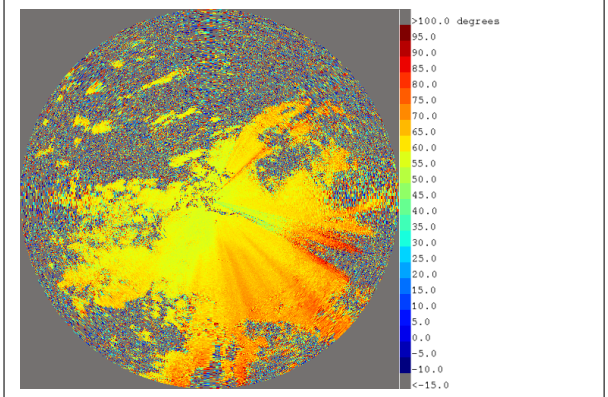

Differential Phase Shift (ϕ_{dp})(Degrees)

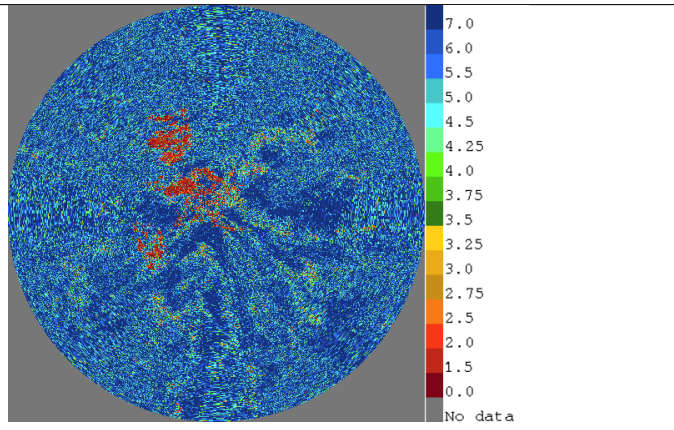

Clutter Indicator (Based on CPA)

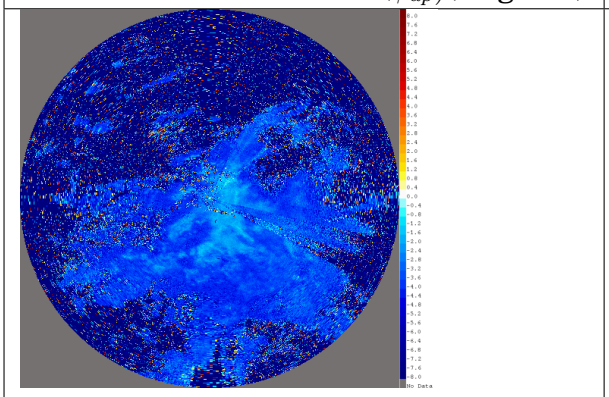

Uncorrected Z_{DR} (dB)

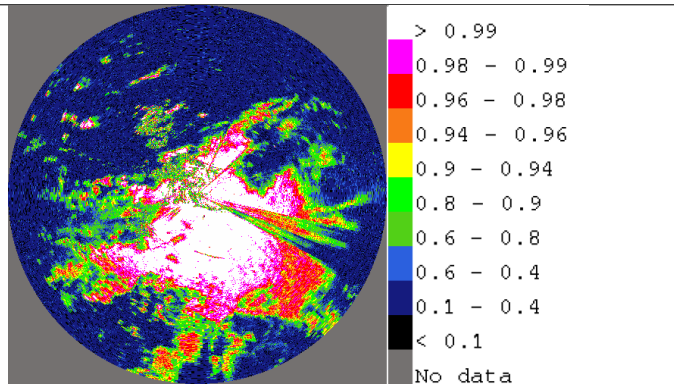

Co-polar correlation coefficient (ρ_{hv})

Figure 3-31: Simultaneous transmit and receive data collected at Wardon Hill on 2013/07/30 0709Z

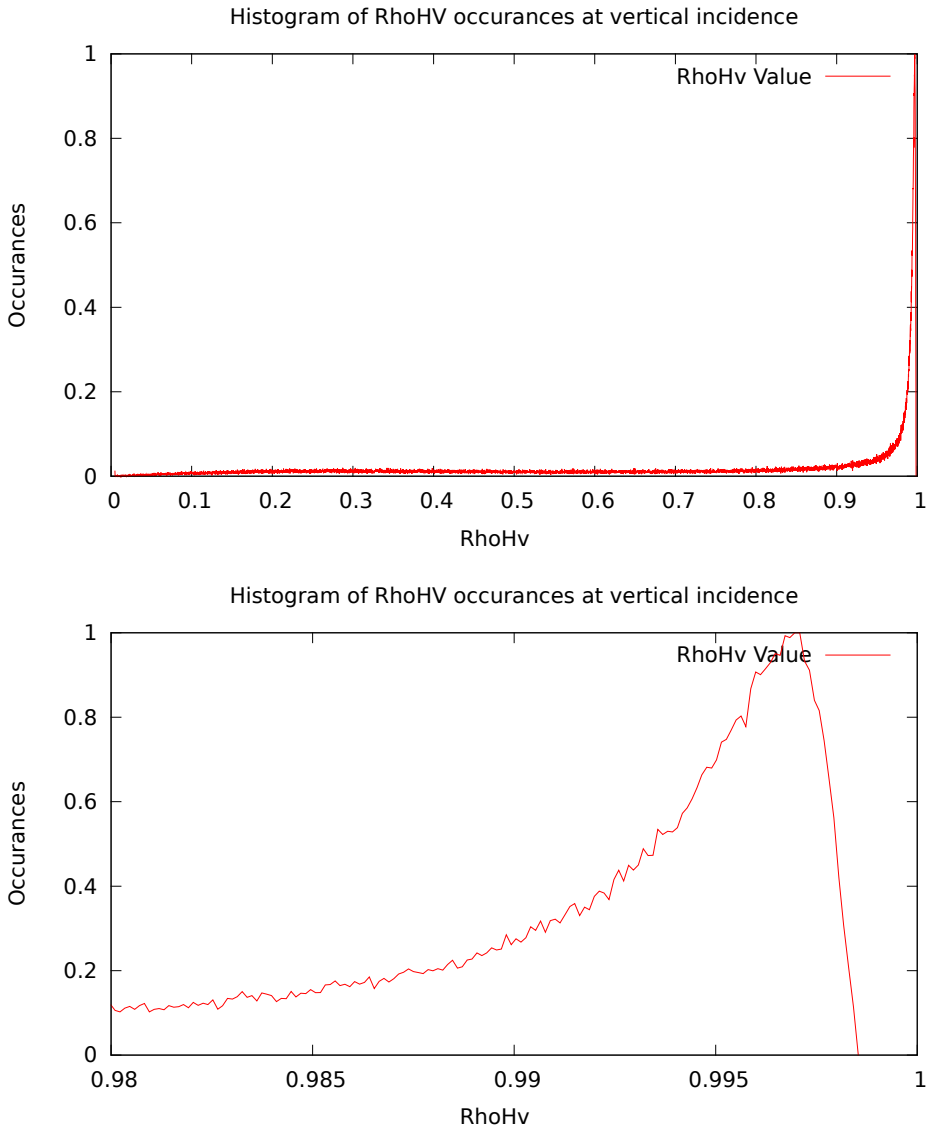

Figure 3-32: Histogram of RhoHV values measured at vertical incidence

by the intrinsic uncertainty in the precipitation being observed rather than by the measurement system. With a peak at 0.997, the performance is comparable to the Colorado State University CHILL radar, a state of the art radar research facility [74].

3.10 Summary

This chapter has presented an overview of the design of a renewed radar for the UK weather radar network. The parameters governing the quality of dual polarization moment estimates from a dual polarization radar were introduced, including the requirements on those parameters in order to make improvements to QPE using dual polarization parameters. The design was presented in overview and then a more detailed description of the key individual components was presented including some of the reasoning behind the selection of the technologies and methods used. A summary of the software design was presented, showing the key classes and their interactions. Finally, an evaluation of the quality of the resultant radar system was made with particular reference to the key dual polarization parameter criteria.

The Cyclops-D/P processing system now forms a platform which can be used by the Met Office and research community to investigate novel radar observations, as described in chapters 4 and 5.

Chapter 4

Application of Cyclops-DP for the measurement of near-surface refractivity

This chapter describes a technique for measuring refractivity using radar, its implementation on magnetron based radars, application of dual polarisation for improved refractivity fields, including verification against surface observations, and target location detection via frequency modulation.

4.1 Introduction

4.1.1 Motivation

Measurements of the refractive index n of the air near the surface can be of great interest to the meteorological community. The refractivity N of the air is defined as [75]:

$$N = (n - 1) \times 10^6 \tag{4.1}$$

i.e. parts per million greater than the refractive index in a vacuum. At microwave frequencies this can be calculated from an empirically derived relationship between the temperature T in K, pressure p in hPa and water vapour pressure e in hPa [76], using :

$$N = 77.6\frac{p}{T} + 3.73 \times 10^5 \frac{e}{T^2} \tag{4.2}$$

This equation has a so-called dry (first) and wet (second) terms and is more sensitive to changes in the wet term. It is this sensitivity to changes in water vapour that makes the refractivity measurement of such interest, as the pressure and temperature of the atmosphere generally do not show very high spatial or temporal variability and therefore are observed representatively by the existing automated surface observing network [77].

The technique for the measurement of near surface refractivity is a relatively new one for the radar meteorology community. It was initially developed by Fabry et al. in 1997 [2] and is based on the fact that for stationary targets, with no changes in transmission or reception characteristics of the radar, the phase of returns should be constant. If any range variation is detected, in the form of changes in the measured target phase, it can be attributed to variations in the refractivity of the atmosphere between the radar and the target. Such variations are small and can be ignored for the purposes of conventional range determination. In [2], the relationship between phase change and change in refractive index is given as:

$$\Delta\phi = 2\pi f \Delta t = \frac{4\pi f r}{c}\Delta n \tag{4.3}$$

Using equation 4.3, at C-band (5.6 GHz) for a change of 1 N unit, a phase shift of 0.234 radians ($13.4°$) is expected over a path length of 1 km. In the paper by Fabry et al. it is noted that at S band, an equivalent change in refractivity would result in a shift of $7.2°$ and as such with a refractivity change on $\pm$25 N units, folding of the phase would have occurred, limiting the range of measurements. At C-band this problem is approximatively twice as bad with folding occurring at about ± 13 N units per km.

Calculating the phase change gradient, G, between two clutter targets gives:

$$G = \frac{\Delta\phi_1 - \Delta\phi_2}{r_1 - r_2} \tag{4.4}$$

and combining this with equations 4.1 and 4.3 gives:

$$\Delta N = \frac{c}{4\pi f_t}\frac{10^6}{G} \tag{4.5}$$

It should be noted that the output of the technique is the change in refractivity rather than absolute values. However, as the fields are intended as an input to NWP and 4-D variational assimilation techniques are available to deal with this, it is still a useful observable.

The technique relies on the observation of targets with very stable phase. A quality indicator is defined to detect high phase stability targets, using the variance of each phase components ($\sigma^2_{I/Q}$) and the mean total power ($\bar{I}^2 + \bar{Q}^2$):

$$QI = \frac{\sigma^2_I + \sigma^2_Q}{\bar{I}^2 + \bar{Q}^2} \tag{4.6}$$

The QI parameter gives the ratio of the instantaneous random power to the mean total power. For incoherent sources this is tends to 1 and tends to zero for highly coherent signals.

While QI is a useful indicator of the instantaneous stability of targets, the scanning of the radar leads to short observation times meaning that it is not sensitive to the longer term swaying movement of targets. This has been investigated by Fabry (2004) [75] and it is shown that, as might be expected, man-made structures such as “power poles” have a greater phase stability in windy conditions when compared to natural, vegetation based targets. The degree to which the QI captures this effect is currently under investigation by Dr John Nicol, University of Reading and NCAR. The effect

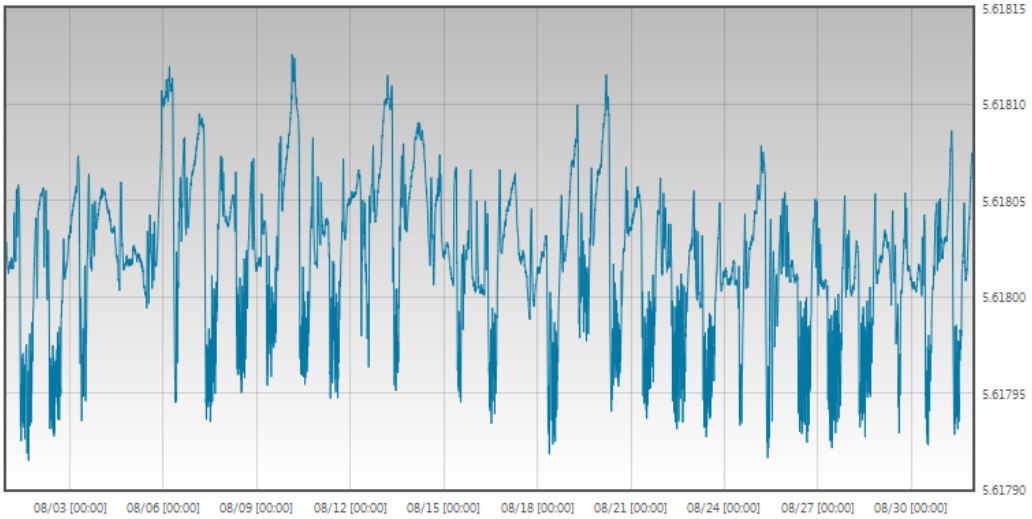

Figure 4-1: Variation of transmitter frequency (GHz) over the month of August for Cobbacombe Weather Radar

of target motion is frequency dependent: for a target displacement of just 2.8 mm, a phase shift of 20°, 36° and 60° is observed at S, C and X bands respectively [78].

It was proposed by Fabry et al. [2] that "To make proper refractive index measurements, good frequency stability is required". From equations 4.3 and the definition of refractivity, equation 4.1, it would seem that a 1 ppm change in frequency would be equal to a change of 1 N unit. This implies that at C-band, the transmitter frequency must be stable to within 5.6kHz between phase measurements. For a magnetron based radar this is unlikely to be the case due to the thermal sensitivity of the magnetron: a thermal drift coefficient of 200 kHz/°C [79] and the temperature control in the radar buildings having a range of several degrees, leading to the possibility of variations as great as 1 MHz. Even in an undisturbed, air conditioned, brick building, such as at Cobbacombe Cross radar site; variations of 200 kHz are observed (figure 4-1). At sites in which the transmitter is located in a metal "shipping container" style cabin (e.g. Wardon Hill figure 3-27) the variations seen are much greater.

Originally, this work was going to investigate the effects of transmitter frequency changes on refractivity and methods of compensating for this.

However, work by Parent du Châtelet in 2007 [80] and subsequently refined by [81],[82], demonstrate that the accuracy to which the down-conversion frequency can be controlled and corrected for is more important than the stability of the transmitted frequency (see sec. 4.1.2).

The refractivity technique has now been demonstrated on a variety of radar technologies such as klystron-based radars with standard parabolic antenna [83], phased arrays[84], as part of CASA X-band magnetron-based radar system [85] and on C-band magnetron-based radars [80, 86].

This work, investigating the retrieval of refractivity using C-band magnetron based radars, forms part of a collaborative effort between the Met Office and Reading University, in particular Dr John Nicol and Professor Anthony Illingworth. The Met Office lead development on the data acquisition, radar control and signal processing aspects, and Reading University focus on the subsequent data processing and analysis.

4.1.2 Effect of transmission frequency changes on phase measurements

In the original paper by Fabry describing the refractivity technique it was considered that it would be unlikely that it would be possible to make refractivity measurements using magnetron transmitters due to variation in the Tx frequency.

Our initial work seemed to suggest that it was possible to make the frequency measurements to the necessary accuracy, then record and adjust the down-conversion frequency in real time to compensate, however a subsequent analysis by [80] demonstrated that in fact it is the case that the down-conversion frequency is the key parameter.

This has been further analysed in Patent du Châtelet et al., 2012 [81] and Nicol et al., 2013 [82], in which both papers investigate the effects of frequency changes. Both papers come to the same conclusion but take

different approaches: The analysis in Parent du Châtelet et al. 2012 [81] is carried out in terms of frequency whereas Nicol et al. 2013 takes a target range based approach. The range based approach leads to the insight that there is an effect due to the position of the target within the range gate.

For convenience the derivation of phase change for a stationary target with changes in frequency from Nicol et al. 2013, as derived by Dr Nicol, is reproduced here.

Taking the transmitted signal to be:

$$T(t) = A(t)e^{j(2\pi f_{Tx}t - \phi_0)} \tag{4.7}$$

Where f_{Tx} is the transmitted angular frequency, ϕ_0 is the magnetron phase on transmission.

And the received signal after reflection by a target at range r_{targ}, to be:

$$R(t) \propto e^{j\left(2\pi f_{Tx}\left[t - \frac{2r_{targ^n}}{c}\right] + \pi\right)} \tag{4.8}$$

Then after mixing with STALO frequency (f_{ST}) gives:

$$R_{IF}(t) \propto e^{j\left(2\pi f_{Tx}\left[t - \frac{2r_{targ^n}}{c}\right] + \pi\right)} e^{-j2\pi f_{ST}t} \tag{4.9}$$

And upon subsequent mixing with the NCO frequency (f_{co}) to give the baseband signal:

$$R_{BB}(t) \propto e^{j\left(2\pi f_{Tx}\left[t - \frac{2r_{targ^n}}{c}\right] + \pi\right)} e^{-j2\pi f_{ST}t} e^{-j2\pi f_{NCO}t} = e^{j\left(2\pi f_{Tx}\left[t - \frac{2r_{targ^n}}{c}\right] + \pi\right)} e^{-j2\pi f_{LO}t} \tag{4.10}$$

where f_{LO} is $f_{ST} + f_{NCO}$ i.e. the overall down-conversion frequency to baseband. “The sign convention for the phase of the transmitter and local oscillator is consistent with down conversion”[82].

Considering a sample of the received signal for a given range gate at time, $t_{gate} = \frac{2r_{gate}}{c}$, where r_{gate} is the equivalent range gate centre in a vacuum ("this definition is necessary to explicitly describe the phase dependence on refractivity changes"[82]):

$$R_{BB}(r_{gate}) \propto e^{j\left(\frac{4\pi f_{Tx}(r_{gate}-nr_{targ})}{c}+\pi\right)} e^{j\frac{4\pi f_{LO} r_{gate}}{c}} \tag{4.11}$$

and only considering the phase terms from a particular target ($targ$):

$$\phi_{gate} = \frac{4\pi}{c}\left(f_{Tx}\left[r_{gate} - nr_{targ}\right] - f_{LO} r_{gate}\right) + \pi \tag{4.12}$$

In terms of refractivity ($N = (n-1)10^6$) and target location relative to the range gate centre ($\delta_{targ,gate} = d_{targ} - d_{gate}$):

$$\phi_{gate} = \frac{-4\pi}{c}\left(f_{LO} r_{gate} + f_{Tx}\delta_{gate} + f_{tx} N 10^{-6} r_{targ}\right) + \pi \tag{4.13}$$

Considering the change in phase at a later time, when it is possible that f_{LO}, f_{TX} and N have changed; subscripts 1 and 2 relate to earlier and later measurements respectively:

$$\Delta\phi_{gate} = -\frac{4\pi}{c}\left(\Delta f_{LO} r_{gate} + \Delta f_{Tx}\delta_{targ} + \left[f_{Tx_2} N_2 - f_{Tx_1} N_1\right] 10^{-6} r_{targ}\right) \tag{4.14}$$

As $N_2 = N_1 + \Delta N$:

$$f_{Tx_2} N_2 - f_{Tx_1} N_1 = f_{Tx_2}\Delta N + \Delta f_{tx} N_1 \tag{4.15}$$

and so having made no approximations thus far, the overall phase change, accounting for sampling and possible changes in frequencies is given by:

$$\Delta\phi_{gate} = -\frac{4\pi}{c}\left(\Delta f_{LO} r_{gate} + \Delta f_{Tx}\delta_{gate} + \left[f_{Tx_2}\Delta N + \Delta f_{Tx} N_1\right] 10^{-6} r_{targ}\right) \quad (4.16)$$

In the case where the change in transmitter frequency is small e.g. 100 ppm or ~550 kHz at C-band. $f_{Tx_2} \approx f_{Tx_1}$ i.e. $\Delta f \ll f_{Tx}$ and substituting $\Delta n = \Delta N 10^{-6}$:

$$\Delta\phi_{targ,gate} = -\frac{4\pi}{c}\left(\Delta f_{LO} r_{gate} + \Delta f_{Tx}\delta_{gate} + f_{Tx}\Delta n(r_{gate} + \delta_{gate})\right) \quad (4.17)$$

It is assumed that the range-gate centre is the equivalent range gate centre in a vacuum.

The first term, $\frac{4\pi}{c}\Delta f_{LO} r_{gate}$, is due to any changes in the local reference oscillator frequency with distance to target, as such it is unlikely to affect power amplifier based transmitters (e.g. klystron).

The second term, $\frac{4\pi}{c}\Delta f_{Tx}\delta_{gate}$ is a change in phase which comes from the difference in the propagation delay and sampling delay and so is proportional to the distance of the target relative to the range gate centre. Errors due to this is are likely to be confined to magnetron based transmitters.

The final term $4\pi f_{Tx}\Delta n(r_{gate} + \delta_{gate})$ contains the refractivity change information that it is desired to be measured and an additional term related to the distance of the target from the centre of the range gate. The term $4\pi f_{Tx}\Delta n\delta_{gate}$ will have the effect of adding phase noise to the phase change measurements. This noise is proportional to the frequency, change in refractivity from the reference time and also the distance of the target from the centre of the range gate. It is this aspect that make it a random phase noise, as the target position within the range gate will randomly distributed. This effect affects both magnetrons and power amplifier based transmitters as it is independent of frequency changes.

From eq. 4.17, considering a stationary target measured at two frequencies within a small time frame such that ΔN and f_{LO} do not change, the phase

change between these two frequencies is a measure of the target location within the sample volume.

$$\Delta\phi_{targ,gate} = \frac{4\pi}{c}\left(\Delta f_{Tx}\delta_{targ,gate}\right) \tag{4.18}$$

In the case where targets have such a large return as to saturate the receiver filters, their influence can spread in to neighbouring range gates. This is a source of bias in the estimation of refractivity. This is described in Nicol et al. (2012) [78], and is due to the fact that the refractivity is calculated from the phase gradient in range. If correlations in the target phase in range are introduced by the effect of the receiver filters, then the phase gradient is biased towards zero. It is hoped that with using information about the target location within the range gate derived from dual frequency measurements, unreliable targets can be removed.

4.1.3 Refractivity processing

The calculation of the refractivity field is carried out in the Radarnet IV central processing system. As described in [75] the procedure for deriving the refractivity field comprises:

- Calculation of the phase difference between the current phase measurement and the reference time (typically one hour difference).
    - ✧ An example of the phase difference can be seen in figure 4-2.
- Using SNR and QI, a quality threshold is applied to the phase difference field.
- In the case of a magnetron based measurement, a correction for the change in down-conversion frequency is made.
    - ✧ An example of quality controlled azimuthally averaged measured phase with the associated calculated down-conversion frequency

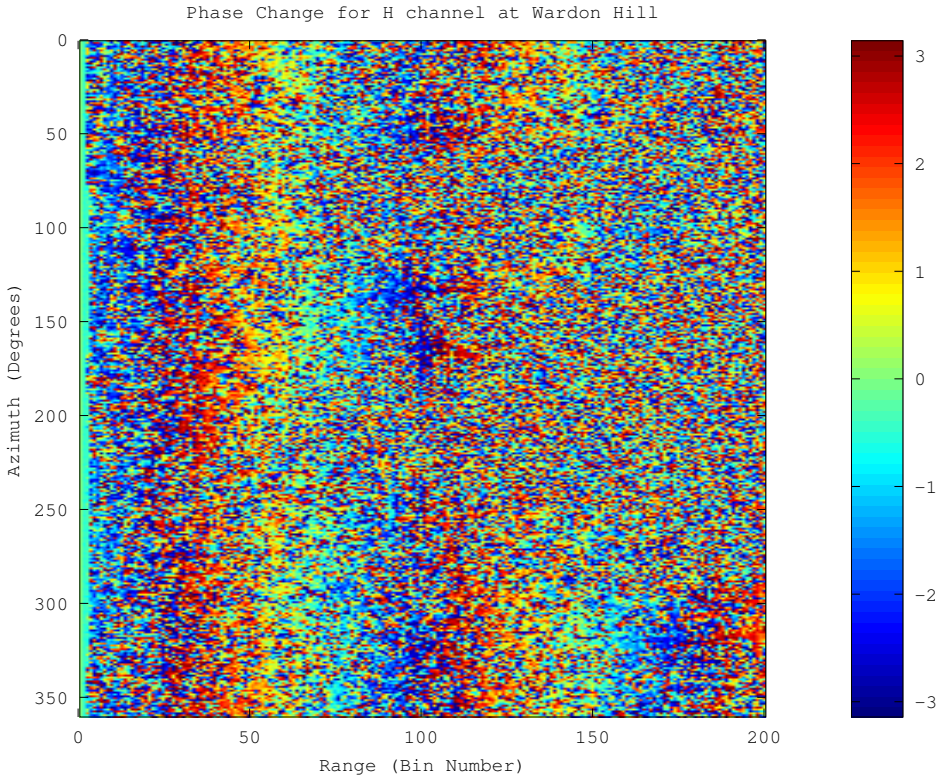

Figure 4-2: Raw phase change from scans separated by 5 minutes, from the H polarisation at Wardon Hill radar site, showing the effect of a change in the downconversion frequency, shown as a phase change with range.

change correction can be seen in figure 4-3. The effect of applying the phase correction is also shown. The scans for which the phase changes are measured are from within 5 minutes of one another and so would be expected to show little change due to refractive index variation, and so the fact that the corrected values are scattered around zero is as expected.

- The phase difference field is then smoothed over a small area to reduce the noise. A pyramidal kernel with base 4 km is used by Fabry.
- The phase gradient of the smoothed fields is then calculated and converted to refractivity.

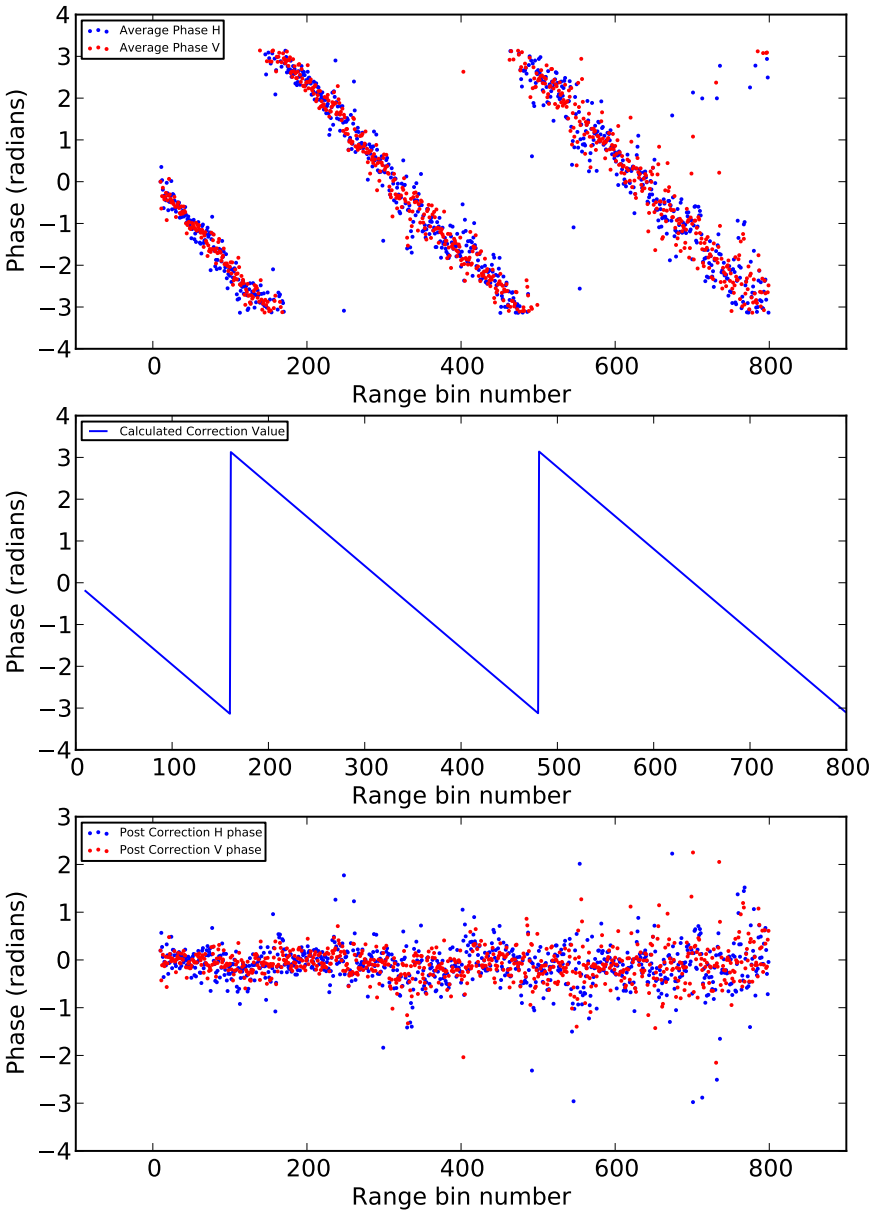

Figure 4-3: Azimuthally averaged phase change showing the effect of a down-conversion frequency change, the associated calculated correction for the frequency change, and the effect of applying that correction to the measured phase values for scans taken 5 minutes apart

The phase differences are calculated in complex vector form in a manner analogous to pulse pair processing (sec. 2.2.1)

It is noted in Nicol and Illingworth (2012) [78], that while the smoothing step is needed to reduce noise on the phase measurements, it can also act as a low pass filter on the phase gradients and so lead to a bias towards zero phase change, with a magnitude dependent on the profile of the kernel in range. They propose that this effect is responsible for biases between radar and surface observations, reported in Bodine et al. 2011[87]. To minimise this effect, an additional stage in the processing is proposed by [78] in which an initial estimate of the mean change in refractivity is subtracted from the quality controlled phase reference field before smoothing, and then added to the results after gradient calculation.

A further improvement is shown, again in [78] , in which the estimate of the mean field is calculated using a least squares fit to azimuthally averaged phase changes over the whole range, rather than a mean field value calculated using the pulse pair processing technique. This gives improved results as small scale effects due to spreading targets are now removed, giving a bias of only 0.2 N units on a phase change of 60 units with a target motion noise of 30° with typical smoothing functions.

An error estimate of the phase change measurement is calculated from the standard deviations of the phases contributing to that area. This is then converted to an equivalent refractivity error estimate.

4.2 Refractivity measurements from dual polarisation radar

In this section the possible benefit of combining the two available polarisation states, to give improved correlation with surface observations, is evaluated.

4.2.1 Comparison of the H and V QI parameters

It might be expected that there is a significant difference in clutter targets in both polarisation states, particularly when looking for suitable targets to make refractivity measurements, with the expectation that the vertical polarisation would have a more stable clutter return, as towers, masts etc. tend to have a more significant vertical aspect. As can be seen in figure 4-4, while there are some targets that only show phase stability in one of the polarisations (represented by points close to each axis), there is no discernible bias with regard to the quality of each polarisation for making refractivity measurements. The mean value of the QI in horizontal polarisation is -8.419 dB and the vertical polarisation is -8.426 dB.

A recent paper by Besson et al. 2013, [88], has looked at a similar measure of the phase quality in each polarisation, and reports slightly better results in horizontal polarisation, with 29% of good targets compared to 26% in the vertical.

4.2.2 Dual Polarisation refractivity measurement

Using data from Wardon Hill radar, refractivity fields were calculated using the Radarnet IV processing system, for each polarisation, including area based error estimates, as described in section 4.1.3 In addition a so called "Best" field was calculated by selecting data from each field with the lowest error estimate. The improvements to the refractivity processing suggested by Nicol and Illingworth [78] have not yet been implemented and so biases towards zero are expected.

When attempting to verify the fields it was found that no Met Office surface observing sites were co-incident with the observed clutter field - this does highlight the need for additional near surface measurements of this type. Field average refractivity changes were calculated and compared to the average of the observations within the radial extent of the clutter field. As the radar refractivity technique calculates changes in refractivity

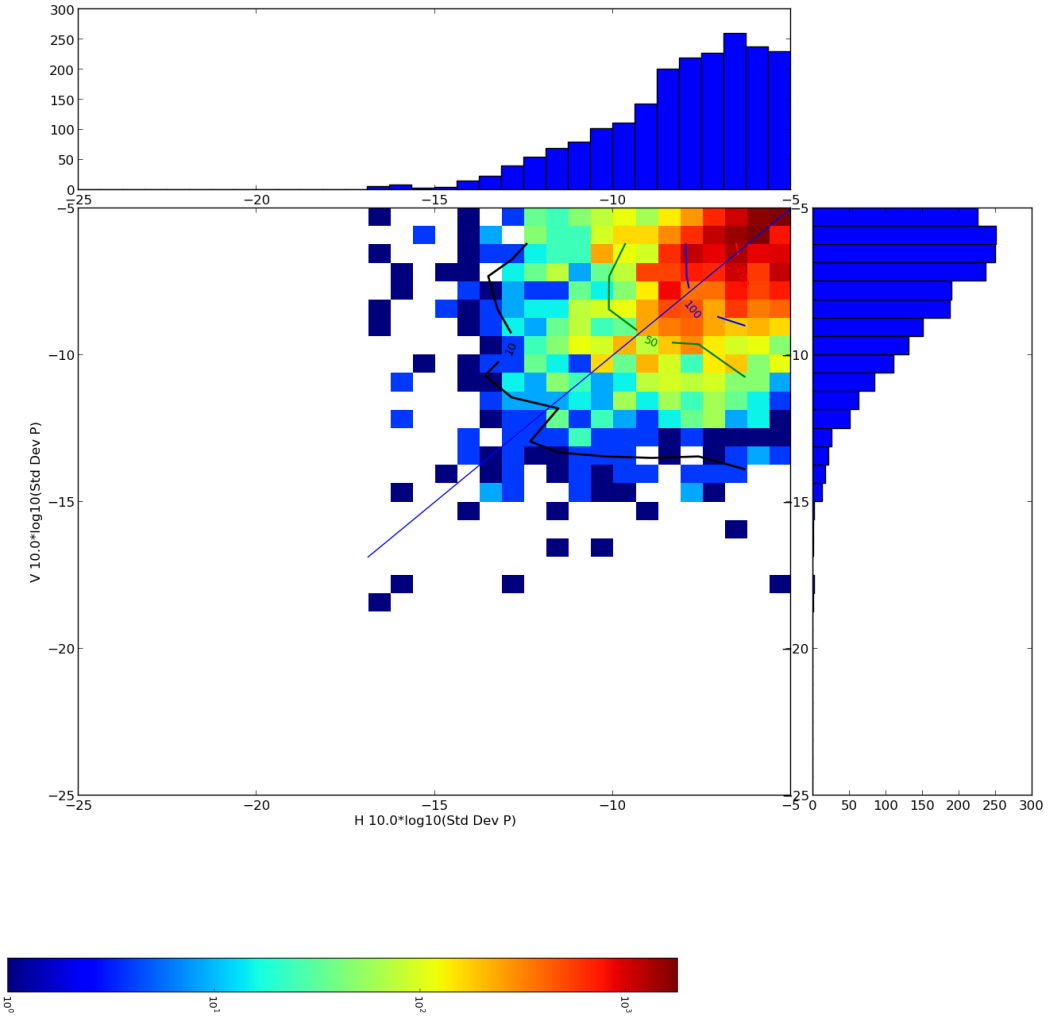

Figure 4-4: 2 dimensional histogram showing the dB form of the QI parameter in the H and V channels for Wardon Hill in clutter

Polarisation	Correlation
H	0.727
V	0.651
Combined	0.743

Table 4.1: Correlation of averaged surface derived refract. to averaged radar fields

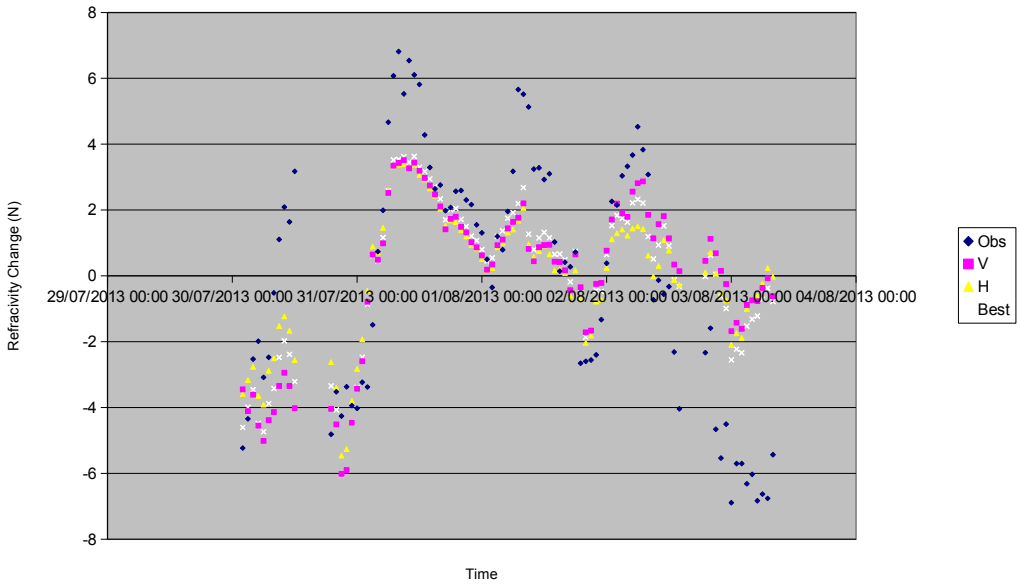

Figure 4-5: Comparison of average field refractivity with average surface observations within the cluttered radius

these were accumulated to give a time-series comparable to the observations based refractivity estimate. The mean of each time-series was then subtracted so that the correlation between the changes could be seen (figure 4-5). Both polarisations show a high degree of correlation with the surface observations as shown in table 4.1. The “best” data shows a higher degree of correlation with surface observations than either of the two individual polarization based estimates, showing that there is benefit to combining both polarisations measurements.

A scatter plot of the changes in refractivity from the radar observations and calculated from the surface observations, is shown in figure 4-6. As the improvements suggested by Nicol and Illingworth (2012) [78], have not

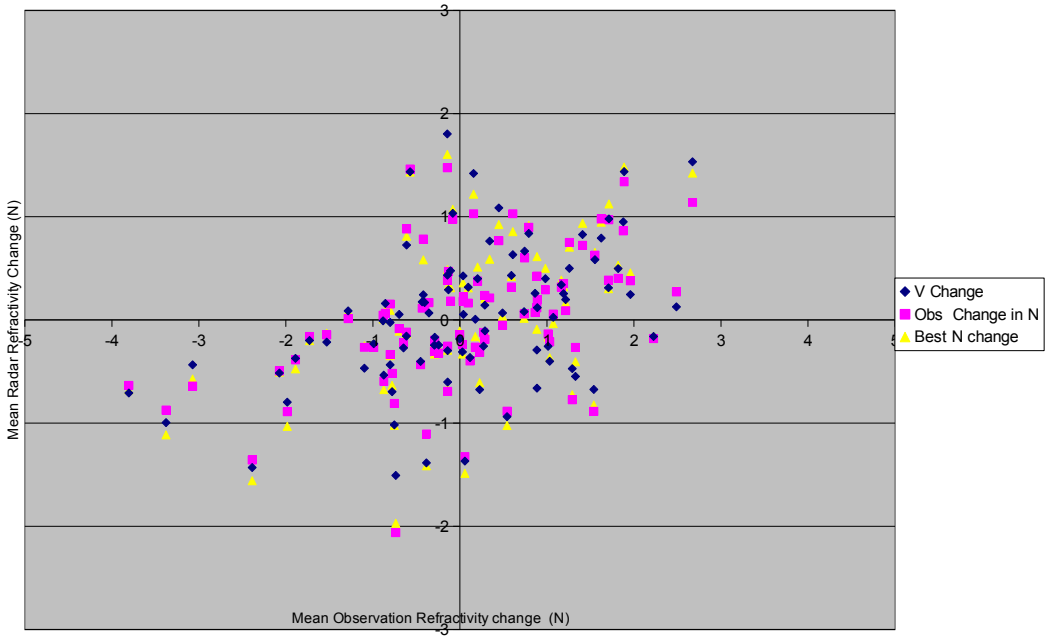

Figure 4-6: Scatter plot of mean field refractivity change as calculated from radar refractivity and observations within the cluttered radius

been implemented within the Radarnet processing system the expected bias of the radar observations towards zero can be seen. A least squares fit to the "best" data gives a gradient of 0.25.

4.3 Dual frequency measurements to reduce refractivity biases

It was suggested by [82], that by using dual frequency measurements, in a manner analogous to frequency domain interferometry [89], that the position of the target within a range gate could be determined. This can be used to mask targets which are distant from the centre of the range gate, and so reduce the bias due to frequency changes. The possibility of making this measurement using the new WRNR transmitter was investigated.

As has been noted by [82], when $\Delta N = 0$ and the down conversion frequency

is unchanged eq. 4.18 can be rewritten as:

$$\delta_{gate} = -\frac{c}{4\pi f_{Tx}} \Delta\phi_{gate} \tag{4.19}$$

The maximum unambiguous range of this measurement is [82]:

$$\delta_{max} = \pm\frac{c}{4\Delta f_{tx}} \tag{4.20}$$

Junyent et al. (2010) [90], show that with an X-band magnetron transmitter, a frequency shift of approximately 200 kHz is seen when alternating between PRFs of 1.6 and 2.4 kHz. With the aim of using the observations of targets at two different frequencies to measure the target position in real time, the behaviour of the CPI WRNR C-band transmitter frequency with changing PRF was investigated. Range estimates can then be used to exclude targets located far from the range gate centre which will add phase noise, and spreading targets which bias the refractivity measurements.

4.3.1 Cyclops automatic frequency control

The initial method of frequency estimation used to track the transmitter frequency was as straightforward as possible, for reasons of robustness and speed of development; using a large number of collected transmitter burst samples, Cyclops-D detects the average number of zero crossings from the set of burst samples and using this and the known sampling frequency can estimate the current burst frequency. This takes advantage of the fact that the magnetron based system has random start-up phase and so the samples are effectively phase dithered.

Samples of the IF raw transmitter pulse were taken to test this technique. As can been seen in figure 4-7, providing the samples are selected from the centre of the pulse the assumption of a discretely sampled sine wave appears to be reasonable. A simulation of this technique was written on this

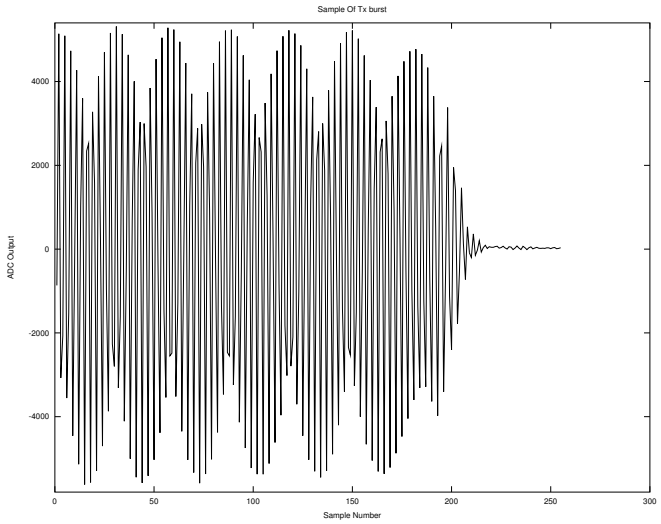

Figure 4-7: An example of the samples of the transmitted pulse

basis, to verify that it gives the desired frequency accuracy in a reasonable amount of time. The transmitter burst was simulated as:

$$TxSample = A\sin(2\pi f_{if} i / f_{sample} + \phi_{random}) \tag{4.21}$$

Where ϕ_{random} represents the random start-up phase of the transmitter, A the amplitude of the transmitted pulse as measured at the IF, f_{IF} the frequency of the IF, i the sample number and f_{sample} the digitiser sampling frequency. The number of zero crossings in the set of calculated samples is then measured and used to estimate the current simulated frequency. A number of these frequency estimates are then averaged together.

As can be seen from figure 4-7, with a 100 MHz sample of the 2μs transmitted pulse and a 300 Hz PRF after only a few seconds the transmitter frequency should be estimated to an accuracy of around 10 kHz. This accuracy is sufficient, as the primary function of the AFC is to correctly align the filters with the transmitted frequency to allow the maximum received pulse power through, without distortion, and to filter out the maximum noise possible, thus maximising the signal to noise ratio of the system. This

error represents just 0.5 % of the full bandwidth of the filter which is well within the excess bandwidth of the filters provided to deal with such errors.

While a number of other more accurate techniques do exist for frequency estimation [91] e.g. MUSIC, Fourier transforms, they are in general more complex and so would have taken more time to implement, and so while the zero crossing method was suitable for the initial Doppler processing stages of the project this aspect was revisited as part of the refractivity measurement work.

The most obvious technique requires Fourier transforms be taken of the IF samples of the transmitter burst and the peak value interpolated. At the time of this work, no FFT code with a suitable license (i.e. non-GPL) could be found and no budget was available for purchase of a commercial product. While this would not usually be an issue in a research environment, in that GPL code could be used, to be replaced if required, the semi-commercial nature of the Met Office means that care has to be taken to protect intellectual property rights (IPR), leading to a policy that no GPL code can be used in Met Office programs.

Best Fit Minimization based processing Using the model of the Tx burst (eqn. 4.21) a multi-parameter best fit to the samples to the Tx burst was used to estimate the IF. This was done using the Nelder–Mead or downhill Simplex method[92]. The accuracy of this technique was evaluated using a reference signal from a signal generator.

Results using samples of Signal Generator A signal generator was used to inject known signals in to Cyclops to test the accuracy of the minimization based frequency estimate. For comparison the accuracy of the zero crossing method was also evaluated.

As shown in figure 4-9 the mean frequency error using the zero crossing technique reaches 10 kHz after approximately 200 pulses have been sampled.

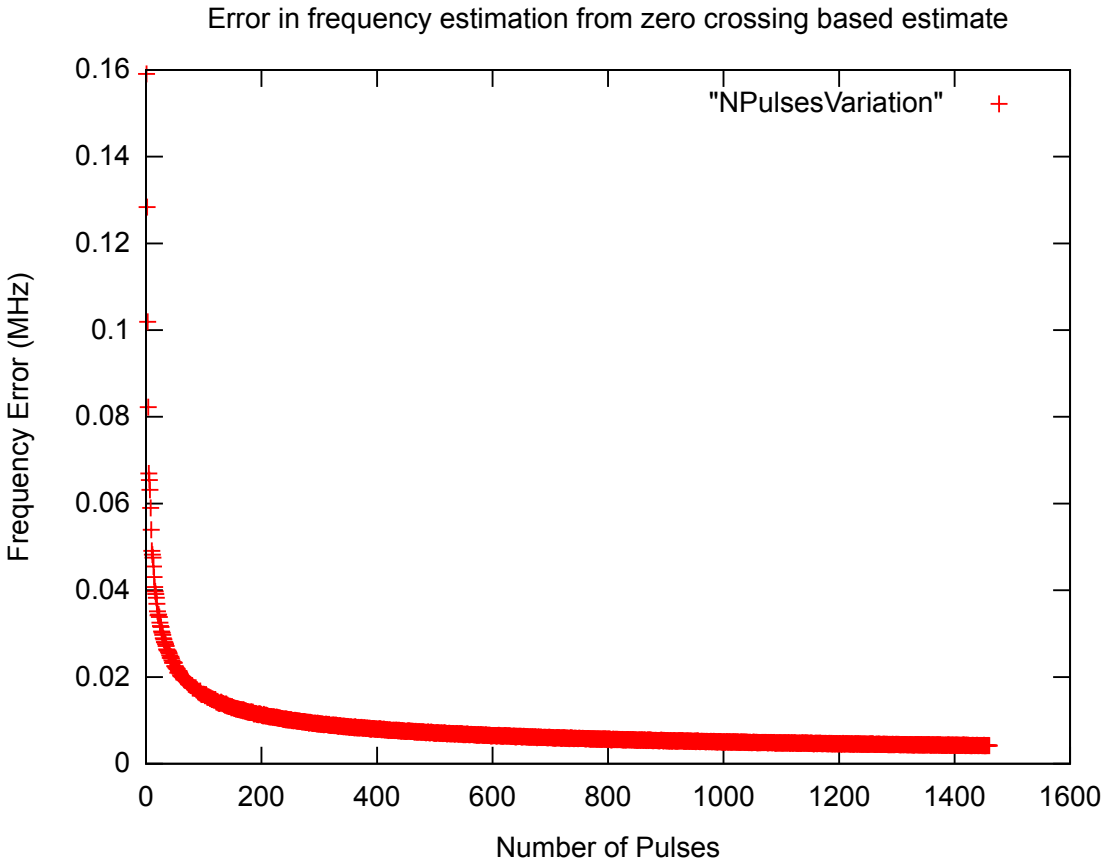

Figure 4-8: Mean error in frequency estimate using zero crossing based technique on samples from a signal generator against number of pulses

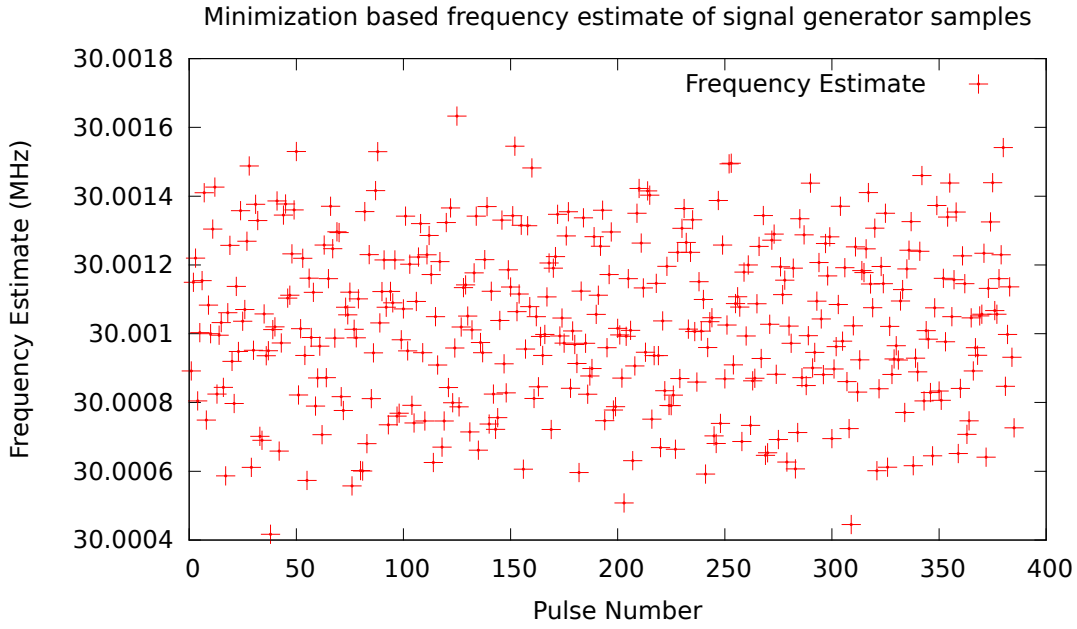

Figure 4-9: Example of frequency estimates using minimization based technique on samples from a signal generator

An example of the output from the minimisation based frequency estimate can be seen in figure 4-9 The effect on the measurement error of varying the number of samples within one pulse is shown in figure 4-10. After 100 samples within one pulse, the minimisation based approach matches the accuracy of 200 pulses using the zero crossing approach.

Samples from Tx

An example of the frequency estimates taken from long (2μs / 300 Hz PRF) pulses at Wardon Hill, is shown in figure 4-11. The short term standard deviation of the frequency at this pulse length is typically of the order 3.5 kHz.

An example of data taken from the short pulse (0.5μs / 900-1200 Hz PRF) can be seen in figure 4-12. The short pulse data oscillates between two frequencies due to the switching of the PRF every 8 pulses, in order to make the dual PRF Doppler measurements. The change in duty cycle between the

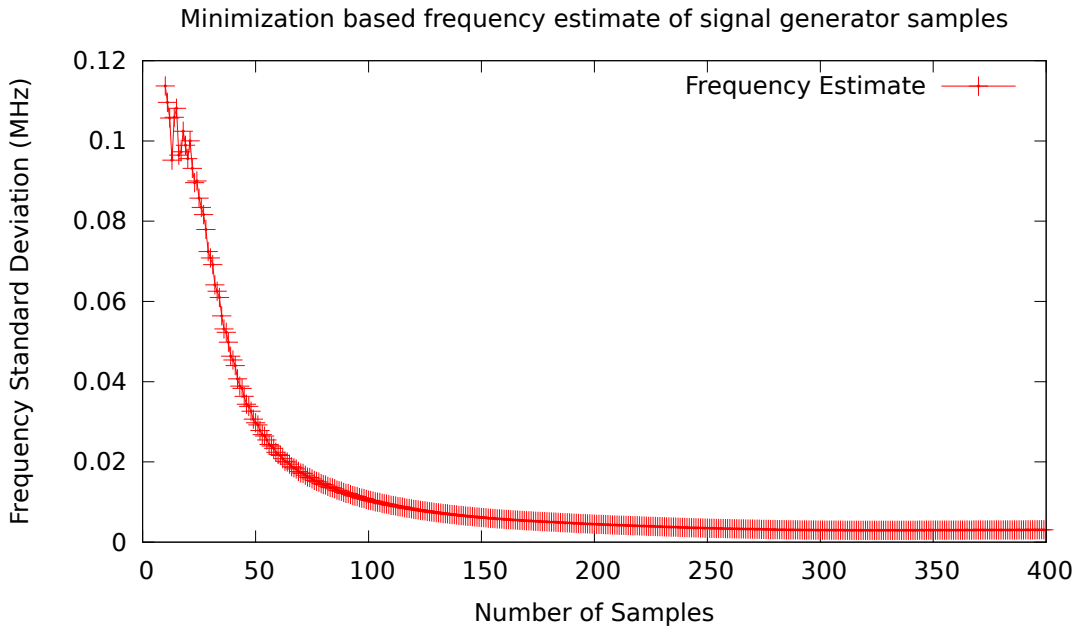

Figure 4-10: Mean error in frequency estimation using minimization based estimation with number of pulse sample points

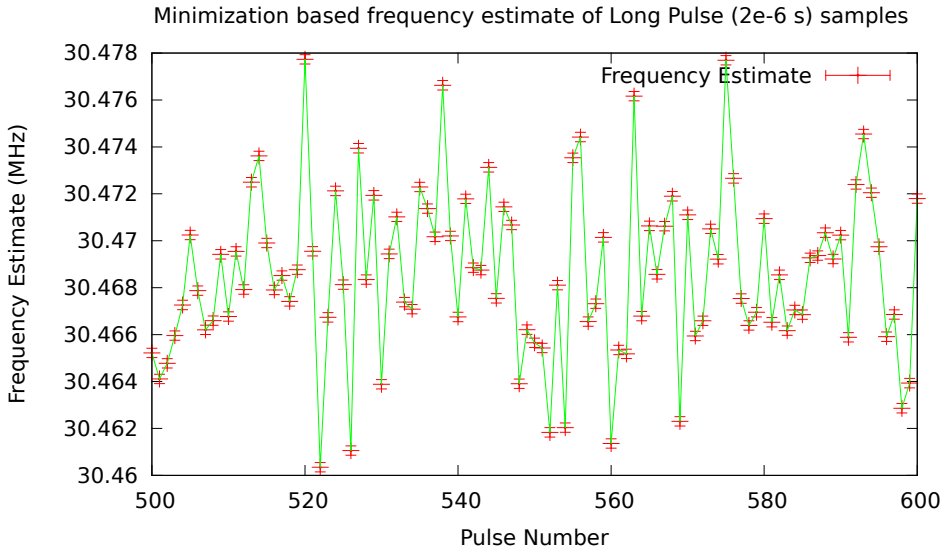

Figure 4-11: IF estimates using minimization method on $2\mu S$ pulse from CPI magnetron transmitter

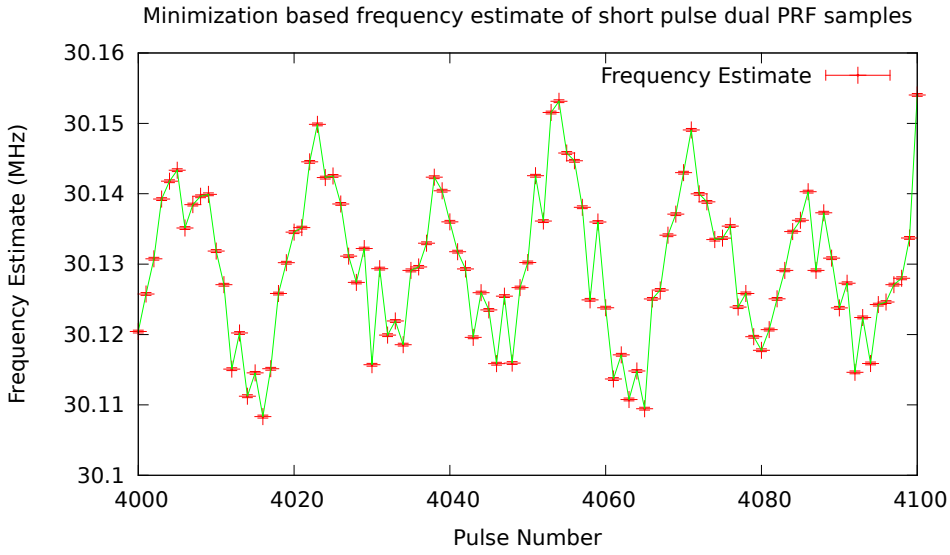

Figure 4-12: Variation in transmitter frequency, measured at the IF, due to the changing of the duty cycle with PRF every 8 pulses when making dual PRF Doppler measurements

900 Hz and 1200Hz PRF, with constant pulse width, leads to variation in the thermal environment of the magnetron, leading to the observed frequency shift. This behaviour has been reported by Junyent et al. using an X-band magnetron as part of the CASA project [90].

Stability of frequency shift

To evaluate the stability of the frequency shift, the frequency estimates from a sequence of dual PRF pulses was collected. These were then aligned in batches of 16, as the PRF changes every 8 pulses (figure 4-13).

The peak to peak variation in frequency within each batch was calculated (figure 4-14) showing a mean peak-to-peak frequency variation of 39.9 kHz with a standard deviation of 3 kHz. The sinusoidal nature of the response means that if the two PRF values are simply averaged, no significant frequency shift is found. Taking the last 4 pulses from each batch leads to a constant frequency shift of ~35 kHz. The ability to make this measurement in real time has been incorporated in to Cyclops.

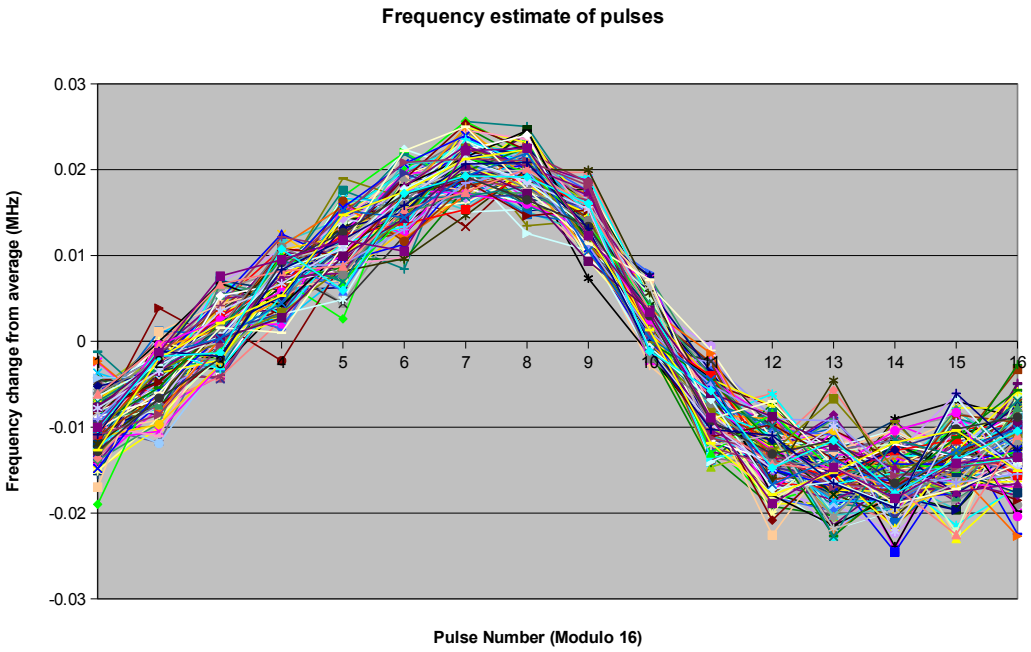

Figure 4-13: Dual PRF Frequency Variation over a number of pulses matched to the 16 pulse dual PRF cycle

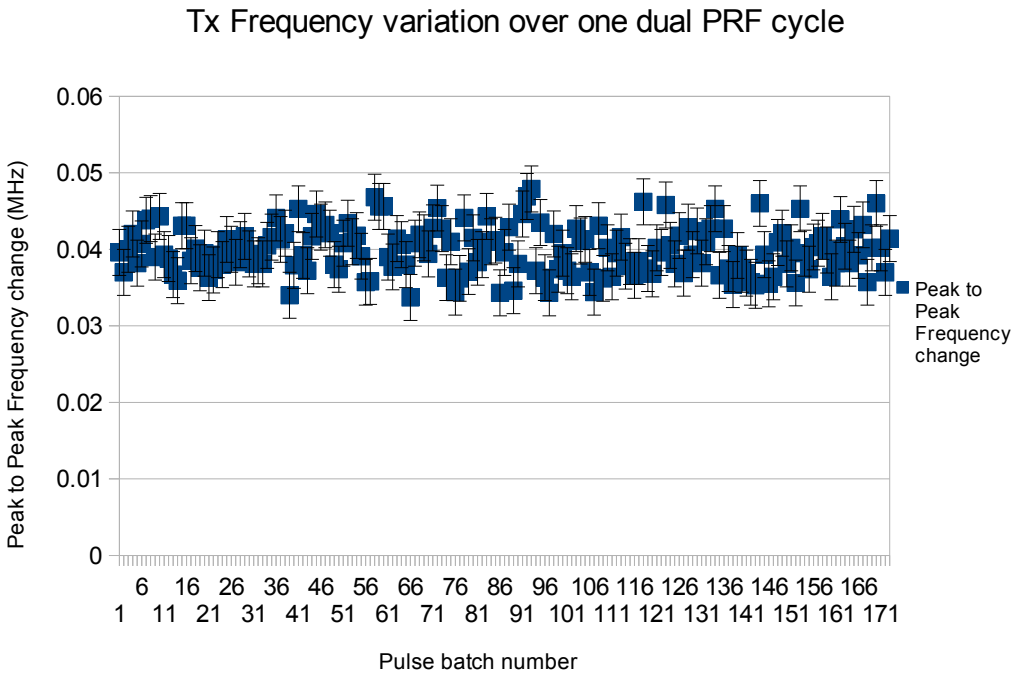

Figure 4-14: Dual PRF Frequency Variation

Using eq. 4.20 the unambiguous range for a frequency change of 35 kHz is 2.142 km, with a sensitivity of $11\text{m}^{\circ-1}$.

STALO Control Accuracy The accuracy of the phase measurement will be limited by the accuracy and stability of the sources, and references used to measure it. One key component in the measurement is the STALO. As one of the reference sources against which the received signal is measured, any variation in its frequency will have significant impacts on the quality of the phase measurements. In addition the response of the STALO to requests for changes to the output frequency will impact the viability of tracking and correcting for any changes in the down-conversion frequency.

The STALO used in Met Office radars is a Pascall part number 1-11670 Iss2 (See figure 4-15), which has an output frequency range of 5.57 - 5.62 GHz,

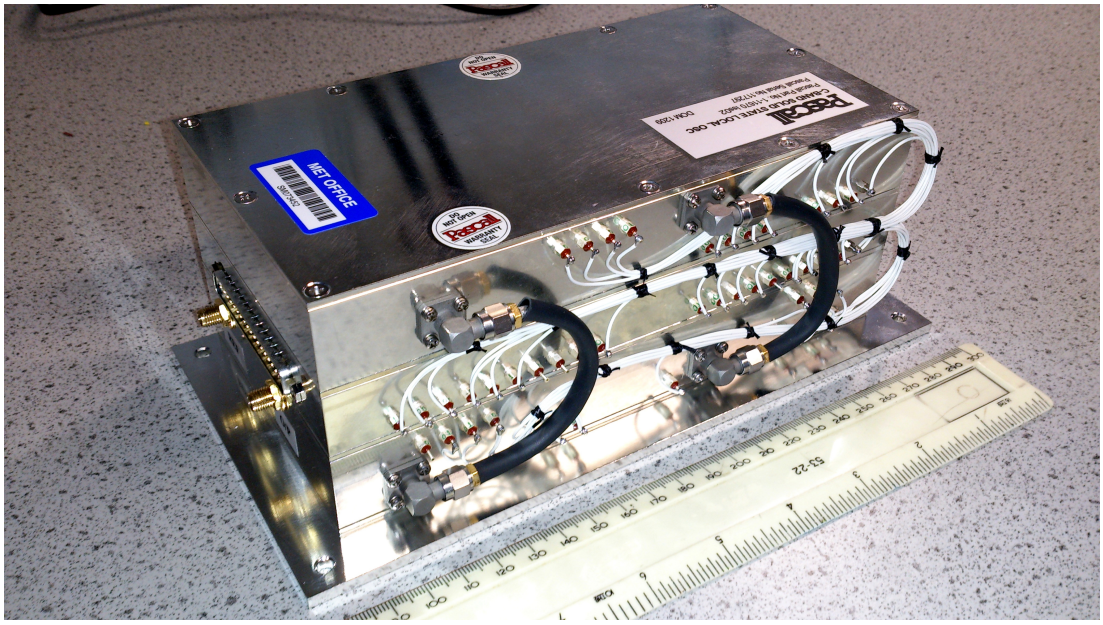

Figure 4-15: Image of Pascall STALO

matched to the UK Met Office's frequency allocation within the C-band of 5.6 to 5.65 GHz, with a 30 MHz intermediate frequency. In practice it is only possible to control the frequency in 100 kHz steps, however this is accounted for in the digital down-conversion section where the frequency used for down-conversion can be controlled very accurately. In practice the frequency of the STALO only changed when an error of 200 kHz is measured, with the DDC responsible for fine tuning. The control interface to the STALO is given as a parallel binary coded decimal value which is provided by the HE-FPGA3 module.

STALO Demand Accuracy

The accuracy of the STALO output was investigated in-order to ensure that the any changes in the demand frequency are indeed accurately matched by changes in the output frequency. The STALO was connected to a Rohde and Schwartz FSH8 spectrum analyser. As the spectrum analyser used was a hand-held portable model a nearby Rohde and Schwartz SMA100A signal generator was used as a frequency reference source, as it was expected that this would be more accurate. See figure4-16 for a diagram of the test configuration. The video bandwidth and resolution bandwidth of the

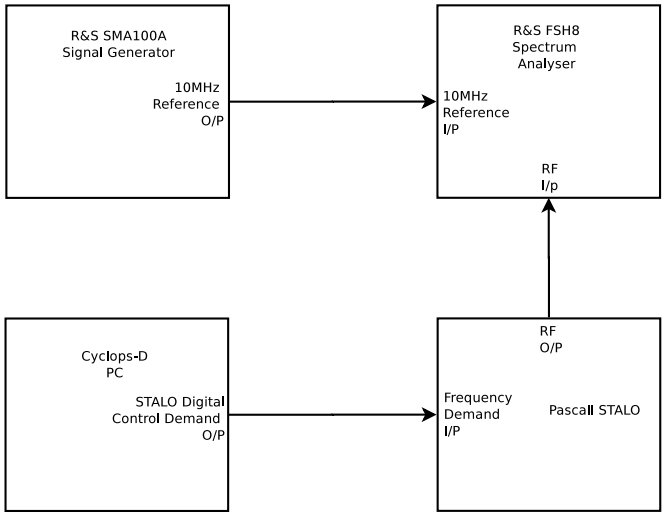

Figure 4-16: STALO Step stability test configuration

spectrum analyser were set to 10 Hz.

A number of different frequencies were the demanded via the Cyclops interface to the STALO and the resulting frequency output of the STALO determined by the marker to peak function of the spectrum analyser.

The frequency output of the STALO moved precisely in the step size that was requested, to the resolution of the spectrum analyser. This accuracy is due to the digitally controlled Phase Locked Loop (PLL) based design of the STALO, in which discrete values of multiplication or division of a reference oscillator are used to produce the output frequency.

4.3.2 Wardon Hill trials of dual frequency measurements for target position estimation

A high reflectivity, isolated, spreading target in the clutter field at Wardon Hill was found (figure 4-17). The target appears to be spread over a large number of range gates, due to the power returned being sufficient to saturate the digital filters. This was geo-located and found to be the Stockland Hill transmission mast (figure 4-18). The Stockland Hill site height is 230 m with a mast height of 228.6 m. As the Wardon Hill site altitude is 240 m

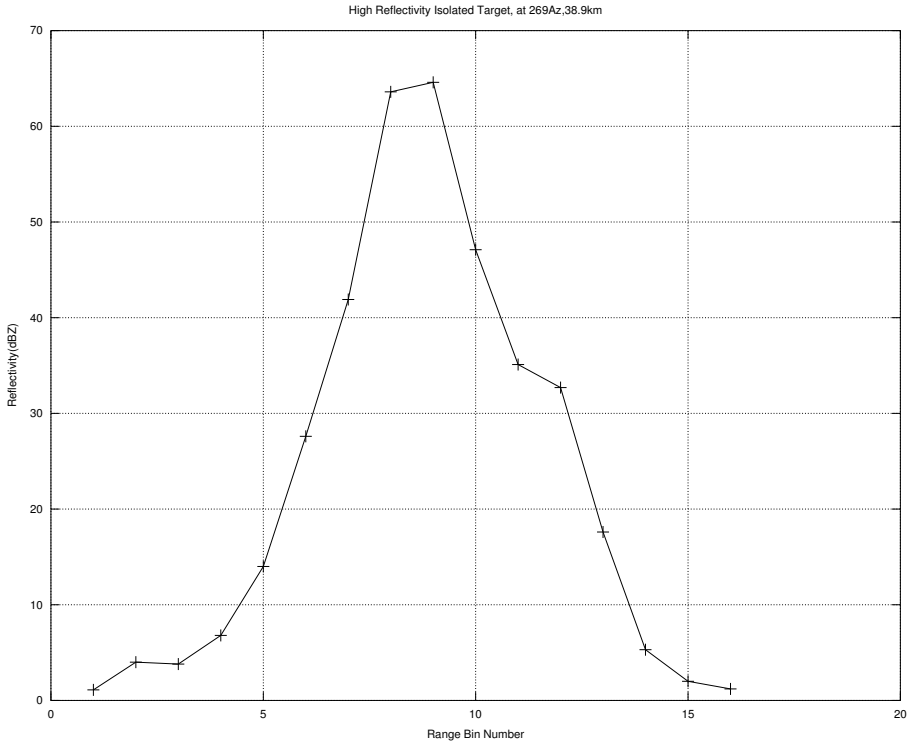

Figure 4-17: Reflectivity response from Stockland Hill transmission mast at 1° elevation.

with a 15 m tower height (to antenna centre), a 1 degree elevation scan ensures that it is only the mast that is in the main beam path.

Figure 4-19 shows the measured phase values in each polarisation from the Stockland Hill mast. As can be seen in bins 8 and 9, which in these plots corresponds to the target range of 39 km from Wardon Hill, matched to the peak reflectivity, the phase gradient is close to zero due to the spreading of the target between range gates. Other areas showing phase correlation can also be seen within the area covered by the reflectivity response of the mast.

The phase difference of the target when measured at two difference frequencies, due to the varying PRF is shown in figure 4-20. In the bins where the target is centred (8 and 9) there is no significant phase shift but up to bin 8 and beyond bin 9, no trend is observed.

Figure 4-18: Stockland Hill transmitting station. lat. 50.80716 , long. -3.104809., Height of mast 235 m. [139]
Image source Wikipedia, copyright public domain

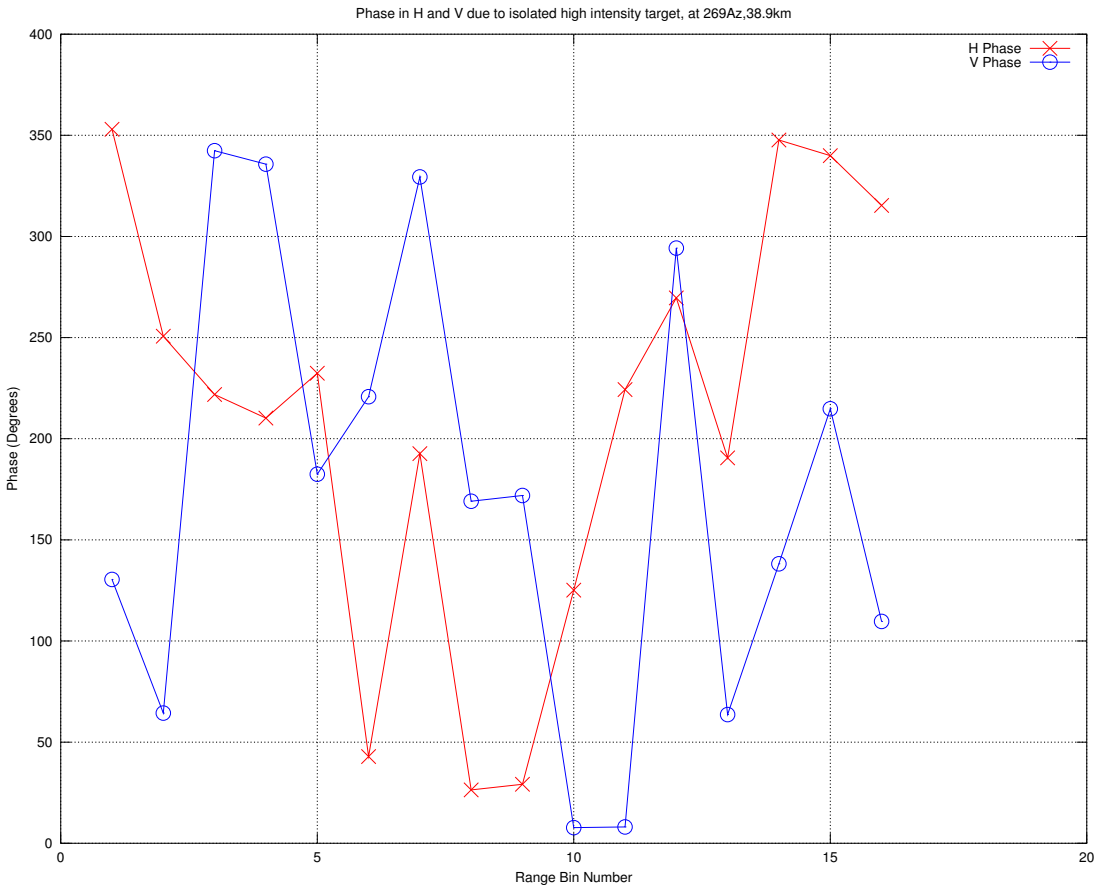

Figure 4-19: Phase Values in H and V from Stockland hill mast at 1° elevation

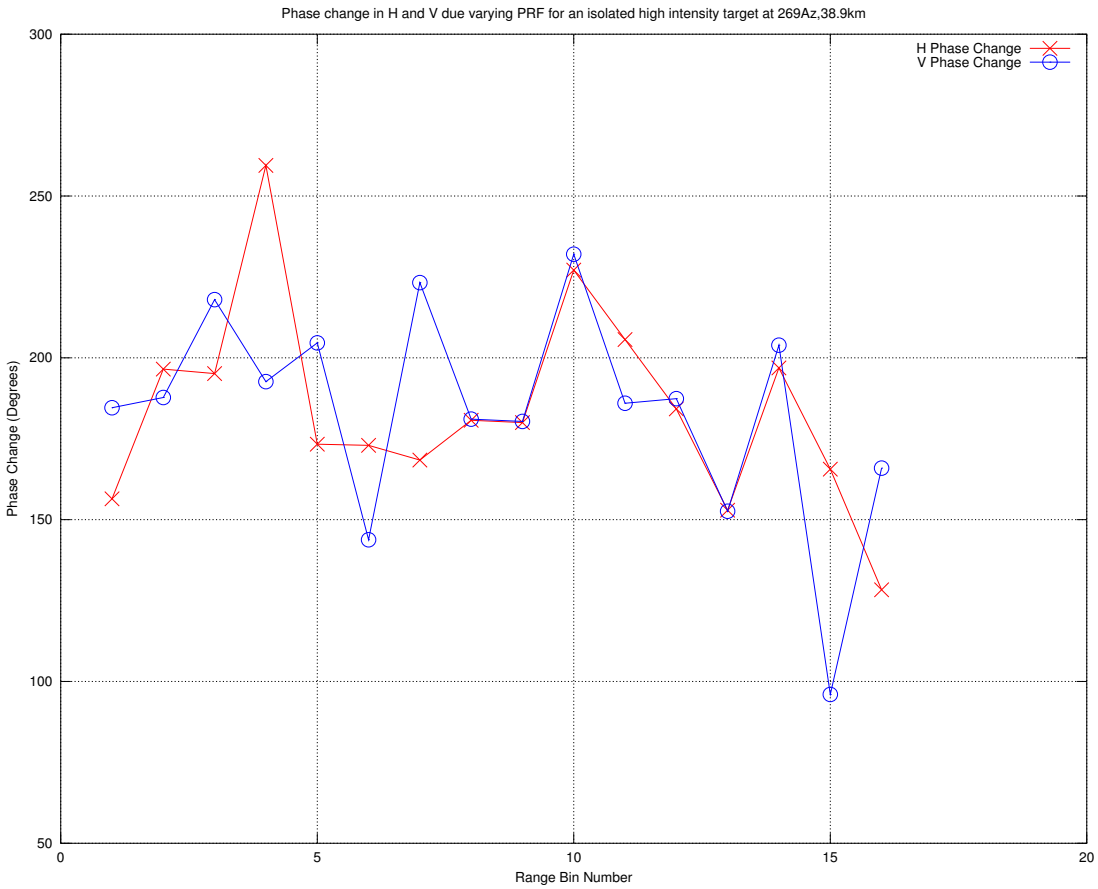

Figure 4-20: Phase change due to magnetron frequency shift from Stockland Hill mast at 1° elevation

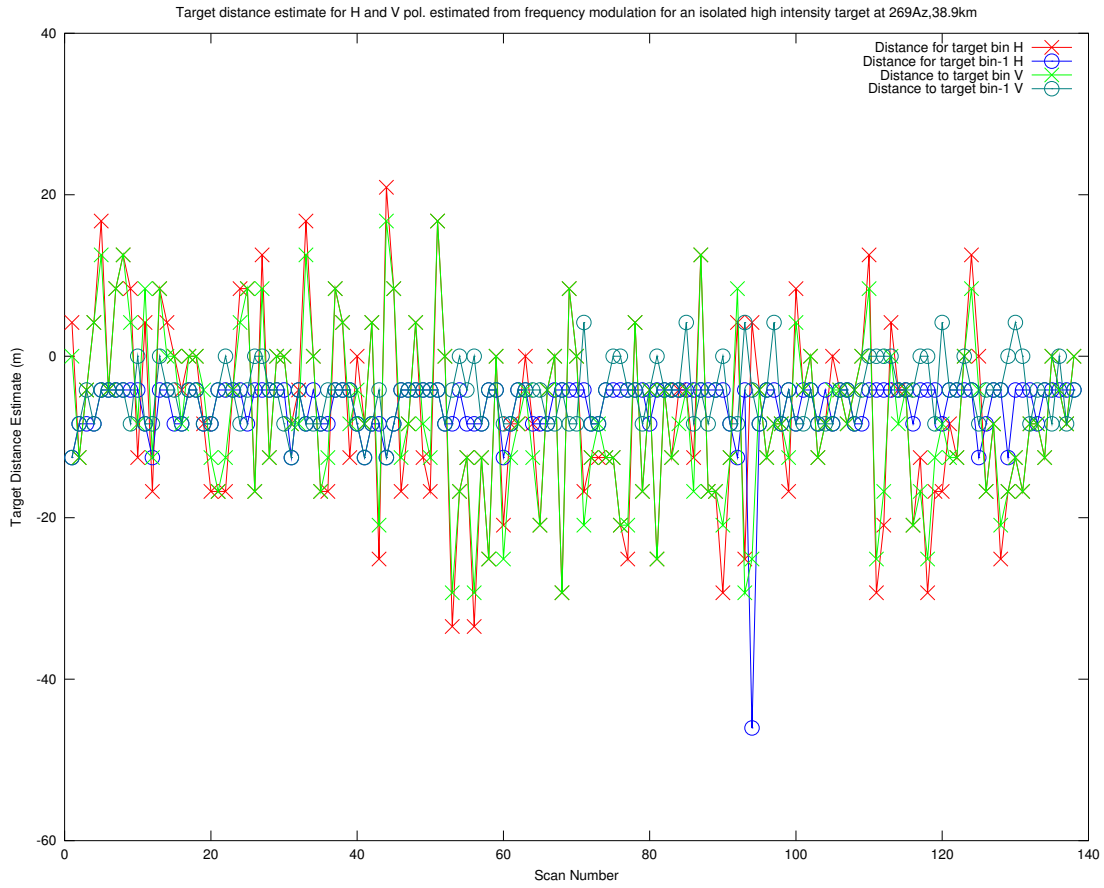

Figure 4-21: Time series of estimated target distance from range gate centre using magnetron frequency modulation for bins 8 and 9 in the previous plots.

The target distance from the centre of the range gate for bins 8 and 9 was estimated for a series of scans. If the technique was performing as expected, a 75 m difference should be measured from the phase differences for the two consecutive range gates, as the scans are performed with the 0.5μs or 75 m pulse with a matched sample rate.

The average estimated target distance from the range gate centre for bins 8 and 9 are -9.1 m and 1.3 m in the horizontal polarisation and -6.8 m and -3.4 m in the vertical polarisation, respectively.

This can possibly be explained by considering the finite nature of the transmitted pulse. In the down-conversion process, for a point-like target, the

received signal duration is equal to that of the transmitted pulse during all the frequency conversion stages. It is only at the final stage that the pulse is spread out by the effects of the digital filters. As such no frequency shift based phase information is present beyond the range bins corresponding to the target.

4.4 Summary

This chapter presented an introduction to making refractivity measurements using radar observations of stable clutter targets, with specific details on the errors that can be anticipated if the transmission frequency is allowed to vary, if the clutter targets are not centred within the range bin, and if the down-conversion frequency is changed between observations.

A comparison was made of observations in both polarizations which did not show an appreciable difference in the bulk characteristics of the clutter, with neither polarization showing significantly different quality indicator value, relative to the other. However, there is some evidence to show that by combining the refractivity results from each polarization, in such a way as to select the one with the lowest error estimate, a slight improvement in correlation with surface observations, relative to single polarization measurements is possible.

It is shown that by using a magnetron transmitter at two alternating PRFs a frequency modulation can be induced. This was used to try to locate a target's positions within range gates in a manner similar to frequency domain interferometry. It was hoped that this could be used to detect when a very high intensity target was spreading, in the radar filtering stages, beyond its own range gate into adjacent gates leading to spurious phase correlations and a biasing of the refractivity change field towards zero, however due to the mechanism by which the spreading is generated, no such detection was possible.

Chapter 5

Use of Cyclops for radiometric measurements

This chapter presents an introduction to radiometric measurements, an evaluation of the suitability of the WRNR receiver to make them, techniques to improve the radiometric sensitivity of a radar receiver, and a comparison of attenuation estimation using different methods.

5.1 Introduction

Motivation

The magnitude of attenuation by heavy rainfall affecting radar propagation varies significantly with the wavelength used; the least affected being S-band, followed by C-band and then X-band, with one way attenuation in dB/km being given by $0.0003R^{1.00}$, $0.002R^{1.17}$ and $0.0074R^{1.31}$ respectively [93]: Ideally weather radar measurements would be made at S-band (10 cm wavelength) where the attenuation due to rain is not significant. However, there are significant engineering challenges and costs associated with the longer wavelength (larger antenna for the equivalent beamwidth, larger

pedestal, larger waveguide, etc.). While there are some drawbacks to C-band (5 cm wavelength), it is a good compromise, especially in the UK where the climatological frequency of severely attenuating storms does not warrant the use of S-band.

The traditional scheme used to correct for attenuation was developed by Hitschfield and Bordan and is widely used, however due to the nature of the correction it is prone to numerical instability and is inherently sensitive to any slight miscalibration in Z [19]. In the Hitschfield and Borden technique, a cumulative correction based on a rain rate (R) is calculated with the (two way) attenuation (A) in dB/km at in any given range gate being given at C-band by [93] :

$$A = 0.0044R^{1.17} \tag{5.1}$$

As the attenuation estimate for a given range gate is calculated from the rain rate, it is assumed that the reflectivity is a measurement of liquid water; and so the Hitschfield and Bordan technique could result in an over-estimation of attenuation above the freezing level. This would be particularly significant in the winter.

In the UK the instability associated with accumulating the attenuation along a ray is resolved by capping the maximum attenuation correction that can be applied to a factor of 5 dB or ~3 times the reflectivity [94]. In very intense storms this can lead to an underestimation of the rain rate in areas beyond the attenuating cell. If a measurement of PIA were available, it would be possible to make a better correction for this, providing the attenuator is not causing complete extinction of the beam. In the case where the attenuation is complete, the measurement would still be of great use as it would indicate that the data beyond the visible attenuating cells is not reliable, and by using an intelligent compositing algorithm e.g.[95], the data from an adjacent radar could be used. The use of the radar as a radiometer provides a means of measuring the PIA.

One possible reason that the radar meteorology community has shown rel-

atively little interest in this radar as radiometer technique is that most National Meteorological Services (NMS) have plans to move to dual polarisation radars in the near future. The dual polarisation measurements also give a measure of the attenuation, using the ϕ_{dp} parameter [29]. If ϕ_{dp} is available, the radiometric measurements can still be of use as an independent measurement of the total attenuation, hopefully leading to better attenuation estimates. It has been shown by Tabary et. al, (2009) [30], that while it is usual to assume a constant γ_H value (the dB attenuation per $^\circ$ phase shift in ϕ_{dp}), in-fact, as suggested by theory [32], the value can vary by up to a factor of 2, due to a dependence on drop temperature, drop shapes, drop size distribution, and the presence of large drops causing Mie scattering particularly during convective events [96]. Carey et al. (2000) [97] quote a typical range for γ_H of 0.05–0.11 dB $^{\circ -1}$. In addition to effects on ϕ_{dp} due to variation in scatters, it has been shown that ϕ_{dp} is also affected by non-uniform beam filling [98].

Radiometric measurements also provide attenuation estimates from sources to which ϕ_{dp} would not be sensitive. Dr Robert Thompson has shown that radiometric emissions can be used to detect attenuation due to wetting of the radome, which has been shown to cause up to 5 dB of attenuation at rain rates of 50 mm/hr [27]. This means that the radiometric technique should allow for the detection of partial or complete beam blocking; the effects of which on the UK composite rain rate image, due to multiple partial beam blockages to the north of Chenies radar, London, can be seen in figure 5-1.

5.1.1 Radars and radiometers

In the past, dedicated microwave radiometers have been used in conjunction with weather radars to make measurements of the attenuation due to liquid water along a path. For example, to measure the effects of attenuation on satellite up/down links [99, 100], for benefits of combined observations with radars [24] (C-band radiometer and S-band radar), and from space-borne platforms [101].

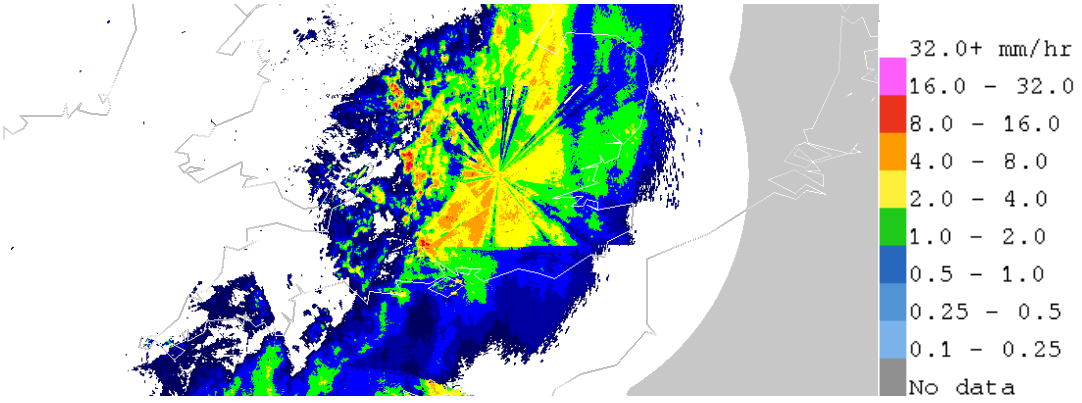

Figure 5-1: Effect of incomplete correction for partial or total beam blocking on the UK rain-rate composite

The idea of using meteorological radars as radiometers arose from an extended abstract by Fabry [22] in which it was pointed out that there are a large number of components shared between radars and radiometers. However, this technique had been suggested previously for use with other types of radar, for non-meteorological purposes e.g. [102]. Fabry [22] points out that radiometric measurements of the emissions from storms can be used as a constraint on attenuation correction schemes, as Kirchhoff's law of thermal radiation [103] states that all absorbers are also emitters. The combination of radar and radiometers has been used in the past as a means of measuring attenuation [99, 100], however the suitability of the weather radar hardware to make radiometric measurements has not been investigated in significant detail in previous work.

5.1.2 Radiometric measurements

A radiometer is designed to measure the power incident on a receiving device within a particular frequency band. This power is typically referred to in terms of the brightness temperature seen at the antenna of the radiometer (T_{ant}), where this brightness temperature is the temperature of a black body that would radiate the equivalent amount of power in the frequency range of interest. In electrical terms this is the same as a terminating resistor which has that physical temperature, at the input of the receiver. This is

of interest when attempting to measure attenuation because the observed temperature of an emitter is the emissivity of the source multiplied by its physical temperature. When in thermal equilibrium the absorptivity of a body is equal to the emissivity.

The power measured by the radiometer is dependent on its input bandwidth B and the gain G of the receiving device, and is given by [104]:

$$P = kBGT \tag{5.2}$$

Where k is Boltzmann's constant and T is the temperature of the object being observed.

However, in practice the system making the measurement, of course, has a non-zero temperature, which contributes to the measured power.

$$P_{meas} = kBG(T_{ant} + T_{sys}) \tag{5.3}$$

Where the T_{ant} is the antenna temperature i.e. the brightness temperature seen at the input of the receiver and T_{Sys} is the brightness temperature equivalent to the noise added by the measuring system.

Radiometric sensitivity

The suitability of any system to make radiometric measurements is governed by two main factors: its sensitivity and stability at the frequencies of interest. The first of these, the sensitivity (ΔT), can be calculated from [104]:

$$\Delta T = \frac{T_{ant} + T_{Sys}}{\sqrt{B\tau}} \tag{5.4}$$

Where τ is the observation time.

Conventional Radiometers

While the Met Office radars are conventionally calibrated by signal injection at varying power levels every 3 months, the measurement of the small variations in noise which are expected due to storm emissions require continuous calibration to account for short term temperature, gain and filter variations. As such, it is useful to review how these challenges have been addressed by the radiometer community and to see whether it is possible to apply these techniques in the context of a weather radar receiver.

Total Power radiometers The total power radiometer [104] is the most straightforward of all radiometers, in that it is simply an amplifier with bandpass filter and a suitable detector.

$$V_{out} = G(T_{ant} + T_{Sys}) \tag{5.5}$$

Where V_{out} is the output voltage of a Square Law detector.

Dicke Switch radiometers The introduction of the Dicke switch [23] was the first refinement made to receivers to enable them to make more accurate radiometric measurements. This improves upon the total power radiometer's stability by rapidly (kHz) switching the receiver between being connected to the antenna and a resistive load at a known temperature (T_R).

From [104], when the receiver is connected to the antenna, the output voltage V_1 is given by:

$$V_1 = G(T_{ant} + T_{Sys}) \tag{5.6}$$

and when connected to the resistive load the output polarity is reversed so that the output voltage V_2 is given by:

$$V_2 = -G(T_R + T_{Sys}) \tag{5.7}$$

When integrated over the alternating measurement cycle, the output voltage V_{out} is given by:

$$V_{out} = V_1 + V_2 = G(T_{ant} - T_R) \tag{5.8}$$

This significantly improves the stability, as any effects due to variation in the receiver temperature T_{Sys} are eliminated, and the output is now proportional to the difference in the antenna temperature and the load, rather than the sum of temperatures in the total power case (eq. 5.5).

Noise Injection radiometers A further increase in the accuracy of radiometers came with the introduction of the noise injection radiometer [105]. This operates in a similar manner to the Dicke switch radiometer, and indeed also incorporates a switch. However in this case, a known noise signal is injected at the antenna and is used in a feedback loop designed to set the output voltage to zero. In this condition, the antenna temperature (T_{ant}) plus the injected temperature (T_{inj}) balance the known reference source temperature (T_R) :

$$V_{out} = G(T_{ant'} - T_R) = 0 \tag{5.9}$$

Where $T_{ant'} = T_{ant} + T_{inj}$. from which it can be deduced that:

$$T_{ant} = T_R - T_{inj} \tag{5.10}$$

The added noise can be accurately controlled and T_R should be well known, so by this means T_{ant} can be measured without the effects of receiver gain variation or T_{sys}.

Noise-adding total power radiometer It has been noted that the "Dicke switch can add 7 K" [106] due to the insertion loss associated with putting a switch in the signal path. As such, for very low noise temperature measurements it is preferable to avoid the switch and use a reference noise standard by injecting the modulated noise via a waveguide coupler.

The measured temperature can then be calculated as [107]:

$$V_{T_{On}} = G(T_{ant} + T_{Inj} + T_{Rx}) \tag{5.11}$$

Where $V_{T_{On}}$ is the measured voltage with the noise source switched on,

$$V_{T_{Off}} = G(T_{ant} + T_{Rx}) \tag{5.12}$$

$V_{T_{Off}}$ is the measured voltage with the noise source switched off. Subtracting one from the other gives:

$$V_{T_{On}} - V_{T_{Off}} = G(T_{Inj}) \tag{5.13}$$

Or:

$$\frac{V_{T_{on}} - V_{T_{Off}}}{T_{Inj}} = G \tag{5.14}$$

and so:

$$T_{sys} = T_{inj}\left[\frac{V_{T_{off}}}{V_{T_{on}} - V_{T_{off}}}\right] \tag{5.15}$$

With a stable, calibrated noise source, this technique enables accurate compensation for the receiver gain but does not compensate for variations in receiver noise temperature. In the past, this has been compensated for by employing a waveguide switch to observe a known temperature termination

[108] and subtracting this value, or simply directing the antenna away from the target of interest to a known empty area of sky [109]. The advantage of directing the antenna away from the radiating object is that if the elevation is kept constant it can also be used to remove the atmospheric component of the noise brightness temperature.

In comparison to the radiometers previously described, the Met Office radar receiver most closely resembles a noise adding total power radiometer. With the radar, an area with the minimum attenuation predicted by the reflectivity or ϕ_{dp} signal could be selected and used as the estimate of the receiver and atmospheric temperature and subtracted leaving the additional contribution due to storm attenuation.

Receiver Calibration The overall receiver calibration of a radiometer is often verified by using hot and cold sources at known temperatures [110]. These often consist of a matched load at a known temperature, enclosed in a temperature controlled oven to act as the hot load, and in liquid nitrogen to act as the cold load. An alternative calibration method uses high emissivity materials which are typically saturated with cryogenic material, often, again liquid nitrogen, and then observed with the antenna beam; for the hot calibration the same material is observed at measured ambient temperatures.

Error due to gain variations Due to the small signal levels measured radiometrically, the gain of the receiver needs to be large. This leads to significant measurement errors if the gain is unstable. While the sensitivity and stability of a radiometer are much improved by the addition of a Dicke switch, it is still subject to the same variations in gain given by:

$$P = GkT_{sys} \tag{5.16}$$

and as this is a linear relationship:

$$\Delta P = \Delta G k T_{sys} \tag{5.17}$$

and so [110]:

$$\Delta T_{Gain} = \frac{T_{sys} \Delta G}{G} \tag{5.18}$$

Where ΔT_{Gain} is the temperature variation that would be observed due to a gain variation of ΔG.

5.1.3 Required Radiometric sensitivity

The emissions due to one way attenuation by rain along a given path are given by [28]:

$$\Delta T_{ant} = (T_p - T_{back})(1 - e^{-\tau}) \tag{5.19}$$

Where ΔT_{ant} is the change in observed brightness temperature at the antenna, $T_p$is the physical temperature of the attenuating storm, T_{back} is the background brightness temperature due to gaseous emission from the atmosphere and receiver and τ is the one way optical thickness at the radar's frequency, i.e. the one way linear attenuation.

As can been seen in figure 5-2, at low values of attenuation the relationship between the emissions and the attenuation is approximately linear with ~0.05 dB per K for one way attenuation, assuming an average precipitation physical temperature of 280 K and a background atmospheric gaseous emission temperature of 30 K. This assumption of linearity at low attenuation values provides a useful rule of thumb that in-order to accurately measure a 1 dB two way PIA, a radiometric sensitivity of better than 10 K is required. This value is reduced at lower elevations due to increasing gaseous emission temperatures. As the radar typically scans at 5 different elevations within

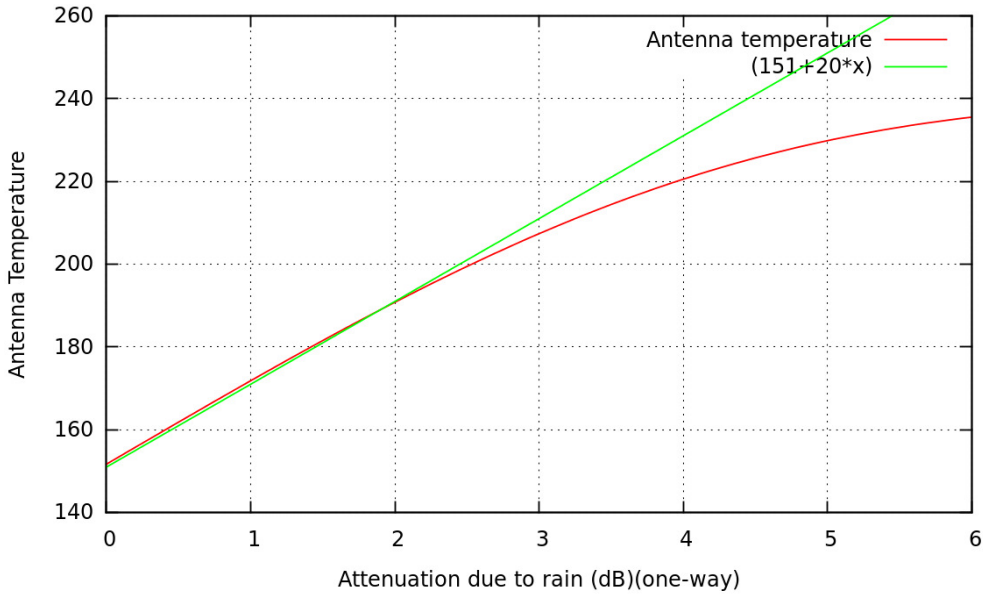

Figure 5-2: Antenna temperature with one way attenuation for a mean precipitation temperature of 280 K and background gaseous emission temperature of 30 K

one 5 minute data volume collection cycle, the radiometric sensitivity of the radar will vary.

5.1.4 Noise Figure/Factor Calibration

The receiver noise factor, a measure of the noise added by passing a signal through an active network, is defined as [111]:

$$F = \frac{SNR_i}{SNR_o} = \frac{S_i N_o}{S_o N_i} = \frac{S_i N_o}{G S_i N_i} = \frac{N_o}{G N_i} = \frac{N_{added} + G N_i}{G N_i} \tag{5.20}$$

Where SNR_i is the input SNR and SNR_o is the output SNR, $S_{i/o}$ is the signal in/out, $N_{i/o}$ is the noise in/out, and G is the gain of the network. N_o is made up of the amplified noise in (GN_i) plus any noise added by the receiver (N_{added}).

The noise figure is then:

$$NF = 10.0 * \log_{10}(F) \tag{5.21}$$

Measurement of the receiver noise figure requires the injection of noise into the receiver, of a known equivalent temperature. The noise power of a system can be related to its equivalent temperature by[110]:

$$N = kTB \tag{5.22}$$

Where k is Boltzmann's constant, T is the temperature of the noise source and B is the effective bandwidth of the network. And so:

$$N_o = FGN_i = FGkTB \tag{5.23}$$

Or by both adding and subtracting $GkTB$:

$$N_o = GkTB + (F-1)GkTB \tag{5.24}$$

From this, it can be seen that the output noise has two components: the amplified input noise and the noise added by the network itself.

The noise source is supplied with a known Excess Noise Ratio (ENR) where [104]:

$$ENR = \frac{T - T_0}{T_0} \tag{5.25}$$

And $T_0$is assumed to be 290 K by convention [104]. This is often given in dB form:

$$ENR_{dB} = 10.0 * \log_{10}\left(\frac{T - T_0}{T_0}\right) \tag{5.26}$$

If noise power at a known equivalent temperature value (T) is injected in to the network, by using these two values GkB can be calculated and with this the noise factor can be computed as:

$$F = \frac{D}{\frac{N_2}{N_1} - 1} \tag{5.27}$$

Where $D = \frac{T+T_0}{T_0}$. In terms of noise figure:

$$NF = 10\log_{10}(D)\text{–}10\log_{10}\left(\frac{N_2}{N_1} - 1\right) \tag{5.28}$$

Noise temperature of the Met Office Receiver The noise temperature of a receiver is governed by both its physical temperature and its noise factor F. This is a measure of how much additional noise is added to a signal passing through the receiver.

$$F = 1 + \frac{T_e}{T_0} \tag{5.29}$$

Where T_e is the effective noise temperature of the device, T_0 is the ambient temperature and F is the (linear) noise factor.

Re-arranging gives:

$$T_e = T_o(F - 1) \tag{5.30}$$

Where T_0 is taken to be 290K .

It is expected that for a well designed receiver system, the noise factor is largely dominated by the noise factor of the first component due to Friis' Formula [112]:

$$F_{TOT} = F_1 + \frac{F_2 - 1}{G_1} + \frac{F_3 - 1}{G_1 G_2} + \frac{F_4 - 1}{G_1 G_2 G_3} + ... \tag{5.31}$$

Where F_n is the noise factor of the nth device and G_n is the gain of the nth device: Therefore it is preferable to have as much gain as early as possible, with as low a noise factor as possible.

5.2 Radiometric calibration techniques

5.2.1 Noise injection calibration

A noise injection diode has a known output ENR, which can be converted to a brightness temperature which can be used to determine a calibration value to convert from output counts to noise temperatures (eq. 5.14). This can then be applied to calculate the output temperature (eq. 5.15).

A Ranatec 35 dB ENR_{dB}, calibrated noise source (model number GN31N) was fitted to the 30 dB waveguide couplers used to perform offline calibration of the receiver by signal injection. The is triggered by the Cyclops digital I/O, via a drive circuitry which creates the required 28 V noise source drive pulse from the LVTTL input. The noise is injected for $6\mu S$ every pulse. After passing through the coupler the noise temperature ENR_{dB} is 5 dB or 1207 K

5.2.2 Tipping Curve Calibration

One technique used to calibrate radiometers is the "Tipping Curve" technique [31]. This models the atmospheric contributions to the noise seen by the antenna and uses a typical profile of atmospheric depth to model the noise as follows [113]:

$$T_b(\theta) = T_{MR}(1 - e^{-\tau.sec(\theta)}) + T_{CMB}e^{-\tau.sec(\theta)} \tag{5.32}$$

Where T_b is the atmospheric brightness temperature at elevation angle θ, T_{MR} is the mean radiative temperature of the atmosphere, T_{CMB} is the

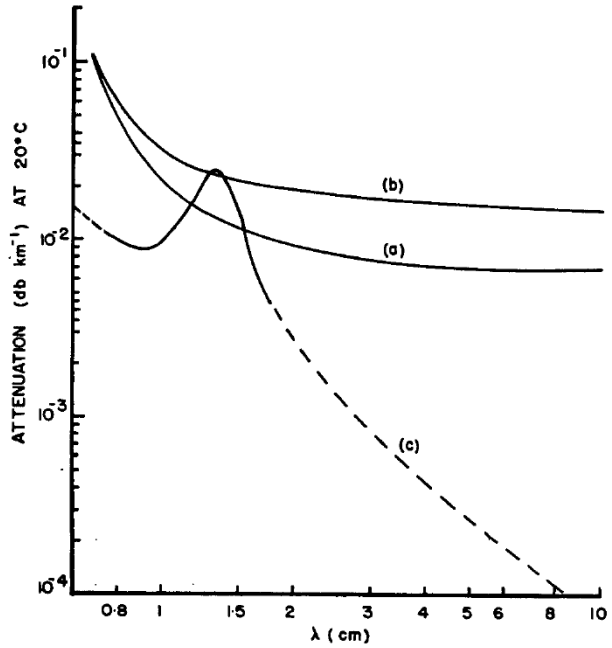

Figure 7. Atmospheric attenuation versus wavelength. (a) Attenuation due to O_2 in air at 1 atmos pressure and 293°K, using $\Delta\nu = 0{\cdot}039$ cm^{-1} for 5 mm lines and $\Delta\nu = 0{\cdot}02$ cm^{-1} for zero-frequency line. (b) As (a), using $\Delta\nu = 0{\cdot}039$ cm^{-1} for 5 mm lines and $\Delta\nu = 0{\cdot}05$ cm^{-1} for zero-frequency line. (c) Attenuation due to 1 g m^{-3} of water vapour in atmosphere : full line, measured (Becker and Autler 1946); dashed line, calculated. Attenuation is approximately proportional to water vapour content.

Figure 5-3: Variation in attenuation with wavelength for O_2 and water vapour (extract from Gunn and East [93])

effective brightness temperature of the cosmic microwave background and τ is the opacity at zenith angle, θ.

This model assumes that the atmosphere is horizontally stratified and optically thin. Care should be taken to avoid carrying out tip curve calibrations when other sources of emission in the frequency of interest are present. For most radiometers this can include clouds as well as rain, due to their water vapour content. However the main contribution to the atmospheric emission at C-band (5 cm) is from O_2 with no significant contribution from water vapour at the wavelengths of interest as shown in figure 5-3. Contamination of the tip curve by rain is easily avoided using the radar measurements: the reflectivity can be used to detect when rain is present.

Calculated brightness temperatures from radiosonde profiles

Using the tipping curve technique for the longer term calibration is dependant on the seasonal stability of the brightness temperature with elevation, so this was investigated further. Vertical profiles of temperature and pressure from radiosonde launches at Larkhill (Lat. 51.20, Long. -1.82) (67 km from Wardon Hill) were used to generate a climatology. Radiosondes are launched from Larkhill on weekdays only so data at the weekends are interpolated from weekday data. From the observed sensitivity (figure 5-4) this is unlikely to have had a significant impact on the results. The Atmospheric Radiative Transfer Simulator (ARTS) [114] was then used to simulate the atmospheric brightness temperature at a range of elevations.

The ARTS package is a freely available (GPL), C++ based, flexible, line by line radiative transfer model, wherein the radiative emissions from selected atmospheric species can be simulated. The emissions from O_2 and water vapour are of most relevance, but at the frequency of interest (5.625GHz - 5.3cm) this is dominated by the effect of the O_2 and shows little variation within the UK weather radar licensed band (5.6 to 5.65 GHz) as seen in figure 5-3. One year of radiosonde data was used as an input to ARTS to model how the brightness temperature varied over the course of a year. The modelled brightness temperature is shown as a function of elevation and time of year in figure 5-4(a) and plotted for typical radar elevation angles in figure 5-4(b).

Figure 5-5 (a) shows the elevational variation over the course of a year with the error bars representing the maximum and minimum brightness temperature for every half degree in elevation. The range of these maxima and minima are shown in figure 5-5 (b). Figure 5-5 (c) shows the errors expected by using a parameterised climatological value of brightness temperature at each elevation.

In the event that radiosonde data is unavailable, then provided elevation angles of greater that 12 degrees are used, the maximum error will be 1 K (from figure 5-5 (c)). Furthermore, for the majority of the time it will be possible to use elevations above 5 degrees and still maintain 1 K accuracy.

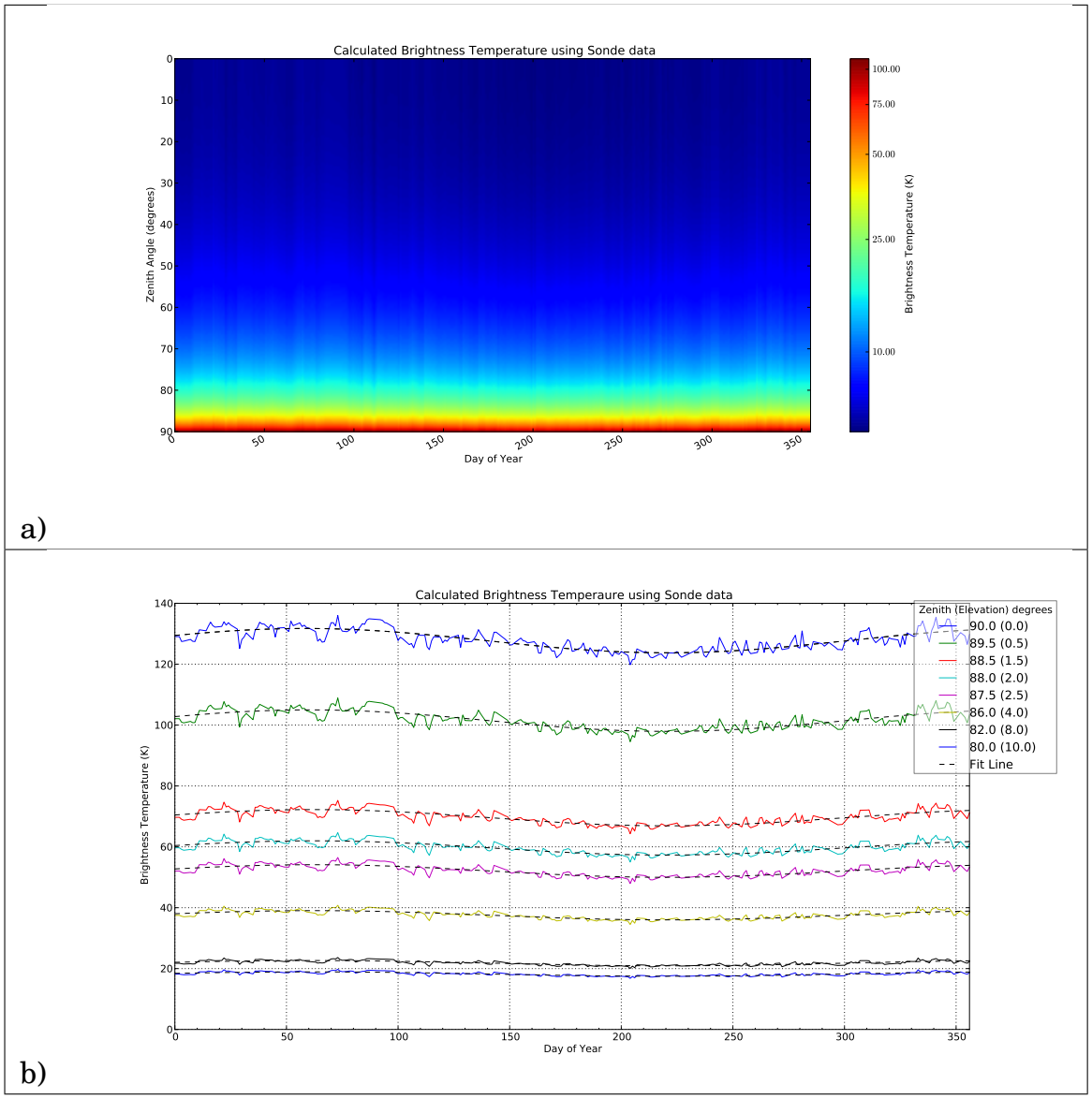

Figure 5-4: a) Calculated brightness temperatures with zenith angle. Based on one year of radiosonde data from Larkhill station
b) Annual variation in brightness temperature at typical radar observing elevations (solid line) including sinusoidal fit (dashed line)

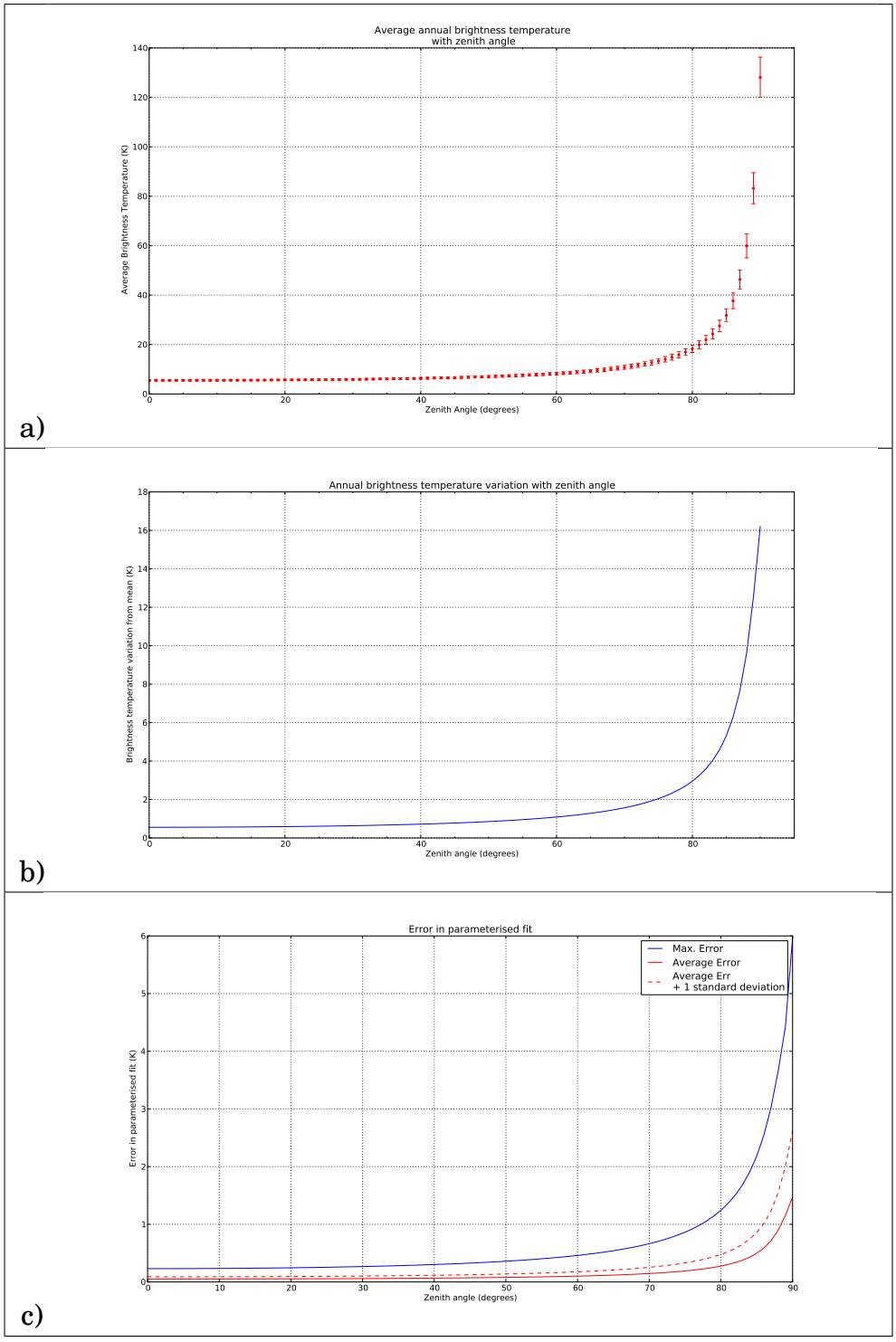

Figure 5-5: a) Annual average value of brightness temperature with zenith angle with error bars representing the annual observed maximum and minimum ranges
b) Annual variation of brightness temperature from annual average value
c) Errors resultant from using parametrised fit value

5.2.3 Suitability of the Met Office receivers to make C band radiometric measurements

The Met Office Receiver

The design of the Met Office receiver is shown in figure 3-12. A detailed description of the components is now given.

Low noise amplifiers The Low Noise Amplifiers (LNA) used in the Met Office receiver are Microwave Amplifiers Ltd. AL16-5.4-5.8-18 with 400 MHz bandwidth centred at 5.6 GHz and a quoted noise figure of 2.7 dB max and 2.5 dB typical. The gain of the device is ~18 dB.

Mixer The mixer is a Pascall C band image reject mixer type 1-10757 Iss02 with a conversion loss of 5.5 dB; this loss dominates the noise contribution of the component.

Intermediate Frequency Amplifiers The IF amplifier used in the Met Office receiver is a Pascall Type 1-12310 Iss. 01, with a gain of 22.8 dB, a noise figure of 6.3 dB and integrated filters giving a 3 dB bandwidth of 5 MHz. The frequency/power response of the IF amplifier can be seen in figure 5-6.

Overall receiver chain noise factor Using Friis' equation (eq 5.31) the cumulative noise factor of the receiver is calculated to be 3.01 dB. From equation 5.30, the receiver noise temperature can be estimated as $290(10^{0.3} - 1) = 290.7$ K.

The measurement time and bandwidth of the radar receiver are constrained by the need to continuously perform rain rate estimation measurements. Therefore it is unlikely that the scanning characteristics can be significantly modified to make radiometric measurements. For the purposes of this

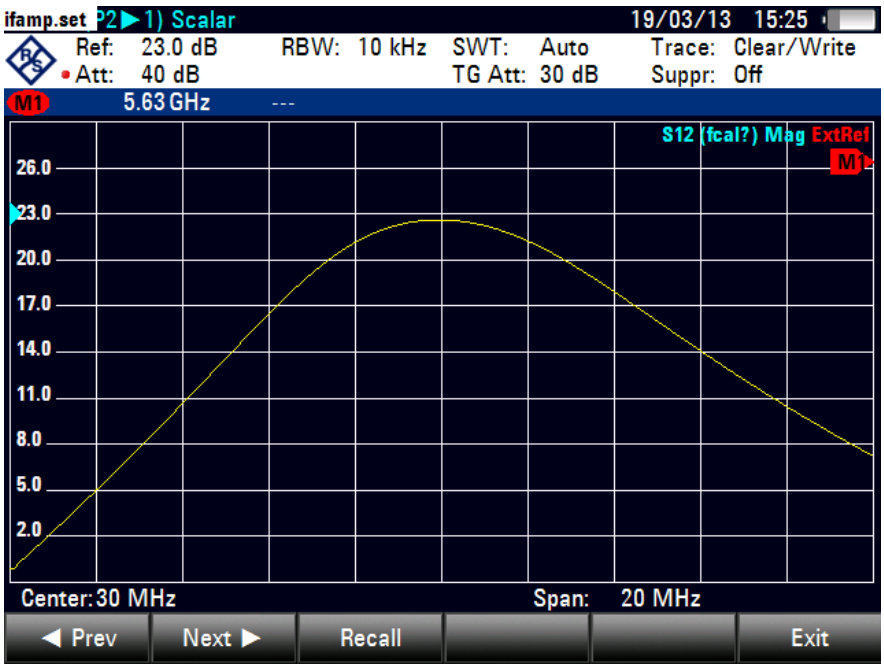

Figure 5-6: Pascall Type 1-12310 Iss. 01 IF amplifier response (5 MHz Bandwidth - 22.8 dB Gain)

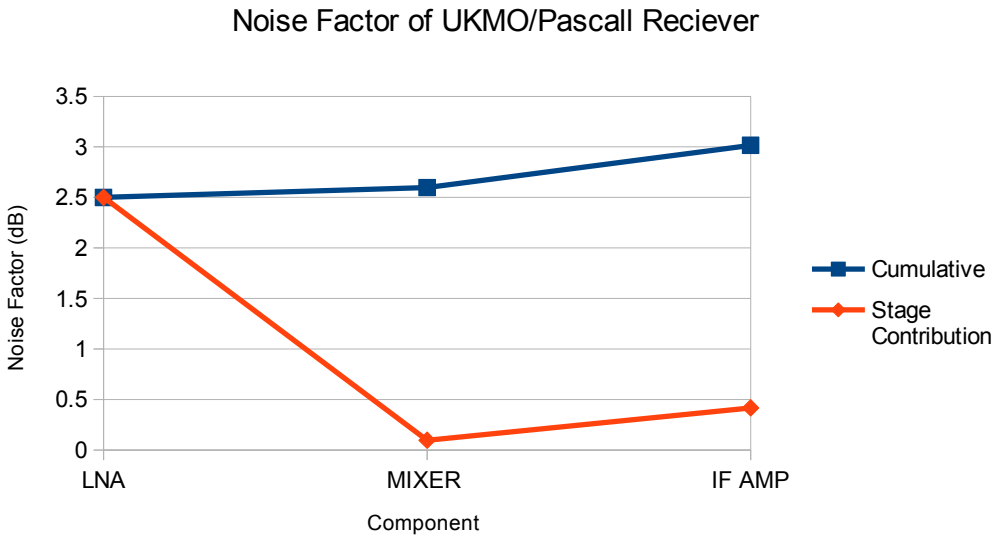

Figure 5-7: Pascall receiver noise factor contributions (Based on Pascall data sheet)

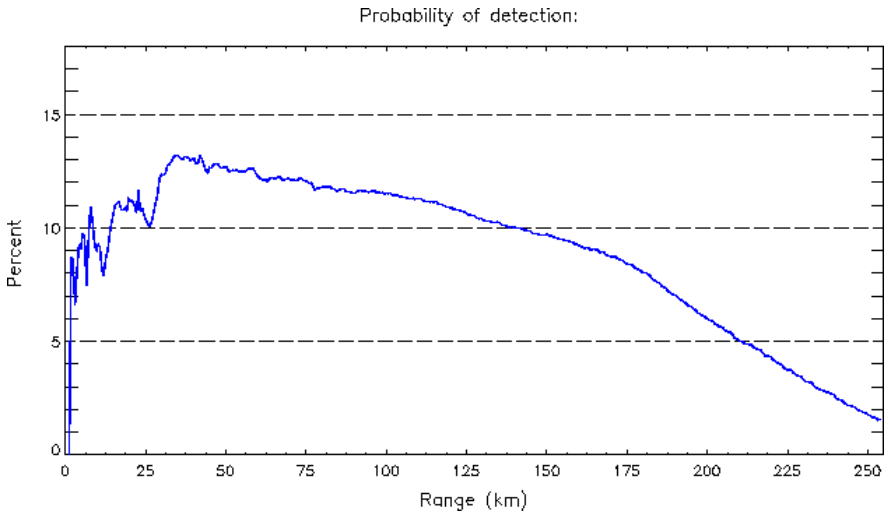

Figure 5-8: Probability of detection for signals flagged as precipitation above the noise threshold, for a three month period, as a function of range for 0.5° elevation scans from a UK weather radar, specifically taken from Cobbacombe Cross site.

analysis typical values for a long pulse, low elevation reflectivity scan will be used as this is where the benefits of any improvement in reflectivity measurement would be most useful. The typical rotation rate for such a scan is 1.4 RPM with a PRF of 300 Hz. This equates to 8.4 degrees per second, or 0.12 seconds per degree. At 1/300 s per pulse this allows ~36 pulses to be integrated into one ray. However, it is not possible to make measurements at all ranges, as these would be contaminated by rain closer to the radar.

From figure 5-8, which shows the percentage of time for which any precipitation signal above the noise threshold is detected, against range, it seems reasonable at low elevations to use ranges beyond 300 km to make radiometric measurements, where the radar is unlikely to be observing rain. At this range at 0.5° elevation, the beam centre height is ~8.7 km and therefore above most precipitation. This gives a time period of 2 ms to the time of transmission of the next pulse (3.3 ms PRT) to make the required measurement: an observation time per pulse of 1.333 ms.

Combining this with the number of pulses used, gives a total observing time of 48 ms per degree. Using eq. 5.4, an estimate of $T_N \approx 300$ K, $B = 0.5$ MHz

and $\tau \approx 50$ ms (based on the previous analysis), and assuming $T_{ant} = 200$ K give a sensitivity$\Delta T = 3.09K$; shows that the receiver is theoretically able to measure the noise to the required accuracy of 10 K. However, it should be noted that this analysis neglects the losses in front of the LNA, created by the OMT, circulator and TR-cell. These are dealt with in section 5.3.

5.2.4 Environmental Receiver testing

Environmental testing of the receiver was carried out to assess the receiver's ability to withstand the physical motion associated with being mounted on the back of the antenna, and its stability with temperature, as the radome has none or very little temperature control. The tests included placing the receiver in a temperature testing chamber to measure the response of the receiver to temperature variations and also the high ENR noise source, that was to act as a calibration for the brightness temperature of the receiver.

Testing of the ENR noise source

The high ENR noise source was placed in the environmental chamber, independent of the receiver, and its response was monitored. The measurement configuration is shown in figure 5-9.

From figure 5-10 it can be seen that the overall variation of the noise output temperature of the ENR noise source is +/- 22.3 K. This is a 1.8 % variation on the noise power injected into the receiver, contributing 1.8 % uncertainty in the calibration.

Testing of the receiver.

Figure 5-11 shows that the receiver is stable in terms of its linearity and gain over a wide range of temperatures. Conventionally, radars are required to be stable to within 1 dB over a long time period to minimise errors in

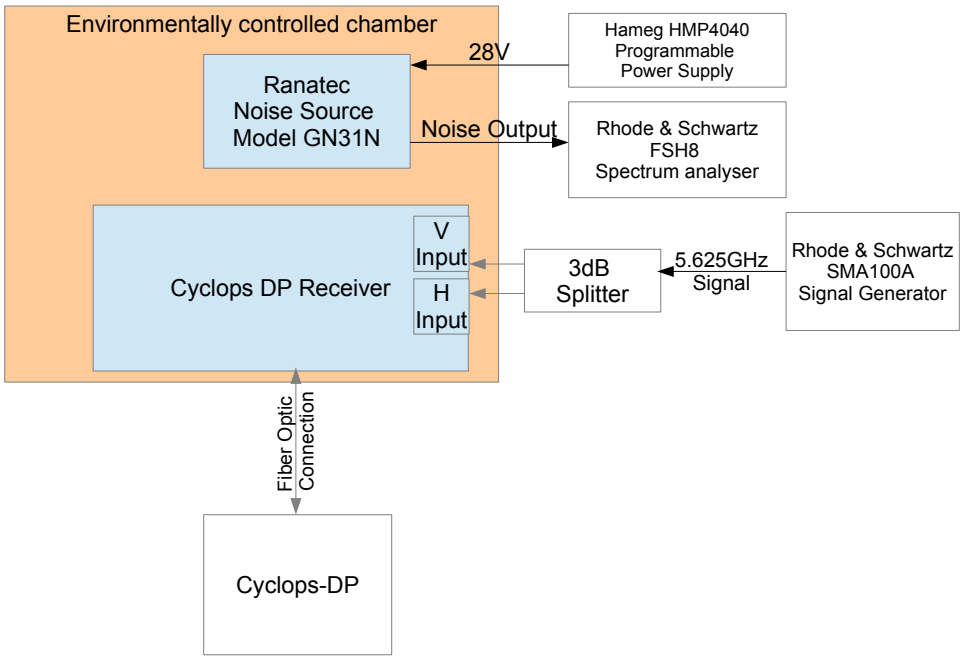

Figure 5-9: Configuration of temperature testing

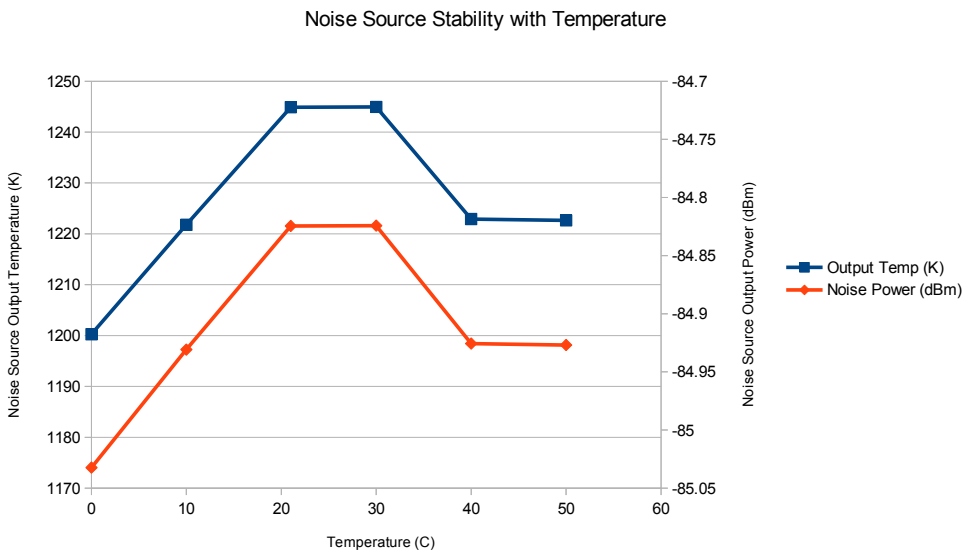

Figure 5-10: Noise Source output variation with temperature

reflectivity measurements. From these results we can be confident that any reasonable annual temperature variation will not result in exceeding this criterion. However there is a more stringent criterion on the stability of Z_{dr}(0.2 dB) [14]. Whilst figure 5-12 (b) shows this criterion is not met for the range of temperatures tested, within typical operating temperatures of 0 to 30 °C (including diurnal temperature changes of ~ 10 °C), the variation of less than ±0.1 dB

Of most concern with respect to making radiometric measurements is the variation of the receiver gain with temperature (figure 5-13). This is due to the large gains required both to make useful radiometric measurements and to get the maximum detection from weather signals when operating as a radar, and so any variation in this gain has a large effect on the output.

Whilst the receiver is reasonably stable; certainly suitable for logarithmic measurements of reflectivity, the effect on the linear brightness temperature measurement is more significant. Using eq. 5.18, a receiver with $T_{sys} = 500$ K, $G = 36$ dB and $\Delta G = 0.1$ dB gives a $\Delta T_{Gain} \approx 11$ K. This is greater than the ~10 K required for 1 dB attenuation estimates.

5.3 Optimisation of the Met Office receiver for making radiometric measurements

5.3.1 Physical optimisation

To reduce the overall noise figure of the receiver, a pair of LNAs with a lower noise figure were purchased and installed at Wardon Hill Radar. The LNAs were Microwave Amplifiers Ltd. AL28-5.4-5.8-18 with 400MHz bandwidth centred at 5.6GHz and a quoted noise figure of 1.5 dB maximum and 1.2 dB typical. The reduced noise figure is due to additional diode protection on the input of the AL16, to protect it from large voltages including any power from the transmitted pulse which breaks through the protection provided

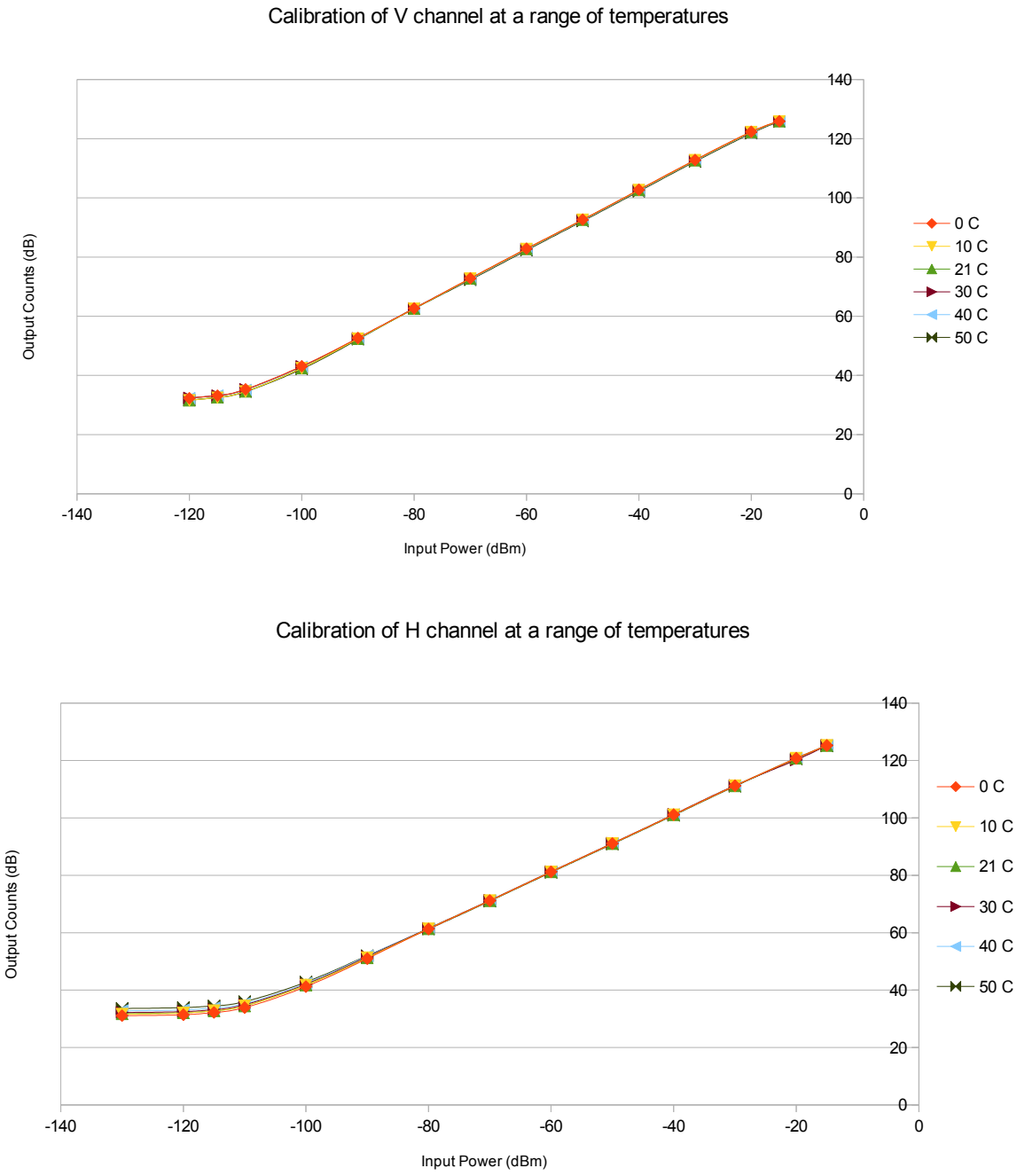

Figure 5-11: Calibration of the H and V channels at a range of temperatures between 0 C and 50 C

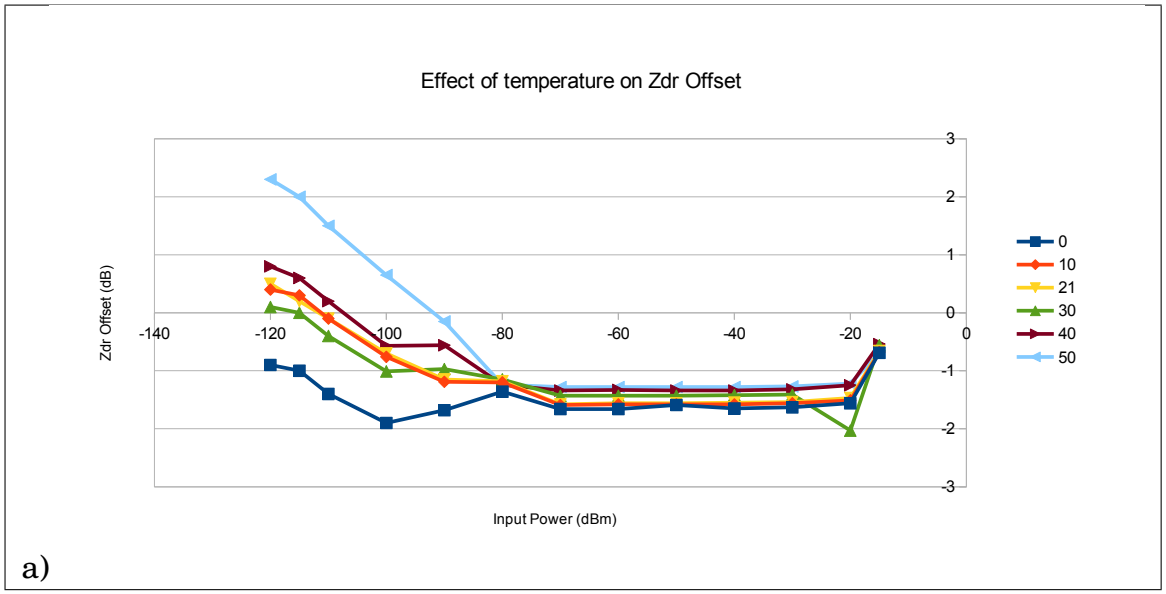

a)

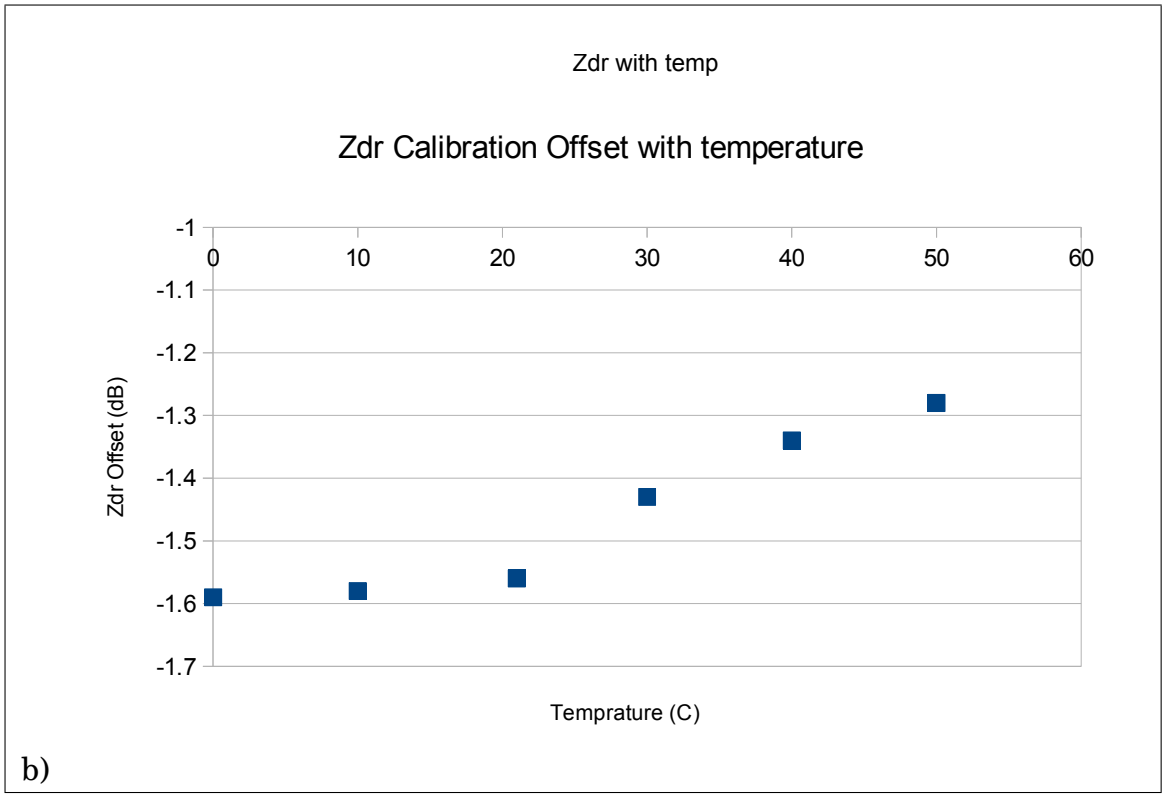

b)

Figure 5-12: Effect of temperature variation on Z_{DR} offset.
a) Z_{DR} calibration offset with temperature and injected power
b) Z_{DR} calibration variation with temperature at -50dBm injected power

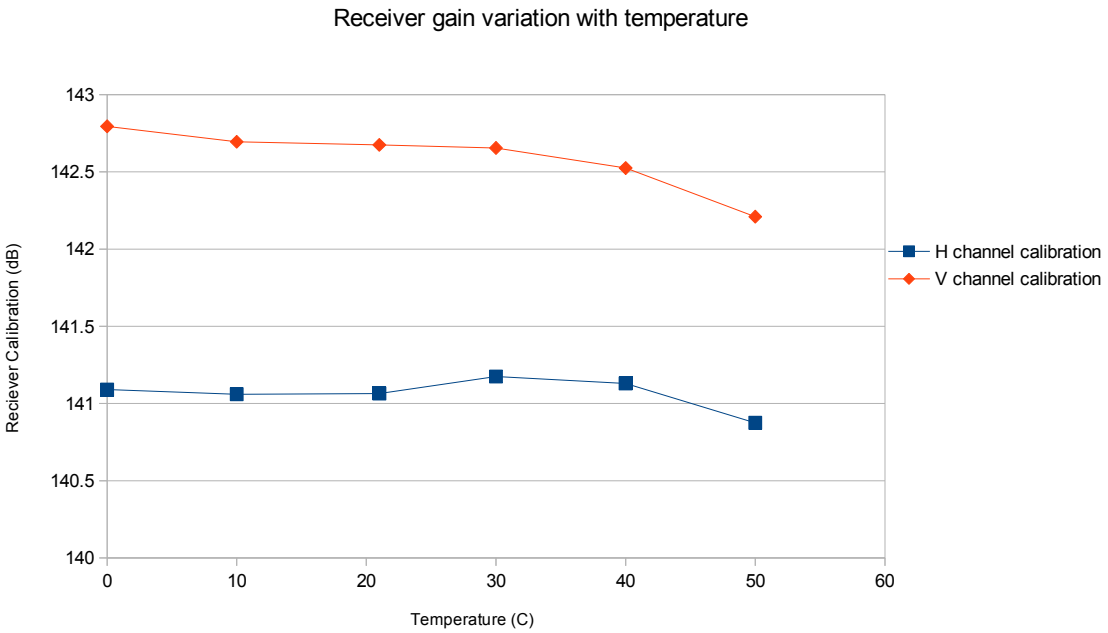

Figure 5-13: Variation of the receiver gain with temperature for the H and V channels

Table 5.1: Results of Receiver noise figure measurements

Filter Bandwidth (MHz)	Noise ENR	T_{eff}	T_{off} output (dB)	T_{on} output (dB)	Noise Factor F_{sys}	Noise Temp. (K)
0.5	5	1207	31.85	36.42	2.30	201.9
2	5	1207	40.65	45.2	2.32	205.4
LNA Only (~ 400 MHz)	5	1207	-89.1	-84.5	2.249	196.7

by the TR-cell. The lower noise figure LNAs give a T_e= $290(10^{0.12} - 1) = 92$ K, an improvement of 133 K relative to the original LNA.

The performance of the receiver with new LNAs was tested in the laboratory environment, the results of which can be seen in table 5.1. The testing was carried out with multiple input bandwidths.

The discrepancy between the expected and observed values of noise temperature/factor is likely to be caused by cable and adaptor losses used to connect to the LNA.

Losses before the LNA

By injecting signals both at the waveguide couplers and directly at the receiver input, the losses due to the components in front of the LNA have been measured as shown in Table 5.2(a) and (b).

Table 5.2 (b) shows that the cables which connect the waveguide coaxial transition piece to the receiver input introduce a significant degradation to the noise temperature of the system. To reduce this impact, the receiver design was further optimised by moving the LNAs from the receiver enclosure to be directly mounted on the waveguide-coaxial adapter, as is conventionally done with ground based receiver LNAs. This reduced the loss before the LNA by the 1.2 dB introduced by the cable. Applying Friis' formula to this reduction in loss gives an improvement in the noise temperature of 212 K.

Table 5.2: a) Losses in signal path and b) Resultant cumulative noise temperature

a)

Component	Loss H (dB)	Loss V (dB)
OMT, Circulator and TR cell	3.6	3.5
RF Cable to RX	1.2	1.2
Total	4.8	4.7

b)

Component	Temperature H (K)	Temperature V (K)
OMT, Circulator and TR cell	374.3	359.2
OMT, Circulator, TR cell and RF Cable to Receiver	585.8	568.9

5.3.2 Soft/firm-ware

In addition to optimizing the radar hardware for making radiometric measurements, improvements to the signal processing have also been made. Cyclops makes use of the "dead time" at the end of a ray to make measurements of the noise. The measurements can only be made in long pulse ($2\mu s$) (300 Hz PRF) mode as short pulse measurements have an unambiguous range of only 120 km. At this range there is a high probability of precipitation so there is no opportunity to make the radiometric measurements.

The available bandwidth in long pulse mode is 0.5 MHz. However by switching the digital filters at the appropriate time in the data collection cycle, the full analogue bandwidth of the analogue components can exploited. From eq. 5.4, if the short pulse filters were used, receiver noise sensitivity would be improved by a factor of 2. This was tested at Wardon Hill and the improvement in sensitivity is shown in figure 5-14 and summarised in Table 5.3.

The effect of four times the long pulse bandwidth with the same integration

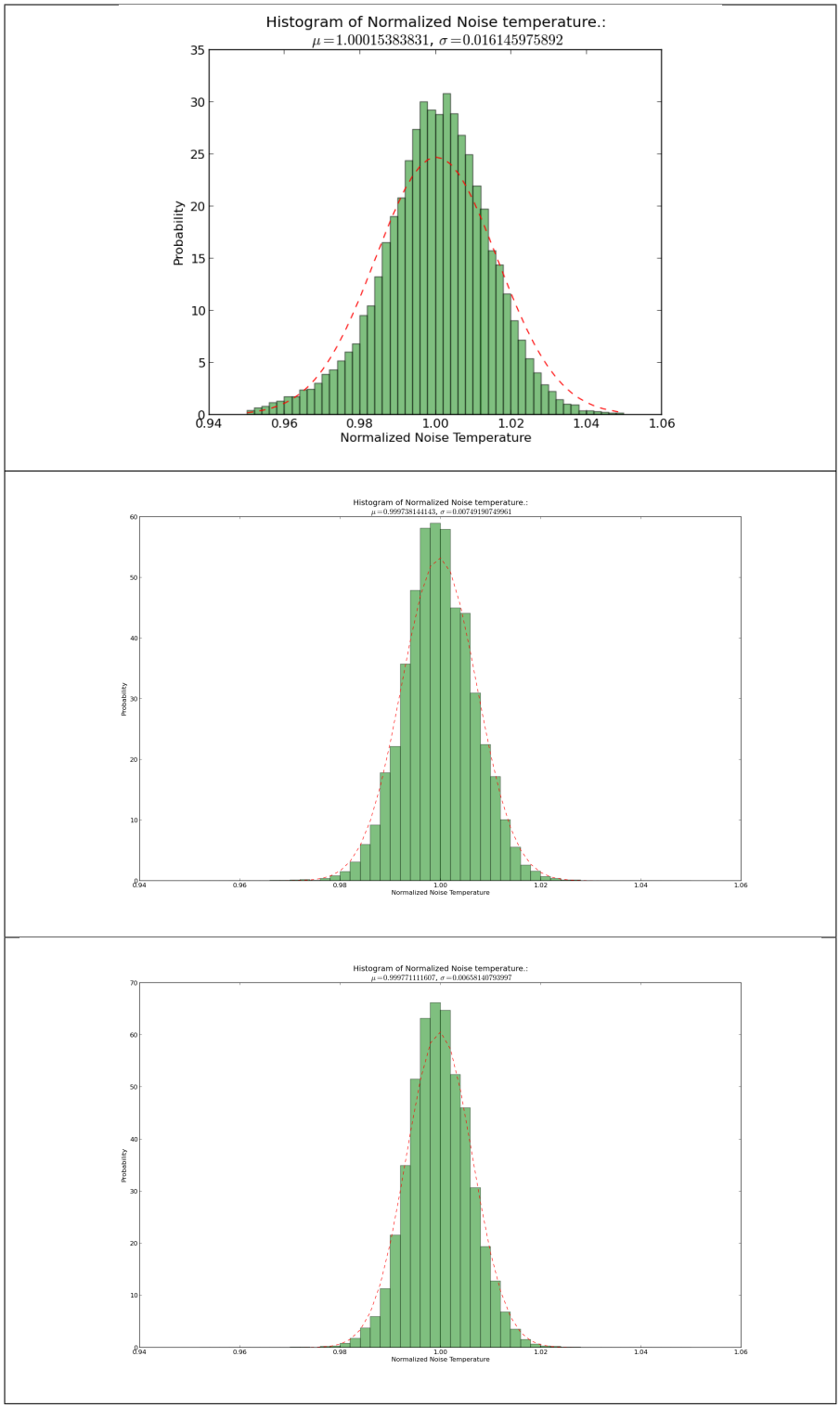

Figure 5-14: Effect of filter bandwidth on noise with average power normalized to 1

Table 5.3: Normalized standard deviation of noise with varying digital filter bandwidth (sec. 3.5.2) from data collected at Wardon Hill

Digital Filter Bandwidth (MHz)	Standard Deviation of normalized noise estimate	Standard Deviation of normalised noise estimates / Standard Deviation of normalised noise estimate with 0.5 MHz Digital Filter Bandwidth
0.5	0.0161	1
2	0.00749	2.14
4	0.00658	2.44

time is to reduce the standard deviation of the noise by a factor of approximately 2, as expected from eq. 5.4. This gain does not apply when the bandwidth is increased from four to eight times the long pulse bandwidth, due to the 5 MHz wide filters in the IF amplifier (figure 3-12). At baseband these are equivalent to 2.5 MHz filters, as they fold about zero frequency so the increase in sensitivity would a factor of $\sqrt{5} = 2.23$. The observed increase of 2.44 is likely to be caused by the slow fall-off with frequency that these filters have (figure 5-6), implying an equivalent bandwidth of 5.95 MHz.

As the full IF bandwidth is digitised, the possibility of adding a second digital down-conversion channel was considered. This could be tuned away from the 30 MHz IF signals so that it is insensitive to radar returns and only sample the noise. This would allow the noise to be integrated over the whole time that the transmitter is not firing. In practice, it is likely that some gating would have to be applied using the reflectivity signal, as the transmitted pulse has significant side-lobes (figure 3-6) which would give a biasing contribution to the noise during large storms. As such, this technique would probably not give significant benefit when it is most needed and was not investigated further.

Table 5.4: Effect of hardware optimization on radiometric sensitivity (Assuming 0.5 MHz bandwidth, 50 ms integration time and T_{ant}= 200 K)

Configuration	Radar Noise Factor	Radar Temperature (K)	Radar radiometric sensitivity (K)
Original	6.0	876	6.8
Low NF LNA	5.5	743	6.0
Low NF LNA fitted directly to waveguide coupler	4.5	531	4.6

Table 5.5: Effect of bandwidth on radar radiometric sensitivity (Assuming 531 K T_{sys}, 50 ms integration time and T_{ant}= 200 K)

Bandwidth (MHz)	Sensitivity (K)
0.5	4.6
2.0	2.3
3	1.9

Overall expected performance

Previous results are combined and shown in table 5.4 and 5.5. These show an overall improvement in radiometric sensitivity from 6.8 K to 1.9 K, a factor of 3.5.

In-situ measurements of receiver noise temperature

The receiver noise temperature was measured using the calibrated noise injection source over a number of dry days at Wardon Hill. The V channel shows good agreement with the theoretical value, showing an average temperature of 545 K. The H channel is not in such good agreement, with an average temperature of 668 K, indicating the presence of additional loss in that channel.

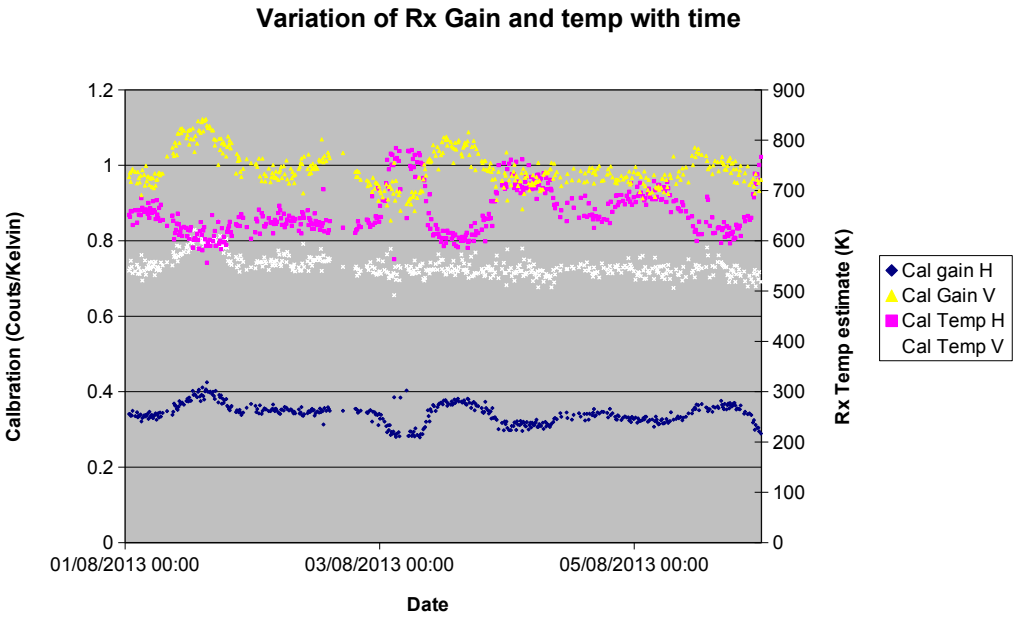

Figure 5-15: In-situ measurements of the receiver gain and estimated system temperature using the calibrated noise source, at Wardon Hill radar.

5.4 Opportunistic tipping curve measurements

To make accurate measurements of Z_{dr} any calibration offset between the two channels that will affect the calculation of Z_{dr} needs to be measured. This is done using data collected whilst pointing vertically. Here, it is expected that the mean Z_{dr} should be zero [115]. This is done regularly (every 10 mins.) to be sure that any rain events above the site are captured. In moving the antenna to make these scans the radar elevation sweeps from 0 to 90 degrees. This gives an opportunity to take a sample of the vertical noise structure. This motion is described as a pseudo-RHI scan. A true RHI is taken at a fixed azimuth, whereas these scans are completed while the radar is still rotating in azimuth.

5.4.1 Results from Tip Curve calibration

A tipping curve fit was calculated using noise data taken during a pseudo-RHI scan shown in figure 5-16. Above approximately 50 degrees from horizontal, the observations significantly deviate from the expected brightness profile. This may be caused by the effects of physical obstructions on the radome in the path of the beam, specifically the lightning conductor and air vent. While these obstacles do not occupy a large area relative to the antenna and therefore do not significantly attenuate the signal; relative to the very low (~5 K) background temperature, their physical temperature (~290 K) is significant. Applying equation 5.19 to the observed difference in brightness temperature when making measurements vertically, the additional attenuation is ~0.4 dB.

For the purposes of attempting a tipping curve calibration, strict restrictions are placed on the input data. Using the reflectivity signal, any bins with rain or clutter are automatically excluded; only data between 1.5 and 50 degrees above horizontal is used, to avoid contamination by low level clutter signals in sidelobes or beam blockages. This quality controlled data is then fitted to the theoretically calculated curve as shown in figure 5-17.

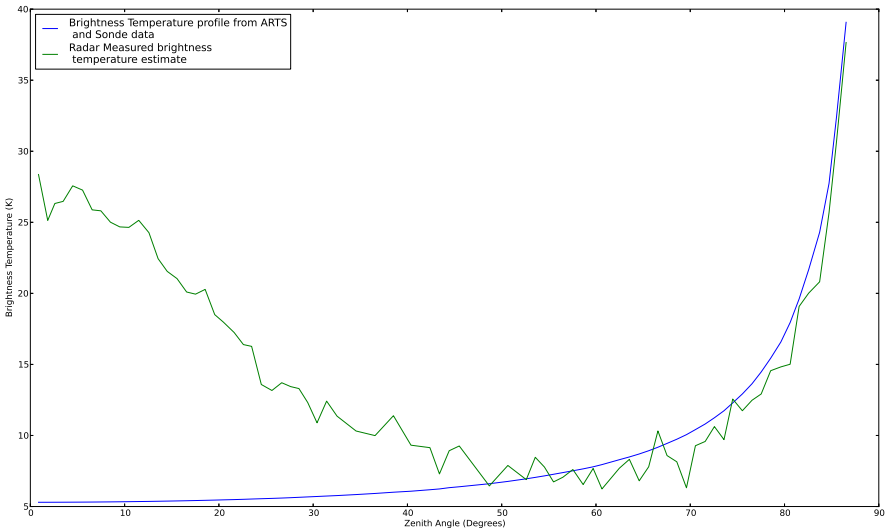

Figure 5-16: Pseudo-RHI tip curve showing the calculated atmospheric noise temperature profile and the measured brightness temperature profile. The effect of attenuation due to radome obstructions can be seen at high elevation angles.

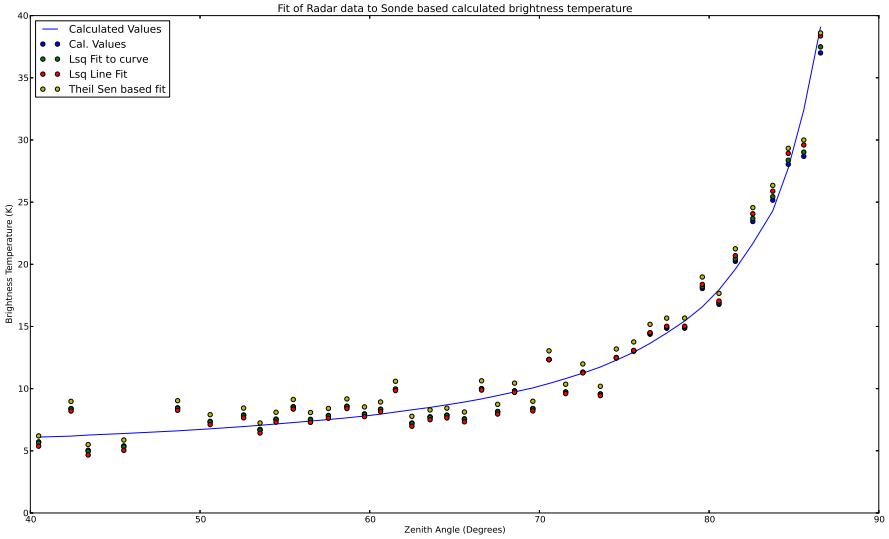

Figure 5-17: Elevation restricted tip curve fit

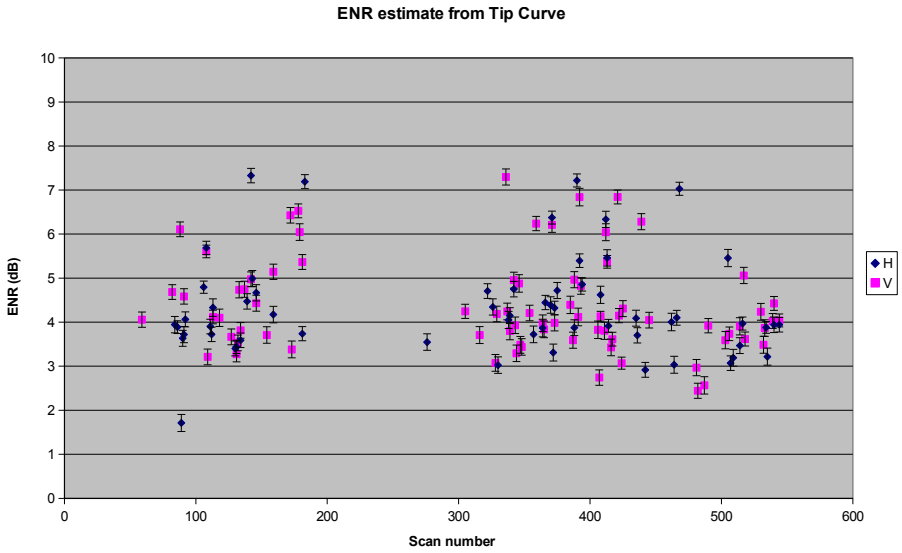

Figure 5-18: Estimate of the noise source ENR using from tipping curve

Although the fit is good, it leads to noisy values of ENR as shown (figure 5-18). Different types of fit were attempted including the Thiel-Sen estimator [116], which attempts to deal with noisy data with outliers, by fitting lines between all possible points pairs and selecting the median gradient, but this did not help improve the noisy ENR. It is thought that the noisy ENR is caused by the exponential nature of the tip curve profile (eq. 5.32). The estimated ENR shows a wide spread of values but the mean values were: H 4.31 dB with a standard deviation of 0.16 and V 4.36 dB with a standard deviation of 0.177.

A calibration was carried out to measure the loss in the signal path between the -30 dB injection coupler and the receiver. This was done by injecting signal at a range of relatively high power levels, to avoid noise effects, both at the coupler and directly into the receiver ports. The power injected at the receiver was -30 dB less than at the coupler and so any variation of the coupler from -30 dB would be included in the final measurement. Table 5.6shows the overall loss through the noise injection / calibration signal path, which totals 30.63 dB in the H channel and 30.52 dB in the V channel.

Table 5.6: Measurement of loss through T-R cell and circulator

Injected power	Via Coupler		Direct to Receiver		Loss (dB)	
(dBm)	H (dB)	V (dB)	H (dB)	V (dB)	H	V
-30	110.84	112.3	111.549	112.986	0.65	0.56
-40	100.9	102.42	101.5	102.92	0.60	0.50
-50	90.93	92.545	91.658	92.95	0.65	0.50
				Mean Loss	0.633±0.029	0.52±0.035

The H channel noise injection source has a calibrated ENR of 34.88 dB and the V channel noise injection source has a calibrated ENR of 34.74 dB. Including the loss through the coupler, circulator and TR cell this gives an ENR at the LNA input of H 4.25 dB and V 4.22 dB. This is in good agreement with the value estimated by the averaged tip curve (H 4.31dB, V 4.36 dB) suggesting that there is benefit to using this technique for long term calibration even though the shorter term results are too noisy to be of use.

5.5 Quality control of radiometric emissions data

An example of typical radiometric emissions data can be seen in figure 5-19. This image shows a number of data quality issues that should be dealt with before use of the data for attenuation correction purposes can be attempted.

The position of the sun is calculable and so its effect can be removed or used as a calibration source for Z_{dr} [117] or the pointing accuracy of the radar [118][119]. Radio Frequency interference is caused by the detection of transmissions from other sources such as wireless local area networks or other radars. As these represent active transmissions, they will typically present a radiometric noise temperature greater than the ambient temperature. This can then be used to filter the affected azimuths. Near field emissions due to beam blockages can be detected by producing climatology

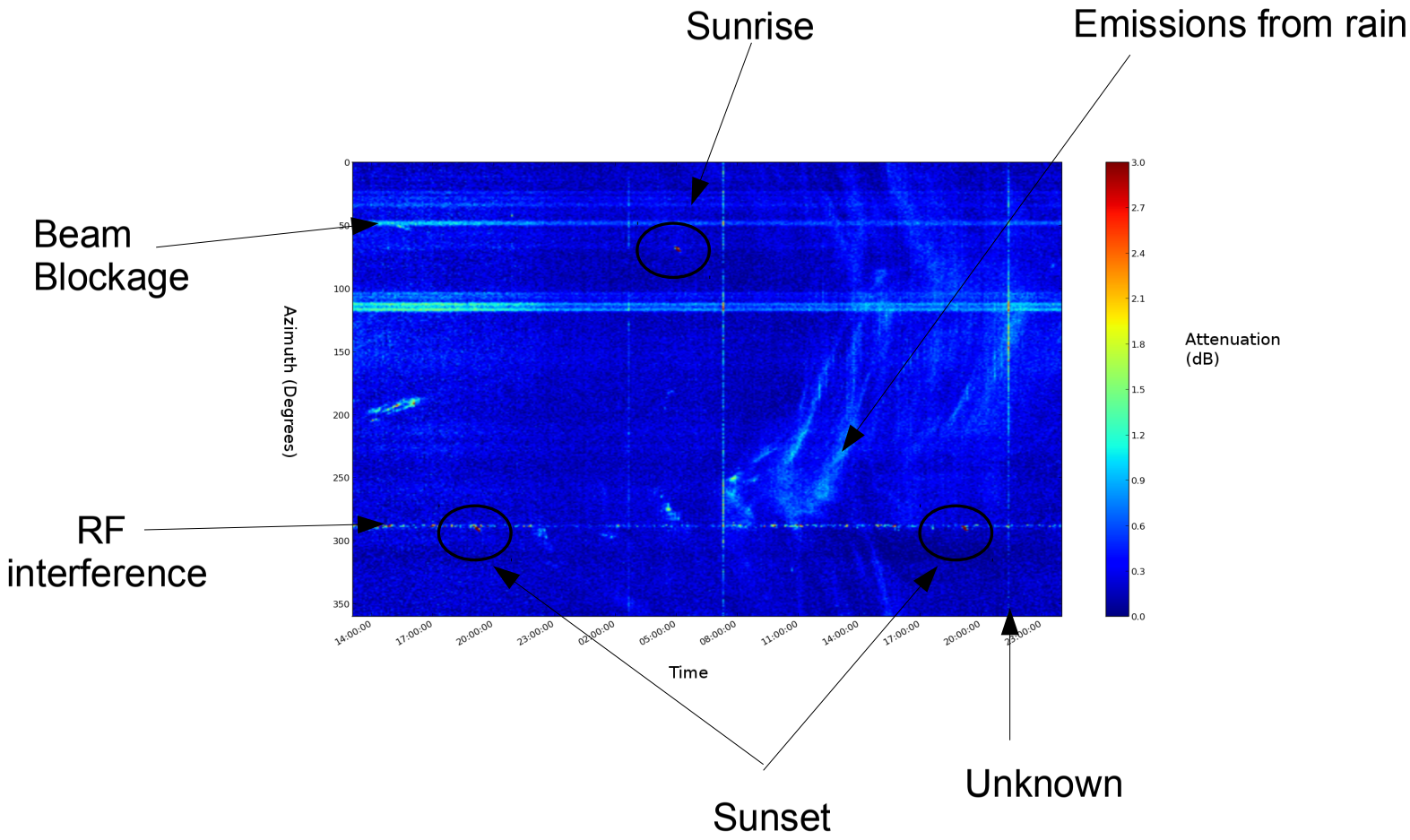

Figure 5-19: Time-series of attenuation derived from noise data showing possible sources of contamination

of the emissions on dry days from which a threshold value can be used to exclude the affected azimuths.

5.6 Comparison with other attenuation estimation methods

A comparison of the different techniques for estimating the PIA was carried out, to verify the skill of the emissions-based PIA estimator. Due to the availability of the radar and time constraints, only the 0.5 MHz bandwidth filter version was available, giving a radiometric sensitivity of 4.6 K and so a sensitivity to attenuation of approximately 0.5 dB; as such, the final performance of the technique should be superior to the results presented here.

The dual polarization data are filtered using a reflectivity-based threshold in order to remove noise; the texture of ϕ_{dp} and a threshold of ρ_{hv}> 0.95 are used to remove clutter; and the PIA calculated using the Hitschfield and Borden technique is used as a threshold on the other two estimators i.e. as a constraint that if there is no reflectivity, there is no attenuation. Azimuths that are known to experience partial beam blocking or are affected by RF interference are also excluded from the analysis, in order to allow for the calculation of meaningful statistics.

The ϕ_{dp} based estimate of PIA was calculated by estimating the phase values at the start and end of an area of rain along a ray, and applying a value of $\gamma = 0.0688$ dB/°[120]. The Z based estimate is based on the conventional Hitschfield and Borden correction as used in Radarnet; and the emissions based estimate uses a 10 K/dB estimate which should be valid in this case as the PIA does not exceed the 6 dB (two way) limit for which this approximation is valid.

A time series of the attenuation estimate along each azimuth, from each of the techniques to be evaluated was calculated. The time frame used

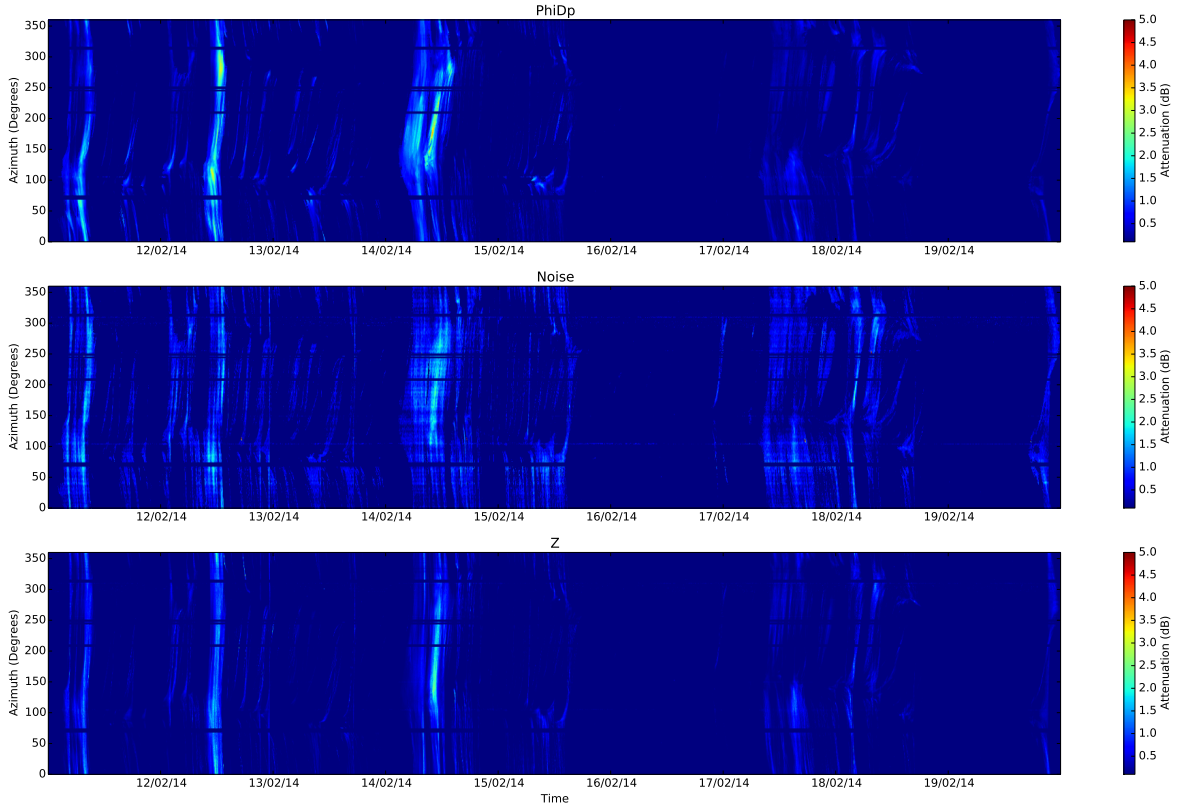

Figure 5-20: Path integrated attenuation estimated from ϕ_{dp} (Phi), Emissions (Noise) and Hitschfield and Borden from Z_h (Z) as measured at Wardon Hill radar from the 11th to the 20th of February 2014, at 1 degree elevation. The date is shown on the horizontal axis with the azimuth at which the PIA is being estimated is shown on the vertical, with scans being taken every 5 minutes, with azimuths affected by RF interference and beam blocking removed

covers a series of storms that occurred between the 11th and the 20th of February 2014 (figure 5-20). As can be seen, in general there is good agreement between the three attenuation estimation techniques with some variations. This agreement, in association with the fact that the ϕ_{dp} technique is based on phase, and so is calibration independent, suggests that both the reflectivity and radiometric estimate of PIA are well calibrated.

The attenuation estimates for the 14th February 2014 storm are shown in figure 5-21. As can be seen, while in general there is good agreement between the estimators, there is a tendency for ϕ_{dp} to over-estimate the attenuation and in some cases generate significant PIA where none is suggested by either of the other methods. This can be seen in both the scatter plots comparing the radiometric PIA estimate and ϕ_{dp} which have a Pearson correlation coefficient of 0.70 (figure 5-22), and Hitschfield and Borden and ϕ_{dp} estimates (figure 5-23), with a correlation of 0.64. However in general the Hitschfield and Borden and ϕ_{dp} comparison shows the largest spread of values.

The comparison between the estimates from Hitschfield and Borden and the radiometric measurements 5-24 show good agreement, particularly at higher values of PIA (correlation of 0.76), however the radiometric technique does appear to overestimate the PIA relative to Hitschfield and Borden at lower values of PIA. This could be due to the noise like nature of the radiometric method in combination with the radiometric attenuation sensitivity being only 0.5 dB, leading to a tendency to produce PIA up to that level, even when no attenuation is present.

The reason for the overestimation of PIA by ϕ_{dp} in this case can be seen in range-azimuth plots of the measured polarimetric variables (figure 5-25). It can be seen that there is an increase in ϕ_{dp} at long range in the affected azimuths (150 to 200 degrees), which is not associated with any significant reflectivity, and so unlikely to be true attenuation. Given the long range and relatively weak reflectivity, it is possible that the discrepancy is due to polarised ice crystals. While it might be hoped that ρ_{hv} could be used to give an indication of when abnormal propagation between two polarization

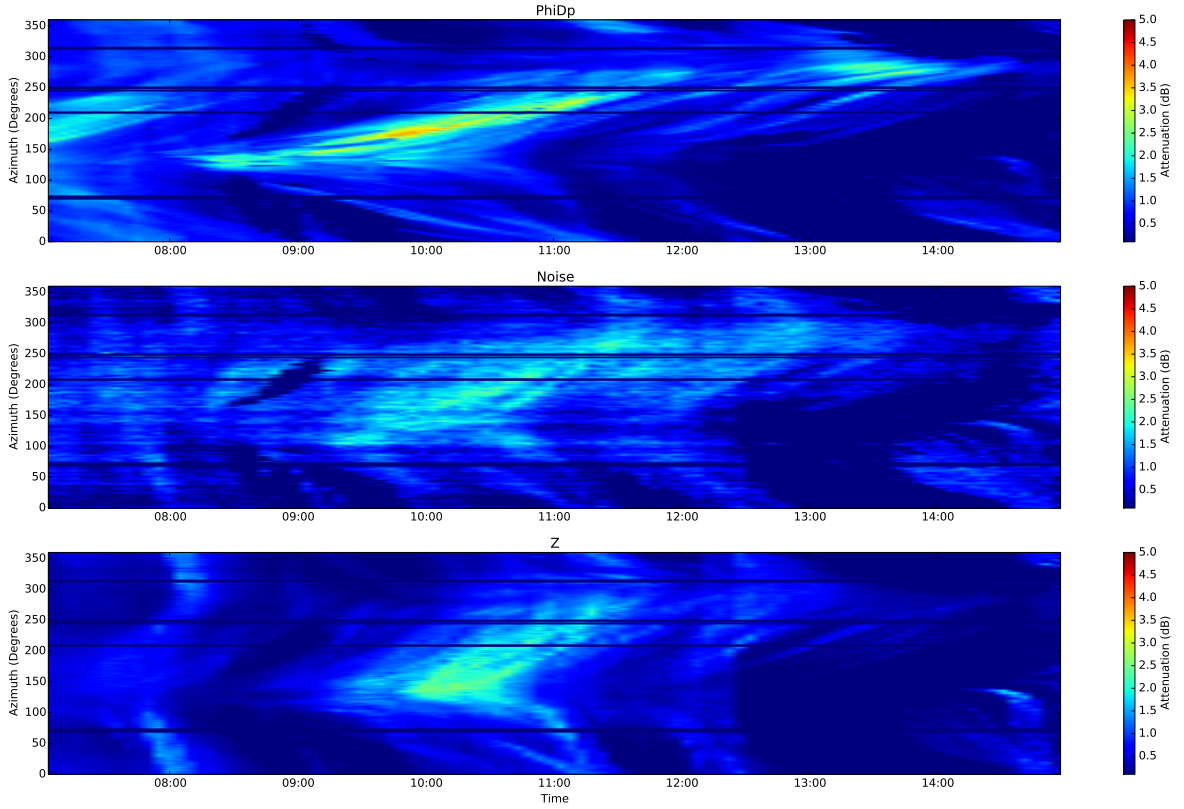

Figure 5-21: Path integrated attenuation estimated from ϕ_{dp} (Phi), Emissions (Noise) and Hitschfield and Borden from Z_h (Z) as measured at Wardon Hill radar on the 14th of February 2014 at 1 degree elevation. The time of day is shown on the horizontal axis with the azimuth at which the PIA is being estimated is shown on the vertical, with scans being taken every 5 minutes, with azimuths affected by RF interference and beam blocking removed

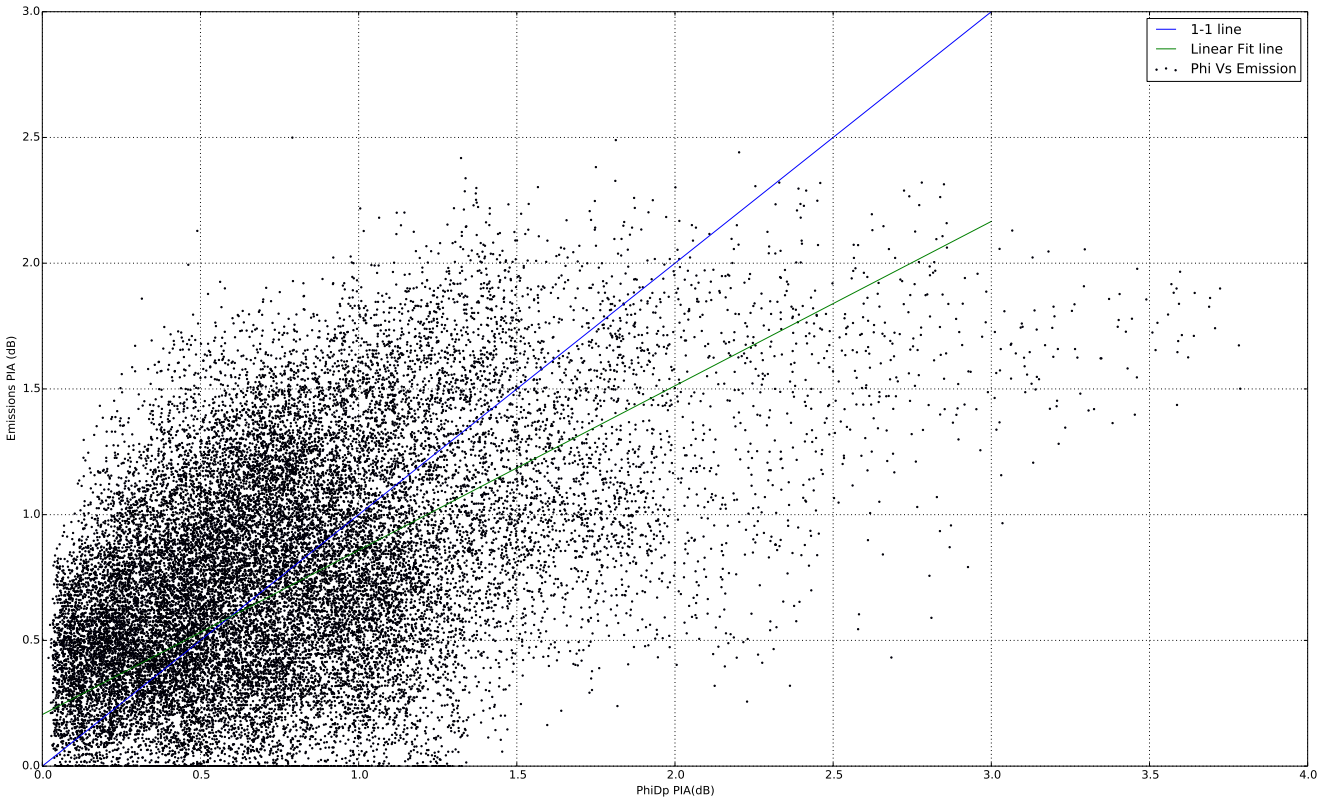

Figure 5-22: A scatter plot showing the estimate of PIA from the radiometric and ϕ_{dp} based measurements for the Feb 14th storm

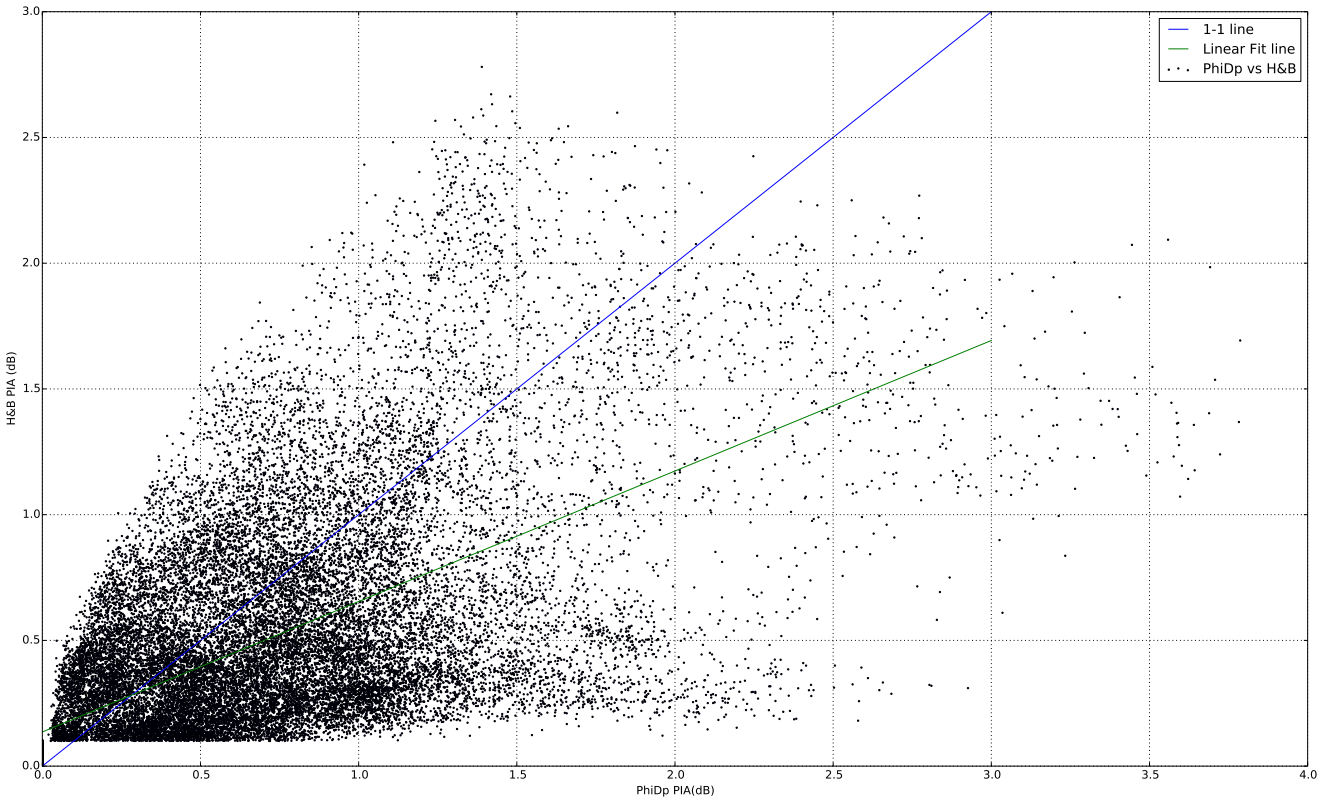

Figure 5-23: A scatter plot showing the estimate of PIA from the Hitschfield and Borden technique and ϕ_{dp} based measurements for the Feb 14th storm

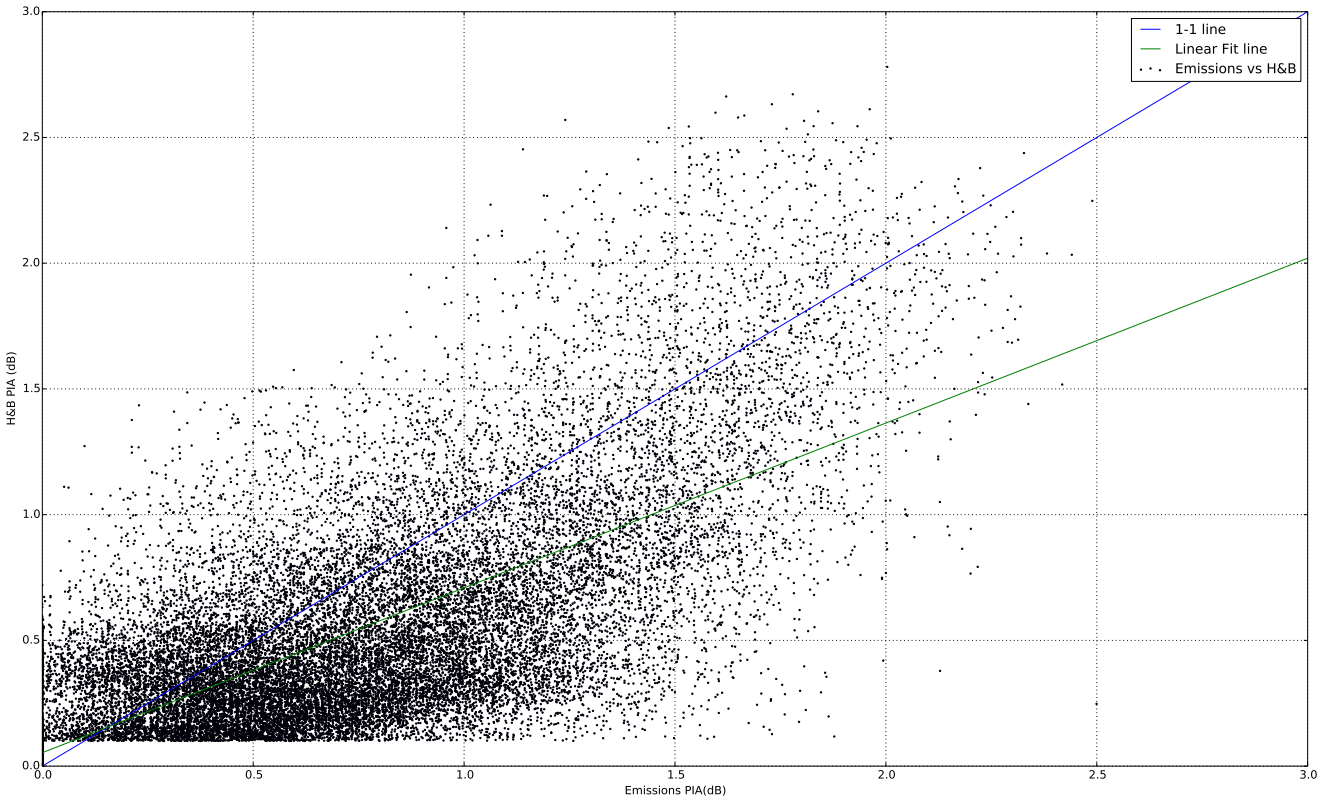

Figure 5-24: A scatter plot showing the estimate of PIA from the radiometric and Hitschfield and Borden based measurements for the Feb 14th storm

states is occurring, the fact that a threshold of 0.95 was used in this case suggests that this is not always sufficient, indicating another possible use for the radiometric estimate - as a quality control parameter for ϕ_{dp}.

5.7 Radiometric measurements for correction of beam blockages

While it was planned to test the technique for estimating the amount of beam blockage due to near-field obstacles using radiometric measurements from Wardon Hill radar, it quickly became apparent that the site was not suitable for this test due to a lack of blockages and the ones present causing almost complete attenuation of the beam. As such, a site with known beam blockage issues, Chenies, was chosen (figure 5-1). Unlike Wardon Hill, Chenies was not evaluated and optimized for the production of radiometric measurements, and so it was found that there was a significant discrepancy between the estimated and expected noise temperature, i.e. measured noise temperatures greater than the ambient temperature. This was found to be due to the noise injection source not producing the expected ENR. By using reflectivity accumulations as a reference, an approximate calibration was found and used to demonstrate the potential of method.

An advantage of using the radiometric technique rather than accumulations alone is that the majority of blockages are due to trees. As such, in the Spring and Autumn the degree of blockage can be changing on a time scale that seasonal accumulations cannot reflect.

An accumulation of reflectivity was produced and the mean reflectivity at each bin calculated for a period in Spring 2014 (figure 5-26). From this, the average reflectivity in each azimuth was calculated, avoiding any clutter remaining after the initial quality control by selecting range gates 150 to 400. A number of significantly attenuating blockages can be seen as dips in the range averaged values.

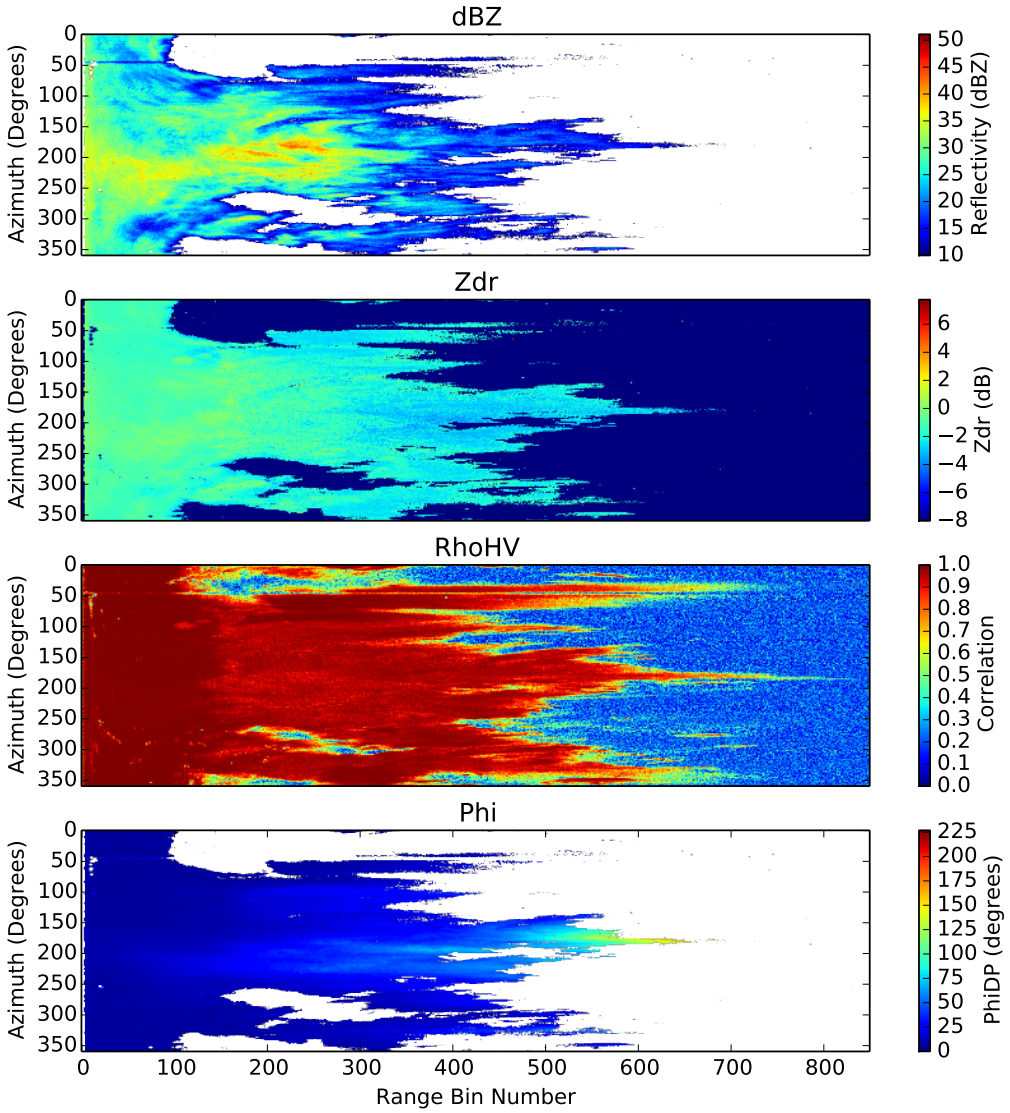

Figure 5-25: Data from Wardon Hill on 14th February 2014 1003 GMT showing (from top to bottom) the reflectivity, differential reflectivity, ρ_{hv} and ϕ_{dp}

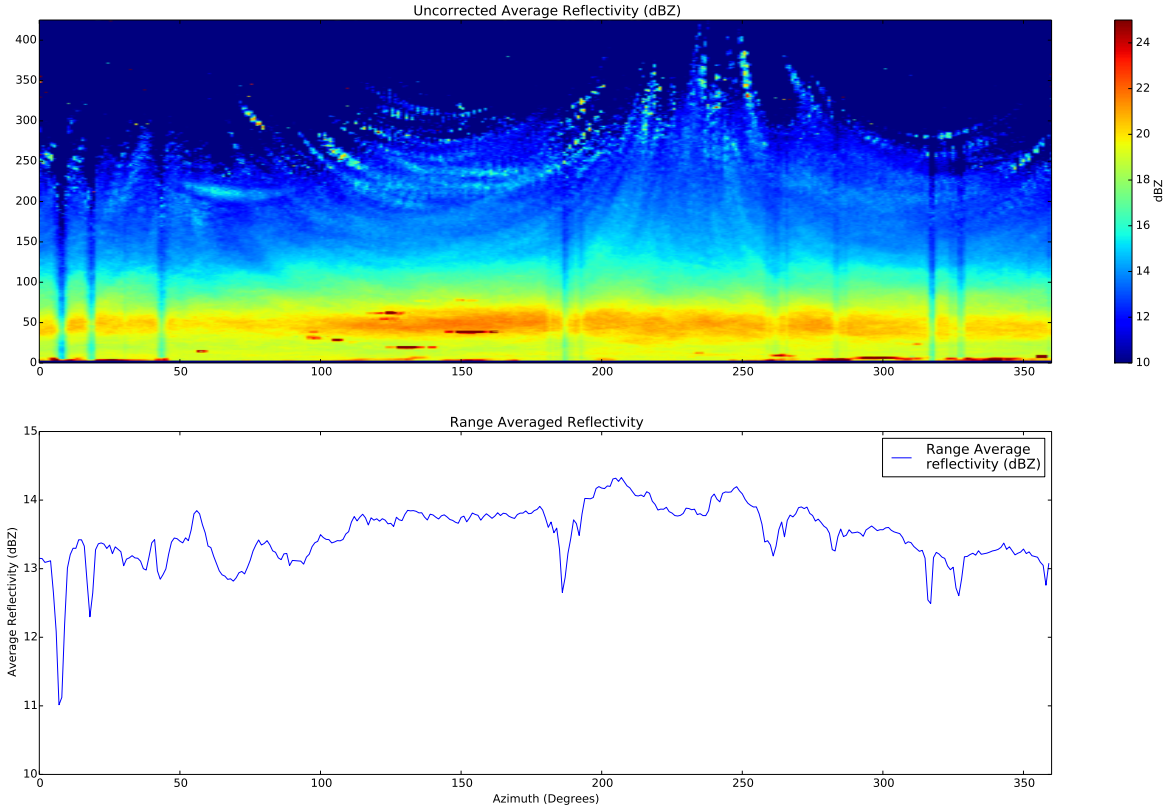

Figure 5-26: Mean accumulated reflectivity at 1 degree elevation from Chenies radar from Jan 1st to Jan 20th and the average reflectivity for each azimuth between range gates 150 and 400

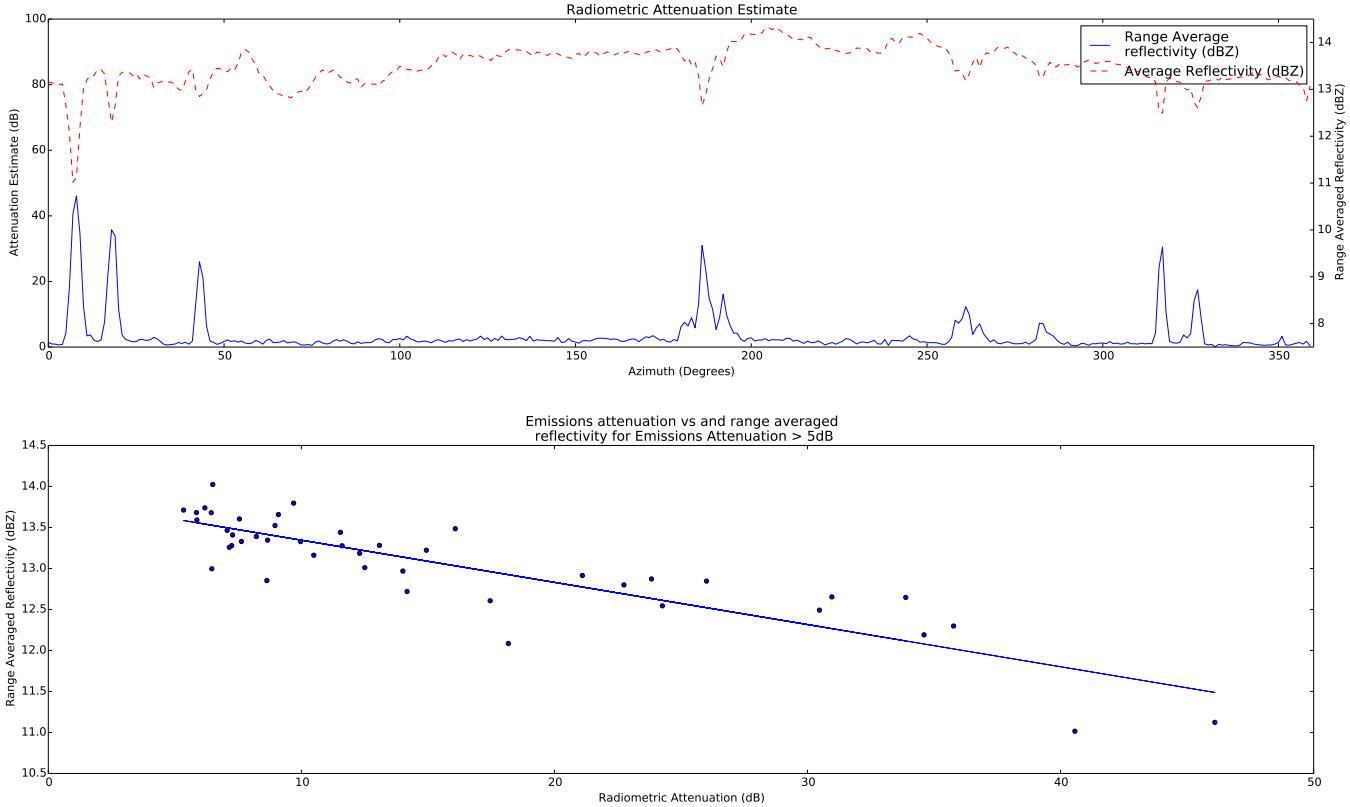

Figure 5-27: Top: Uncalibrated estimate of near-field attenuation from dry day radiometric emissions at 1 degree elevation from Chenies radar, plotted with the average reflectivity on a rainy, at each azimuth.
Bottom: Uncalibrated radiometric dry day, beam blocking attenuation estimate plotted as a function of range averaged rainy day reflectivity, where the radiometric attenuation estimate > 5 dB (uncalibrated)

When the radiometric attenuation estimate is plotted against the averaged reflectivity accumulation (figure 5-27) it can be seen that the pattern of attenuation estimates matches the accumulation very well, reproducing the inverse of the structures seen in the range averaged accumulation.

In order to estimate the calibration, the radiometric attenuation estimate was plotted against the accumulation for uncalibrated radiometric attenuation estimates greater than 5 dB. This gives a value of 0.181 to be applied to the radiometric estimate in order to match the accumulation estimate, with a correlation coefficient of 0.76.

The resulting calibrated radiometric attenuation estimate was then applied as a correction to the accumulations (figure 5-28). From this it can be seen that the character of the accumulations is much improved visually and that the averages are significantly smoother, with a reduction in standard deviation from 0.43 to 0.36.

The fact that the radiometric estimate of beam blocking had to be calibrated using the accumulations is disappointing, but that the radiometric estimate gives such a good match to the observed accumulated blockages is very encouraging, and suggests that the technique does have skill in detecting beam blockages.

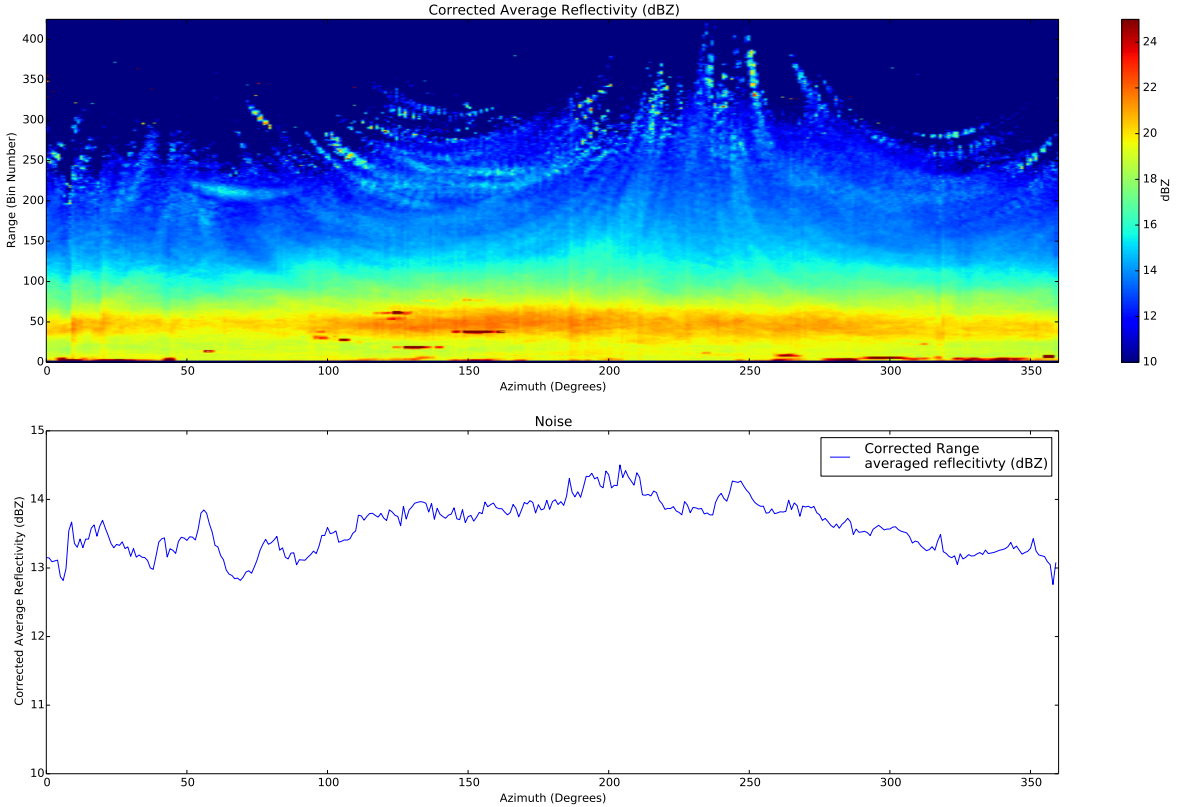

Figure 5-28: (Top) Azimuth-Range plot of mean accumulated reflectivity at 1 degree elevation from Chenies radar from Jan 1st to Jan 20th and (Bottom) the average reflectivity in range between range gates 150 and 400, both after correction using radiometric attenuation estimate calibrated using range average reflectivity

5.8 Summary

This chapter presents an introduction to radiometric measurements and the techniques that have been used to make accurate radiometric measurements with dedicated hardware. The suitability for making such measurements using radar hardware is evaluated and the benefits of applying optimizations in hardware and software to improve the radars suitability to make radiometric measurements is demonstrated.

The tip curve technique, used in the calibration of conventional radiometers, is described. Atmospheric brightness temperature profiles at C-band are calculated using radiosonde observations allowing the annual variation of atmospheric brightness with elevation and time of year to be estimated. It is show that it is sufficient to use a climatological profile of noise temperatures providing certain criteria are respected.

Potential challenges to making radiometric measurements, due to sources of emissions other than precipitation, are discussed and mitigations for these are proposed.

A comparison between estimators of PIA based on reflectivity, radiometric emissions and ϕ_{dp} is presented, and the benefits of radiometric PIA compared to ϕ_{dp} PIA demonstrated.

The possibility of using radiometric emissions to detect and correct for partial beam blocking is shown, however this represents a preliminary, uncalibrated demonstration. The technique is shown to have some skill in predicting beam blocking despite this drawback.

Chapter 6

Conclusions and Future Work

6.1 The Weather Radar Network Renewal project

The WRNR project had the aim of producing an updated radar for the UK Weather Radar network, with performance equal to or better than that of commercial offerings, at the same time as removing obsolescent hardware, and giving best value for money possible.

A summary of the performance of the Wardon Hill Radar is given in Table 6.1. When compared to the Thurnham dual polarisation evaluation radar (peak $\rho_{hv} = 0.97$ and peak Ldr -29 dB), Wardon Hill shows vastly superior performance.

The open source architecture of the Met Office radar allowed the selection of the best available components in a very cost-effective manner. This has led to the development of a weather radar comparable in quality to the best available research systems. For example, the CSU-CHILL National Weather Radar facility uses a 8.7 m antenna specifically engineered to optimise the cross-polar isolation by using a dual-offset feed Gregorian antenna design. The CSU_CHILL radar has an average cross polar isolation of -45 dB from range testing and side-lobes at -33 dB [74].

Table 6.1: Specifications of the WRNR weather radar

Half-power (3 dB) Beam-width	1.07 °
Antenna Type	Circular Parabolic Reflector
Antenna Gain	43 dBi typical
Peak Power	250 kW
Transmitter Type	Pulsed Magnetron
Transmitter Frequency	5.6 to 5.65 GHz (C-band)
Average Power	150 W
PRF	100 to 1200 Hz continuously variable
Range Resolution	75 m (for 0.5 μS pulse), 300 m (for $2\mu S$ pulse)
Receiver Noise Figure	3.0 dB
Receiver Dynamic Range	90 dB
Polarisation Capabilities (Transmit/Receive)	H/HV or HV/HV
Cross polar isolation	Antenna plot mean -42 dB System (Modal, in rain) -36.5 dB
Peak ρ_{hv}	0.997

As a result of this work, a flexible new processing and control system for UK weather radar network has been created, which due to full access to all stages of processing, acts as a platform from which, in collaboration with the research community, novel measurements can be made. This system has now been controlling all the Met Office weather radar for the last 5 years and recently including the Jersey Met Office radar at La Moye. A renewed dual polarisation radar has been designed and evaluated showing performance comparable to high quality research radars.

Obsolescence Issues As the old transmitter was particularly prone to failure, the CPI transmitter has been installed at all sites in advance of the roll-out of the full dual polarisation system. This is considered a “quick win” in terms of enabling useful Doppler radial winds to be collected from all sites, rather than just the ones that have the $0.5\mu S$ capable PFN. The early release will also increase the reliability of the operational network.

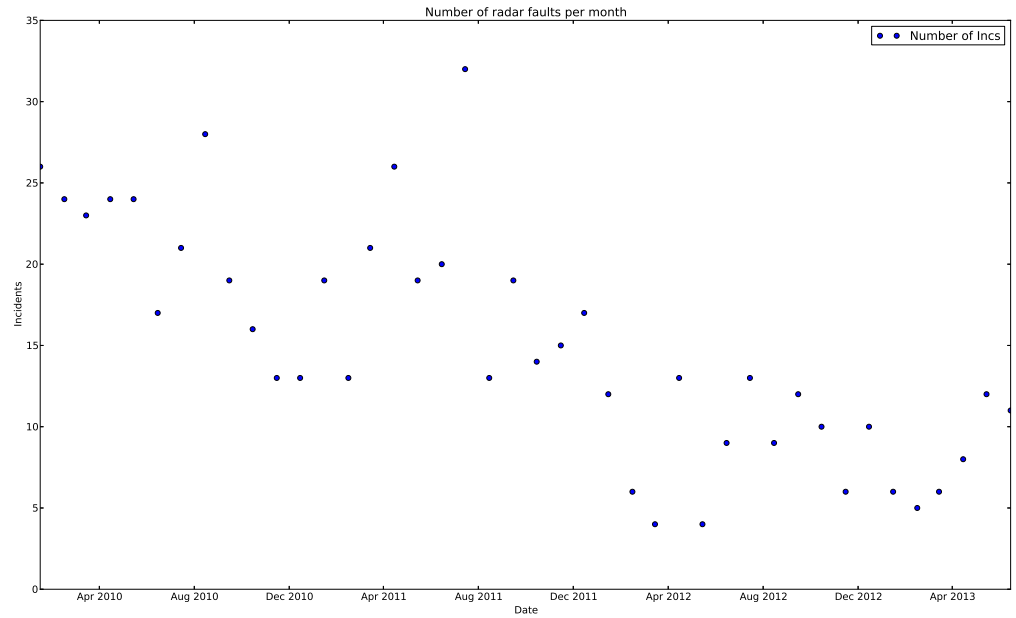

Figure 6-1: Radar faults per month since the beginning of the roll out of the new transmitter over the whole Met Office weather radar network.

The early roll-out of the new transmitter was possible due to the modular, hardware auto-sensing, nature of the Cyclops processing system and the relatively standalone nature of the transmitter. This has been very successful in reducing the maintenance burden of the network as can be seen in figure 6-1 which shows the number of times a problem with a radar has been recorded in recent years.

Towards the end of the design project, the owner of Hunt Engineering decided to close the company thus introducing a new obsolescence risk to the UK weather radar network. A review of the market was undertaken and a data acquisition system from Pentek was sourced. The Pentek data acquisition system provides 4 channels of 200 MSPS 16 bit ADC, with 40 bits of digital I/O, controlled by a single Xilinx Virtex-6 FPGA. Due to the hardware abstraction approach taken in the Cyclops software design this was relatively quickly integrated into the receiver and now forms the basis for ongoing development.

Current status of the Weather Radar Network Renewal Project The work described previously has lead to a high quality, flexible radar processing system, which is able to control both original and renewed hardware. Cyclops-D/P is now responsible for the radar control and signal processing at all Met Office radar sites and also the Jersey Met Office radar at La Moye. All Met Office sites now have a new transmitter which enables them to produce Doppler radial wind data. This data is currently being evaluated by the Met Office data assimilation group before the assimilation of radial winds from each site into operational NWP can commence.

Three Met Office radar sites have been fully upgraded to the dual polarisation system, in addition to the research and development site at Wardon Hill. These sites have gained Met Office operational acceptance and are contributing data to the Met Office rain rate composite. Projects are now underway to develop, evaluate and implement algorithms to make use of the dual polarisation moments for improved QPE and hydrometeor classification.

6.2 Refractivity from Magnetron Radars

As part of this work, the UK weather radar network was adapted to produce single polarization phase measurements in order to derive refractivity estimates. The evaluation of the quality of these refractivity estimates formed the basis of a Ph.D. by Dr K. Bartholomew [121]. The refractivity measurements from radar were compared with surface observations and NWP derived fields. It was found that when compared against surface observations the daily correlations of hourly refractivity changes from radar refractivity consistently out-perform the NWP estimate. When comparing the component fields of the model that go to make up refractivity against surface observations, the correlation is found to be 0.55 for temperature, 0.61 for pressure but only 0.13 for humidity [122] which suggests that humidity is not well represented within the model, and that the radar refractivity measurements will be a valuable new source of information. This comparison showed that on sunny Summer days the minute to minute variability

of the surface observations of refractivity could be up to 3 N units, possibly accounting for some of the discrepancy between the two observing types, however despite this, radar refractivity estimates were shown to have an error of between 0.7 and 1.4 N units within 30 km of the radar.

The possibility of making dual polarisation refractivity measurements has been demonstrated, showing that by combining the results from both polarization states by choosing the refractivity estimate derived from the pixel with the lowest local standard deviation of phase, correlation with area mean observations is slightly improved. This suggests that there is additional information to be gained by using the two different polarizations and that the use of the consistency of the local phase measurements provides some information about quality of the phase measurements.

The application of dual PRF scans to deliberately frequency modulate a magnetron, in order to try to measure the target position within the range gate for the reduction of errors and biases in refractivity measurements is described. It is shown that it is possible to produce a consistent frequency shift by varying the PRF, the application of this to improve refractivity measurements was not demonstrated.

6.3 Use of radars for radiometric measurements

The radar hardware was adapted to optimise its use as what is thought to be the first combined dual polarization weather radar and radiometer, without degrading any of its functionality as a weather radar. It has been shown that the radar radiometric sensitivity can be improved by a factor of 3.5; from 6.8 K to 1.9 K. This leads to an improvement in sensitivity to attenuation from approximately 0.7 dB to 0.2 dB.

With the use of radiosonde data as an input to the ARTS radiative transfer code the seasonal variation in background brightness temperature profiles was calculated at C band. This lead to the conclusion that with restrictions, a climatological profile of brightness temperature can be used for tip curve

calibration, for long term stability monitoring. A pseudo RHI based tip curve technique has been developed which makes opportunistic use of pre-existing scan patterns to calibrate the radiometric measurements. The resulting tip curve calibration was found to be noisy but potentially useful for longer term stability monitoring.

When comparing the PIA from three very different measurement techniques: directly from radiometric emissions, from range based integrations of attenuation estimated from rain rates derived from reflectivity measurements, and from phase differences in orthogonal polarizations due to propagation differences, it is seen that while in general there is good agreement between the different methods, the ϕ_{dp} based estimate can be contaminated by abnormal propagation effects. While it might conventionally have been thought that using a threshold of ρ_{hv} >0.95 would be sufficient to avoid such effects it has been shown that this is not the case, suggesting that additional quality control measures, such as use of the radiometric PIA estimate to indicate when abnormal propagation is occurring, would be beneficial when deriving QPEs.

Comparison of radiometric measurements with Hitschfield and Borden based attenuation estimates give a good correlation, suggesting that both are well calibrated. It was not possible to show an event in which the Hitschfield and Borden estimate had to be capped or seemingly became numerically unstable, perhaps due to the stratiform nature of the events evaluated. It is more likely that this will be an issue in higher intensity, convective events.

The potential to use the radiometric measurements on dry days to estimate partial beam blocking was demonstrated and seen to have skill in qualitatively predicting the degree of attenuation due to near by objects.

6.4 Future work

The continued development of Cyclops is planned, with a project being initiated to investigate the suitability of using Cyclops as a wind profiler processing and control system.

To truly demonstrate the benefit of the refractivity measurements to NWP, observation operators should be developed to model the radar refractivity fields in order for them to be assimilated into the model. Comparisons can then be done between model runs with and without radar refractivity and any improvement in forecasts quantified.

The RAINGAIN project aims to generate high resolution (100 m scale) radar data as an input to street-scale hydrological models. As part of the RAINGAIN project, the benefits of oversampling and whitening, or oversampling and range deconvolution, via the RETRO algorithm, are to be investigated. The possible benefits to refractivity measurement from oversampling and deconvolution, in order to reduce the effects of mismatches between the range gate centre and the clutter target location should be investigated.

The radiometric measurements should be developed to incorporate filter bandwidth switching and the improvement in the PIA estimates evaluated, preferably during the summer when convective storms are more frequent, and so the merits of the radiometric measurements compared to, what would represent difficult conditions for Hitschfield and Borden, can be seen. The possibility of comparing the attenuation correction against attenuation measurements from microwave links should be investigated.

In order to evaluate the benefits of this technique for QPE, an attenuation scheme that makes use of this data, such as that suggested in [123], should be implemented and incorporated into the Radarnet central processing system. This could include the use of enhanced ϕ_{dp} schemes, using radiometric measurements to detect abnormal propagation effects. Comparison of the QPEs against rain gauge measurements of rainfall accumulation can then be carried out in order to quantify the benefits to end users.

At a site with a significant partial beam blocking problem such as Chenies, the improvements and measurements to quantify noise performance that were made at Wardon Hill should be repeated and a radiometrically accurate measurement of the noise temperature of near-by beam blocking objects should be made. This should be compared to the estimates from reflectivity accumulations to determine whether the method has quantitative skill in estimating the attenuation due to partial beam blocking.

In recent years there has been a resurgence of interest in X-band weather radar e.g. the CASA [90] and RAINGAIN[124] projects. This can probably be traced to the introduction of dual polarisation technology, which brings with it the promise of attenuation corrections to reflectivity using ϕ_{dp} or the use of calibration independent rain-rate estimates, such as those derived from K_{dp}. Where previously at X-band the rain rate estimates were unreliable due to the greater attenuation, by applying these techniques, within a limited range, X-band radar becomes a useful tool. The greater attenuation at this frequency, relative to C-band, means that the accuracy of the radiometric attenuation estimates should be better than at C-band and so it would be interesting to investigate the performance of the radiometric measurements at X-band.

References

[1] L. Lemon, "Operational uses of velocity spectrum width data," in *International Conference on Radar Meteorology, 29 th, Montreal, Canada*, pp. 776–779, 1999.

[2] F. Fabry, C. Frush, I. Zawadzki, and A. Kilambi, "Extraction of near-surface index of refraction using radar phase measurements from ground targets," in *Antennas and Propagation Society International Symposium, 1997. IEEE., 1997 Digest*, vol. 4, pp. 2625–2628, IEEE, 1997.

[3] M. S. Buban, C. L. Ziegler, E. N. Rasmussen, and Y. P. Richardson, "The dryline on 22 may 2002 during ihop: Ground-radar and in situ data analyses of the dryline and boundary layer evolution," *Monthly Weather Review*, vol. 135, pp. 2473–2505, July 2007.

[4] R. Roberts, F. Fabry, P. Kennedy, E. Nelson, J. Wilson, N. Rehak, J. Fritz, V. Chandrasekar, J. Braun, J. J. Sun, *et al.*, "REFRACTT 2006: Real-time retrieval of high-resolution, low-level moisture fields from operational NEXRAD and research radars," *Bulletin of the American Meteorological Society*, vol. 89, no. 10, pp. 1535–1548, 2008.

[5] L. Bengtsson, M. Ghil, and E. Källén, *Dynamic meteorology: data assimilation methods*, vol. 36. Springer, 1981.

[6] M. Ghil and P. Malanotte-Rizzoli, "Data assimilation in meteorology and oceanography," *Adv. Geophys*, vol. 33, pp. 141–266, 1991.

[7] A. Lorenc, S. Ballard, R. Bell, N. Ingleby, P. Andrews, D. Barker, J. Bray, A. Clayton, T. Dalby, D. Li, *et al.*, "The met. office global three-dimensional variational data assimilation scheme," *Quarterly Journal of the Royal Meteorological Society*, vol. 126, no. 570, pp. 2991–3012, 2000.

[8] F. Rawlins, S. Ballard, K. Bovis, A. Clayton, D. Li, G. Inverarity, A. Lorenc, and T. Payne, "The met office global four-dimensional variational data assimilation scheme," *Quarterly Journal of the Royal Meteorological Society*, vol. 133, no. 623, pp. 347–362, 2007.

[9] O. Talagrand, "Assimilation of observations, an introduction," *JOURNAL-METEOROLOGICAL SOCIETY OF JAPAN SERIES 2*, vol. 75, pp. 81–99, 1997.

[10] C. Jones and B. Macpherson, "A latent heat nudging scheme for the assimilation of precipitation data into an operational mesoscale model," *Meteorological Applications*, vol. 4, no. 3, pp. 269–277, 1997.

[11] P. Meischner, *Weather radar: principles and advanced applications*. Springer Verlag, 2004.

[12] P. Alberoni, V. Ducrocq, G. Gregoric, G. Haase, I. Holleman, M. Lindskog, B. Macpherson, M. Nuret, and A. Rossa, "Quality and assimilation of radar data for NWP–a review," *COST-717 report*, 2003.

[13] J. Sun, "Convective-scale assimilation of radar data: progress and challenges," *Quarterly Journal of the Royal Meteorological Society*, vol. 131, no. 613, pp. 3439–3463, 2005.

[14] A. Illingworth, "Improved precipitation rates and data quality by using polarimetric measurements," in *Weather Radar* (P. Meischner, ed.), Physics of Earth and Space Environments, pp. 130–166, Springer Berlin Heidelberg, 2004.

[15] M. Balaji, J. R. Ellis, W. H. Walker, D. R. Cartwright, J. H. Lee, J. Romines, and M. Balaji, "An engineering illustration of the dual polarization upgrade for the WSR-88D," 2012.

[16] J. J. Gourley, P. Tabary, and J. P. du Chatelet, "Data quality of the Meteo-France C-band polarimetric radar," *Journal of Atmospheric and Oceanic Technology*, vol. 23, no. 10, pp. 1340–1356, 2006. doi: 10.1175/JTECH1912.1.

[17] M. Bevis, S. Businger, T. Herring, C. Rocken, R. Anthes, and R. Ware, "GPS meteorology- remote sensing of atmospheric water vapor using the global positioning system," *Journal of Geophysical Research*, vol. 97, no. D14, pp. 15787–15801, 1992.

[18] F. Fabry and C. Creese, "If fine lines fail, try ground targets," in *International Conference on Radar Meteorology, 29 th, Montreal, Canada*, pp. 21–23, 1999.

[19] W. Hitschfeld and J. Bordan, "Errors inherent in the radar measurement of rainfall at attenuating wavelengths," *Journal of Meteorology*, vol. 11, pp. 58–67, Feb. 1954.

[20] P. Hildebrand, "Iterative correction for attenuation of 5 cm radar in rain.," *Journal of Applied Meteorology*, vol. 17, pp. 508–514, 1978.

[21] D. Harrison, S. Driscoll, and M. Kitchen, "Improving precipitation estimates from weather radar using quality control and correction techniques," *Meteorological Applications*, vol. 7, no. 2, pp. 135–144, 2000.

[22] F. Fabry, "Using radars as radiometers: Promises and pitfalls.," in *30th Int. Conf. on Radar Meteorology,*, vol. preprints, (Munich, Germany), pp. 197–198, American Meteorological Society, 2001.

[23] R. Dicke, "The measurement of thermal radiation at microwave frequencies," *Review of Scientific Instruments*, vol. 17, no. 7, pp. 268–275, 1946.

[24] D. C. Hogg, "Rain, radiometry, and radar," *Geoscience and Remote Sensing, IEEE Transactions on*, vol. 27, no. 5, pp. 576–585, 1989.

[25] J. Tan, D. H. O. Bebbington, and A. Holt, "Theoretical studies of differential propagation phase shift in meteorological polarization diversity

radars at centimeter wavelengths," in *Antennas and Propagation, 1991. ICAP 91., Seventh International Conference on (IEE)*, pp. 95–98 vol.1, Apr 1991.

[26] J. Tan, J. W. F. Goddard, and M. Thurai, "Applications of differential propagation phase in polarisation-diversity radars at s-band and c-band," in *Antennas and Propagation, 1995., Ninth International Conference on (Conf. Publ. No. 407)*, vol. 2, pp. 336–341 vol.2, Apr 1995.

[27] F. Merceret and J. Ward, "Attenuation of weather radar signals due to wetting of the radome by rainwater or incomplete filling of the beam volume," *NASA/TM-2002-211171, NASA/YA-D, Kennedy Space Center, FL, 32899*, 2002.

[28] R. Thompson, A. Illingworth, and J. Ovens, "Emission: a simple new technique to correct rainfall estimates from attenuation due to both the radome and heavy rainfall.," *Proc. International Symposium on Weather Radar and Hydrology (WRaH 2011)*, pp. 39–44, Apr 2012.

[29] T. Smyth and A. Illingworth, "Correction for attenuation of radar reflectivity using polarization data," *Quarterly Journal of the Royal Meteorological Society*, vol. 124, no. 551, pp. 2393–2415, 1998.

[30] P. Tabary, G. Vulpiani, J. J. Gourley, A. J. Illingworth, R. J. Thompson, and O. Bousquet, "Unusually high differential attenuation at c band: Results from a two-year analysis of the french trappes polarimetric radar data," *J. Appl. Meteor. Climatol.*, vol. 48, pp. 2037–2053, Oct. 2009.

[31] Y. Han and E. Westwater, "Analysis and improvement of tipping calibration for ground-based microwave radiometers," *Geoscience and Remote Sensing, IEEE Transactions on*, vol. 38, no. 3, pp. 1260–1276, 2000.

[32] V. Bringi and V. Chandrasekar, *Polarimetric Doppler weather radar: principles and applications*. Cambridge University Press, 2001.

[33] R. J. Doviak and D. S. Zrnic, *Doppler radar and weather observations*. Courier Dover Publications, 1993.

[34] M. I. Skolnik, *Introduction to radar systems*. McGraw-hill New York, 2001.

[35] D. S. Zrnic, "Estimation of spectral moments for weather echoes," *Geoscience Electronics, IEEE Transactions on*, vol. 17, no. 4, pp. 113–128, 1979.

[36] S. Silver, *Microwave antenna theory and design*, vol. 19. Inspec/Iee, 1984.

[37] J. Probert-Jones, "The radar equation in meteorology," *Quarterly Journal of the Royal Meteorological Society*, vol. 88, no. 378, pp. 485–495, 1962.

[38] H. C. Hulst and H. C. van de Hulst, *Light scattering: by small particles*. Courier Dover Publications, 1957.

[39] A. Illingworth and T. Blackman, "The need to represent raindrop size spectra as normalized gamma distributions for the interpretation of polarization radar observations," *Journal of Applied Meteorology*, vol. 41, no. 3, pp. 286–297, 2002.

[40] J. Marshall and W. Palmer, "The distribution of raindrops with size," *Journal of Meteorology*, vol. 5, no. 4, pp. 165–166, 1948.

[41] J. Marshall, W. Hitschfeld, and K. Gunn, "Advances in radar weather," *Advances in Geophysics*, vol. 2, pp. 1–56, 1955.

[42] T. Dazhang, S. Geotis, and R. Passarelli, "Evaluation of an alternating-PRF method for extending the range of unambiguous doppler velocity," in *Conference on Radar Meteorology, 22 nd, Zurich, Switzerland*, pp. 523–527, 1984.

[43] E. Dounce and G. Morris, "Digital phase correction for coherent-on-receive pulsed radar system," June 13 1978. US Patent 4,095,224.

[44] P. Mahapatra and D. Zrnic, "Practical algorithms for mean velocity estimation in pulse doppler weather radars using a small number of samples," *Geoscience and Remote Sensing, IEEE Transactions on*, no. 4, pp. 491–501, 1983.

[45] D. Zrnic, "Spectral moment estimates from correlated pulse pairs," *Aerospace and Electronic Systems, IEEE Transactions on*, vol. AES-13, pp. 344–354, July 1977.

[46] P. Joe and P. May, "Correction of dual PRF velocity errors for operational doppler weather radars," *Journal of Atmospheric and Oceanic Technology*, vol. 20, no. 4, pp. 429–442, 2003.

[47] I. Holleman and H. Beekhuis, "Analysis and correction of dual PRF velocity data," *Journal of Atmospheric and Oceanic Technology*, vol. 20, no. 4, pp. 443–453, 2003.

[48] J. Sugier, J. du Chatelet, P. Roquain, and A. Smith, "Detection and removal of clutter and anaprop in radar data using a statistical scheme based on echo fluctuation," *Proceedings of ERAD*, pp. 17–24, 2002.

[49] J. C. Hubbert, M. Dixon, S. M. Ellis, and G. Meymaris, "Weather radar ground clutter. part i: Identification, modeling, and simulation," *J. Atmos. Oceanic Technol.*, vol. 26, pp. 1165–1180, July 2009.

[50] J. Nicol, A. Illingworth, T. Darlington, and J. Sugier, "Techniques for improving ground clutter identification," in *Proc. Symp. Weather Radar Hydrol., Exeter, UK*, 2011.

[51] K. V. Beard and C. Chuang, "A new model for the equilibrium shape of raindrops," *J. Atmos. Sci.*, vol. 44, pp. 1509–1524, June 1987.

[52] M. Sachidananda and D. Zrnic, "Rain rate estimates from differential polarization measurements," *Journal of Atmospheric and Oceanic Technology*, vol. 4, no. 4, pp. 588–598, 1987.

[53] M. Rico-Ramirez and I. Cluckie, "Classification of ground clutter and anomalous propagation using dual-polarization weather radar,"

Geoscience and Remote Sensing, IEEE Transactions on, vol. 46, no. 7, pp. 1892–1904, 2008.

[54] V. Lakshmanan, C. Karstens, J. Krause, and L. Tang, "Quality control of weather radar data using polarimetric variables," *J. Atm. Ocea. Tech*, 2013.

[55] K. Friedrich, U. Germann, and P. Tabary, "Influence of ground clutter contamination on polarimetric radar parameters," *J. Atmos. Oceanic Technol.*, vol. 26, pp. 251–269, Feb. 2009.

[56] J. Goddard, J. Tan, and M. Thuari, "Technique for calibration of meteorological radars using differential phase," *Electronics Letters*, vol. 30, p. 166, 1994.

[57] R. J. Thompson, *Rainfall Estimation Using Polarmetric Weather Radar*. PhD thesis, University of Reading, January 2007.

[58] J. Testud, E. Le Bouar, E. Obligis, and M. Ali-Mehenni, "The rain profiling algorithm applied to polarimetric weather radar," *J. Atmos. Oceanic Technol.*, vol. 17, pp. 332–356, Mar. 2000.

[59] V. Melnikov and D. Zrnic, "Simultaneous transmission mode for the palarimetric WSR-88D: Statistical biases and standard deviations of polarimetric variables.," Tech. Rep. 84 pp., NOAA/NSSL, 2004. SHV_statistics.pdf.

[60] D. Brunkow, V. N. Bringi, P. C. Kennedy, S. A. Rutledge, V. Chandrasekar, E. A. Mueller, and R. K. Bowie, "A description of the csu-chill national radar facility," *J. Atmos. Oceanic Technol.*, vol. 17, pp. 1596–1608, Dec. 2000.

[61] J. C. Hubbert, S. M. Ellis, M. Dixon, and G. Meymaris, "Modeling, error analysis, and evaluation of dual-polarization variables obtained from simultaneous horizontal and vertical polarization transmit radar. part i: Modeling and antenna errors," *J. Atmos. Oceanic Technol.*, vol. 27, pp. 1583–1598, May 2010.

[62] Siemans Plessey Radar Limited, *Weather Radar 45C System Handbook*, 24200-060-00-3 687/12570/050 ed. TB1158-3 Cover 1.

[63] Beverly Microwave Division, "Magnetron theory of operation," tech. rep., Communication & Power Industries LLC., 150 Sohier Road Beverly, Massachusetts 01915.

[64] S. Rong-di Dai Guang-ming, "Application of IGBT in modulator of radar transmitter," *Modern Radar*, vol. 4, p. 019, 2002.

[65] J. J. Gourley, P. Tabary, and J. Parent du Chatelet, "Data quality of the Meteo-France C-band polarimetric radar," *Journal of Atmospheric and Oceanic Technology*, vol. 23, pp. 1340–1356, Oct. 2006.

[66] R. J. Watson, S. Talebi, and P. S. Cannon, "Development of a digital IF radar transceiver system," in *31st Conference on Radar Meteorology, Vols 1 and 2*, 31st Conference on Radar Meteorology, Vols 1 and 2, pp. 688–689, 2003.

[67] B. Brannon and A. Barlow, "Aperture uncertainty and ADC system performance," *Applications Note AN-501. Analog Devices, Inc.(September)*, 2000.

[68] A. Devices, *Data Conversion Handbook*. Analog Devices, Inc, 1989.

[69] E. Hogenauer, "An economical class of digital filters for decimation and interpolation," *Acoustics, Speech and Signal Processing, IEEE Transactions on*, vol. 29, no. 2, pp. 155–162, 1981.

[70] S. Committee *et al.*, "INF-8074i: Specification for SFP (small form-factor pluggable) transceiver," 2001.

[71] I. Integration, "Clockgen module datasheet," tech. rep., Innovative Integration, Innovative Integration, Inc. 2390A Ward Avenue, Simi Valley, California 93065, 2007.

[72] M. Fang, R. Doviak, and V. Melnikov, "Spectrum width measured by WSR-88D: Error sources and statistics of various weather phenomena," *Journal of Atmospheric and Oceanic Technology*, vol. 21, no. 6, pp. 888–904, 2004.

[73] M. Frech, B. Lange, T. Mammen, J. Seltmann, C. Morehead, and J. Rowan, "Influence of a radome on antenna performance.," *Journal of Atmospheric & Oceanic Technology*, vol. 30, no. 2, 2013.

[74] V. Bringi, R. Hoferer, D. A. Brunkow, R. Schwerdtfeger, V. Chandrasekar, S. A. Rutledge, J. George, and P. C. Kennedy, "Design and performance characteristics of the new 8.5-m dual-offset gregorian antenna for the csu-chill radar," *Journal of Atmospheric and Oceanic Technology*, vol. 28, p. 907, July 2011.

[75] F. Fabry, "Meterological value of ground target measurements by radar," *Journal of Atmospheric and Oceanic Technology*, vol. 21, pp. 560–573, 04 2004.

[76] B. Bean and E. Dutton, "Radio meteorology, national bureau of standards monograph no. 92," *Washingtons, DC, US Government Printing Office*, 1996.

[77] D. Bodine, P. L. Heinselman, B. L. Cheong, R. D. Palmer, and D. Michaud, "A case study on the impact of moisture variability on convection initiation using radar refractivity retrievals," *J. Appl. Meteor. Climatol.*, vol. 49, pp. 1766–1778, Mar. 2010.

[78] J. C. Nicol and A. J. Illingworth, "The effect of phase-correlated returns and spatial smoothing on the accuracy of radar refractivity retrievals," *Journal of Atmospheric and Oceanic Technology*, vol. 30, pp. 22–39, Aug. 2012.

[79] CPI, *VMC-1891A CPI Magnetron Testing Specification*. Communications & Power Industries Beverly Microwave Division, 1999.

[80] J. Parent du Chatelet, P. Tabary, and C. Boudjabi, "Evaluation of the refractivity measurement feasibility with a C-band radar equipped with a magnetron transmitter," in *Preprints, 33rd Conf. on Radar Meteorology, Cairns, Australia, Amer. Meteor. Soc. B*, vol. 8, 2007.

[81] J. Parent du Chatelet, C. Boudjabi, L. Besson, and O. Caumont, "Errors caused by long-term drifts of magnetron frequencies for refrac-

tivity measurement with a radar: Theoretical formulation and initial validation," *Journal of Atmospheric and Oceanic Technology*, vol. 29, pp. 1428–1434, July 2012.

[82] J. Nicol, A. Illingworth, T. Darlington, and M. Kitchen, "Quantifying errors due to frequency changes and target location uncertainty for radar refractivity retrievals," *Journal of Atmospheric and Oceanic Technology*, no. 2013, 2013.

[83] T. M. Weckwerth, C. R. Pettet, F. Fabry, S. J. Park, M. A. LeMone, and J. W. Wilson, "Radar refractivity retrieval: Validation and application to short-term forecasting," *Journal of Applied Meteorology*, vol. 44, pp. 285–300, Mar. 2005.

[84] B. L. Cheong, R. D. Palmer, C. D. Curtis, T.-Y. Yu, D. S. Zrnic, and D. Forsyth, "Refractivity retrieval using the phased-array radar: First results and potential for multimission operation," *Geoscience and Remote Sensing, IEEE Transactions on*, vol. 46, no. 9, pp. 2527–2537, 2008.

[85] B. L. Cheong, R. Palmer, V. Chandrasekar, and F. Junyent, "Real-time refractivity retrieval using the magnetron-based CASA X-band radar network during the spring 2008 campaign," in *Geoscience and Remote Sensing Symposium, 2008. IGARSS 2008. IEEE International*, vol. 5, pp. V–306, IEEE, 2008.

[86] J. Nicol, T. Darlington, A. Illingworth, K. Bartholemew, M. Kitchen, and E. Delaygue, "Operational testing of radar refractivity retrieval for the uk radar network," in *Proc. Fifth European Conf. on Radar Meteorology and Hydrology*, 2008.

[87] D. Bodine, D. Michaud, R. D. Palmer, P. L. Heinselman, J. Brotzge, N. Gasperoni, B. Leng Cheong, M. Xue, and J. Gao, "Understanding radar refractivity: Sources of uncertainty," *J. Appl. Meteor. Climatol.*, vol. 50, pp. 2543–2560, Aug. 2011.

[88] L. Besson and J. Parent du Chatelet, "Solutions for improving the radar refractivity measurement by taking operational constraints

into account," *J. Atmos. Oceanic Technol.*, vol. 30, pp. 1730–1742, May 2013.

[89] E. Kudeki and G. R. Stitt, "Frequency domain interferometry: A high resolution radar technique for studies of atmospheric turbulence," *Geophysical research letters*, vol. 14, no. 3, pp. 198–201, 1987.

[90] F. Junyent, V. Chandrasekar, D. McLaughlin, E. Insanic, and N. Bharadwaj, "The CASA integrated project 1 networked radar system," *J. Atmos. Oceanic Technol.*, vol. 27, pp. 61–78, Jan. 2010.

[91] P. J. Kootsookos, "A review of the frequency estimation and tracking problems.," tech. rep., Systems Engineering Department, Australian National University, 1993.

[92] J. A. Nelder and R. Mead, "A simplex method for function minimization," *The Computer Journal*, vol. 7, no. 4, pp. 308–313, 1965.

[93] K. L. S. Gunn and T. W. R. East, "The microwave properties of precipitation particles," *Quarterly Journal of the Royal Meteorological Society*, vol. 80, no. 346, pp. 522–545, 1954.

[94] C. G. Collier, *Radar in meteorology*. Boston: American Meteorological Society, first ed., 1990. Radar data processing and short-period forecasting in the United Kingdom.

[95] C. Sandford and N. Gaussiat, "Evaluation of an error-based quality index for compositing using UK radar data," tech. rep., OPERA, 2012.

[96] J.-Y. Gu, A. Ryzhkov, P. Zhang, P. Neilley, M. Knight, B. Wolf, and D.-I. Lee, "Polarimetric attenuation correction in heavy rain at c band," *J. Appl. Meteor. Climatol.*, vol. 50, pp. 39–58, Sept. 2010.

[97] L. D. Carey, S. A. Rutledge, D. A. Ahijevych, and T. D. Keenan, "Correcting propagation effects in c-band polarimetric radar observations of tropical convection using differential propagation phase," *J. Appl. Meteor.*, vol. 39, pp. 1405–1433, Sept. 2000.

[98] A. V. Ryzhkov, "The impact of beam broadening on the quality of radar polarimetric data," *J. Atmos. Oceanic Technol.*, vol. 24, pp. 729–744, May 2007.

[99] D. B. Hodge and G. L. Austin, "The comparison between radar- and radiometer-derived rain attenuation for earth-space links," *Radio Science*, vol. 12, no. 5, pp. 733–740, 1977.

[100] R. Rogers, S. Radhakant, and O. Massambani, "New radar studies of slant-path attenuation due to rain," *Annales des Telecommunications*, vol. 36, no. 1-2, pp. 40–47, 1981.

[101] H. Masunaga and C. D. Kummerow, "Combined radar and radiometer analysis of precipitation profiles for a parametric retrieval algorithm," *J. Atmos. Oceanic Technol.*, vol. 22, pp. 909–929, July 2005.

[102] R. H. Pearce *et al.*, "Combined frequency modulated radar and radiometer," aug 1971. US Patent 3,599,207.

[103] G. Kirchhoff, "Ueber das verhaltniss zwischen dem emissionsvermogen und dem absorptionsvermogen der korper fur warme und licht," *Annalen der Physik*, vol. 185, no. 2, pp. 275–301, 1860.

[104] N. Skou, *Microwave radiometer systems: design and analysis, Second Edition*. 2006.

[105] W. B. Goggins, "A microwave feedback radiometer," *Aerospace and Electronic Systems, IEEE Transactions on*, no. 1, pp. 83–90, 1967.

[106] P. Batelaan, C. Stelzried, and R. Goldstein, "Improved noise-adding radiometer for microwave receivers," Tech. Rep. 73-10345, NASA, JPL, 1974.

[107] C. Stelzried, "Noise adding radiometer performance analysis," *The Telecommunications and Data Acquisition Progress Report 42-59, July and August*, pp. 98–106, 1980.

[108] M. Reid, B. Parham, and R. Gardner, "An X-band radiometer for the microwave weather project," *Deep Space Network Progress Report*, vol. 29, pp. 54–59, 1975.

[109] A. E. Wright, G. J. Nelson, R. T. Stewart, O. B. Slee, and J. D. Murray, "A novel noise-adding radiometer," *Astronomical Society of Australia, Proceedings (ISSN 0066-9997)*, vol. 6, pp. 512–516., 1986.

[110] F. Ulaby, R. Moore, and A. Fung, *Microwave Remote Sensing Active and Passing Vol. 1: Microwave Remote Sensing Fundamentals and Radiometry*. Artech house, 1981.

[111] Ranatec AB, Flojelbergsgatan 1c,SE-431 35 Molndal,Sweden, *Ranatec Monitor 9000*.

[112] H. T. Friis, "Noise figures of radio receivers," *Proceedings of the IRE*, vol. 32, no. 7, pp. 419–422, 1944.

[113] T. Hewison and C. Gaffard, "Radiometrics MP3000 microwave radiometer performance assessment," tech. rep., UK Met Office, 2003.

[114] S. Buehler, P. Eriksson, T. Kuhn, A. Von Engeln, and C. Verdes, "Arts, the atmospheric radiative transfer simulator," *Journal of Quantitative Spectroscopy and Radiative Transfer*, vol. 91, no. 1, pp. 65–93, 2005.

[115] E. Gorgucci, G. Scarchilli, and V. Chandrasekar, "A procedure to calibrate multiparameter weather radar using properties of the rain medium," *IEEE transactions on geoscience and remote sensing*, vol. 37, p. 269, 1999.

[116] P. K. Sen, "Estimates of the regression coefficient based on kendall's tau," *Journal of the American Statistical Association*, vol. 63, no. 324, pp. 1379–1389, 1968.

[117] I. Holleman, A. Huuskonen, R. Gill, and P. Tabary, "Operational monitoring of radar differential reflectivity using the sun," *Journal of Atmospheric and Oceanic Technology*, vol. 27, pp. 881–887, Jan. 2010.

[118] T. Darlington, M. Kitchen, J. Sugier, and J. de Rohan-Truba, "Automated real-time monitoring of radar sensitivity and antenna pointing accuracy," *31st Conference on Radar Meteorology, AMS*, pp. 538–541, 2003.

[119] A. Huuksonen and I. Holleman, "Determining weather radar antenna pointing using signals detected from the sun at low antenna elevations," *Journal of Atmospheric and Oceanic Technology*, vol. 24, p. 476, 2007.

[120] J. J. Gourley, P. Tabary, and J. Parent du Chatelet, "Empirical estimation of attenuation from differential propagation phase measurements at C-band," *J. Appl. Meteor. Climatol.*, vol. 46, pp. 306–317, Mar. 2007.

[121] K. Bartholemew, *Assessing the Potential of Radar Refractivity Retrievals for Improved High Resolution Weather Prediction*. PhD thesis, University of Reading, 2012.

[122] J. Nicol, K. Bartholemew, T. Darlington, and A. Illingworth, "Operational radar refractivity retrieval for numerical weather prediction," in *Proceedings of the 8th International Symposium Weather Radar and Hydrology, Exeter, UK*, 2011.

[123] J. C. Nicol and G. L. Austin, "Attenuation correction constraint for single-polarisation weather radar," *Meteorological Applications*, vol. 10, no. 4, pp. 345–354, 2003.

[124] J. ten Veldhuis, C. Maksimovic, D. Schertzer, and P. Willems, "Raingain–radar for high resolution urban rainfall estimation and flood prediction," in *Geophysical Research Abstracts*, vol. 14, 2012.

Appendix A

Antenna Plots

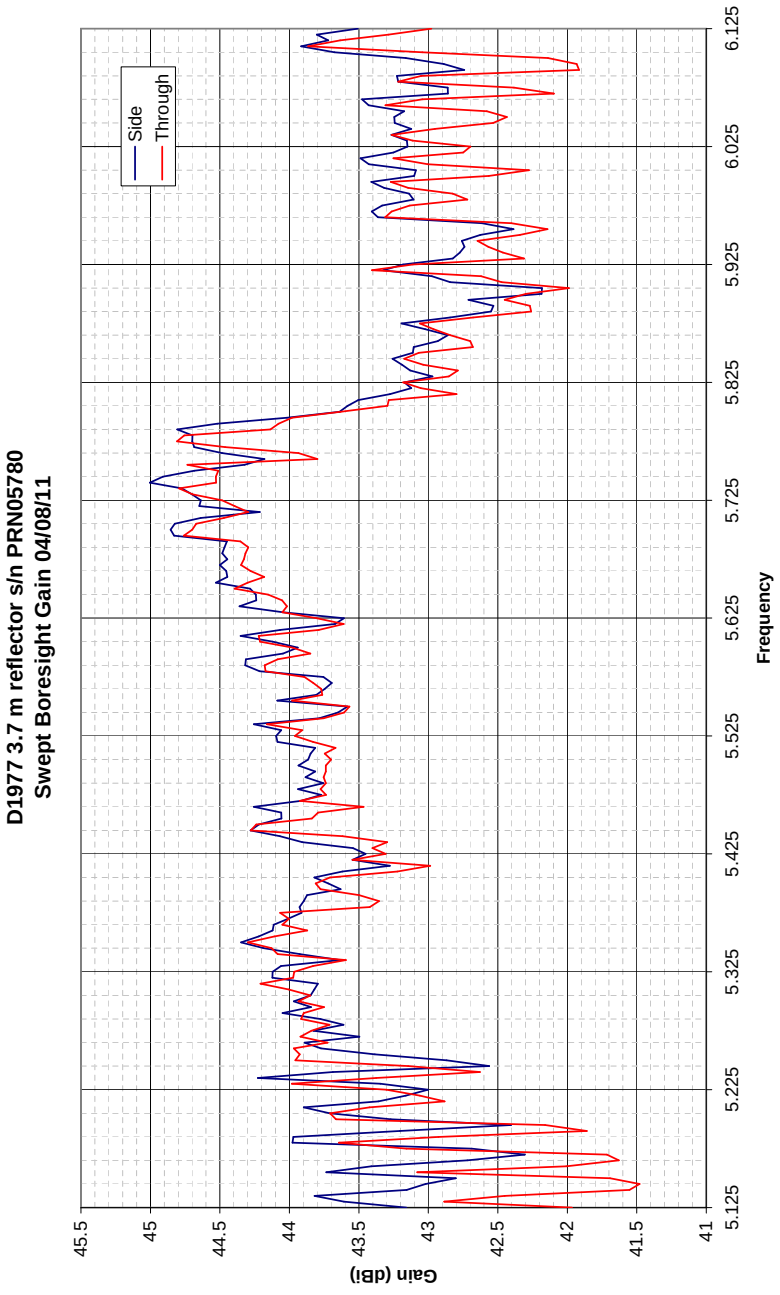

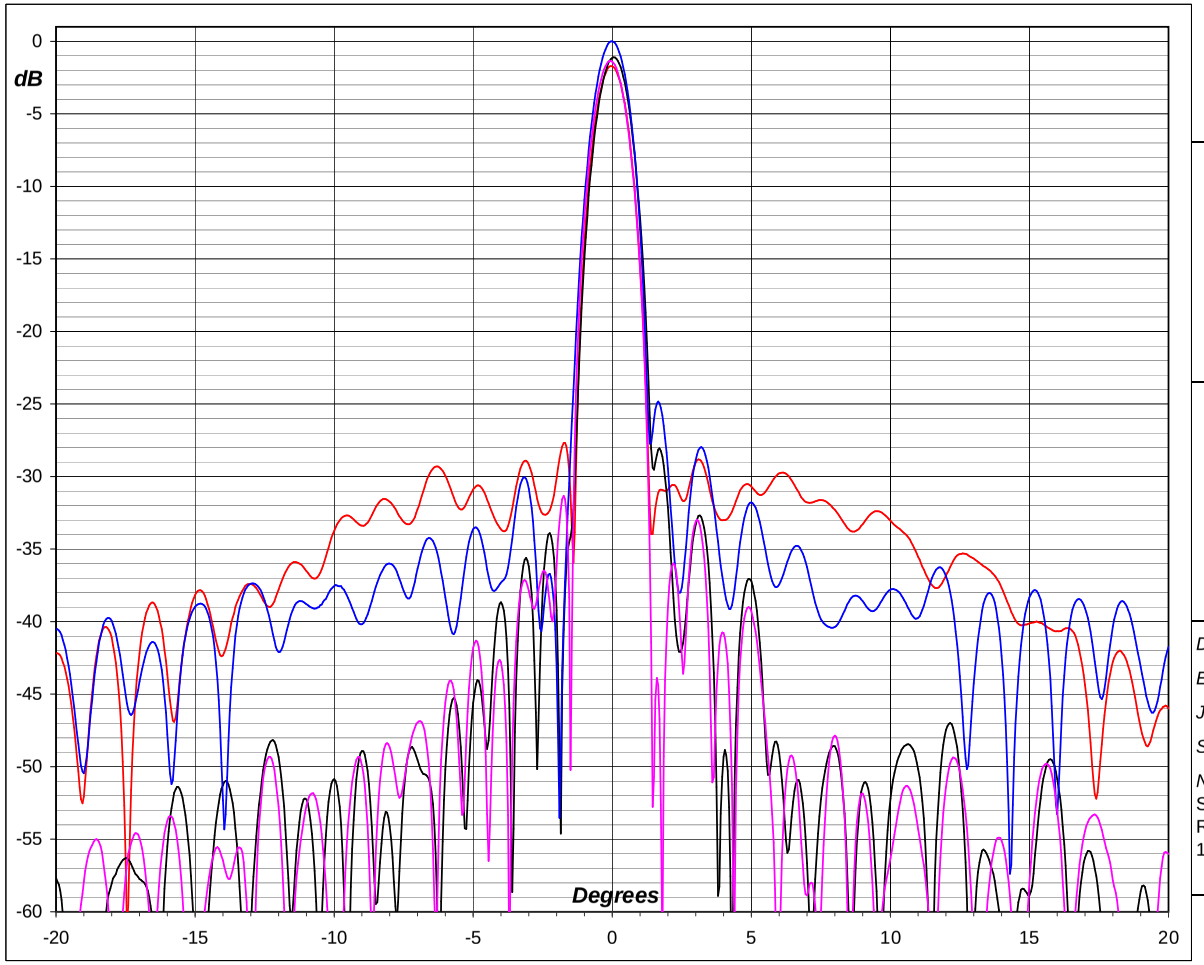

Q-par Angus Ltd
IDEAS ENGINEERED
Tel: +44 (0)1568 612138
Web: www.q-par.com
Email sales@q-par.com

FD_001

3 dB beamwidth (°)
1.0
6 dB beamwidth (°)
1.4
10 dB beamwidth (°)
1.8

FD_025

3 dB beamwidth (°)
1.0
6 dB beamwidth (°)
1.4
10 dB beamwidth (°)
1.8

Date 01/08/2011
Engr SD
Job D1977
S/N PRN05780

Notes
Side (V) port. Copol.
Roll cuts 0, 45, 90 and 135 degrees.

Frequency (GHz)
5.600

Pattern_Plot v1.18 Funtington data

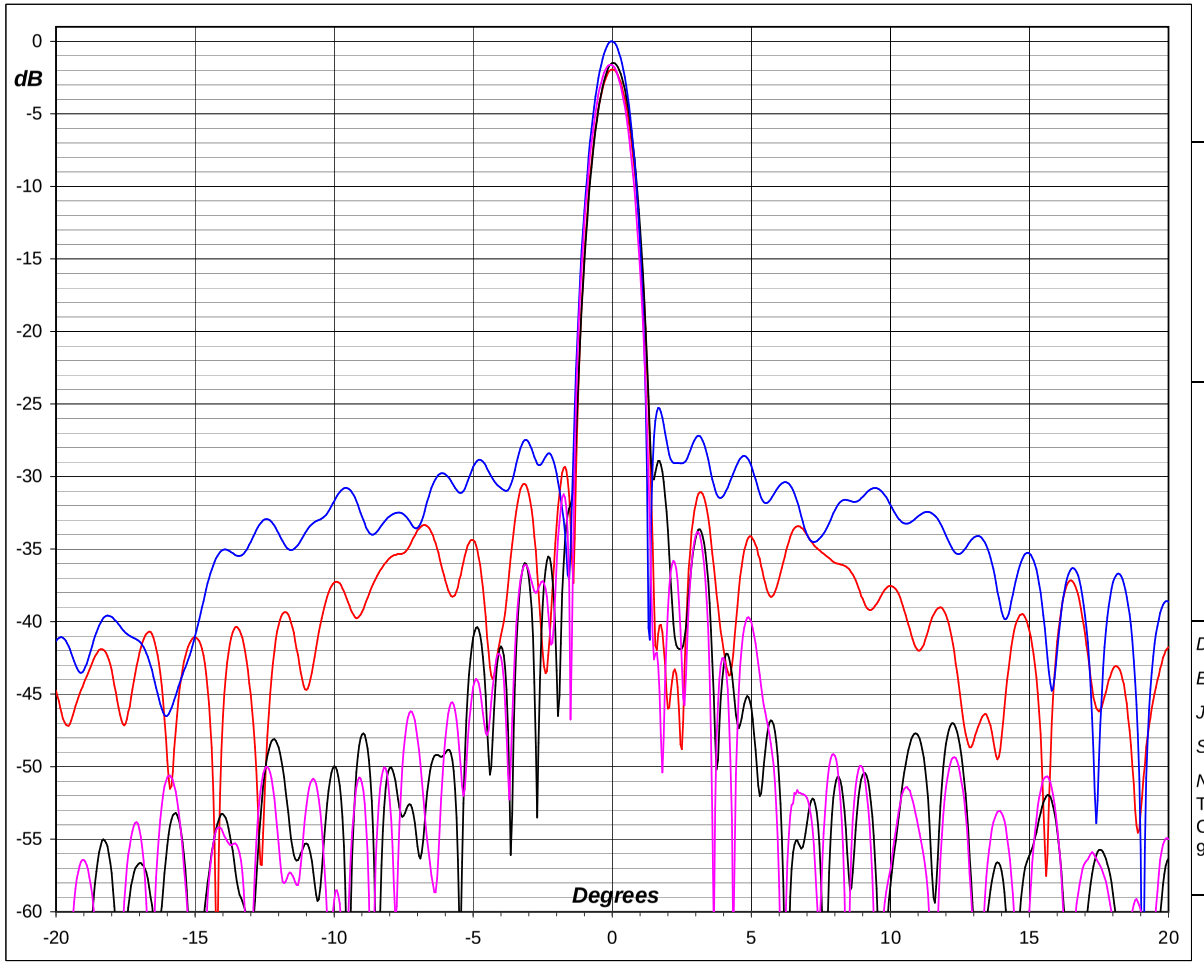

Pattern_Plot v1.18 Funtington data

Q-par Angus Ltd
IDEAS ENGINEERED
Tel: +44 (0)1568 612138
Web: www.q-par.com
Email sales@q-par.com

FD_019

3 dB beamwidth (°)
1.1
6 dB beamwidth (°)
1.5
10 dB beamwidth (°)
1.8

FD_043

3 dB beamwidth (°)
1.0
6 dB beamwidth (°)
1.4
10 dB beamwidth (°)
1.8

Date 01/08/2011
Engr SD
Job D1977
S/N PRN05780

Notes
Through (H) port.
Copol. Roll cuts 0, 45, 90 and 135 degrees.

Frequency (GHz)
5.600

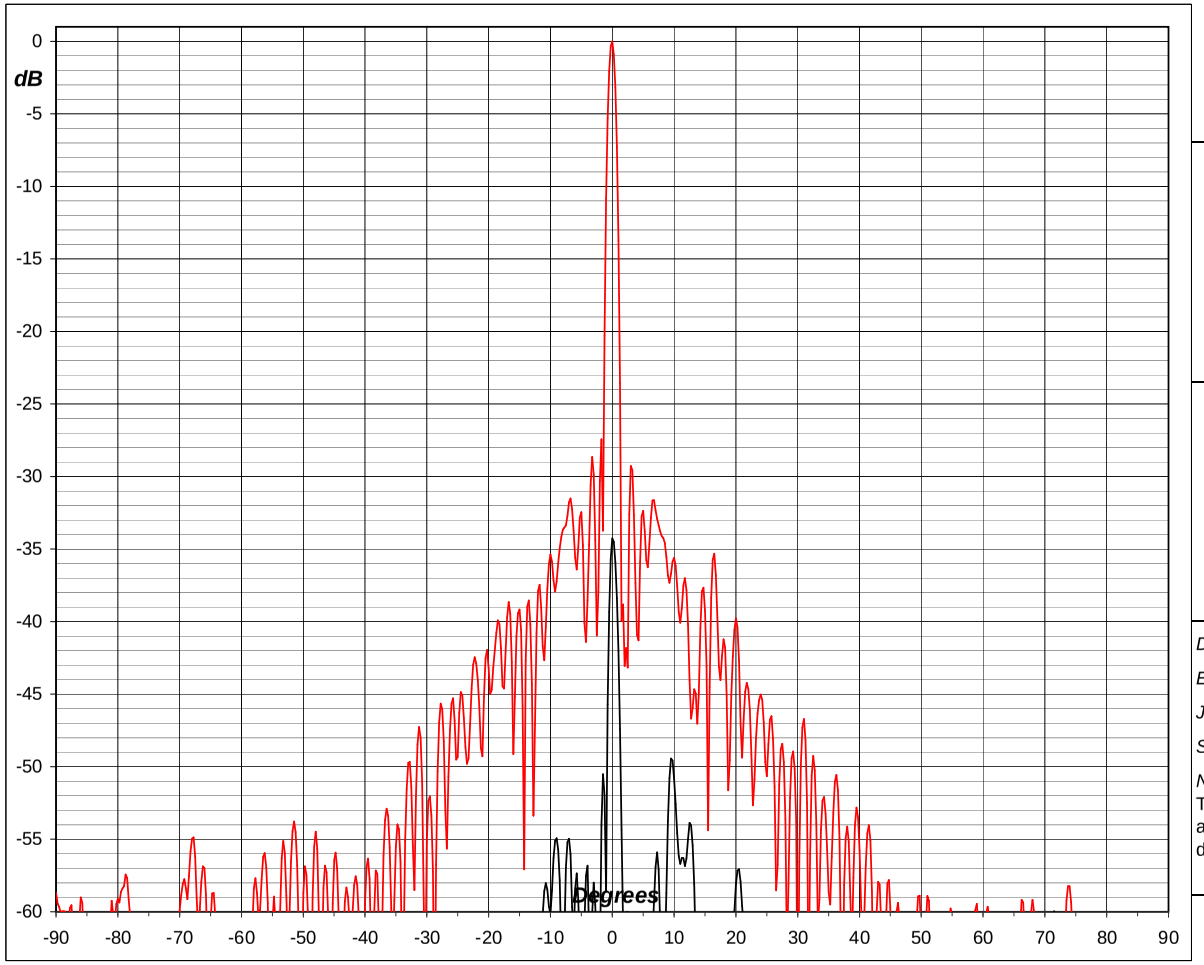

Pattern_Plot v1.18 Funtington data

Q-par Angus Ltd
IDEAS ENGINEERED
Tel: +44 (0)1568 612138
Web: www.q-par.com
Email sales@q-par.com

FD_020

3 dB beamwidth (°)
1.1

6 dB beamwidth (°)
1.5

10 dB beamwidth (°)
1.8

FD_008

3 dB beamwidth (°)
1.0

6 dB beamwidth (°)
1.4

10 dB beamwidth (°)
1.8

Date	01/08/2011
Engr	SD
Job	D1977
S/N	PRN05780

Notes
Through (H) port. Co and X pol. Roll cut 0 degrees.

Frequency (GHz)
5.600

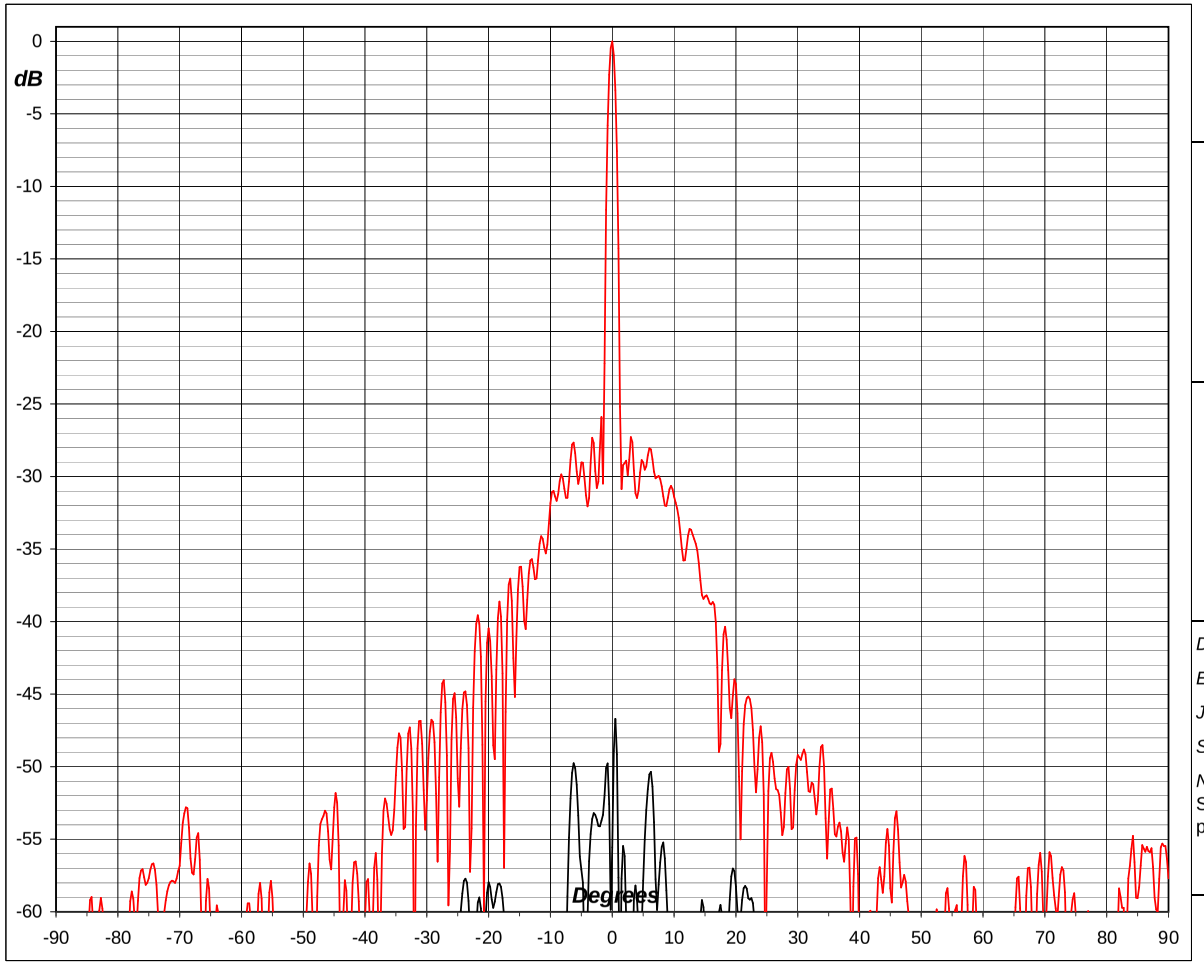

Pattern_Plot v1.18 Funtington data

Q-par Angus Ltd
IDEAS ENGINEERED
Tel: +44 (0)1568 612138
Web: www.q-par.com
Email sales@q-par.com

FD_002

3 dB beamwidth (°)
1.0

6 dB beamwidth (°)
1.4

10 dB beamwidth (°)
1.8

FD_014

3 dB beamwidth (°)
0.5

6 dB beamwidth (°)
0.7

10 dB beamwidth (°)
1.0

Date	01/08/2011
Engr	SD
Job	D1977
S/N	PRN05780

Notes
Side (V) port. Co and X pol. Roll cut 0 degrees.

Frequency (GHz)
5.600

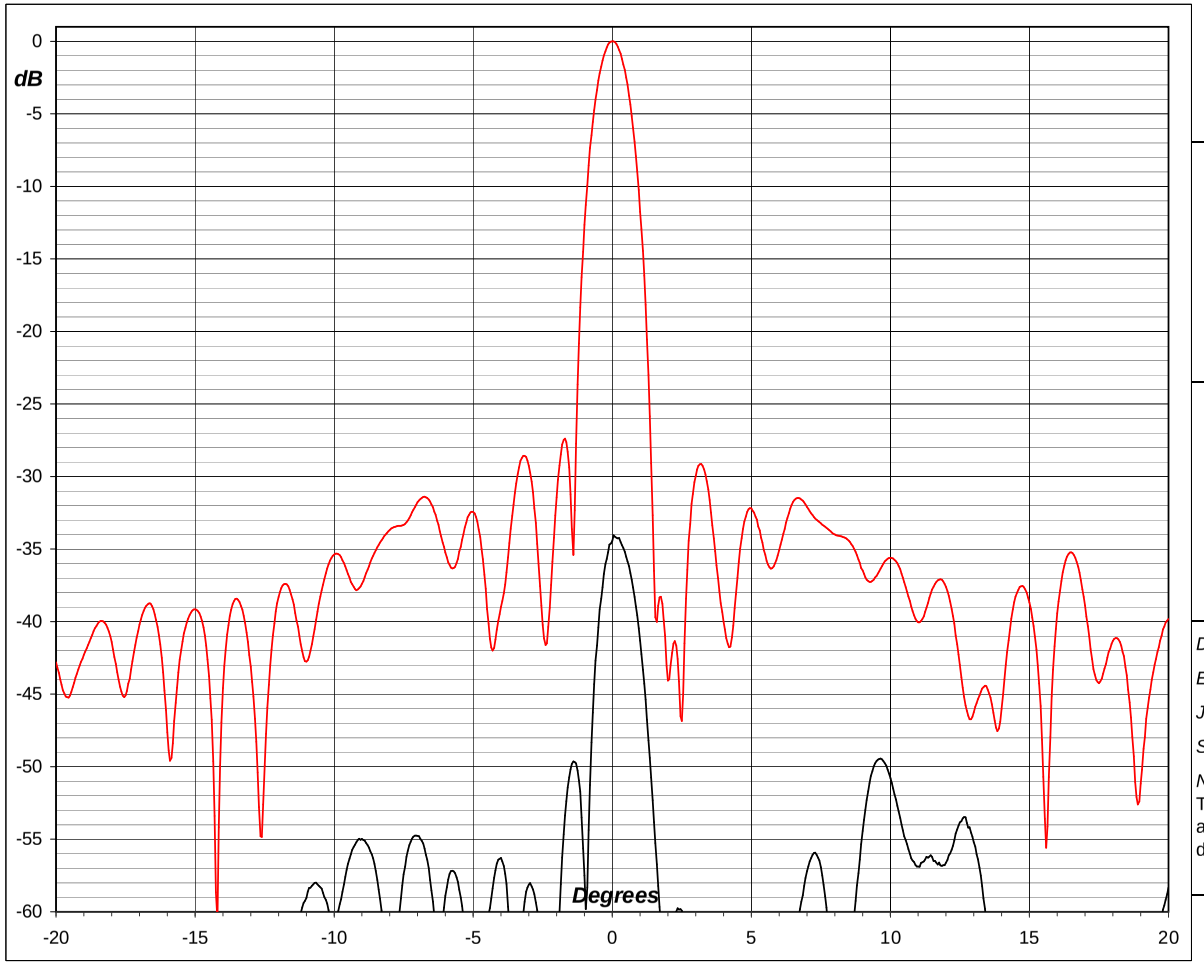

Q-par Angus Ltd
IDEAS ENGINEERED
Tel: +44 (0)1568 612138
Web: www.q-par.com
Email sales@q-par.com

FD_019

3 dB beamwidth (°)
1.1

6 dB beamwidth (°)
1.5

10 dB beamwidth (°)
1.8

FD_007

3 dB beamwidth (°)
1.0

6 dB beamwidth (°)
1.4

10 dB beamwidth (°)
1.8

Date 01/08/2011
Engr SD
Job D1977
S/N PRN05780

Notes
Through (H) port. Co and X pol. Roll cut 0 degrees.

Frequency (GHz)
5.600

Pattern_Plot v1.18 Funtington data

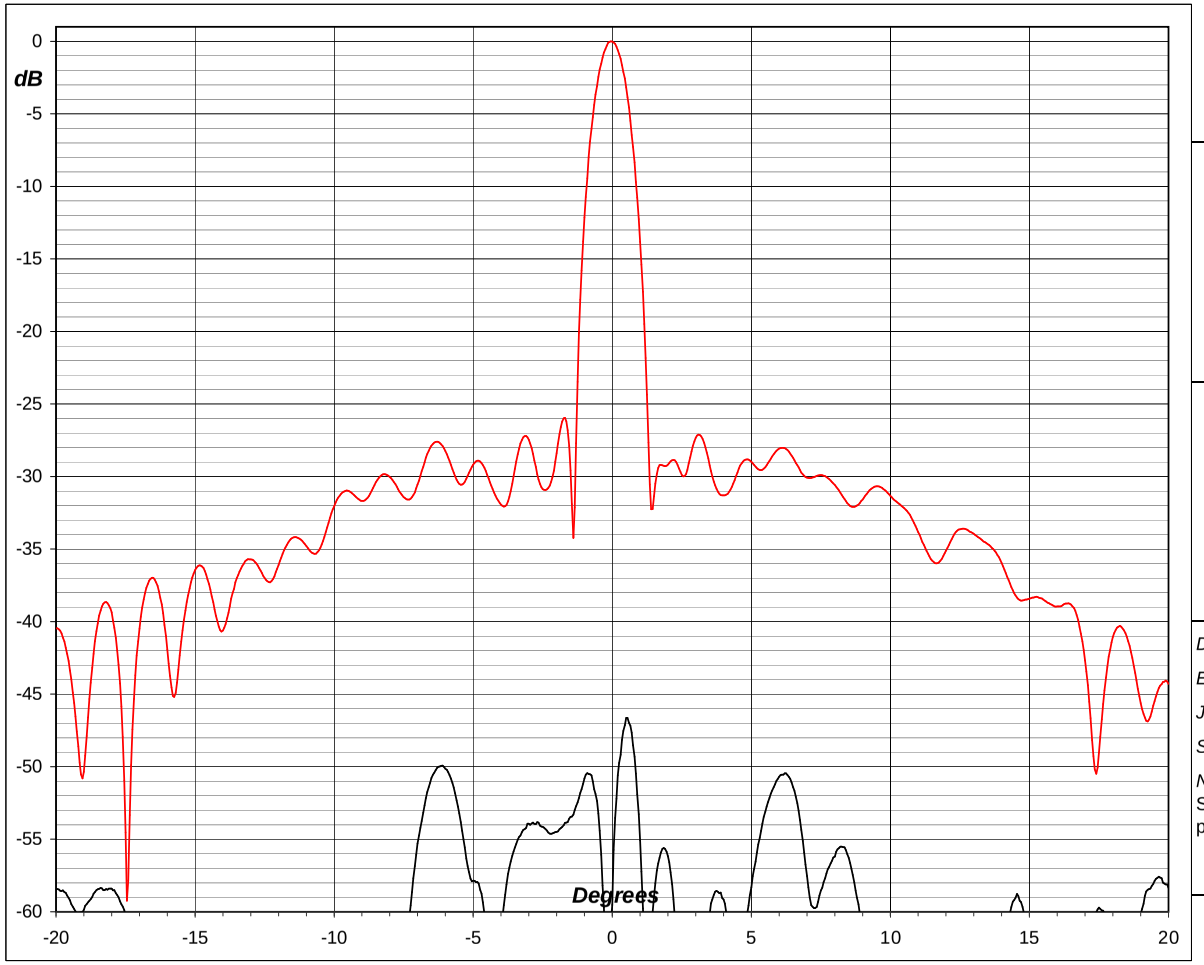

Q-par Angus Ltd
IDEAS ENGINEERED
Tel: +44 (0)1568 612138
Web: www.q-par.com
Email sales@q-par.com

FD_001

3 dB beamwidth (°)
1.0
6 dB beamwidth (°)
1.4
10 dB beamwidth (°)
1.8

FD_013

3 dB beamwidth (°)
0.6
6 dB beamwidth (°)
0.8
10 dB beamwidth (°)
1.0

Date 01/08/2011
Engr SD
Job D1977
S/N PRN05780

Notes
Side (V) port. Co and X pol. Roll cut 0 degrees.

Frequency (GHz)
5.600

Pattern_Plot v1.18 Funtington data

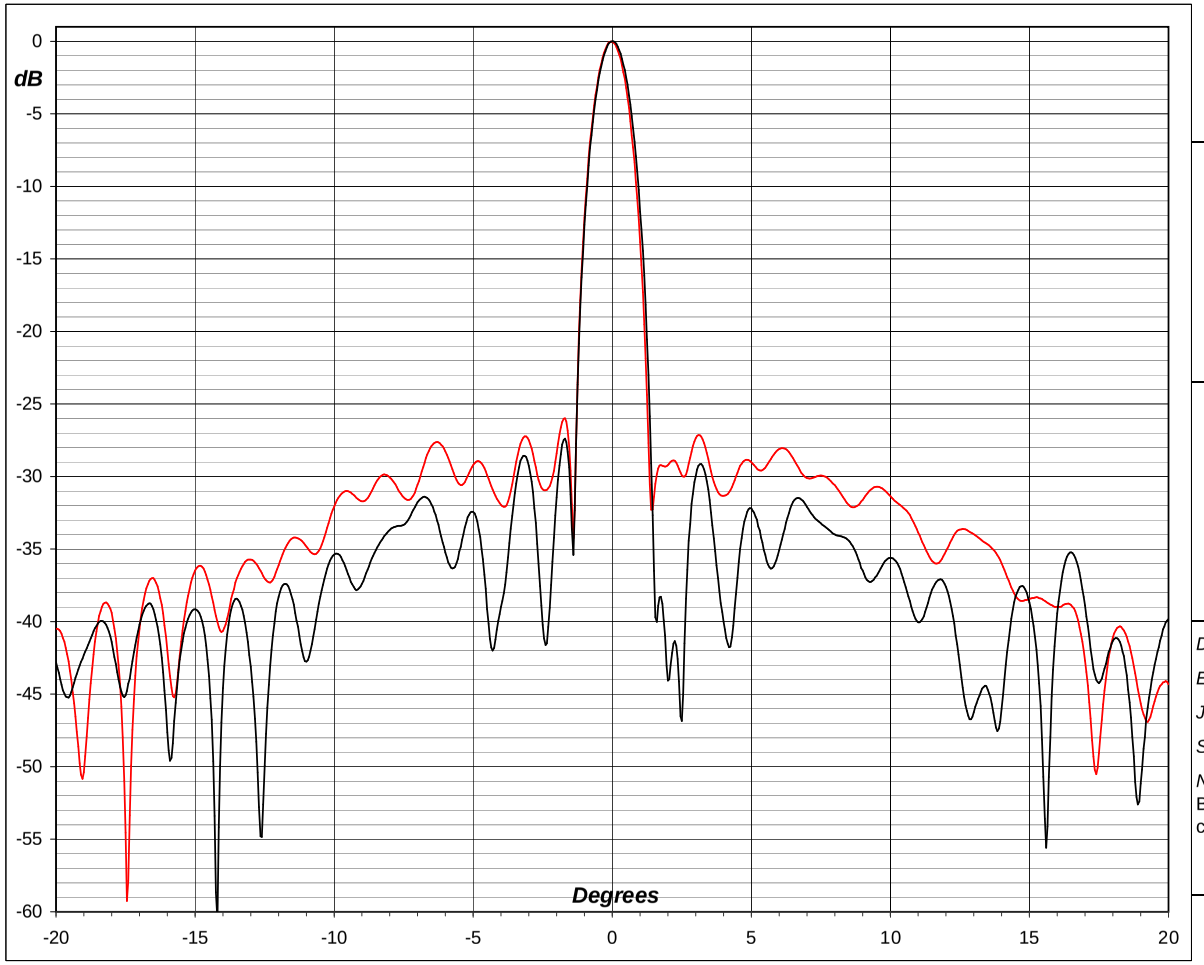

Q-par Angus Ltd
IDEAS ENGINEERED
Tel: +44 (0)1568 612138
Web: www.q-par.com
Email sales@q-par.com

FD_001

3 dB beamwidth (°)
1.0

6 dB beamwidth (°)
1.4

10 dB beamwidth (°)
1.8

FD_019

3 dB beamwidth (°)
1.1

6 dB beamwidth (°)
1.5

10 dB beamwidth (°)
1.8

Date 01/08/2011
Engr SD
Job D1977
S/N PRN05780

Notes
Both ports. Copol. Roll cut 0 degrees.

Frequency (GHz)
5.600

Pattern_Plot v1.18 Funtington data

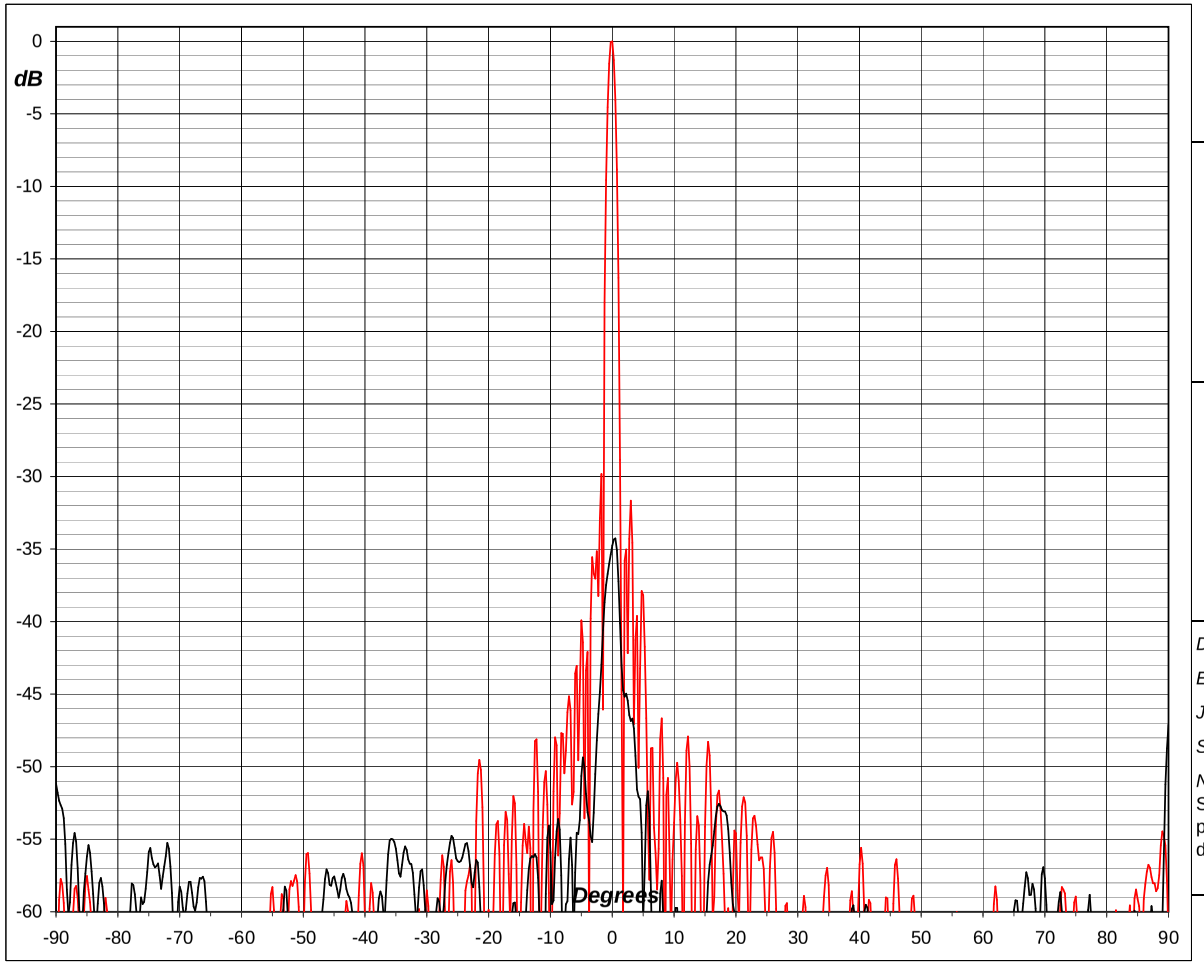

Pattern_Plot v1.18 Funtington data

Q-par Angus Ltd
IDEAS ENGINEERED
Tel: +44 (0)1568 612138
Web: www.q-par.com
Email sales@q-par.com

FD_074

3 dB beamwidth (°)
1.0

6 dB beamwidth (°)
1.4

10 dB beamwidth (°)
1.8

FD_086

3 dB beamwidth (°)
1.9

6 dB beamwidth (°)
2.7

10 dB beamwidth (°)
3.6

Date	03/08/2011
Engr	SD
Job	D1977
S/N	PRN05780

Notes
Side (V) port. Co and X pol. Roll cut 135 degrees.

Frequency (GHz)
5.600

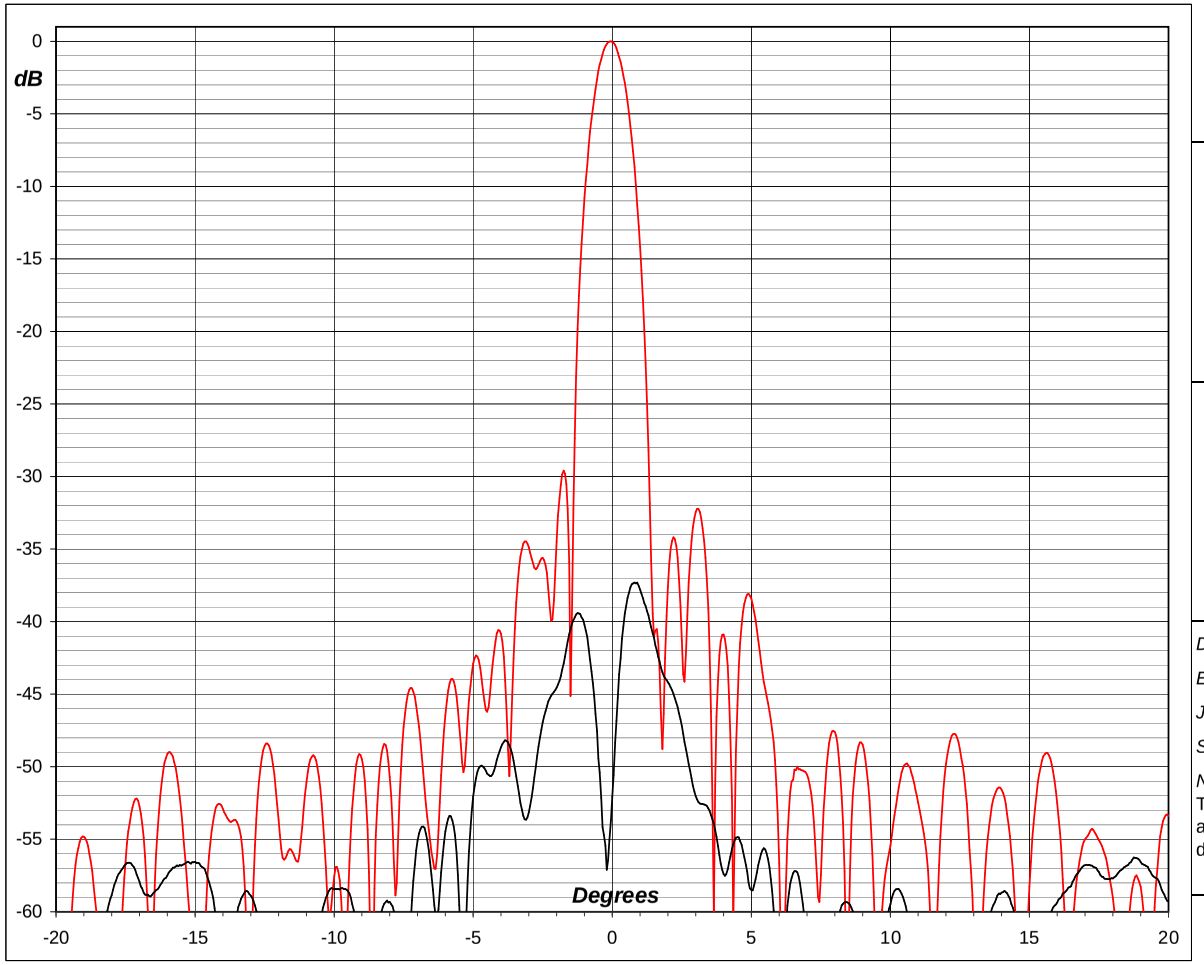

Q-par Angus Ltd
IDEAS ENGINEERED
Tel: +44 (0)1568 612138
Web: www.q-par.com
Email sales@q-par.com

FD_091

3 dB beamwidth (°)
1.0
6 dB beamwidth (°)
1.4
10 dB beamwidth (°)
1.8

FD_079

3 dB beamwidth (°)
1.0
6 dB beamwidth (°)
1.5
10 dB beamwidth (°)
2.4

Date 03/08/2011
Engr SD
Job D1977
S/N PRN05780

Notes
Through (H) port. Co and X pol. Roll cut 135 degrees.

Frequency (GHz)
5.600

Pattern_Plot v1.18 Funtington data

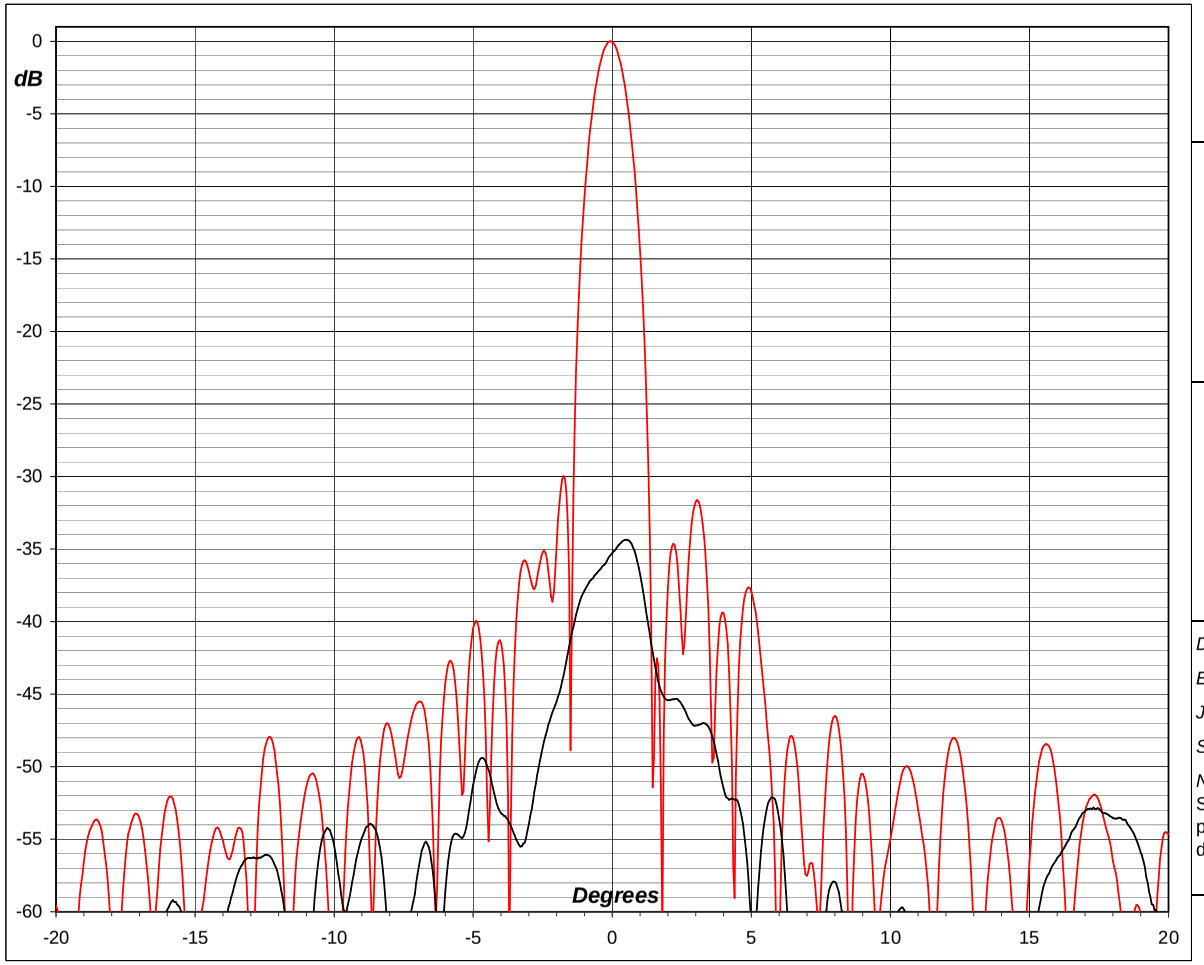

Pattern_Plot v1.18 Funtington data

Q-par Angus Ltd
IDEAS ENGINEERED
Tel: +44 (0)1568 612138
Web: www.q-par.com
Email sales@q-par.com

FD_073

3 dB beamwidth (°)
1.0

6 dB beamwidth (°)
1.4

10 dB beamwidth (°)
1.8

FD_085

3 dB beamwidth (°)
1.9

6 dB beamwidth (°)
2.7

10 dB beamwidth (°)
3.5

Date	03/08/2011
Engr	SD
Job	D1977
S/N	PRN05780

Notes
Side (V) port. Co and X pol. Roll cut 135 degrees.

Frequency (GHz)
5.600

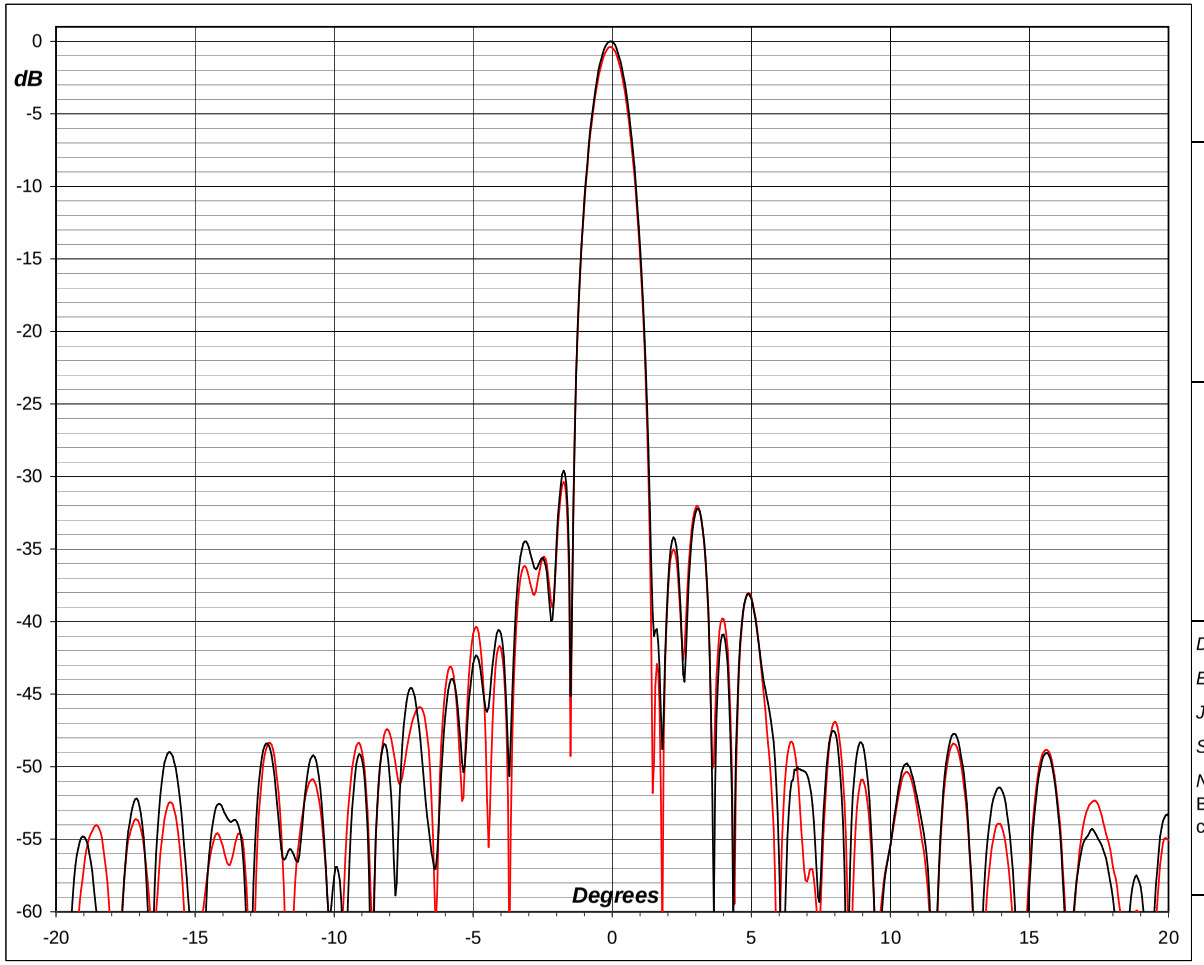

Pattern_Plot v1.18 Funtington data

Q-par Angus Ltd
IDEAS ENGINEERED
Tel: +44 (0)1568 612138
Web: www.q-par.com
Email sales@q-par.com

FD_073

3 dB beamwidth (°)
1.0
6 dB beamwidth (°)
1.4
10 dB beamwidth (°)
1.8

FD_091

3 dB beamwidth (°)
1.0
6 dB beamwidth (°)
1.4
10 dB beamwidth (°)
1.8

Date	03/08/2011
Engr	SD
Job	D1977
S/N	PRN05780

Notes
Both ports. Copol . Roll cut 135 degrees.

Frequency (GHz)
5.600

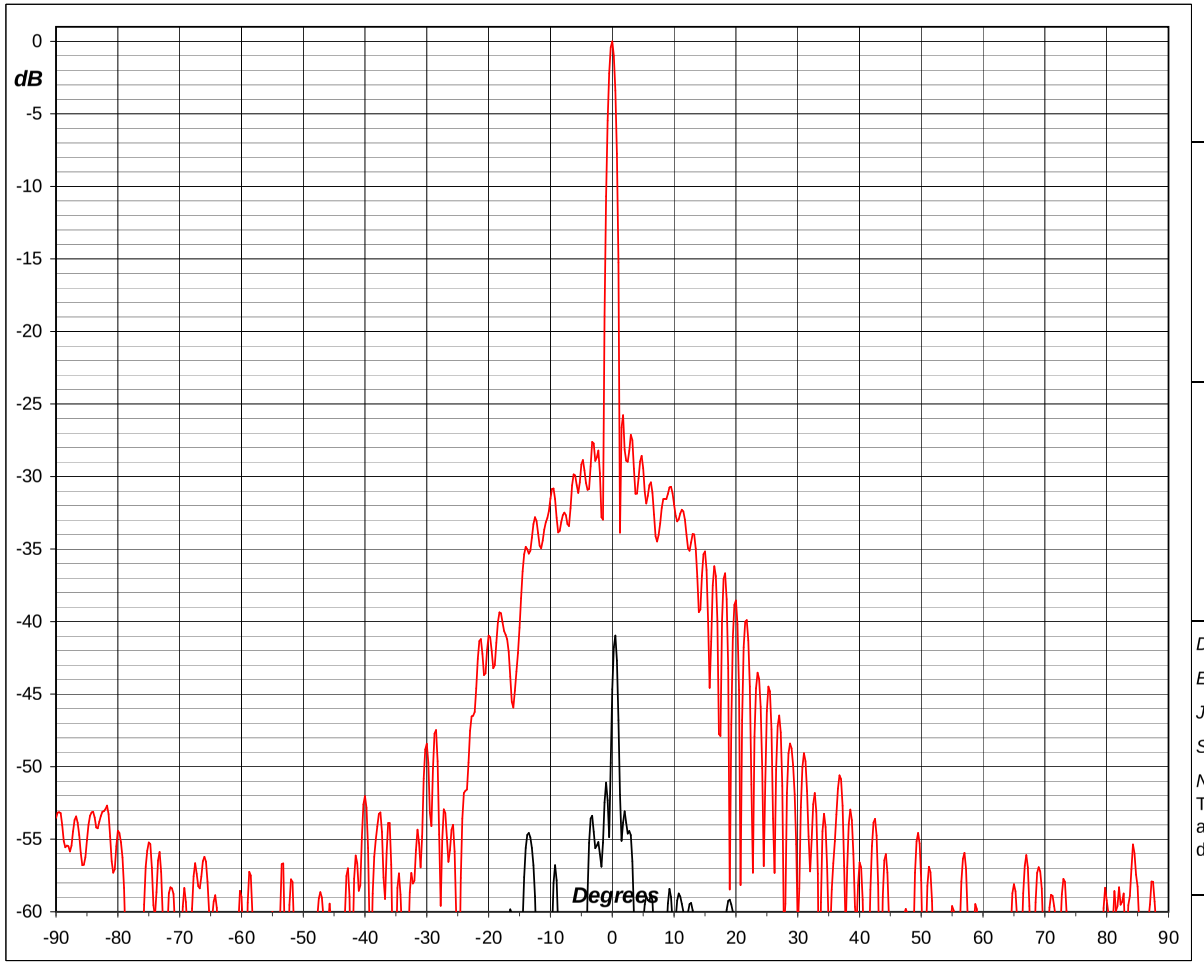

Pattern_Plot v1.18 Funtington data

Q-par Angus Ltd
IDEAS ENGINEERED
Tel: +44 (0)1568 612138
Web: www.q-par.com
Email sales@q-par.com

FD_068

3 dB beamwidth (°)
1.0

6 dB beamwidth (°)
1.4

10 dB beamwidth (°)
1.8

FD_056

3 dB beamwidth (°)
0.8

6 dB beamwidth (°)
1.1

10 dB beamwidth (°)
1.5

Date 02/08/2011
Engr SD
Job D1977
S/N PRN05780

Notes
Through (H) port. Co and X pol. Roll cut 90 degrees.

Frequency (GHz)
5.600

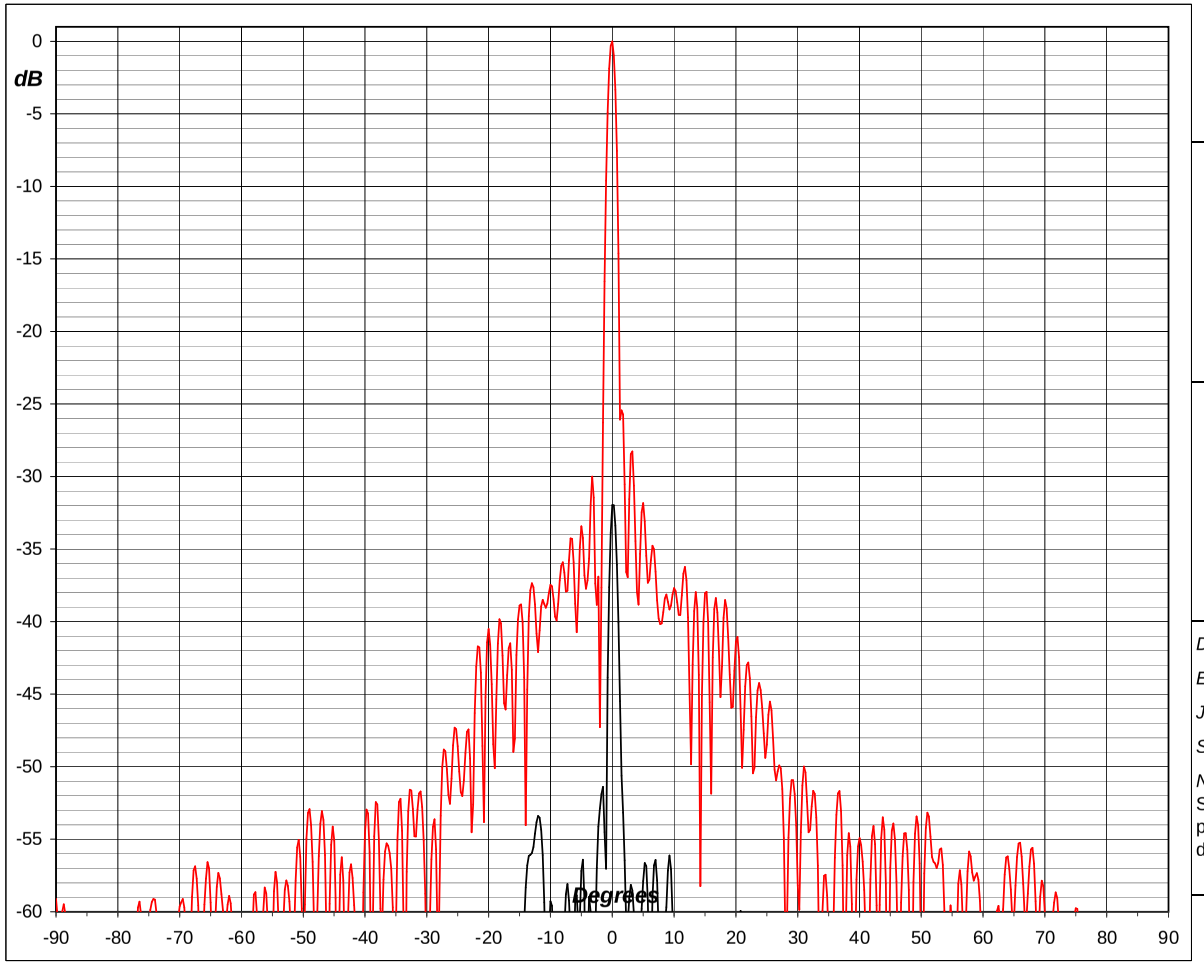

Pattern_Plot v1.18 Funtington data

Q-par Angus Ltd
IDEAS ENGINEERED
Tel: +44 (0)1568 612138
Web: www.q-par.com
Email sales@q-par.com

FD_050

3 dB beamwidth (°)
1.1

6 dB beamwidth (°)
1.5

10 dB beamwidth (°)
1.9

FD_062

3 dB beamwidth (°)
1.0

6 dB beamwidth (°)
1.4

10 dB beamwidth (°)
1.8

Date 02/08/2011
Engr SD
Job D1977
S/N PRN05780

Notes
Side (V) port. Co and X pol. Roll cut 45 degrees.

Frequency (GHz)
5.600

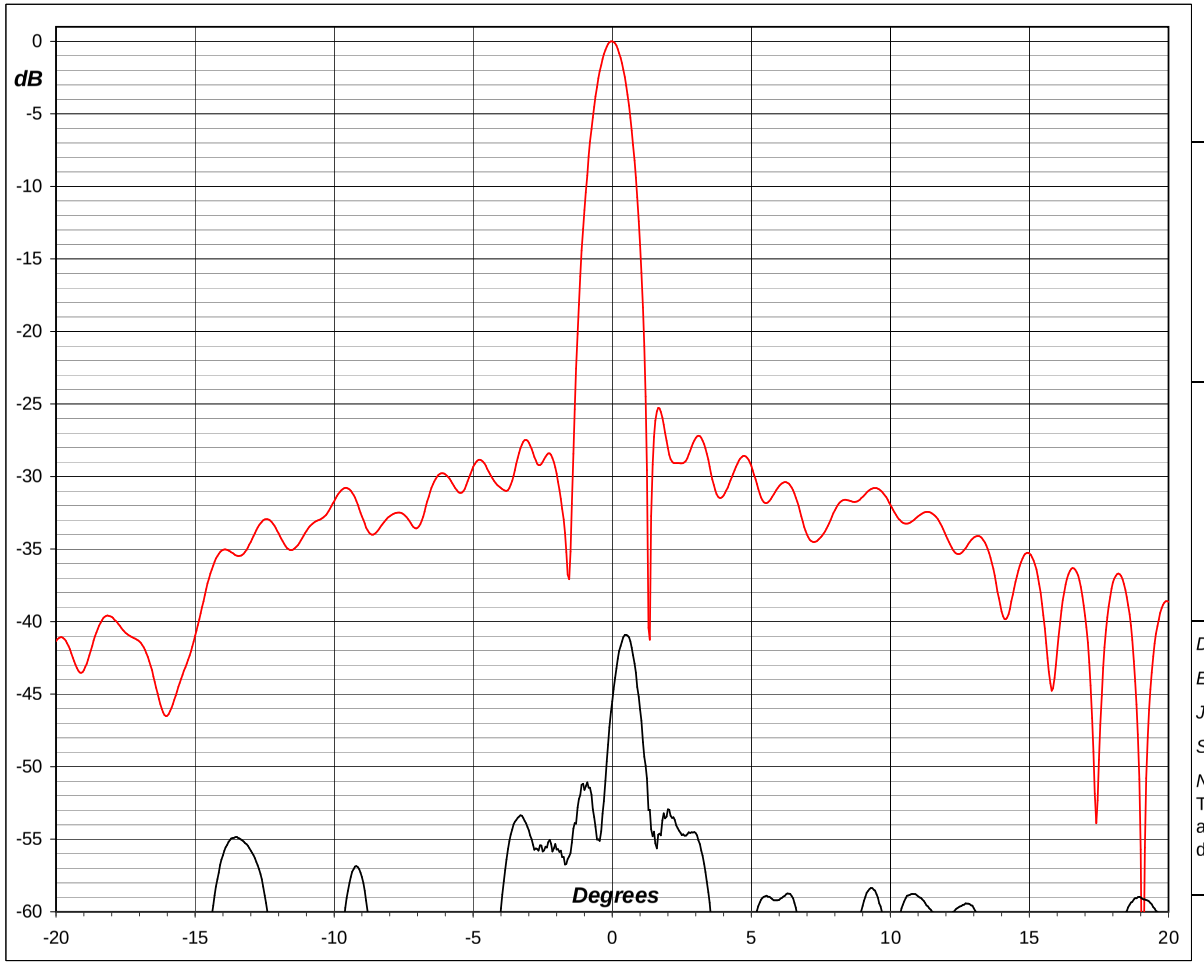

Q-par Angus Ltd
IDEAS ENGINEERED
Tel: +44 (0)1568 612138
Web: www.q-par.com
Email sales@q-par.com

FD_067

3 dB beamwidth (°)
1.0

6 dB beamwidth (°)
1.4

10 dB beamwidth (°)
1.8

FD_055

3 dB beamwidth (°)
0.8

6 dB beamwidth (°)
1.1

10 dB beamwidth (°)
1.5

Date 02/08/2011
Engr SD
Job D1977
S/N PRN05780

Notes
Through (H) port. Co and X pol. Roll cut 90 degrees.

Frequency (GHz)
5.600

Pattern_Plot v1.18 Funtington data

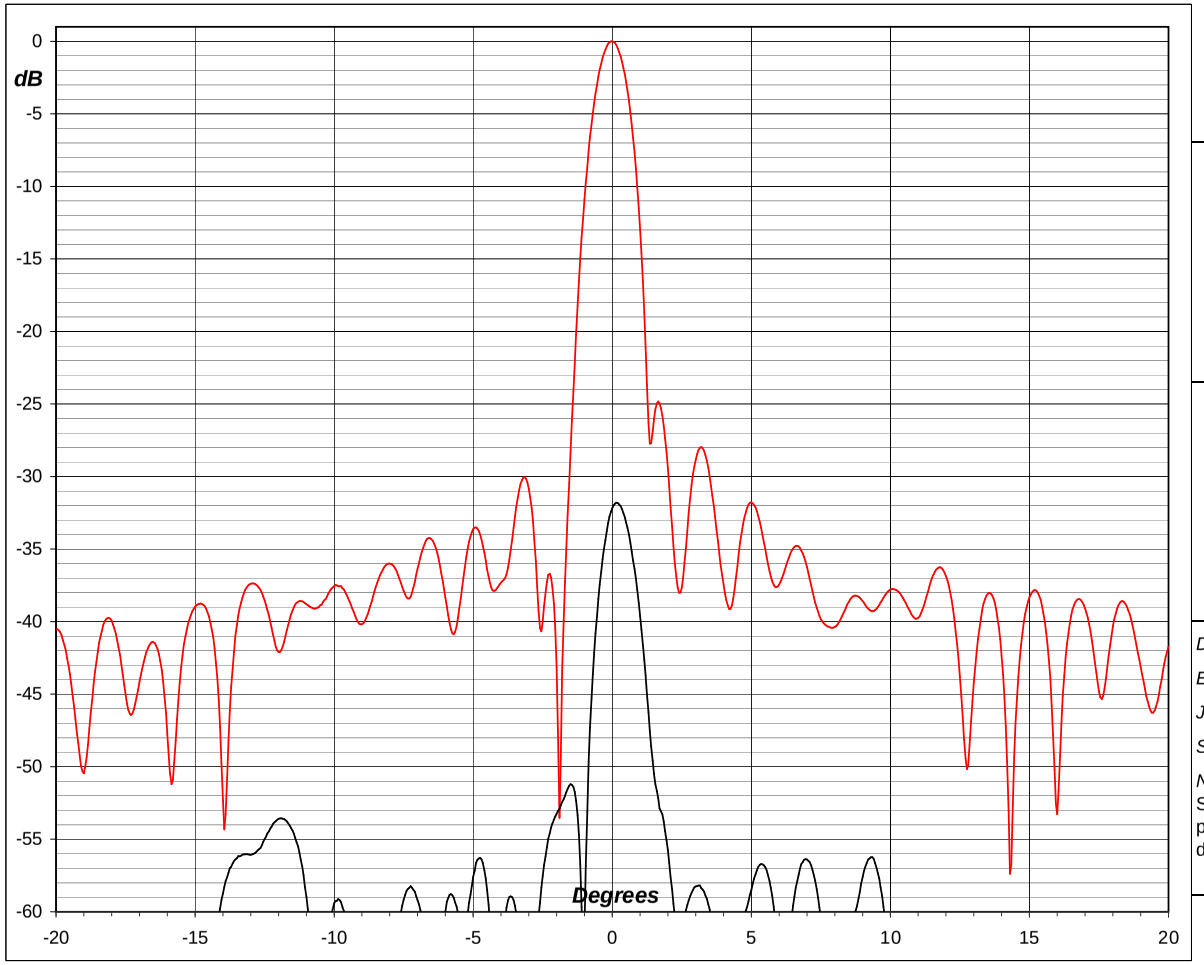

Q-par Angus Ltd
IDEAS ENGINEERED
Tel: +44 (0)1568 612138
Web: www.q-par.com
Email sales@q-par.com

FD_049

3 dB beamwidth (°)
1.1

6 dB beamwidth (°)
1.5

10 dB beamwidth (°)
1.9

FD_061

3 dB beamwidth (°)
1.0

6 dB beamwidth (°)
1.4

10 dB beamwidth (°)
1.7

Date	02/08/2011
Engr	SD
Job	D1977
S/N	PRN05780

Notes
Side (V) port. Co and X pol.. Roll cut 90 degrees.

Frequency (GHz)
5.600

Pattern_Plot v1.18 Funtington data

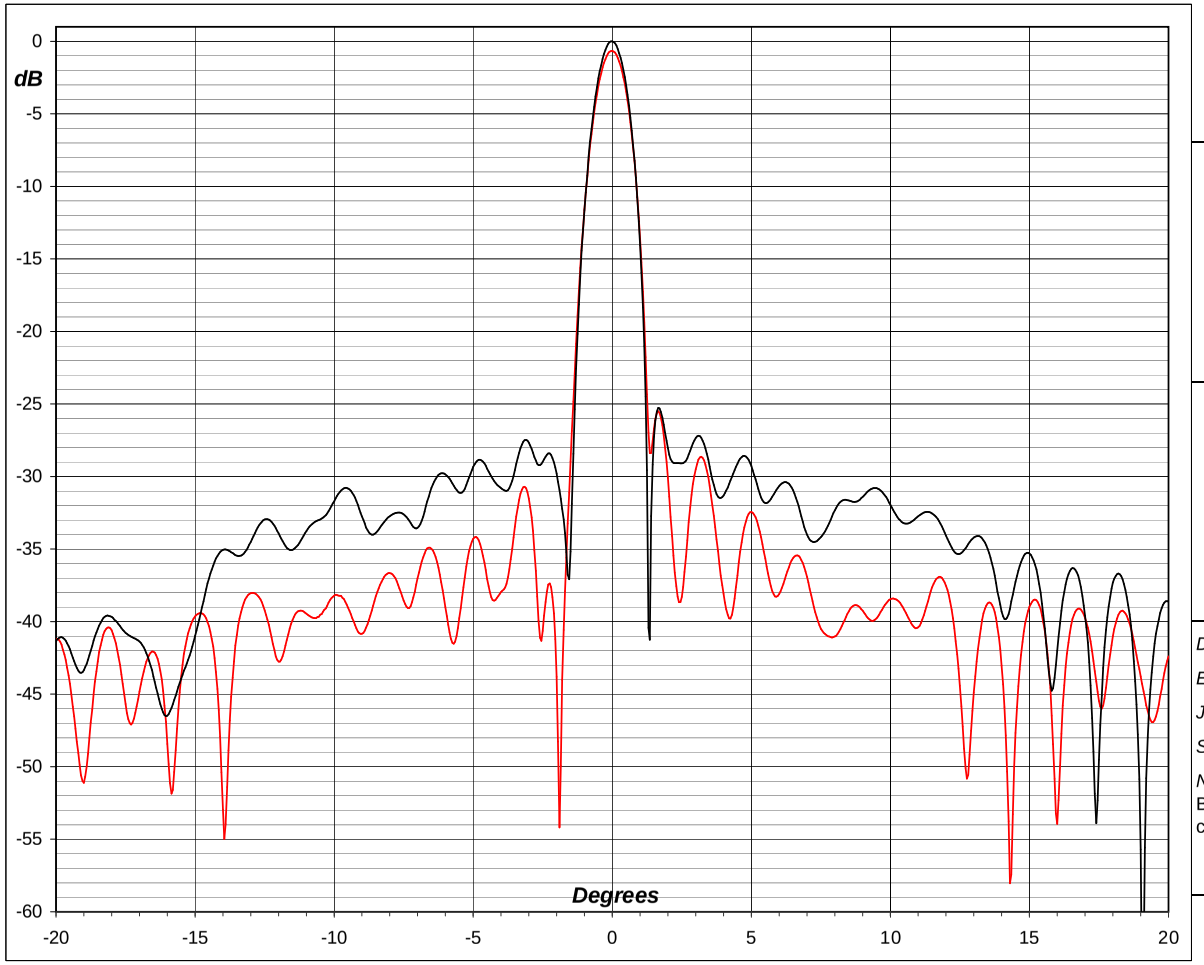

Q-par Angus Ltd
IDEAS ENGINEERED
Tel: +44 (0)1568 612138
Web: www.q-par.com
Email sales@q-par.com

FD_049

3 dB beamwidth (°)
1.1

6 dB beamwidth (°)
1.5

10 dB beamwidth (°)
1.9

FD_067

3 dB beamwidth (°)
1.0

6 dB beamwidth (°)
1.4

10 dB beamwidth (°)
1.8

Date 02/08/2011
Engr SD
Job D1977
S/N PRN05780

Notes
Both ports. Copol. Roll cut 90 degrees.

Frequency (GHz)
5.600

Pattern_Plot v1.18 Funtington data

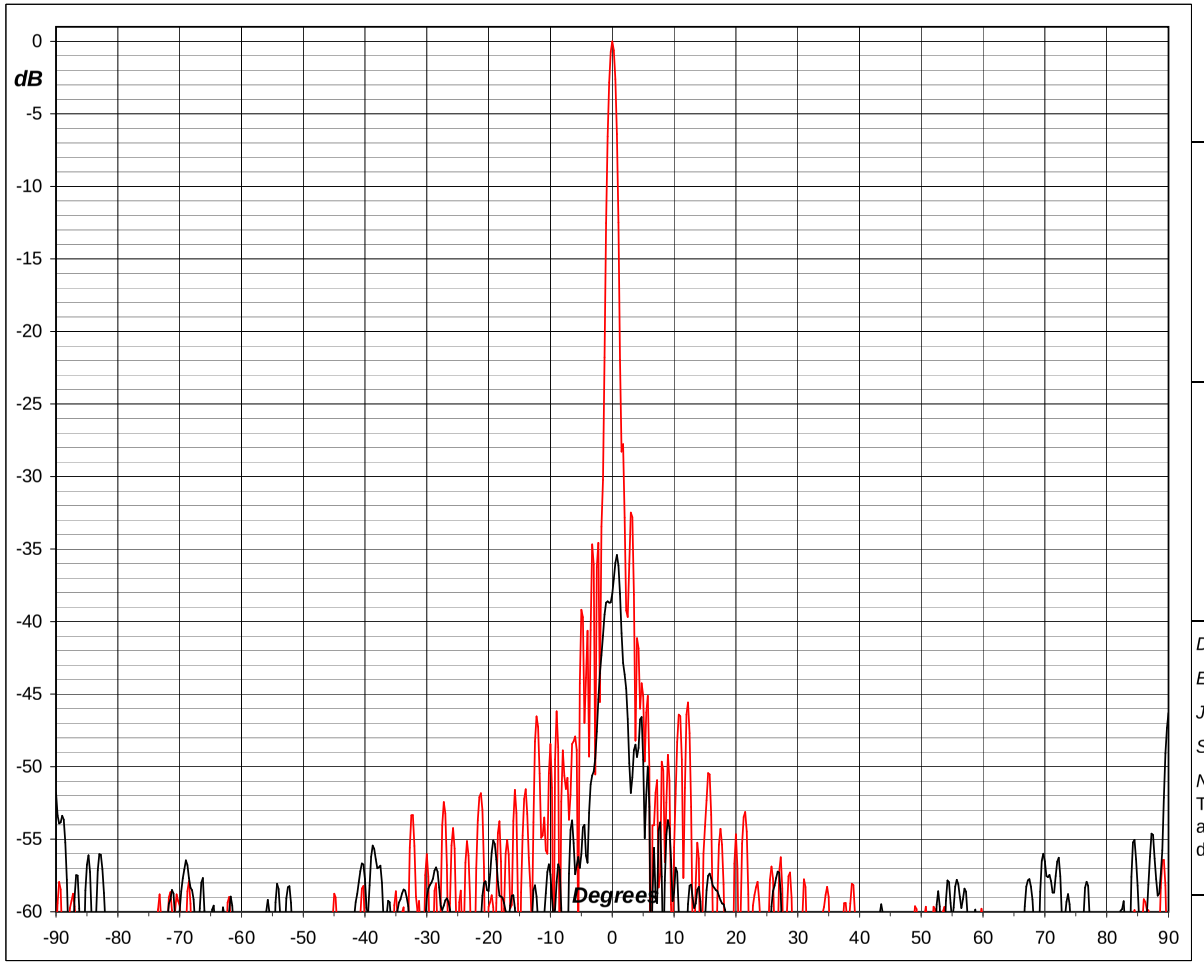

Pattern_Plot v1.18 Funtington data

Q-par Angus Ltd
IDEAS ENGINEERED
Tel: +44 (0)1568 612138
Web: www.q-par.com
Email sales@q-par.com

FD_044

3 dB beamwidth (°)
1.0

6 dB beamwidth (°)
1.4

10 dB beamwidth (°)
1.8

FD_032

3 dB beamwidth (°)
1.4

6 dB beamwidth (°)
3.2

10 dB beamwidth (°)
4.6

Date	03/08/2011
Engr	SD
Job	D1977
S/N	PRN05870

Notes
Through (H) port. Co and X pol. Roll cut 45 degrees.

Frequency (GHz)
5.600

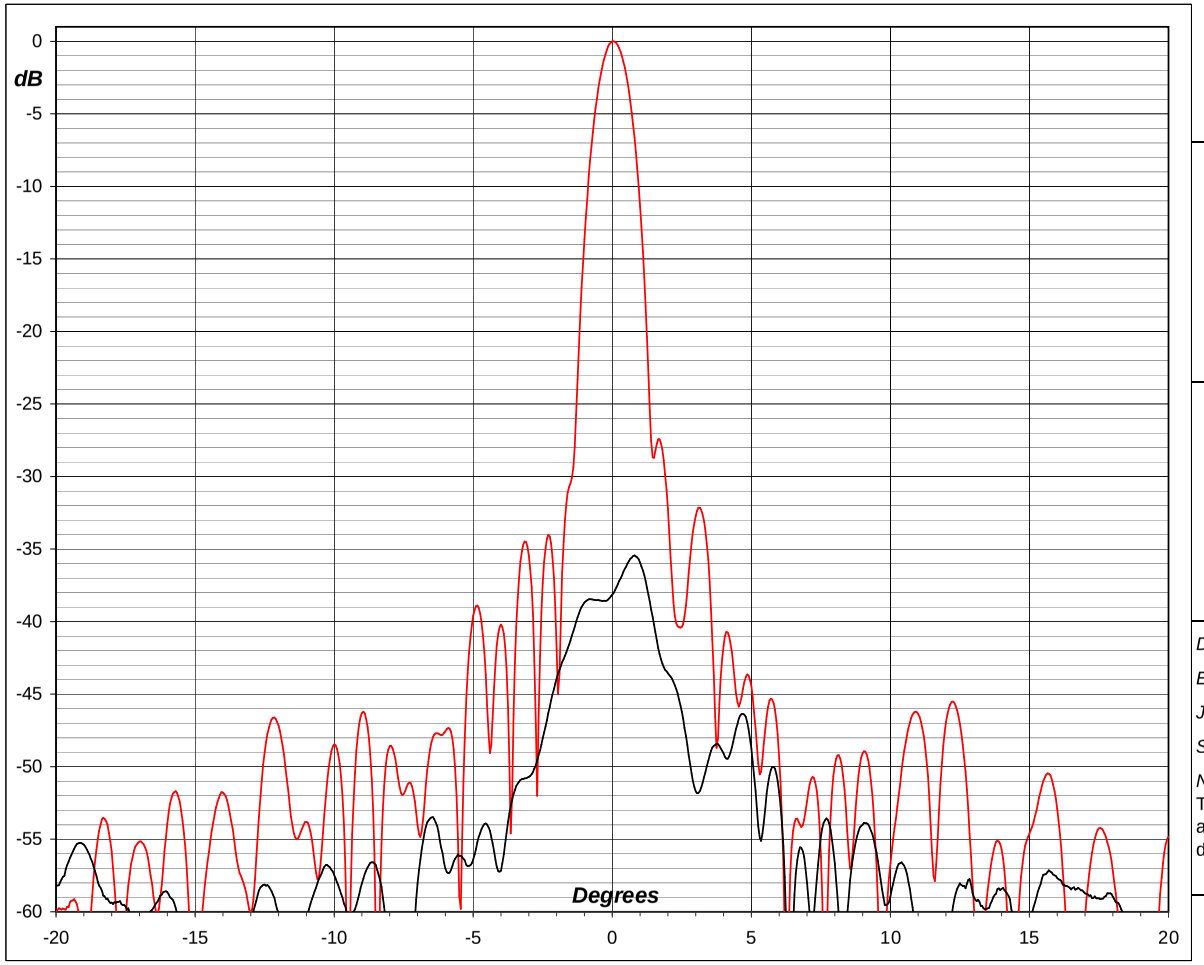

Q-par Angus Ltd
IDEAS ENGINEERED
Tel: +44 (0)1568 612138
Web: www.q-par.com
Email sales@q-par.com

FD_043

3 dB beamwidth (°)
1.0

6 dB beamwidth (°)
1.4

10 dB beamwidth (°)
1.8

FD_031

3 dB beamwidth (°)
1.5

6 dB beamwidth (°)
3.1

10 dB beamwidth (°)
4.6

Date	03/08/2011
Engr	SD
Job	D1977
S/N	PRN05780

Notes
Through (H) port. Co and X pol. Roll cut 45 degrees.

Frequency (GHz)
5.600

Pattern_Plot v1.18 Funtington data

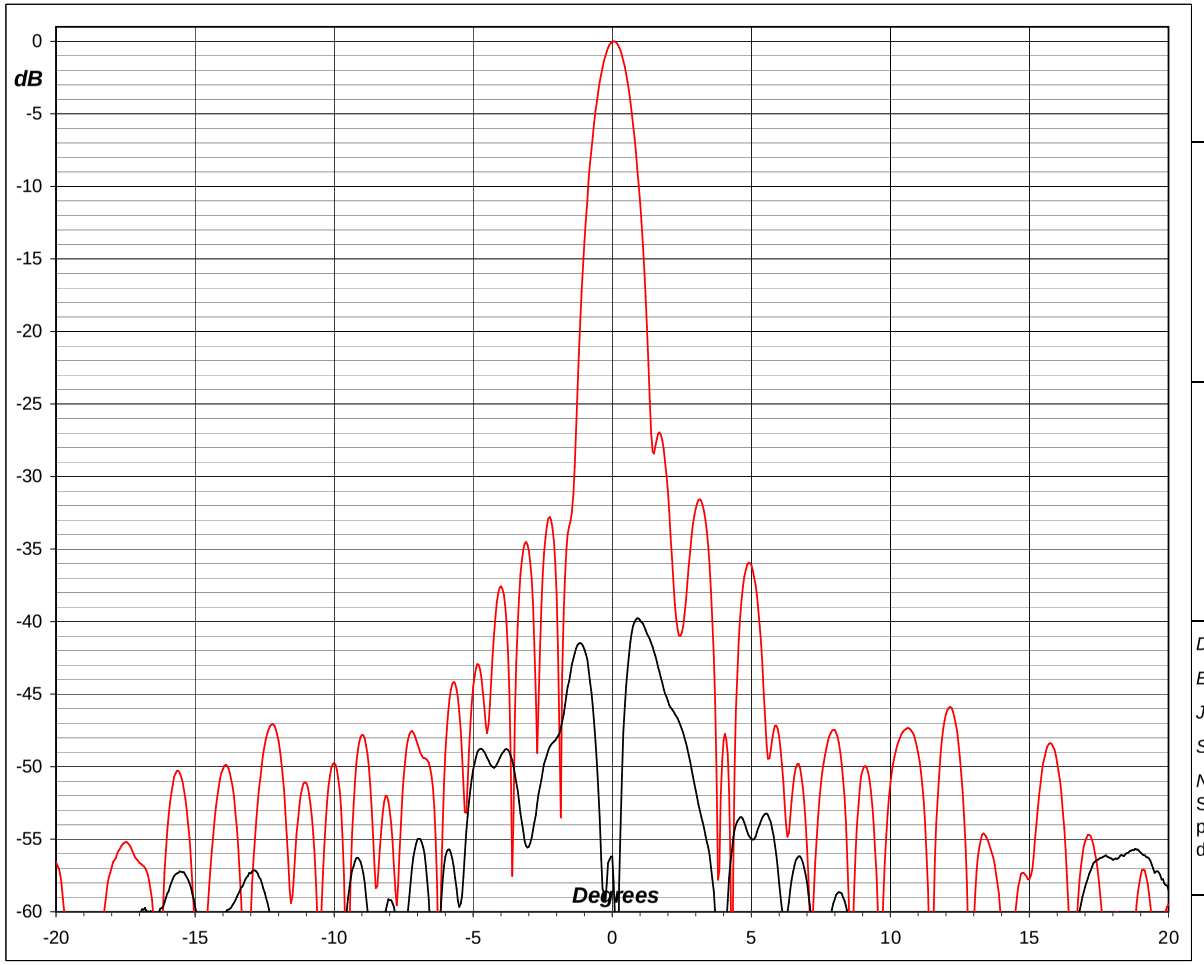

Q-par Angus Ltd
IDEAS ENGINEERED
Tel: +44 (0)1568 612138
Web: www.q-par.com
Email sales@q-par.com

FD_025

3 dB beamwidth (°)
1.0

6 dB beamwidth (°)
1.4

10 dB beamwidth (°)
1.8

FD_037

3 dB beamwidth (°)
1.0

6 dB beamwidth (°)
1.6

10 dB beamwidth (°)
2.4

Date 03/08/2011
Engr SD
Job D1977
S/N PRN05780

Notes
Side (V) port. Co and X pol. Roll cut 45 degrees.

Frequency (GHz)
5.600

Pattern_Plot v1.18 Funtington data

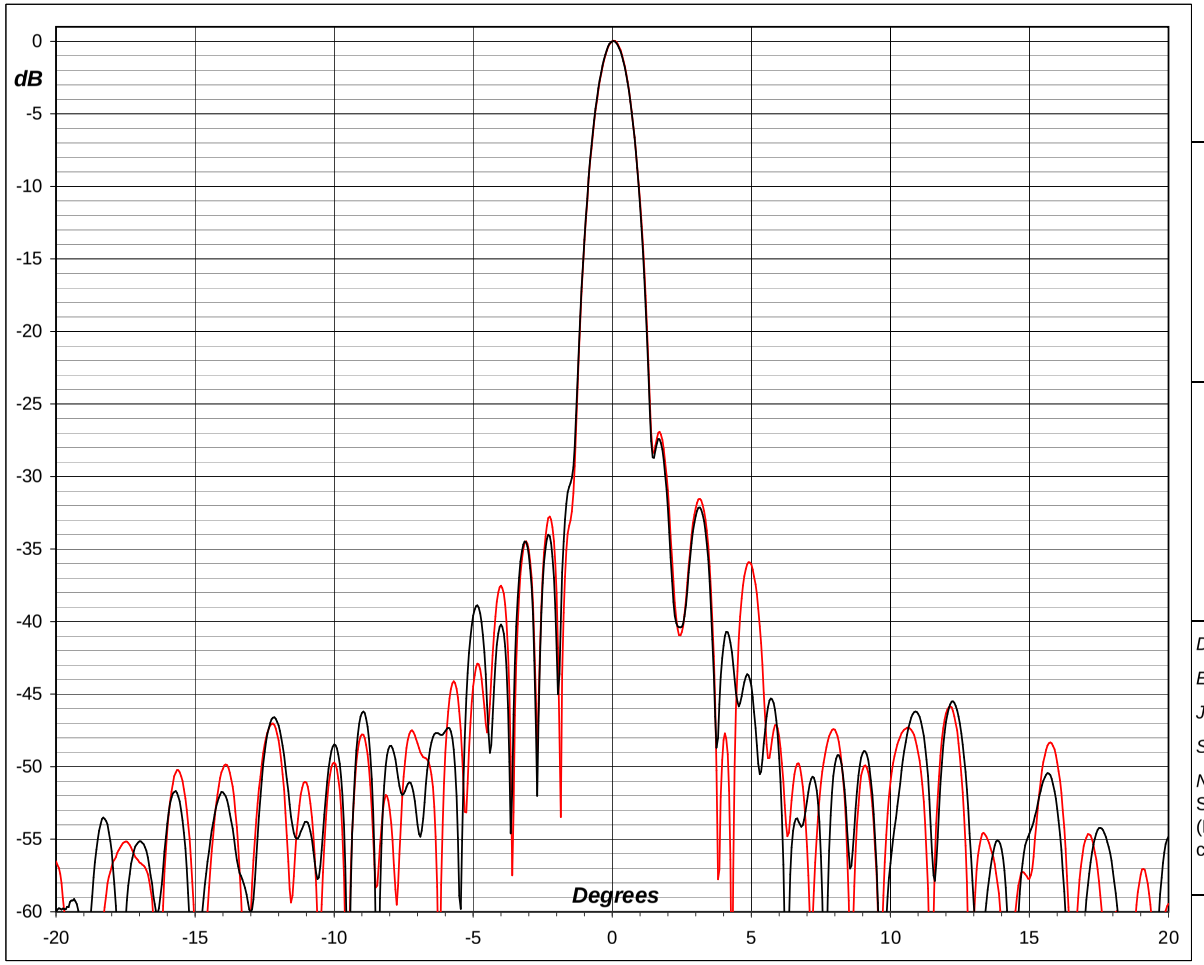

Q-par Angus Ltd
IDEAS ENGINEERED
Tel: +44 (0)1568 612138
Web: www.q-par.com
Email sales@q-par.com

FD_025

3 dB beamwidth (°)
1.0
6 dB beamwidth (°)
1.4
10 dB beamwidth (°)
1.8

FD_043

3 dB beamwidth (°)
1.0
6 dB beamwidth (°)
1.4
10 dB beamwidth (°)
1.8

Date	03/08/2011
Engr	SD
Job	D1977
S/N	PRN05780

Notes
Side (V) and Through (H) ports. Copol. Roll cut 45 degrees.

Frequency (GHz)
5.600

Pattern_Plot v1.18 Funtington data